ACTIVE FLOW CONTROL STUDIES AT MACH 5: MEASUREMENT AND COMPUTATION

A thesis submitted to the University of Manchester
for the degree of Doctor of Philosophy
in the Faculty of Engineering and Physical Sciences

2011

By
Erinc Erdem
School of Mechanical, Aerospace and Civil Engineering

Contents

List of Tables **5**

List of Figures **6**

Nomenclature **17**

Abstract **23**

Declaration **25**

Copyright **26**

Acknowledgements **27**

1 Introduction **29**

1.1 Transverse jets in high speed crossflow 30

1.1.1 Scramjet combustors 30

1.1.2 Thrust vector control systems 33

1.1.3 Reaction control jets 36

1.1.4 Flowfield features of transverse jets in high-speed crossflows 37

1.1.5 CFD studies of transverse jets in high speed crossflows . . 41

1.2 Roughness effects in high speed flows 43

1.3 Energy deposition for blunt body shock wave moderation 44

1.3.1 Microwave radiation 52

1.3.2 Laser energy deposition 54

1.3.3 Electric discharges 57

1.4 Aims and objectives 60

1.5 Overview of the thesis 60

2 Experimental and Numerical Methodologies **62**
2.1 University of Manchester HSST 62
2.2 Flow diagnostics 66
2.2.1 Pressure and temperature measurements 66
2.2.2 Schlieren photography 67
2.2.3 Oil dot visualisation 68
2.2.4 3-component force measurements 69
2.2.5 Particle image velocimetry (PIV) measurements 69
2.3 Calibration of HSST 72
2.4 Experimental setup for transverse jets in high speed cross flow . . 78
2.4.1 Model 79
2.5 Experimental setup for energy deposition for drag reduction . . . 82
2.5.1 Axisymmetric models 82
2.5.2 High voltage arc discharge generation 83
2.5.3 Electrode arrangement 84
2.5.4 Laser focusing arrangement 84
2.6 Numerical considerations 85
2.6.1 Numerical solver 86
2.6.2 Turbulence Model and solver parameters 88

3 Transverse Jets at Mach 5 Cross Flow **91**
3.1 Experimental test campaign 91
3.1.1 Baseline tests 93
3.1.2 Effect of unit Reynolds number 114
3.1.3 Effect of injectant gas 120
3.1.4 Effect of roughness 144
3.2 Numerical campaign 151
3.2.1 Spaid and Zukoski Case 151
3.2.2 Three dimensional case 165

4 Energy Deposition Studies **171**
4.1 Baseline tests 171
4.1.1 Experimental test campaign 171
4.1.2 Numerical simulations 178
4.1.3 Comparison of experiments with CFD 192
4.2 Energy deposition via electric arc discharge 194

4.2.1 Tests without discharge 194
4.2.2 Tests with discharge 195
4.3 Energy deposition via laser focusing 204

5 Conclusion and Future Recommendations 208
5.1 Transverse jets at Mach 5 cross flow 208
5.2 Energy deposition 210
5.3 Future recommendations 211

Bibliography 213

A Flat Plate Theory in Hypersonic Flow 223
A.1 Hypersonic viscous interactions 223
A.2 Exact solutions from Van Driest 225
A.3 Reference temperature concept and Reynolds analogy 226

B Experimental Uncertainty Calculation 229

C Publication Information 231
C.1 Journal articles 231
C.2 Conference articles 231

List of Tables

2.1 HSST calibration conditions at Mach 5. 73
2.2 Calibration results 79
2.3 Free stream conditions at Mach 5. 79

3.1 Experimental test conditions. 94
3.2 Experimental boundary layer thicknesses (δ), Mach disc heights (h) and separation lengths (x_{sep}) tests 1-3. 98
3.3 Experimental boundary layer thicknesses (δ), Mach disc heights (h) and separation lengths (x_{sep}) for tests 4-9. 118
3.4 Experimental boundary layer thicknesses (δ), Mach disc heights (h) and separation lengths (x_{sep}) for tests 10-15. 124
3.5 Particle characteristics for transverse jets for tests 1-3 and tests 10-15. 130
3.6 Experimental boundary layer thicknesses (δ), Mach disc heights (h) and separation lengths (x_{sep}) for tests 16-24. 149
3.7 Flow conditions by Spaid and Zukoski [1]. 155
3.8 M_1 and p_1 values with boundary layer properties for Case 7. . . . 155
3.9 Upstream flow conditions, Mach disc height and non-dimensional transition locations and separation lengths. 164
3.10 Computational grid parameters. 167

4.1 Computational grid parameters. 180
4.2 Drag force comparison of the models (Baseline configuration). All the values are in N. 193
4.3 Drag force comparison of the truncated cone-cylinder models without and with discharge. All the values are in N. 204

List of Figures

1.1 Compressible shear layer diagram and nomenclature by Papamoschou [17]. 31
1.2 Mixing features of an underexpanded transverse injection into a supersonic cross flow by BenYakar [18]. 32
1.3 Mixing schematics of injection/flame-holding schemes for supersonic combustors; a) underexpanded fuel injection normal to the crossflow, b) fuel injection at angle, c) injection behind a sudden expansion produced by a step by Ben Yakar [18]. 34
1.4 Top: SITVC flowfield inside a rocket nozzle by Balu [27]; bottom: bow shock and recompression shock structures with non-dimensional pressure distribution inside a rocket nozzle by Masuya et al. [8]. 35
1.5 Flowfield around a missile geometry in the presence of lateral control jet by Seiler et al. [32]. 37
1.6 Two dimensional transverse slot injection flow field features by [1]. 38
1.7 3-D perspective of the averaged features of the flowfield by Gruber [20]. 40
1.8 Effects of finite span nozzles in jet in uniform cross flow by Cassell [40]. 40
1.9 Roughness effects on turbulent boundary layers by Babinsky and Inger [55]; left: intermediate roughness regime $10 < k^+ < 70$, right: fully rough regime $k^+ > 70$. 45
1.10 Left: roughness effects on turbulent compression corner flows, right: Schlieren visualisation of compression corner flows at Mach 8.2 with smooth and rough walls by Prince [56] S:separation, R: reattachment. 46
1.11 Counterflow plasma jet injection by Shang et al. [62]. 47

1.12 Len's effect by Zheltovodov [70]. 50
1.13 Temporal behaviour of localised energy deposition. 51
1.14 Left: Schlieren and chemiluminescent images of the MW/blunt body interaction, right: corresponding numerical schlieren images by Kolesnichenko et al. [67]. 53
1.15 Temporal Behaviour of Surface Pressure For Nd: YAG Laser Energy Deposition by Adelgren et al. [75]. 55
1.16 Top: virtual spikes at different energy deposition frequencies, bottom: energy trade-off for energy deposition over truncated cones by Sakai et al. [78]. 56
1.17 Sequential Schlieren photographs of the interaction between the pulsed laser deposition and blunt body flow field in hypersonic flow by Oliveira et al. [80]. 57
1.18 The flow model proposed by Satheesh and Jagadeesh [82] showing the interaction between the wake of the heated channel and consequent compression waves. 59
1.19 Effects of external flow heating upstream of a blunt body; a: global effect, b: localized hot-spike (or thermal-spike) effect by Schulein and Zheltovodov [83]. 59

2.1 University of Manchester HSST schematic layout. 64
2.2 Test section of HSST with a cone-cylinder model placed on a sting. 64
2.3 Unit Re number variation for different stagnation temperatures and pressures. 65
2.4 Unit Re number variation with freestream Mach number for fixed reservoir conditions. 66
2.5 Schematic setup of Schlieren visualisation with DAQ architecture. 68
2.6 Left: the picture of force balance with arc system; right: the picture of DSCU. 69
2.7 Schematic of PS-10 powder seeder device. 70
2.8 Schematic of pitot rake. 72
2.9 Time histories of stagnation pressure and temperature signals with a typical pitot signal, note the right axis for stagnation temperature. 73
2.10 Top: time history of p_{pitot} signal non-dimensionalised by p_0, bottom: frequency content of the pitot pressure signal. 75

2.11 Time history of stagnation temperature signal with theoretical first order estimation for a thermocouple behaviour with τ=0.6sec. . . 76
2.12 Schlieren pictures during the test run, vertical pitot rake at 2mm from the nozzle exit. 77
2.13 Representative Schlieren pictures with different orientations and streamwise locations of the pitot rake; left: horizontal at 2mm from the nozzle exit, middle: vertical 62mm from the nozzle exit, right: horizontal 62mm from the nozzle exit. 77
2.14 Minimum test section available area for models. 78
2.15 Technical drawing of the model specifying dimensions. 80
2.16 Left: flat plate model placed inside test section (smooth case), right: flat plate covered with P1000 sandpaper. 80
2.17 Oil dot visualisation setup. 81
2.18 PIV setup. 82
2.19 Left: axisymmetric cone-cylinder models, right: axisymmetric cone-cylinder models with flare. 83
2.20 Electrodes arrangement inside test section. 85
2.21 Laser deposition arrangement inside test section. 86
2.22 Cell nomenclature 87
2.23 Green-Gauss node based gradient evaluation stencil 87

3.1 High speed schlieren visualisation of the sonic transverse jet captured at 3000fps with 20μsec exposure time. 92
3.2 Schlieren visualisation of the flowfield in the presence of the sonic transverse jet with three different momentum flux ratios; top: test 1, middle: test 2, bottom: test 3 with annotated flow structures. . 95
3.3 Top: Correlation of viscous-dominated supersonic/hypersonic flat plate transition data: transition Reynolds number, Re_{tr} versus unit Reynolds number by Mach number, $Re/m/M$; bottom: Correlation of leading edge bluntness-dominated supersonic/hypersonic flat plate transition data: Mx_{tr}/b against Re_b/M^2 by Simeonides [93]. 96
3.4 Left: Mach disc height non-dimensionalised by jet diameter versus momentum flux ratio; right: separation distance non-dimensionalised by jet diameter versus momentum flux ratio for tests1-3. 99

3.5 Time histories of tunnel and jet stagnation pressure signals with a representative wall static pressure signal. 100
3.6 High speed schlieren visualisation of the sonic transverse jet captured at 16000fps with 1 μsec exposure time and annotated flow structures. 101
3.7 Three instantaneous schlieren images of air injection; top: test 1, middle: test 2, bottom: test 3. 102
3.8 RMS of instantaneous schlieren images of air injection of a time series of 1000 samples; top: test 1, middle: test 2, bottom: test 3 with annotated flow structures. 103
3.9 PIV raw image visualisation of the sonic transverse jet captured at 15fps. Only first frames of the PIV recording are shown. 104
3.10 Three instantaneous raw PIV images and associated vector fields for test 1. 105
3.11 Three instantaneous raw PIV images and associated vector fields for test 2. 106
3.12 Three instantaneous raw PIV images and associated vector fields for test 3. 107
3.13 Averaged flow field velocity magnitude contours; top: test 1, middle: test 2, bottom: test 3. 108
3.14 Averaged flow field turbulence intensity (TI) contours; top: test 1, middle: test 2, bottom: test 3. 109
3.15 Overlaid RMS images of 1000 instantaneous schlieren images on PIV turbulence intensity (TI) contours; top: test 1, middle: test 2, bottom: test 3. 111
3.16 Non dimensional wall pressure distribution against non dimensional distance at the centreline (top), $z/djet$=4.77 (bottom left) and $z/djet$=9.1 (bottom right) for test 1-3. 112
3.17 Oil dot visualisation of the sonic transverse jet captured at 30fps with 0.1msec exposure time for test 3. 114
3.18 Oil dot visualisation of the sonic transverse air jet; top: test 1, middle: test 2, bottom: test 3. 115

3.19 Schlieren visualisation of the flowfield in the presence of the sonic transverse jet with three different momentum flux ratios; top: test 4, middle: test 5, bottom: test 6 with annotated flow structures with J values of 1.26, 3.02 and 5.77 respectively. 116
3.20 Schlieren visualisation of the flowfield in the presence of the sonic transverse jet with three different momentum flux ratios; top: test 7, middle: test 8, bottom: test 9 with annotated flow structures with J values of 1.37, 3.21 and 6.18 respectively. 117
3.21 Left: Mach disc height non-dimensionalised by jet diameter versus momentum flux ratio; right: separation distance versus Mach disc height for tests 1-9. 118
3.22 Non dimensional wall pressure distribution against non dimensional distance at the centreline (top), $z/djet$=4.77 (bottom left) and $z/djet$=9.1 (bottom right) for tests 4-6. 120
3.23 Non dimensional wall pressure distribution against non dimensional distance at the centreline (top), $z/djet$=4.77 (bottom left) and $z/djet$=9.1 (bottom right) for tests 7-9. 121
3.24 Non dimensional wall pressure distribution against non dimensional distance for different unit Reynolds numbers at the centreline with increasing momentum flux ratio from top to bottom. . 122
3.25 Schlieren visualisation of the flowfield in the presence of the Helium sonic transverse jet with three different momentum flux ratios; top: test 10, middle: test 11, bottom: test 12 with annotated flow structures with J values of 1.33, 2.65 and 3.96 respectively. 123
3.26 Schlieren visualisation of the flowfield in the presence of the Carbon Dioxide sonic transverse jet with three different momentum flux ratios; top: test 13, middle: test 14, bottom: test 15 with annotated flow structures with J values of 1.13, 2.64 and 3.61 respectively. 124
3.27 Left: Mach disc height non-dimensionalised by jet diameter versus momentum flux ratio; right: separation distance versus Mach disc height for tests 1-3 and tests 13-15. 125
3.28 Three instantaneous schlieren images of Helium injection; top: test 10, middle: test 11, bottom: test 12. 126

3.29 Three instantaneous schlieren of CO_2 injection; top: test 13, middle: test 14, bottom: test 15. 127
3.30 RMS of instantaneous schlieren images of Helium injection of a time series of 1000 samples; top: test 10, middle: test 11, bottom: test 12 with annotated flow structures. 128
3.31 RMS of instantaneous schlieren images of CO_2 injection of a time series of 1000 samples; top: test 13, middle: test 14, bottom: test 15 with annotated flow structures. 129
3.32 Three instantaneous raw PIV images and associated vector fields for test 10. 131
3.33 Three instantaneous raw PIV images and associated vector fields for test 11. 132
3.34 Three instantaneous raw PIV images and associated vector fields for test 12. 133
3.35 Three instantaneous raw PIV images and associated vector fields for test 13. 134
3.36 Three instantaneous raw PIV images and associated vector fields for test 14. 135
3.37 Three instantaneous raw PIV images and associated vector fields for test 15. 136
3.38 Averaged flow field velocity magnitude contours; top: test 10, middle: test 11, bottom: test 12. 137
3.39 Averaged flow field turbulence intensity (TI) contours; top: test 10, middle: test 11, bottom: test 12. 138
3.40 Averaged flow field velocity magnitude contours; top: test 13, middle: test 14, bottom: test 15. 139
3.41 Averaged flow field turbulence intensity (TI) contours; top: test 13, middle: test 14, bottom: test 15. 140
3.42 Non dimensional wall pressure distribution against non dimensional distance at the centreline (top), $z/djet$=4.77 (bottom left) and $z/djet$=9.1 (bottom right) for tests 10-12. 141
3.43 Non dimensional wall pressure distribution against non dimensional distance at the centreline (top), $z/djet$=4.77 (bottom left) and $z/djet$=9.1 (bottom right) for tests 13-15. 142

3.44 Non dimensional wall pressure distribution against non dimensional distance for air, $Helium$ and CO_2 injections at the centreline with increasing momentum flux ratio from top to bottom. 143
3.45 Oil dot visualisation of the sonic transverse Helium jet; top: test 10, middle: test 11, bottom: test 12. 144
3.46 Oil dot visualisation of the sonic transverse Carbon Dioxide jet; top: test 13, middle: test 14, bottom: test 15. 145
3.47 Schlieren visualisation of the flowfield in the presence of the sonic transverse jet with P1000 sand paper and three different momentum flux ratios; top: test 16, middle: test 17, bottom: test 18 with annotated flow structures with J values of 1.17, 2.78 and 5.25 respectively. 146
3.48 Schlieren visualisation of the flowfield in the presence of the sonic transverse jet with P400 sand paper and three different momentum flux ratios; top: test 19, middle: test 20, bottom: test 21 with annotated flow structures with J values of 1.19, 2.77 and 5.30 respectively. 147
3.49 Schlieren visualisation of the flowfield in the presence of the sonic transverse jet with P120 sand paper and three different momentum flux ratios; top: test 22, middle: test 23, bottom: test 24 with annotated flow structures with J values of 1.20, 2.76 and 5.26 respectively. 148
3.50 Left: Mach disc height non-dimensionalised by jet diameter versus momentum flux ratio; right: separation distance versus Mach disc height for tests 1-3 and tests 16-24. 149
3.51 Non dimensional wall pressure distribution against non dimensional distance at the centreline (top), z/d_{jet}=4.77 (bottom left) and z/d_{jet}=9.1 (bottom right) for tests 16-18. 151
3.52 Non dimensional wall pressure distribution against non dimensional distance at the centreline (top), z/d_{jet}=4.77 (bottom left) and z/d_{jet}=9.1 (bottom right) for tests 19-21. 152
3.53 Non dimensional wall pressure distribution against non dimensional distance at the centreline (top), $z/djet$=4.77 (bottom left) and $z/djet$=9.1 (bottom right) for tests 22-24. 153

3.54 Non dimensional wall pressure distribution against non dimensional distance for different rough surfaces at the centreline with increasing momentum flux ratio from top to bottom. 154
3.55 Non-dimensional pressure (top), skin friction coefficient (middle) and wall y^+ (bottom) distributions at the wall for successive grid refinement in y direction. 157
3.56 Non-dimensional pressure (top) and skin friction coefficient (bottom) distributions at the wall for successive grid refinement in x direction. 158
3.57 Non-dimensional pressure (top) and skin friction coefficient (bottom) distributions at the wall for different jet turbulence intensities. 159
3.58 Non-dimensional pressure (top) and skin friction coefficient (bottom) distributions at the wall for different inlet turbulence intensities. 160
3.59 Mach number contours for case 7. 161
3.60 Streamlines around the jet injection port for case 7. 161
3.61 Comparison of non-dimensional wall pressure distributions for cases 1-3. 162
3.62 Comparison of non-dimensional wall pressure distributions for cases 4-7. 162
3.63 Skin friction coefficient distributions for cases 1-3. 162
3.64 Skin friction coefficient distributions for cases 4-7. 163
3.65 Mach disc height non-dimensionalised by undisturbed boundary layer thickness versus momentum flux ratio. 164
3.66 Separation location versus Mach disc height. 165
3.67 Computational domain and mesh for transverse injection on a flat plate. 166
3.68 Non-dimensional pressure (top) and skin friction coefficient (bottom) distributions at the centreline for successive grid refinement. 168
3.69 Computed Mach number contours on the centreline (top), isometric view of Mach number contours (middle) and density gradient contours in vertical direction, $\partial\rho/\partial y$, on the centreline (bottom) for medium grid. 169
3.70 Computed density gradient contours in vertical direction, $\partial\rho/\partial y$, (top) and experimental schlieren image (bottom). 170

4.1 Schlieren visualisation of cone-cylinder models, left: no truncation, middle: $d_t/d_b = 0.5$, right: $d_t/d_b = 0.75$. 172
4.2 Schlieren visualisation of cone-cylinder models with flare, left: no truncation, right: $(d_t/d_b = 0.75)$ 172
4.3 Top left: Schematic of a separated-flow pattern for a shock wave boundary layer interaction at a ramp by Bertin [102], top right: PSP visualisation of a truncated cone-cylinder model with flare by Yang et al. [104], bottom: schlieren visualisation of a compression corner in hypersonic flow by Simeonides and Haase [103]. 174
4.4 High speed schlieren visualisation of cone-cylinder model with flare captured at 15000fps with 4μsec exposure time. 175
4.5 High speed schlieren visualisation of cone-cylinder model with flare captured at 15000fps with 4μsec exposure time, annotated flow structures. 175
4.6 High speed schlieren visualisation of truncated cone-cylinder model with flare captured at 15000fps with 4μsec exposure time. 176
4.7 High speed schlieren visualisation of truncated cone-cylinder model with flare captured at 15000fps with 4μsec exposure time, annotated flow structures. 177
4.8 RMS of 100 schlieren images of cone-cylinder models with flare, left: no truncation, right: $(d_t/d_b = 0.75)$; white regions indicate higher rms levels. 177
4.9 Oil dot visualisation of cone-cylinder models with flare, left: no truncation, right: $(d_t/d_b = 0.75)$ 177
4.10 Drag force histories of all models during the test runs. 178
4.11 Computational domain and mesh for truncated cone-cylinder with flare model (top), mesh distributions in nose region (bottom left), flare junction region (bottom middle) and base region (bottom right). 179
4.12 Non-dimensional pressure (top), axial (middle) and radial (bottom) skin friction coefficient distributions at the wall of the truncated cone-cylinder model with flare for successive grid refinement. 183
4.13 Non-dimensional pressure distributions at the axis (left) and at the nose (right) of the truncated cone-cylinder model with flare for successive grid refinement. 184

4.14 Mach number contours for medium and fine computational grids. 184
4.15 Non-dimensional pressure (top), axial (middle) and radial (bottom) skin friction coefficient distributions at the wall of truncated cone-cylinder model with flare for different incoming turbulence intensities. 185
4.16 Non-dimensional pressure (top), axial (middle) and radial (bottom) skin friction coefficient distributions at the wall of truncated cone-cylinder model with flare for two different wall temperature boundary conditions. 186
4.17 Skin friction (axial and radial) coefficient and Stanton number distributions at the wall of truncated cone-cylinder model with flare for 295K wall temperature. 187
4.18 Turbulence intensity contours of truncated cone-cylinder model with flare. 187
4.19 Non-dimensional pressure (top), axial (middle) and radial (bottom) skin friction coefficient distributions at the wall for successive grid refinement. 189
4.20 Non-dimensional pressure (top), axial (middle) and radial (bottom) skin friction coefficient distributions at the wall of cone-cylinder model with flare for two different wall temperature boundary conditions. 190
4.21 Skin friction (axial and radial) coefficient and Stanton number distributions at the wall of cone-cylinder model with flare for 295K wall temperature. 191
4.22 Turbulence intensity contours of cone-cylinder model with flare. . 191
4.23 Numerical and theoretical skin friction coefficient and Stanton number distributions at the wall of cone-cylinder model with flare for 295K wall temperature. 192
4.24 Non-dimensional pressure (top) and skin friction coefficient (bottom) distributions at the wall for successive grid refinement in x direction. 192
4.25 Mach contours of cone models, left: no truncation, middle: $d_t/d_b = 0.5$, right: $d_t/d_b = 0.75$. 193
4.26 Schlieren visualisation of the effect of electrodes on the flow over the truncated cone-cylinder with $d_t/d_b = 0.75$ during the test. . . 196

4.27 Voltage history during a test run with discharge over a truncated cone-cylinder with $d_t/d_b = 0.75$. 197
4.28 Schlieren visualisation of the effect of arc discharge on the flow over the truncated cone-cylinder with $d_t/d_b = 0.75$ during the test. 198
4.29 Comparison of discharge-on case with discharge-off case in terms of averaged and rms schlieren images over a truncated cone-cylinder with $d_t/d_b = 0.75$ and $l/d_t = 1.3$. 199
4.30 Comparison of discharge-on case with discharge-off case in terms of drag force histories over the truncation cone-cylinder with $d_t/d_b = 0.75$; top left: $l/d_t = 0.9$, top right: $l/d_t = 1.3$, bottom left: $l/d_t = 1.5$, bottom right: $l/d_t = 1.8$. 201
4.31 Frequency content of the drag signals of the truncated cone with $d_t/d_b = 0.75$ with/without discharge for $l/d_t = 1.3$. 202
4.32 Comparison of discharge-on case with discharge-off case in terms of drag force histories over the truncation cone-cylinder with $d_t/d_b = 0.5$; top left: $l/d_t = 0.9$, top right: $l/d_t = 1.3$, bottom middle: $l/d_t = 1.5$. 203
4.33 Comparison of discharge-on case with discharge-off case in terms of drag force histories over the flared truncation cone-cylinder with $d_t/d_b = 0.75$. 203
4.34 The effectiveness of arc discharge on truncated models against distance between the electrodes and the frontal area. 205
4.35 Schlieren visualisation of the effect of the focussed laser deposition on the truncation cone-cylinder with $d_t/d_b = 0.75$ and $l/d_t = 1.3$. 206

A.1 Hypersonic viscous interaction phenomenon by Anderson [94]. . . 224
A.2 Flat plate skin friction coefficients (left) and Stanton numbers (right) by van Driest [108] 226

Nomenclature

Roman Symbols

A	area, m^2
a	speed of sound, m/s
b	leading edge thickness, m
C	Chapman-Rubesin constant
c	constant
c_d	discharge coefficient
c_f	skin friction coefficient
c_H	heat transfer coefficient
c_p	pressure coefficient
cp	specific heat at constant pressure, $J/(kg.K)$
D	Drag force, N, diffusivity term
d	diameter, m
Eff	Efficiency
G	Production term
h	Mach disc height, m
Isp	specific impulse, $1/s$
J	momentum flux ratio

K	hypersonic similarity parameter
Kn	Knudsen number
l	distance between model and spot, m
M	Mach number
n	nodes
P	perimeter, m
p	pressure, Pa or mbar
Pr	Prandtl number
Q	energy, J
q	heat transfer, W/m^2
Re	Reynolds number
Re/m	unit Reynolds number, $1/m$
R	gas constant, $J/(kg.K)$
r	recovery factor, radius, m
$\bar{s}$	displacement vector
Sk	Stokes number
T	temperature, K
t	time, sec
U	velocity, m/s
u	streamwise velocity, m/s
x	streamwise distance, m
y	vertical distance, m
z	spanwise distance, m

Greek Symbols

β	bluntness parameter
$\bar{\chi}$	viscous interaction parameter
δ	shear layer thickness, boundary layer thickness, m
δ^*	displacement thickness, m
δ_e	ratio of the pulse duration
δ_i	ratio of the pulse cycle
ϵ	turbulent dissipation rate, m^2/s^3
γ	specific heat ratio
κ	turbulent kinetic energy, m^2/s^2
μ	viscosity, $Pa.s$
θ	momentum thickness, m, local inclination angle, rad
ϕ	flow variable
ψ	numerical limiter
ρ	density, kg/m^3
τ	shear stress, stress tensor, Pa
τ_e	pulse duration, s
τ_i	total pulse cycle, s
ω	vorticity, $1/s$, specific dissipation rate, $Pa.s$

Subscripts

0	baseline case, stagnation condition
aw	adiabatic wall
b	base

c	convective, cell
d	based on diameter
e	boundary layer edge
f	face
i	index, injection
∞	free stream
jet	jet
k	turbulent kinetic energy
n	nose
pitot	pitot
p	particle, primarily
reattach	reattachment
sec	test section
sep	separation
spot	energy spot
s	secondary
supply	supply conditions
trans	transition
t	turbulent, truncation
theo	theoretical
vac	vacuum
w	wall
x	based on streamwise distance

Superscripts

*	at reference temperature
+	wall coordinate

Acrynoms

CFD	Computational Fluid Dynamics
CFL	Courant-Friedrichs-Lewy
DES	Detached Eddy Simulation
DSCM	Digital Signal Conditioning Manager
DSCU	Digital Signal Conditioning Units
FANS	Favre Averaged Navier-Stokes
FFT	Fast Fourier Transform
FoV	Field of View
HSST	High Supersonic Tunnel
LDV	Laser Doppler Velocimetry
LES	Large Eddy Simulation
MW	Micro Wave
PDV	Primary Downstream Vortices
PIV	Particle Image Velocimetry
PTU	Programmable Timing Unit
RMS	Root Mean Square
RSM	Reynolds Stress Model
SDV	Secondary Downstream Vortices
SITVC	Secondary Injection Thrust Vector Control

SOU	Spatially Accurate Upwind Scheme
SST	Shear Stress Transport
TI	Turbulence Intensity
TUV	Third Upstream Vortex
TVC	Thrust Vector Control

Abstract

The difficulties regarding the control of high velocity flying vehicles in supersonic/hypersonic flight regime are still prevailing. Whether it is mixing enhancement, side force generation or aerodynamic steering, wall cooling or any other favourable method to control the flow, the resultant effects of different flow control techniques on the associated flowfield demands careful experimental and numerical investigations. Traditional aerodynamic control surfaces are subjected to severe flight conditions and loadings in different flight regimes resulting in impaired the control effectiveness. Active flow control methods serve strong alternative to achieve separation postponement, transition control, lift enhancement, mixing enhancement, drag reduction, turbulence modification and/or noise suppression, etc. This thesis deals with two main active flow control techniques; transverse jets at Mach 5 cross flow and energy deposition using arc discharge at Mach 5 flow. The influence of roughness on the control effectiveness of transverse jet interactions is also examined.

The first objective of this thesis is to investigate experimentally the flow physics of the sonic transverse jets at Mach 5 laminar cross flow both in time averaged and time resolved manner to provide reliable experimental data and better understanding at high Mach numbers. The parameters such as momentum flux ratio, incoming Reynolds number, type of the gas and the surface roughness are studied. The size and structures of the upstream and downstream separation regions and jet penetration characteristics together with jet shear layer behaviour are examined. Moreover CFD simulations are conducted on a two dimensional case of Spaid and Zukoski and the numerical solver/procedure is validated. Then a three dimensional experimental case is simulated to provide greater understanding on the flow physics as well as to cross check measurements.

As the main finding; jet interaction flow field can not be oversimplified and represented with only one parameter that is momentum flux ratio, J, as suggested

by the literature; the incoming Reynolds number, type of injectant and roughness are clearly affecting the interaction resulting in advantages or drawbacks for flow control point of view.

The second objective of this thesis is to investigate experimentally the dynamics between the localised energy spot and the blunt body shock for drag reduction at Mach 5 flow. The localised energy spot is created firstly via steady electric arc struck between two electrodes using a small amount of energy and secondly via pulsed laser focusing with a significant amount of energy. In case of electric discharge, the effects of discharge are evaluated in comparison to no discharge case with the electrodes. The unsteady wake/compression structures are examined between the steadily deposited energy spot and the modified bow shock wave. And for the laser focussing unsteady interaction that is happening in a short duration of time is investigated. The effect of the truncation, the distance between the electrodes and the model as well as the type and amount of the energy input on this phenomenon are examined. Moreover CFD simulations are conducted on the baseline cases to cross check measurements together with theoretical estimates.

As the main finding; the effectiveness of the arc discharge is increasing with increased truncation or the frontal area and when the arc to nose distance is the shortest. However an important thing to note is that energy deposition at shorter distances might result higher stagnation point heating rates which are detrimental. The test campaign clearly renders that the use of small amount of onboard energy to create a local focused thermal spot in front of a vehicle is an efficient way of reducing drag.

Declaration

No portion of the work referred to in this thesis has been submitted in support of an application for another degree or qualification of this or any other university or other institute of learning.

Copyright

i. The author of this thesis (including any appendices and/or schedules to this thesis) owns any copyright in it (the "Copyright") and s/he has given The University of Manchester the right to use such Copyright for any administrative, promotional, educational and/or teaching purposes.

ii. Copies of this thesis, either in full or in extracts, may be made only in accordance with the regulations of the John Rylands University Library of Manchester. Details of these regulations may be obtained from the Librarian. This page must form part of any such copies made.

iii. The ownership of any patents, designs, trade marks and any and all other intellectual property rights except for the Copyright (the "Intellectual Property Rights") and any reproductions of copyright works, for example graphs and tables ("Reproductions"), which may be described in this thesis, may not be owned by the author and may be owned by third parties. Such Intellectual Property Rights and Reproductions cannot and must not be made available for use without the prior written permission of the owner(s) of the relevant Intellectual Property Rights and/or Reproductions.

iv. Further information on the conditions under which disclosure, publication and exploitation of this thesis, the Copyright and any Intellectual Property Rights and/or Reproductions described in it may take place is available from the Head of School of Mechanical, Aerospace and Civil Engineering (or the Vice-President).

Acknowledgements

I am indebted to Dr. K. Kontis for his valuable advice, the technical staff at The University of Manchester for their assistance. Also I am very grateful to the School of MACE, The University of Manchester, for granting the scholarship for my study.

Many thanks go in particular to Ceylan, the love and meaning of my life, for her kind motivations, understanding and support. Without her radiant green eyes this PhD would not come to a conclusion.

I always remain indebted to my parents, Fatma and Hilmi, for their kind supports no matter what happens in my life.

I would also like to thank my friends and my colleagues during these years in the school of MACE; especially Dr. Neel Shah, Leichao Yang, Raffaello Mariani, Dr. Nalleli Gongora-Orozco, Craig Hale, Rasool Erfani, Mark Quinn, etc. Also the provision of equipment by Adrian Walker of EPSRC pool is highly appreciated.

To ***Ceylan*** *and* ***my parents Fatma and Hilmi****;*

Chapter 1

Introduction

Supersonic/hypersonic flight within the atmosphere is of current interest, both military and civilian. Even though it has been become more reachable with the advent of new technologies and progress in propulsion systems, the difficulties regarding the control of high velocity flying vehicles are still prevailing. Traditional aerodynamic control surfaces are extensively utilised for control purposes; therefore are subjected to severe flight conditions and loadings in different flight regimes. In addition, for high altitude flights, these surfaces might not function properly due to low density of air and/or significant aerodynamic heating resulting from different interaction phenomena impairing the control effectiveness. As a consequence alternative ways of flow control have been sought by researchers and groups throughout the years. Several active flow control techniques were developed to achieve separation postponement, transition control, lift enhancement, mixing enhancement, drag reduction, turbulence modification and/or noise suppression using surface heating/cooling, wall injection of lower/higher viscosity fluid, suction, etc. Thorough characterisation of these active flow control techniques and the resultant effects on the associated flowfield demands careful experimental and numerical investigations. The present thesis deals with two active control methods; transverse jets and energy deposition using arc discharge at Mach 5 flow. The influence of roughness on the control effectiveness of transverse jet interactions is also examined.

1.1 Transverse jets in high speed crossflow

Transverse injection into supersonic/hypersonic cross flow has been encountered in many engineering applications ranging from scramjet combustors and solid rocket motor or liquid engine thrust vector control (TVC) systems to high speed flying vehicle reaction control jets. Mixing enhancement for efficient combustion is the goal in scramjet applications whereas in thrust vector control systems and reaction control jet applications the objective is to divert the main flow in order to gain additional side forces. These applications all involve complex three dimensional flow patterns comprising separated regions, shock waves, shear layers and wakes in common. Owing to numerous applications and these complicated flow features, transverse injections over different geometries and various forebodies have been received significant amount of interest for last 50 years. Earlier studies were focused on wind tunnel experiments and the utilisation of conventional measurement techniques such as Schlieren/Shadowgraph photography, wall pressure and concentration measurements to better understand physical phenomena [1, 2, 3, 4, 5, 6]. These studies aimed to assess the effect of injection pressure ratio, location of injection and state of incoming boundary layer and type of injectant gas on transverse jet interaction and penetration in supersonic/hypersonic cross flow. Theoretical studies were also conducted using tools as Blast-wave analogy to model the penetration of the secondary jet into main flow [7]. The blast wave analogy is based on the similarity between the cylindrical unsteady flow produced by the explosion of a line charge and axially symmetrical steady flow, which was applied to the flows about blunt bodies at hypersonic and high supersonic speeds. The flow field is determined by the energy added per unit length of gas, a quantity that, in the usual applications of the theory, is equal to the drag of the body under consideration [7]. However theoretical models hold only for very low injection flow rates and lack generality. Cold flow and static firing tests especially for TVC systems [8, 9, 10] provide important performance data for macroscopic performance estimations. Following sections explain the application areas and the associated flow physics in detail.

1.1.1 Scramjet combustors

Recent studies for scramjet engine combustors mainly focused on the mixing characteristics of crossing streams, namely fuel and air, specifically around fuel

injectors, which are primarily dependent on the growth of the compressible shear layer and turbulence evolution between streams. Several studies of compressible shear layers have provided strong evidence that increasing compressibility affects the mixing layer growth rate [11], stability [12, 13], turbulence levels and turbulent structures [14, 15, 16]. The level of compressibility is described in terms of the convective Mach number, M_c as given in Eq.1.1 based on the definition shown in Fig. 1.1. δ is the shear layer thickness.

$$M_{c_1} = \frac{U_1 - U_c}{a_1}, M_{c_2} = \frac{U_c - U_2}{a_2} \tag{1.1}$$

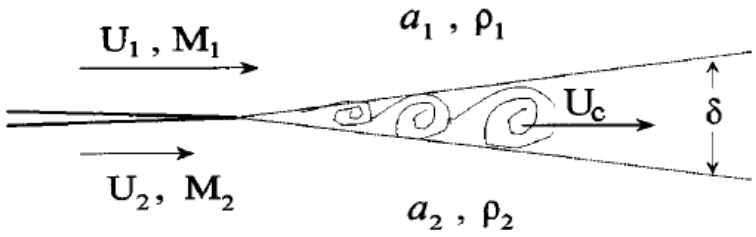

Figure 1.1: Compressible shear layer diagram and nomenclature by Papamoschou [17].

With the increasing convective Mach number, the growth rate of shear layer decreases, hence mixing is effectively hindered [17]. In fact successful mixing lies in the small scale structures rather than global manipulations of the main stream since chemical reactions occur at the molecular level [18, 19, 20]. However the near field mixing of transverse jets is dominated by the so called "entrainment-stretching-mixing process", driven by large scale jet shear layer vortices. In the region near the injector exit, the injectant fluid moves with a higher velocity tangent to the interface than the free stream fluid. As a result, large vortices are periodically formed engulfing large quantities of free stream fluid and drawing it into the jet shear layer (macro-mixing), and then are convected downstream at high speeds, where the fuel and air are mixed by slow molecular diffusion as shown in Fig. 1.2 (top figure). In general, large scale structures are beneficial for the enhancement of bulk mixing, but they hinder fine scale or molecular mixing. They also stretch the interface between unmixed fluids. Stretching increases the interfacial area and simultaneously steepens the local concentration gradients along the entire surface while enhancing the diffusive micro mixing [18].

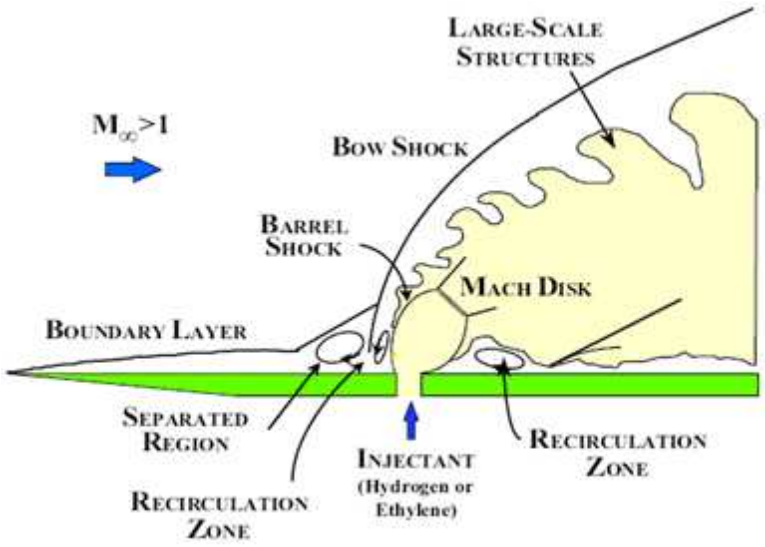

Figure 1.2: Mixing features of an underexpanded transverse injection into a supersonic cross flow by BenYakar [18].

Therefore various injection strategies have been developed to increase mixing both on macro and micro scales, based on different designs of injectors, and injection configurations. They all typically rely on the organization of a recirculation area where the fuel and air can be mixed partially at low velocities. The interaction of a shock wave with partially or fully mixed fuel and oxidizer, and the formation of coherent structures containing unmixed fuel and air are the key mechanisms for mixing. Large quantities of air are entrained into the fuel and due to stretching of the fuel air interface micro mixing is enhanced [18, 19, 21]. Common types of fuel injection from the side wall of a supersonic combustor are normal or inclined injection into the main air stream and inclined injection downstream of a backward facing step as shown in Fig. 1.3. Injection at a right angle, or close to it, has the advantage of allowing a high degree of penetration into the flow and promotes high mixing rates. Nonetheless, the jet causes large total pressure losses due to the stronger bow shock and consequent mixing behind it. Stagnation pressure losses result degradation in propulsion performance and furthermore the momentum of the jet does not contribute to the thrust generation. Stagnation and recirculation regions produced at the upstream and downstream of the jet penetration region create hot spots on the combustor wall [19]. Tangential fuel injection, which is the limiting case for inclined injection, causes minimal total pressure losses, and the fuel jet momentum contributes to the net thrust of

the combustor. The low temperature fuel jet can also participate in wall cooling. Yet the mixing rate will be extremely low without a means of mixing augmentation. By combining tangential and normal injection (i.e. inclined injection), one can maximize the advantages and minimize the disadvantages of the two schemes when used separately. Drummond and Makunda [22] optimized a combination parallel and transverse injection behind rearward facing steps. It was showed numerically that injection of the parallel fuel jet upstream of the transverse jet improves mixing by allowing the parallel jet to interact with the bow shock induced by the normal fuel jet. King et al. [23] also investigated a combined injection system. A fraction of the fuel (16-26%) was injected normal to a Mach 3 free-stream flow through multiple circular jets located at a half step height downstream of the backward facing step. The main part of the fuel was injected tangential to the main stream from a slot whose width spanned the entire step height. The scheme increased the mixing layer growth rate downstream of the step by 70% relative to a tangential injection alone. Large scale structures were observed in the combined injection shear layer; these promoted the rapid mixing.

1.1.2 Thrust vector control systems

In addition to providing a propulsive force to a flying vehicle or a rocket, a rocket propulsion system can also provide certain control mechanisms to change vehicle's attitude and trajectory via Thrust Vector Control (TVC) systems. By controlling the direction of the thrust vector pitching, yawing and rolling moments can be achieved on the flying body. There are many ways to deflect the thrust vector using gimbaled nozzles, flexible nozzle joints, jet vanes/tabs, jetavators, secondary injectants, and etc. Among different techniques to generate deflection of thrust vector of a rocket system, Secondary Injection Thrust Vector Control (SITVC, a shock producing TVC technique) has been used in various systems successfully since 1960's and is accomplished by injecting a secondary fluid inside the supersonic flow from the diverging part of the converging-diverging nozzles. On contrary to mechanically operating TVC systems, such as gimbaled nozzles, jet vanes/tabs, etc., which require actuators to deflect mechanical parts, SITVC does not require any moving parts and is entirely regulated by the fluid injection, which reduces axial thrust force losses while changing the direction of the vector [24]. The secondary fluid injected, gas or liquid can be produced from a separate gas generator or tapped from the main motor as bleed and it creates a complex

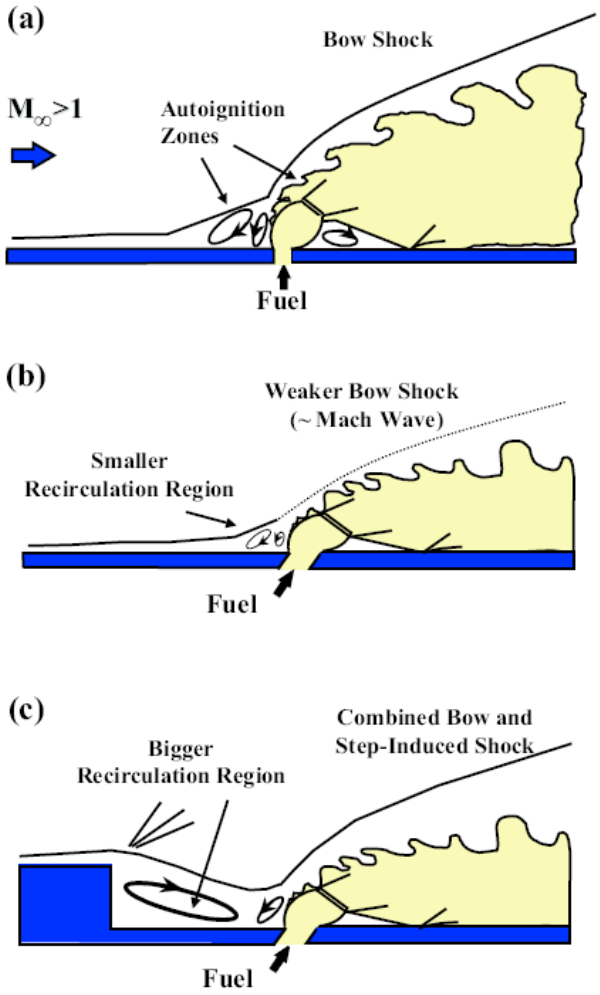

Figure 1.3: Mixing schematics of injection/flame-holding schemes for supersonic combustors; a) underexpanded fuel injection normal to the crossflow, b) fuel injection at angle, c) injection behind a sudden expansion produced by a step by Ben Yakar [18].

three-dimensional flow field inside the nozzle. The causes of the deflection or more appropriately the side force to create deflection over the body are primarily the upstream and downstream asymmetrical pressure distribution on nozzle wall due to jet induced strong bow shock and secondarily the normal component of the momentum of the secondary injectant [25]. Another aspect of SITVC is that the moment arm of the resultant force is bigger than the mechanical TVC techniques enabling to have lesser side forces since the ratio of the side force to the axial force allowed by this technique is limited [25]. Several researchers have examined the TVC characteristics of both cold and hot gas injection into rocket nozzles to yield

performance maps of this technique [7, 8, 9, 10, 26, 27, 28]. The jet interaction flow pattern inside a rocket nozzle is depicted in Fig. 1.4.

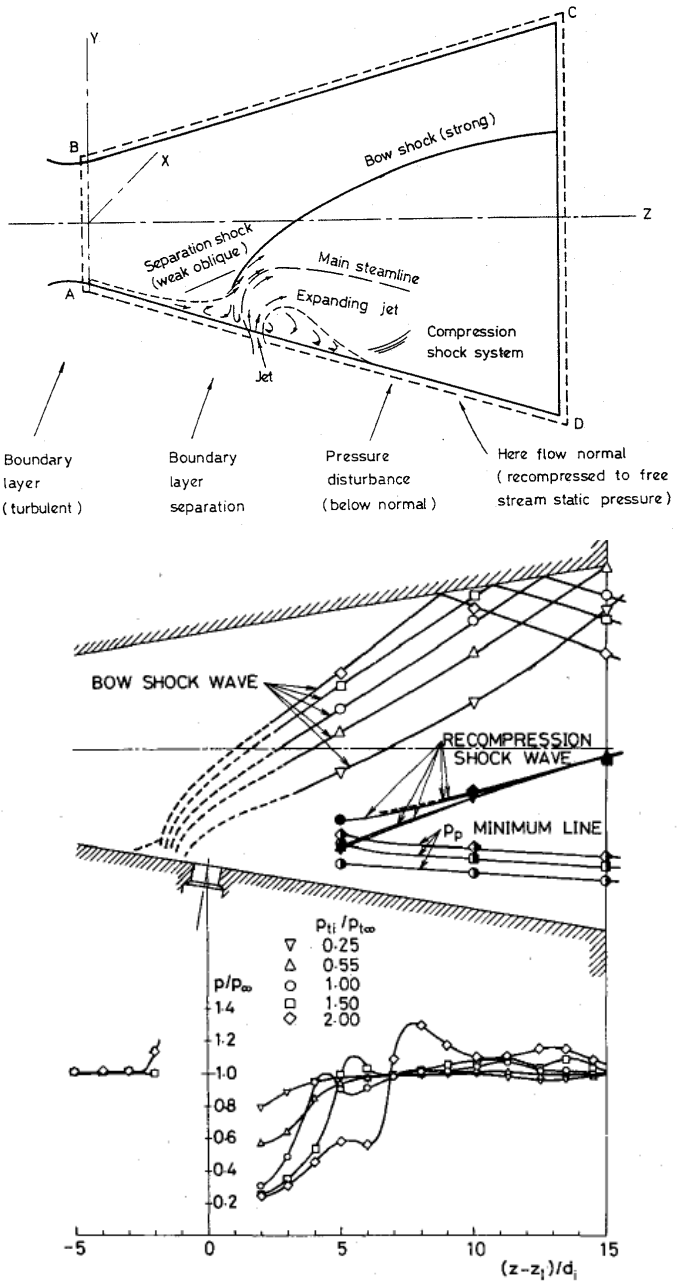

Fig. 4 Effect of $p_{ti}/p_{t\infty}$ on flow structure on the plane of symmetry.

Figure 1.4: Top: SITVC flowfield inside a rocket nozzle by Balu [27]; bottom: bow shock and recompression shock structures with non-dimensional pressure distribution inside a rocket nozzle by Masuya et al. [8].

In general for small divergence angle rocket nozzles, downstream and/or angled injections whereas for nozzles with moderate traditional divergence angles (i.e. about 15°), upstream and/or normal injections are preferred due to their ability to avert bow shock impingement and then reflection from the opposite wall. In terms of mass flow rate higher injectant rates do not necessarily provide desired performance due to impingement mechanism of the bow shock caused by the excessive jet penetration. The optimum performance lies within moderate flow rates from 2-3 throat diameter locations downstream [25].

1.1.3 Reaction control jets

For high speed flight vehicle reaction control jets, transverse/lateral injection offers a convenient way to steer high speed bodies flying in the earth's atmosphere. At high flight altitudes with low stagnation pressures, lateral side jet is the only possibility to exert sufficient aerodynamic forces for flight control. Compared to rudders or flaps, no aerothermal loads are present and it is fully controlled by regulation. Moreover no drag is induced when the side jet is inactive. These aerodynamics forces and moments add to the reaction thrust forces produced by the jet. It is a vector addition because the aerodynamically induced forces can frequently occur in different directions than the reaction control force. A disadvantage of lateral control jets, however, is the complex flow pattern to control as it is shown in Fig. 1.5 and is explained above. Several researchers have investigated jet interaction phenomenon on various missile/forebody configurations at supersonic/hypersonic speeds [29, 30, 31, 32, 33]. Their aim was to investigate control effectiveness of transverse/lateral jets on different missile body configurations. In terms of performance of the technique two main aspects are elaborated; firstly low-pressure region behind the jet effectively creates suction. Even though the amount of suction is moderate it acts over a large area aft of the injector thus creating a strong upward force. The second, and in many aspects most detrimental effect is the coupling with the high pressure region ahead of the jet and the formation of a nose down moment about the injector. The contribution to the nose down moment from the low pressure region is particularly high since this region sustains far aft of the injector. This shift in the center of pressure of the vehicle has to be corrected through the use of an attitude control system that actuates counterbalancing jet thrusters [34]. The important performance parameters are; i) the thrust ratio, which is the ratio of the side force to axial thrust

force, ii) amplification, which is the ratio of side specific impulse Isp_s to main axial specific impulse Isp_p and it determines the amount of fluid to be injected to have a specified side force [25], and iii) axial thrust augmentation, is the ratio of the augmented axial impulse ΔIsp_p to main specific axial impulse and is a measure of the penalty of the overall system to obtain this side force. Following sections discuss the flow physics of the jet interaction phenomena.

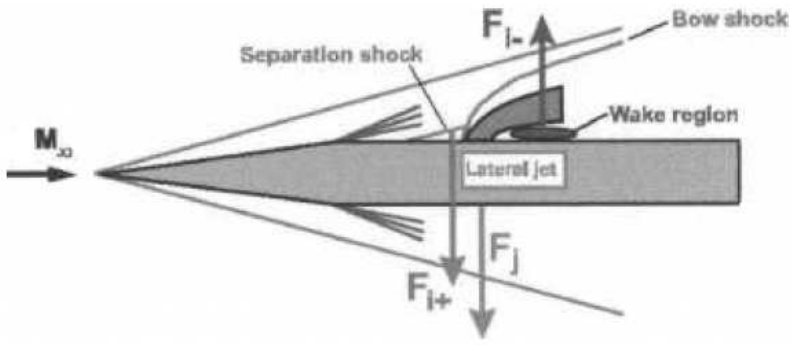

Figure 1.5: Flowfield around a missile geometry in the presence of lateral control jet by Seiler et al. [32].

1.1.4 Flowfield features of transverse jets in high-speed crossflows

The detailed averaged flow features of two dimensional transverse jets in supersonic crossflows over a flat plate are shown in Fig. 1.6. The secondary jet basically acts as an obstruction on the main flow, diverting it to move above the injection plume. This blockage projects itself by a strong jet induced bow shock upstream in the inviscid region. Consequently due to the presence of this bow shock an adverse pressure gradient is imposed on the incoming turbulent boundary layer; causing it to separate upstream. The flow structure in the turbulent boundary layer involves two counter rotating vortices, primary upstream vortex (PUV) and secondary upstream vortex (SUV). These structures provide a region where the boundary layer and jet fluids mix subsonically upstream of the jet exit. The size of the separation region is bigger for laminar boundary layer due to its less energetic nature, hence less resistant to adverse pressure gradients. The boundary layer displacement of upstream vortices causes a weak separation shock that interacts with the strong bow shock. In between the recirculation region and separation

shock there is a sonic surface which essentially displaces the incoming flow. On the injection port the under-expanded sonic transverse jet suddenly accelerates and expands into the main flow and results reduced pressures. This expansion is ended by a normal shock; resulting a Mach surface surrounding the jet plume. Penetration of the jet was shown to be dependent primarily on the jet to free stream momentum flux ratio, J, as mentioned below in Eqn. 1.2. Finally at the downstream of the injection location the diverted main flow is turned parallel to the nozzle wall via a recompression shock accompanied by a recirculation region forming primary and secondary downstream vortices (PDV and SDV). A third upstream vortex (TUV) might occur occasionally.

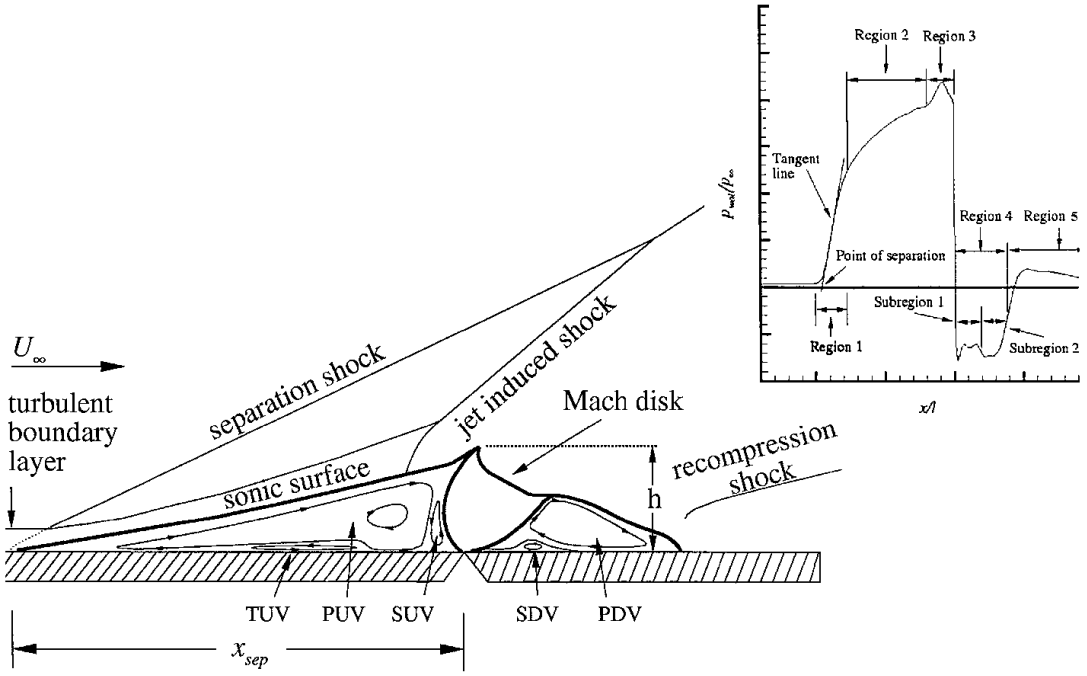

Figure 1.6: Two dimensional transverse slot injection flow field features by [1].

$$J = \frac{\gamma_{jet} p_{jet} M_{jet}^2}{\gamma_\infty p_\infty M_\infty^2} \tag{1.2}$$

In the wall static pressure profile (Fig. 1.6) there are five distinct regions reported by Spaid [1]; an upstream region of steep pressure rise (region 1) as a result of boundary-layer separation, then a flattening of the pressure upstream of the jet (region 2) caused by PUV. The pressure plateau is followed by a pressure spike (region 3) caused by the SUV. Immediately downstream of the jet is a large pressure drop (region 4) with two subregions. The first subregion is a slight

pressure rise caused by the leading edge of the PDV. The second subregion is a pressure drop caused by the SDV. The pressure drop is followed by a pressure hump (region 5) associated with the trailing edge of the PDV, boundary-layer reattachment, and the recompression shock. For laminar interactions the pressure plateau is more gradual and the pressure spike is smaller.

In case of a transverse injection through a single circular hole into a cross flow, namely three dimensional jet interaction, significant fluid motion in span wise direction is observed additionally. Two counter rotating vortices, emerging on top of Mach disc and a horseshoe vortex, formed by the SUV, wrap around the upstream side of the jet and propagate downstream; moreover the bow shock is curved in spanwise direction as well and the main flow is diverted both above and on the sides of the injection port [35, 36, 37] as it is shown in Fig. 1.7. This pair of counter rotating cross flow vortices is assessed by [37] as the primary source of entrainment of the surrounding incoming flow air into the injectant's flow that is important for farfield mixing. These structures are produced by folding of the vortex ring, which is a downstream manifestation of the vorticity arising from the injectors sidewall boundary layers. Haven and Kurosaka [38] demonstrated that the injector geometry has a strong influence on the near field character of the these vortices. The jet shear layer vortices on the windward boundary of the jet are stemming from KelvinHelmholtz instabilities due to the significant shear layer formed between the low speed fluid behind the bow shock and the high speed jet. The horseshoe vortices wrap around the upstream side of the jet and trail downstream; wake vortices periodically shed near the base of the inner jet core and trail downstream under the jet plume [37, 39].

In terms of pressure distribution, the three dimensional relieving effect assists the main flow to move around the transverse jet, which reduces maximum value of the surface static pressure and it causes upstream separation point move closer to the jet. Hence the extent the affected area due to the transverse jet is reduced as well as the magnitude of the pressure peak for the same J value. At the same time, higher pressures that are observed near the interaction shocks, which are wrapped around the plume, are augmenting the interaction force component generated in this region. Whether the net effect is an addition or subtraction, for a finite span plate, it is likely to depend on all of the parameters that affect the interaction [40]. The effects of finite span jet nozzles on interaction phenomena is shown in Fig. 1.8.

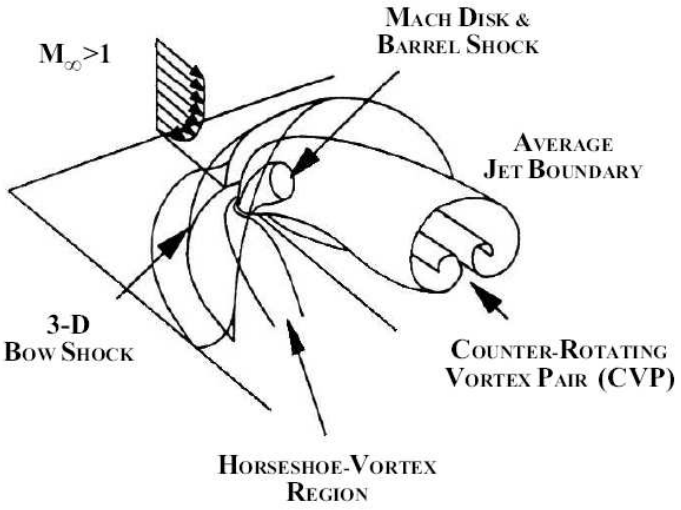

Figure 1.7: 3-D perspective of the averaged features of the flowfield by Gruber [20].

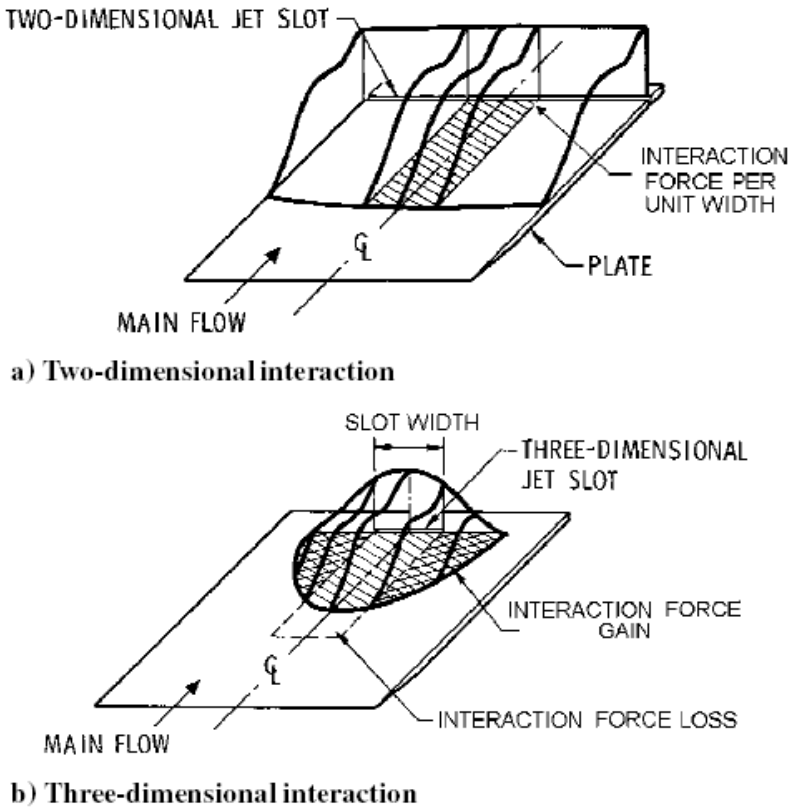

Figure 1.8: Effects of finite span nozzles in jet in uniform cross flow by Cassell [40].

1.1.5 CFD studies of transverse jets in high speed crossflows

Computational Fluid Dynamics (CFD) has been utilised for transverse jets interactions since 90's. Due to complex flow features occurring simultaneously, transverse jet injection flows have served as good candidate to validate and test the performance of turbulence models ranging from two equation models to Detached Eddy Simulation (DES) and Large Eddy Simulation (LES) models. Earlier attempts started by Rizetta [41], who solved two dimensional Navier-Stokes equations on a flat plate with slot injection over a range of slot widths and slot total pressure ratios. Low Reynolds number $\kappa-\epsilon$ model with compressibility correction was applied. Results show considerable disagreement between numerical and the experimental data in terms of wall pressure distributions and the extent of the separation region. The primary cause for disagreement was believed to come from three dimensional effects in the experiment and the compressibility correction applied. Dhinagaran and Bose [42] employed $Baldwin - Lomax$ algebraic turbulence model to simulate the two dimensional experimental case of Spaid and Zukoski [1].

They paid extra attention to capture transitional separation at the highest Mach number case; results suggested poor agreement for the cases with turbulent separation, especially at high pressure ratios however for the cases with transitional separation agreement was satisfactory. Chenault and Beran [43] studied the effect of turbulence models such as $\kappa - \epsilon$ model with a compressibility correction and Reynolds Stress Model (RSM). As an experimental data set, authors emphasised the use of data from Spaid and Zukoski [1] for proper comparison. Results showed very good agreement at low and moderate pressure ratios however as the jet pressure ratio was increased the computed wall pressure distributions started to differ at the upstream region and the injection port vicinity. The discrepancies were addressed to the lack of knowledge of incoming turbulent conditions at the nozzle exit during wind tunnel tests. The superiority of RSM over $\kappa - \epsilon$ model was recognized at Reynolds stress profiles; the inconsistency in vorticity values for $\kappa-\epsilon$ model was associated with the evaluation of wall functions under adverse pressure gradients.

Qin and Redlich [44] examined the case of a laminar separation due to a slot jet injection over a flat plate and compared results with experimental data. The agreement was satisfactory in terms of wall pressure distribution yet not perfect

implying complex character of the flow field to model even in the absence of a turbulence model.

Recently Srinivasan and Bowersox [39] assessed the performance of $\kappa - \omega$ Shear Stress Transport (SST) model, which is a low Reynolds number models and DES models for two and three dimensional sonic/supersonic injection flows with different injectors by solving three dimensional Navier-Stokes equations. Results revealed no significant discrepancies between models when compared to experimental data except for the resolution of unsteady vortical flow structures where DES performed better. Won et al. [45] compared $\kappa - \omega$ SST and DES models as well for the case of Spaid and Zukoski [1]; the agreement was found to be satisfactory at low and moderate jet pressure ratios nevertheless computed pressure distributions showed disparities at high pressure ratios at the upstream separation region and the injection port neighbourhood. DES model generally overpredicted mean flow properties compared to SST model. Sriram and Mathew [46] solved two dimensional flow field with $\kappa - \omega$ SST model for the case of Spaid and Zukoski [1]. They improved previous results by refining the computational grid over the boundary layer up to Mach disc height (see Figure 1.6), yet wall pressure levels were still overpredicted at high pressure ratios. Erdem and Kontis [47] managed to get very good agreement for a broad range of pressure ratios with $\kappa - \omega$ SST model for the case of Spaid and Zukoski [1].

In case of three dimensional test cases, Chenault et al. [36] first utilised an experimental data set and solved three dimensional Favre Averaged Navier-Stokes (FANS) equations using $\kappa - \epsilon$ and RSM. The $\kappa - \epsilon$ model resulted in nonphysical and inconsistent turbulence prediction similar to their finding before in Ref. [43]. Another valuable experimental data set is provided by Santiago and Dutton [37] using Laser Doppler Velocimetry (LDV) to map the velocity distribution the symmetry plane and two crossflow planes across the jet as it develops downstream. At approximately the same conditions, Everett et al. [48] recorded wall pressure measurements with Pressure Sensitive Paints (PSP). Hence this data set serves as a complete set of data for code validation. Sriram and Mathew [49] using $\kappa - \omega$ model of Wilcox and Kawai and Lele [50] with LES tried to tackle problem using this data set. In case of Sriram and Mathew [49], computations capture various flow features and show very good qualitative agreement. Quantitative agreement is very good in the upstream regions and close to the jet. Yet small differences appear in the downstream portion as the jet develops. LES studies by Kawai and

Lele [50] aimed at detailed validation and a progressive mesh refinement study to assess the quality of the simulated results as a start, however only a smaller scale of jet Reynolds number is simulated due to computational cost and there are non-negligible differences in velocity profiles at different stations and also in non dimensional wall pressure distributions between numerical and experimental results. Nevertheless the power of LES lies on the identification the key vortex structures and large scale dynamics in the flow that are responsible for the jet mixing [50]. Understanding the effect of the approaching turbulent boundary layer on the jet mixing allowed a much deeper exploration of the unsteady flow physics. It has been found out that pressure fluctuations inside the recirculation region are coupled with the large scale unsteady dynamics of the barrel shock and the bow shock deformation and accompanying large scale vortex formation in the windward jet boundary. Rolled-up windward jet shear layer is entrained into a upstream separation region, showing the intermittent upstream jet fluid mixing [50].

1.2 Roughness effects in high speed flows

The significant effects of roughness on the boundary layer flow behaviour in low speed flow have been known for years. The direct effect of roughness is the breaking up of the laminar sublayer and increasing wall shear stress associated with the downward shift of the intercept of velocity profile in semi logarithmic coordinates compared to the smooth case as it is shown in Fig. 1.9. k is the roughness height and k^+ is the roughness Reynolds number based on roughness height at the wall. The fullness of the boundary is reduced resulting increased skin friction and surface heat transfer. Nevertheless in high speed flight the effect of surface roughness, which can develop due to the mechanism of ablation, poses a particular problem. When the boundary layer over the surface transits from laminar to turbulent once the vehicle has descended to an altitude, increased values of skin friction and heat transfer are experienced through the rough boundary layer owing to ablation. Furthermore high speed flow over rough surfaces can generate shock and expansion waves that interact with boundary layer turbulence as opposed to low speed counterpart. This interaction is especially prominent at higher Mach numbers where most of the boundary layer is supersonic [51]. A

limited number of studies have been performed on the effect of roughness on complex high speed flows; Disimile and Scaggs [52] studied the effects of roughness on Mach 6 compressible turbulent boundary layer characteristics in the presence of a 22deg ramp deflection, at three unit Reynolds numbers. The roughness consisted of machined hemispherical protuberances 0.508mm in radius. It was found that the extent of the separated region for the roughened surface was ten times that for the smooth. The smooth surface test indicated no change in the location of the separation point for the three Reynolds numbers. Christoph and Fiore [53] stated that in a hypersonic boundary layer it is possible to generate shocklets small weak shock waves associated with individual roughness elements, even for small roughness heights. The shocklets start at the sonic line, are detached and approach the flow Mach angle at the boundary layer edge. They argued that such shocklets are very weak and suggested that they have a minor effect in reducing the strength of shock waves which may be generated downstream. Babinsky and Edwards [54] investigated large scale roughness influence on turbulent hypersonic boundary layers approaching compression corners and they found that the shock wave boundary layer interaction was only marginally affected. Yet in another study considering small scale roughness at Mach 2.5 Babinsky and Inger [55] showed that nominally unseparated shock-wave turbulent boundary layer interaction was considerably affected by the roughness and the length of the interaction region was increased. Also the scaling based on upstream boundary layer displacement thickness was found to be satisfactory. Recently Prince et al. [56] investigated Mach 8.2 hypersonic turbulent shock wave boundary layer interaction characteristics of a deflected control flap configuration. It was found that surface roughness, of scale 10% of the hinge line boundary layer thickness, significantly increased the extent of the interaction, while increasing the magnitude of the peak pressure and heat flux just aft of reattachment. Fig. 1.10 explains the overshoot in surface pressure and heat flux distribution as well as the major findings from schlieren images.

1.3 Energy deposition for blunt body shock wave moderation

For blunt bodies in hypersonic flight there has always been a historical trade-off between desirable thermal protection characteristics and the high wave drag

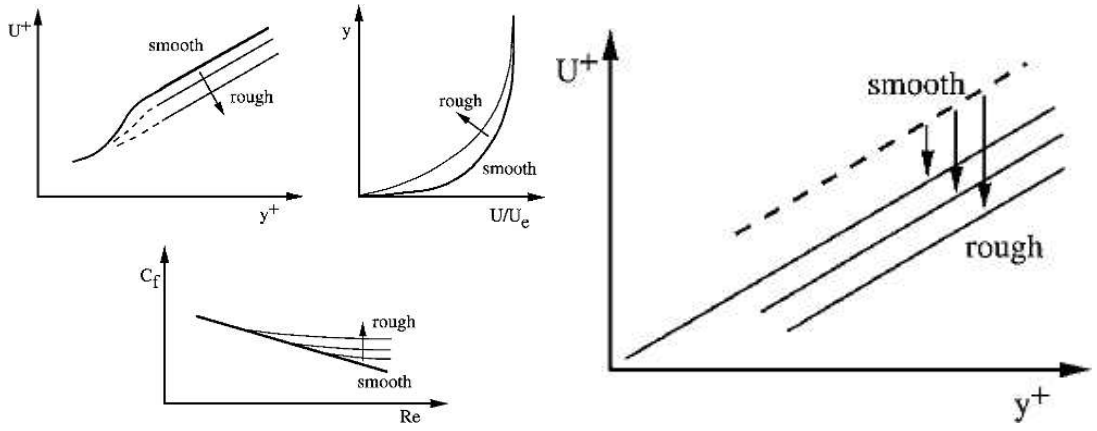

Figure 1.9: Roughness effects on turbulent boundary layers by Babinsky and Inger [55]; left: intermediate roughness regime $10 < k^+ < 70$, right: fully rough regime $k^+ > 70$.

associated with shock wave formation. While the structural considerations dictate the body shape, the high wave drag associated with this shape dictates the necessary propulsive capabilities during ascent [57]. Significant reductions of hypersonic wave drag should result in considerably smaller propulsion system requirements, reduced fuel consumption, substantial improvements in structural integrity, smaller system demands, and considerably larger payloads at smaller take-off gross weight [58]. It is well known that this can be achieved using a spike extending forward from the blunt-body nose. For an axisymmetric body, the spike generates a conical oblique shock wave, which encompasses the body and turns the flow upstream of the body. Pressure drag on the body can drop 50% or more because the detached normal shock associated with a blunt body is no longer present. Experimental investigations by Bogdonoff and Vas [59], in a hypersonic wind tunnel, on spiked bodies showed considerable reduction in the fore-body heating rates and pressure levels on a hemispherical nose cylinder in presence of the spike. However, the usefulness of the spike is limited due to cooling requirements (viscous heating of the spike results in unacceptably high thermal stresses) and frictional drag occurring on the spike structure, especially at high incidences. Another method is counterflow jet injection, which is the injection of fluid from the nose of a blunt body exposed to supersonic flow. Finley [60] has investigated this method and the possibility of using it as a drag reduction device was acknowledged. The counterflow jet of a blunt body in supersonic regime has two distinct states. At the lower injection pressure, the jet displaces the bow shock upstream. The modified shock envelope is generally conical,and the flow

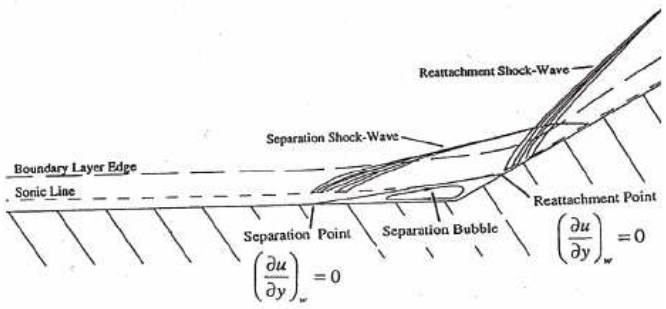

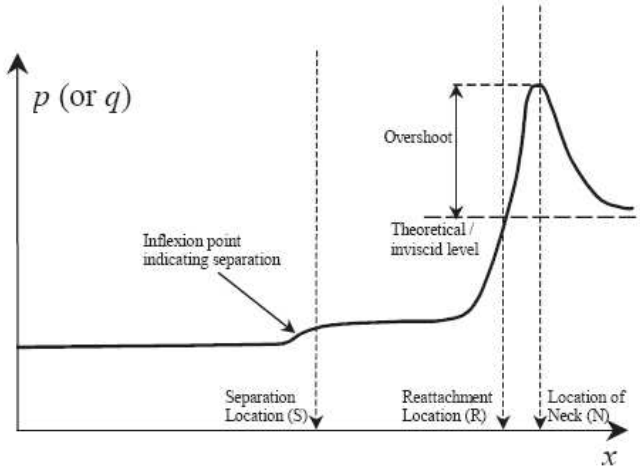

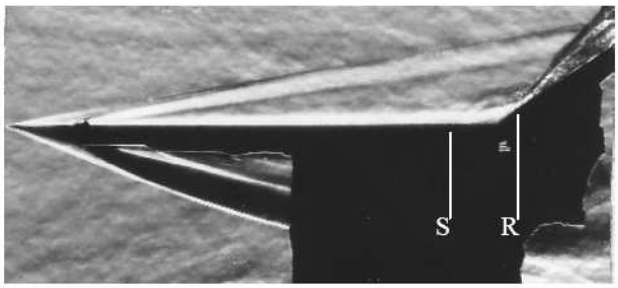

(a) Experimental Schlieren: smooth plate and flap.

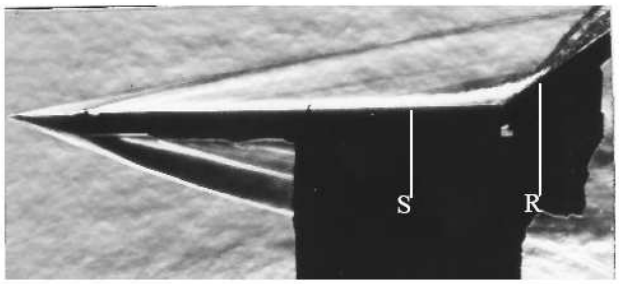

(b) Experimental Schlieren: roughened plate, smooth flap.

Figure 1.10: Left: roughness effects on turbulent compression corner flows, right: Schlieren visualisation of compression corner flows at Mach 8.2 with smooth and rough walls by Prince [56] S:separation, R: reattachment.

field is unsteady. At higher injection pressures, the displaced shock actually retracts back from the conical to a blunt configuration and returns to steady state [61]. For counterflow plasma jet injection, the nonequilibrium weakly ionized air not only changes the temperature but also the thermodynamic properties of the injectant. Shang et al. [62] utilized a plasma torch to create a high temperature plasma jet (shown in Fig. 1.11 and they managed to get a greater drag reduction than the cold jet through thermal energy deposition at an identical mass flow rate. From experimental measurements, an overwhelming major portion of the drag reduction is derived from the viscousinviscid interaction of the counterflow jet and thermal energy deposition.

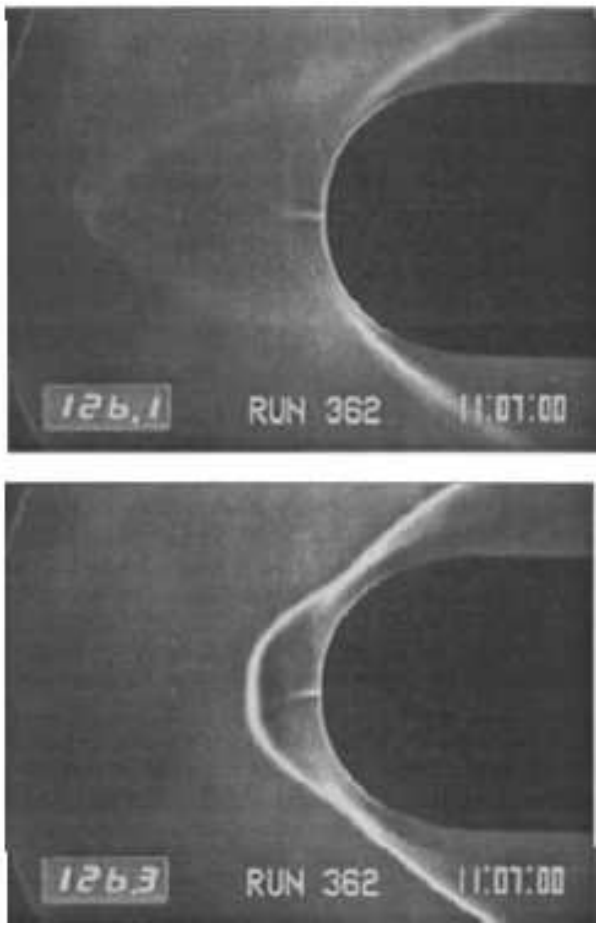

Figure 1.11: Counterflow plasma jet injection by Shang et al. [62].

Localised/focused energy addition in high speed flow, on the other hand, is a strong alternative to methods mentioned above and accomplished by localising/focussing energy by various means in front of a blunt body exposed to supersonic/hypersonic flows. There are two main physical effects of localised heat

addition to the flowfield. The first effect is to reduce the density in front of the body (due to the temperature increase), but this assumes either constant heating or that a pulsed heating source has time to reach equilibrium in pressure before impinging on the surface. It also results an increase in the local sound speed that leads to the changes in pressure distribution around a vehicle due to the decrease in local Mach number. The heat addition in one dimensional supersonic flow is known as Rayleigh flow where heat addition decelerates the flow and drives it to sonic point if sufficient heating is applied. Thus the first effect is similar to Rayleigh flow effect. The other mechanism is peculiar to high speed flows where the interaction of the low density wake from the heated zone with the flowfield around the body results in a dramatically different flowfield [63]. This latter effect is very large for blunt bodies, and the resultant is to change a blunt body flowfield into something more akin to conical flow.

Historically the potential of energy-assisted shaping of high-speed flows with modest on board power requirements has been the subject of a number of earlier investigations. The possibility of obtaining drag reduction using energy sources upstream of blunt bodies has been pioneered by Georgievskii and Levin [64] and Myrabo and Raizer [65] in theoretical studies. In their studies, the magnitude of the drag reduction was found to be insensitive to the location of energy deposition at a sufficiently large distance from the body. This was followed up by various computational studies; Levin and Terenteva [66] and Riggins et al. [58] showed power savings over cones and blunt bodies using two dimensional Euler/laminar computations. Off-axis energy deposition in case of sharp cones resulted a marginal reduction in drag force but created lift hence an aerodynamic moment [66]. Kolesnichenko et al. [67] conducted unsteady/quasi steady Euler computations over a rectangular body. They observed that quasi-steady energy deposition was more efficient than unsteady energy deposition in reducing the time integrated frontal drag. The strongest effect on drag reduction was the magnitude of the density gradient around the localised thermal spot. Girgis et al. [68] suggested that there was an optimum energy source distance, 0.4 times the base diameter, for drag reduction for a given power for a cone in supersonic flow, and energy distribution was assumed to have a Gaussian profile. This can lead to irregularities due to the complex nature of equations involved. But in this case, the study yielded promising results with drag reduction of up to 35%. Georgievskii and Levin [69] carried out numerical simulations at various

supersonic/hypersonic Mach numbers at different energy deposition levels and ellipsoidal energy deposition shapes of different aspect ratios with one axis aligned with the axis of symmetry of the body. A continuous flow deceleration regime was identified wherein the flow Mach number decreased continuously to subsonic values without shock formation on the axis. This regime allowed an efficient drag reduction for conecylinder (i.e., streamlined) bodies.

The correlation between numerical analysis using unsteady Euler equations and results gathered from an earlier experimental data was rendered in a study by Zheltovodov et al. [70]. Their study clearly shows the mechanism behind the drag reduction. The energy input results in the creation of high temperature plasma, which creates a localised blast wave. The blast wave penetrates into the bow shock and reflects off the surface. The thermally heated region that is created interacts with the bow shock which becomes distorted. This is the first step of the interaction, and is know as the Lens effect, shown in Fig. 1.12. The area of intersection between the bow shock and the blast wave is a region of recirculation, which induces streamwise vortical systems to be formed. The effect of this is an alteration in the overall surface pressure distribution, leading to a reduction in drag. These counter rotating vortices stem from the baroclinic torque (see the last term in vorticity equation, i.e. Eqn. 1.3), which is nothing but the cross product of the density gradient caused by the energy spot with the pressure gradient caused by the blunt body bow shock.

$$\frac{\partial \omega}{\partial t} = (\omega \bullet \nabla)\mathbf{u} - \omega(\nabla \bullet \mathbf{u}) + \frac{1}{\rho^2}\nabla\rho \times \nabla p \tag{1.3}$$

The stagnation pressure reduction is directly related to the circulation production, which varies with the length of the thermal spot and the density in the heated zone. Longer spots reduce Mach number further due Rayleigh flow effect and significant heating causes lower density values, thus significant density gradient between the energy spot and the surrounding. It is noted by Kolesnichenko [67] that the lateral extent of the filament does not impact the circulation production, and so the most efficient energy addition processes will be the ones with very thin channels. The results again suggest that the energy should be concentrated on the centreline and located far enough upstream for the pressure equilibrium that occurs after energy deposition is completed prior to the heated air impacting the body, which is detrimental for aerodynamics heating naturally. The vorticity generation is a dissipative process even in an inviscid flow since the directed shock

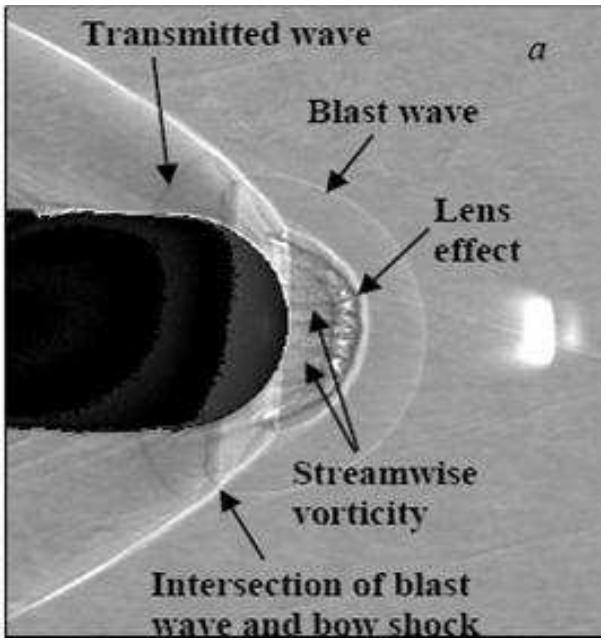

Figure 1.12: Len's effect by Zheltovodov [70].

kinetic energy loses some of its energy to the generation of increased transverse velocity component which could lead to drag reduction with high efficiency even for aerodynamically shaped objects.

The efficiency of energy deposition on drag reduction is defined in Eqn. 1.4. It is the ratio of the propulsive power savings due to flowfield modification divided by the power required to modify the flow, or the energy deposition rate. It can also be interpreted as the measure of the efficiency of the energy-deposition process from a propulsive/energy management standpoint. It grows significantly with increasing Mach number and larger bluntness [63, 71]. The relation is shown in Eqn. 1.5. In fact the impulse I is relatively insensitive to area ratio thus the efficiency increases dramatically with decreasing spot/filament diameter to nose diameter, d_n.

$$Eff = \frac{\int U_\infty (D_0 - D) dt}{\sum Q} \tag{1.4}$$

$$Eff \propto 0.37 M_\infty^2 \left(d_n/d\right)^2 \left(I/\left(1 - \rho_{spot}/\rho_\infty\right)\right) \tag{1.5}$$

Energy deposition methods may be characterised by their temporal behaviour into three distinct families: steady, unsteady and quasi-steady methods. Steady methods involve, as the name implies, steady-state energy deposition into the

flow. Unsteady methods involve some change of the energy deposition with time, usually a single pulse or for ongoing deposition, a cyclic pulsing of the energy source, either from a zero to active state, or between two different energy intensities. Quasi-steady methods are technically a family of unsteady methods, but they appear to affect the flow field in a similar fashion as a steady method. Knight [71] provides a brief explanation of the dimensionless timescales used in such characterisation. Consider an unsteady deposition of energy with an energy profile and with spatial arrangement near a model as shown in Fig. 1.13. The pulse duration is given by τ_e and the total pulse cycle by τ_i. The diameter of the energy spot is given by d and the distance between the model and the spot is given by l.

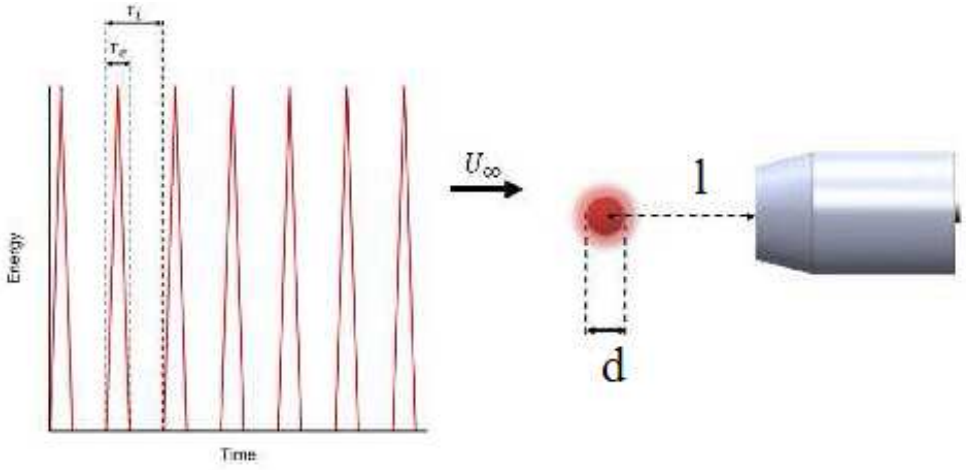

Figure 1.13: Temporal behaviour of localised energy deposition.

The foundation of establishing the dimensionless timescales is then given by equations below;

$$\delta_e = \frac{\tau_e U_\infty}{d} \tag{1.6}$$

$$\delta_i = \frac{\tau_i U_\infty}{d} \tag{1.7}$$

$$\delta_l = \frac{\tau_i U_\infty}{l} \tag{1.8}$$

δ_e and δ_i are defined as the ratio of the pulse duration and the pulse cycle

respectively to the transition times of a gas particle as it passes through the energy spot. Therefore, if $\delta_e << 1$, then the transiting gas particle has moved a negligible distance as energy is added, and energy addition may be assumed to be instantaneous. This is typical of a pulsed laser energy deposition. Additionally, $\delta_i >> 1$ implies that the interval between energy pulses (assuming $\tau_e << \tau_i$) is large compared with the time required for the fluid to move through the energy deposition region. This means fluid particles going though the energy spot experience only one pulse during its life cycle before hitting or going around the blunt body. Quasi-steady flow is characterised by the third parameter, δ_l. If $\delta_l << 1$, then the modified bow shock structure is unable to relax back to its original position - hence the flowfield behaves as if the energy deposition was steady. In addition having a $\tau_i << 1$ value also refers to steady energy deposition as the pulsing frequency is increased to a very big value. Usually high frequencies are favourable for better steady state performance.

Regarding the effect of distance on the dynamics of the interaction of the energy spot with blunt body flowfield, there is an optimum distance beyond which the efficiency drops. The magnitude of the drag reduction was found to be insensitive to the location of energy deposition at a sufficiently large distance from the body. This phenomenon was denoted as "distance stabilization". Also, the increment in drag reduction diminished with increasing energy addition [71]. However shorter distances and high energy levels are detrimental in terms of stagnation point heating rates.

In practical applications there are different methods of applying the energy inputs, laser and micro-wave (MW) radiation inputs being the ones used at the forefront of research right now. Both of these have respective advantages and disadvantages; as laser breakdown has an inherent spherical shape, MW filaments are jittery in localisation and electric discharges require intrusive physical means to localise energy. Following subsections explain the findings from different methods in detail.

1.3.1 Microwave radiation

The work of Kolesnichenko et al. [67] has provided a greater understanding of microwave filament discharge, obtaining detailed spectral measurements of microwave pulse generated plasma. Flowfield visualisation was accomplished through schlieren technique, displaying the lensing of the blunt body shock as

it interacts with the pulse-generated thermal spot. This was observed in both physical images obtained during experimental testing and numerical schlieren images shown below in Fig. 1.14 generated by 2-dimensional Euler CFD simulation. Additionally Lashkov et al. [72] also conducted experiments at low supersonic Mach numbers, where the interaction of pulse energy spots with flat and blunt face cylinders was investigated using schlieren visualisation and stagnation pressure measurements. A significant reduction in stagnation pressure was reported in these studies.

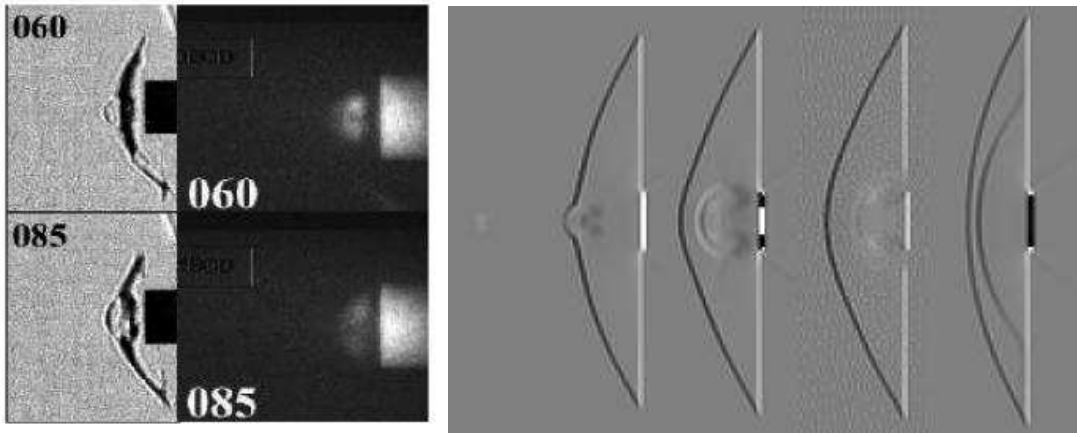

Figure 1.14: Left: Schlieren and chemiluminescent images of the MW/blunt body interaction, right: corresponding numerical schlieren images by Kolesnichenko et al. [67].

Previous to these studies, Exton et al. [73] studied the unsteady microwave energy deposition into hypersonic flow which offered valuable insights into the topology and behaviour of the various plasmas generated. A plasma mirror was observed during the early stages of each energy pulse, showing how as a greater amount of plasma is generated, the increased concentration of free electrons begins to reflect electromagnetic, and in particular, microwave radiation. A more dramatic example of this phenomenon is observed during the communications blackouts experienced by spacecraft and their crews upon atmospheric reentry - as the spacecraft travel at very high Mach numbers along their reentry trajectories, the extremely high speeds give rise to similarly strong shock systems and exotic thermochemical effects not usually observed in conventional, lower speed aerodynamics. Chemically reacting gas around the vehicle forms plasma as the overall kinetic energy of individual gas species is abruptly transformed to high internal and vibrational molecular energies. Magneto-aerodynamic effects become

significant in magnitude, with strong electromagnetic fields generated due to high free electron concentrations caused by the plasma generation - this has the effect of reflecting radio waves, leaving the crews unable to communicate with any other parties until they have decelerated to a speed where the electro magnetic reflection becomes weak enough to once again establish radio communication. The importance of this study, then, was to highlight the need for quasi-steady or unsteady energy deposition versus the continual deposition of energy due to this effect: in addition to the prohibitive input energy demand and unwanted body heating effects highlighted earlier, the effectiveness of the deposition itself regardless of any such body in the flow would decay with time with steady microwave irradiation.

1.3.2 Laser energy deposition

Initial experimental studies were pioneered by Tretyakov et al. [74]. The team used high frequency carbon dioxide lasers to deposit energy in a supersonic argon stream with a freestream Mach number of 2 around a cone cylinder and hemisphere cylinder. This study focused on observing the effects of varying the pulse interval using the non-dimensional pulse interval parameter, δ_L as a suitable metric. A promising 45% reduction in the average drag levels was observed when $\delta_L \approx 1$. Adelgren et al. [75] extended this work by using Neodymium-doped Yttrium Aluminium Garnet (Nd:YAG) laser at Mach number of 3.45 with a sphere in air flow and obtained a detailed image of the temporal behaviour of the surface pressure for selected energy pulse levels as shown below in Fig. 1.15.

A thermal spot is generated upstream of the bow shock of the sphere. Initially, the bow shock lenses forward in reaction to this stimulus, causing the initial surface pressure rise. As the thermal spot and bow shock interact, an expansion wave is generated, and the pressure relaxes. Once the thermal spot transits the bow shock, compression waves form as the thermal spot is then convected towards the sphere, and the pressure returns to its original value. Both studies provided valuable insight into the shock behaviour when using laser energy deposition, and contributed significantly to the understanding of the steady vs. unsteady vs. quasi-steady deposition behaviour. The exploration of these parameters and their individual effects is important; they must be known in order to correctly model the interaction of the laser blast wave with the flowfield.

Yan et al. [76] observed that at μsec range, the temperature in the laser spot

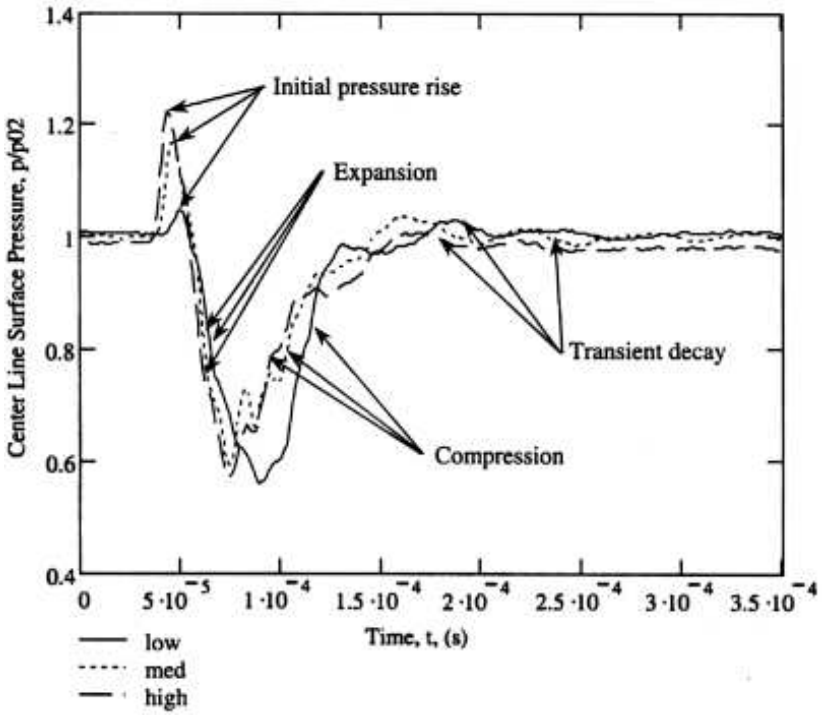

Figure 1.15: Temporal Behaviour of Surface Pressure For Nd: YAG Laser Energy Deposition by Adelgren et al. [75].

remains steady enough for the behaviour to be predictable. Studies focusing on the interactions between laser generated hot spots and the freestream flow were also conducted by Salyer et al. [77]. The general purpose of this study was to categorise laser spot behaviour for further studies regarding the receptivity of a body to hypersonic flow. The receptivity of a body is the process by which freestream disturbances enter the hypersonic shock layer to cause instability waves - therefore, this study provided useful insight into how the laser spot affected the shock geometry, and how the interaction between the energy deposition and the flowfield would propagate instabilities.

Recently Sakai et al. [78] used a high repetition Neodymium-doped Yttrium Lithium Fluoride (Nd:YLF) laser to deposit energy upstream of a truncated cone with repetitive pulses at Mach 3 and emphasised the trade-off between energy input and energy saved as a means of performance. The principle of this is exactly the same; with a "virtual spike" due to vortices and significant drag reduction can be achieved. Effective interaction time was found to be longer with larger bluntness (i.e. flat surfaces rather than hemispheres). Moreover they numerically examined the effect of frequency on the virtual spike and found out that for the

same configuration higher pulsing frequency is more efficient as shown below in Fig. 1.16.

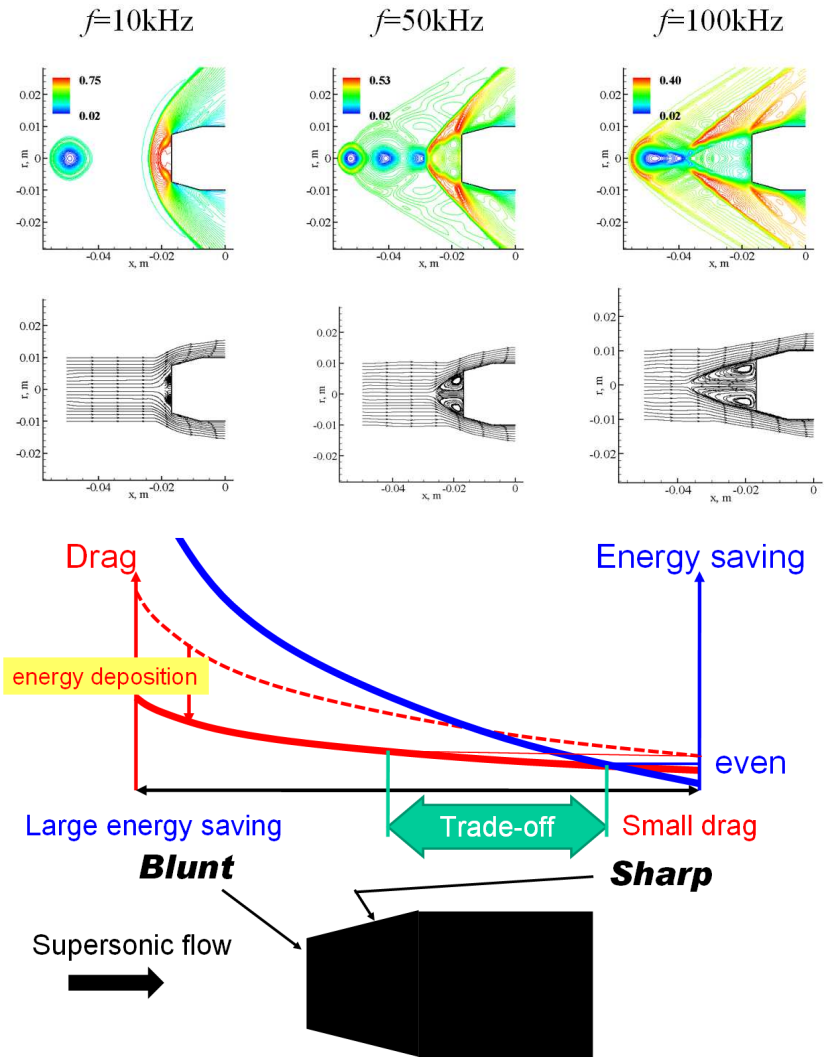

Figure 1.16: Top: virtual spikes at different energy deposition frequencies, bottom: energy trade-off for energy deposition over truncated cones by Sakai et al. [78].

Recently Minucci et al. [79] and Oliveira et al. [80] conducted experiments in a hypersonic shock tunnel using CO_2 laser upstream of a hemispherical model. Schlieren technique was used to visualize the time evolution of energy addition to the flow and the interaction between the heated region and the blunt body flowfield at Mach 7. A complete mitigation of the bow shock profile under action of the energy addition was observed as shown below. The impact pressure on the hemispherical model measured by piezoelectric pressure transducers at the stagnation point reveals the correlation between the schlieren images and the

pressure reduction.

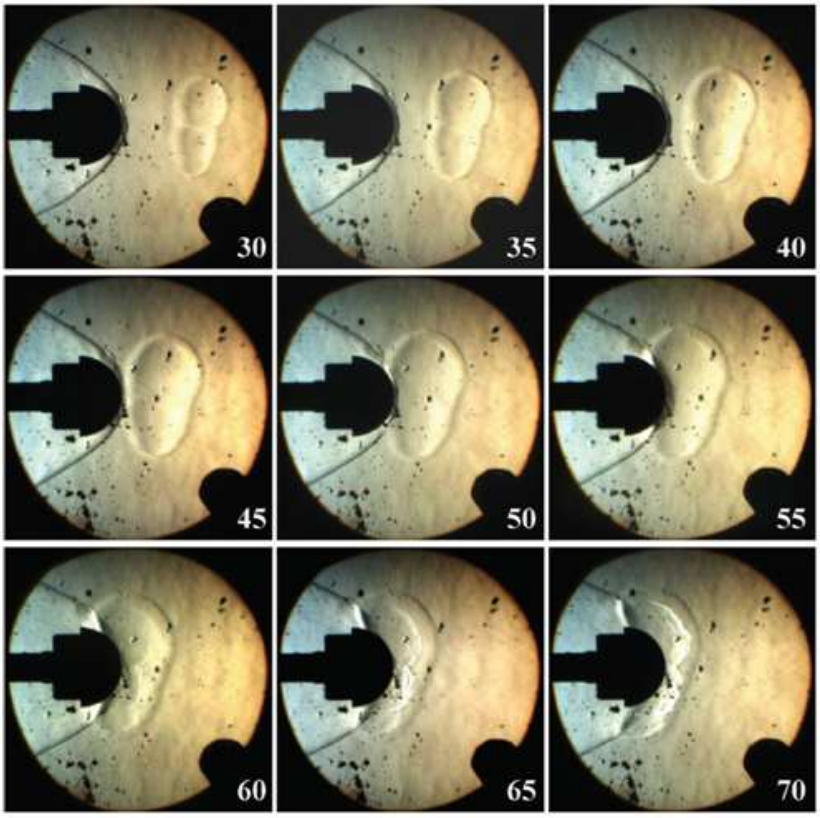

Figure 1.17: Sequential Schlieren photographs of the interaction between the pulsed laser deposition and blunt body flow field in hypersonic flow by Oliveira et al. [80].

1.3.3 Electric discharges

The concept of arc-discharge methods is relatively simple and consistent. Two electrodes are placed in front of the model such that the imaginary line between their tips is normal to the streamwise direction. A high potential difference across the electrodes generates an electric spark filament - the arc discharge as the gas particles between the electrode tips serve as conductors. Any gas particle flowing through the path of the discharge experiences a large amount of heat addition, creating the plasma spot. The studies investigating electric discharges are relatively new. Firstly Myrabo et al. [81] used thin rods of a tungsten-zirconium alloy electrodes to deliver the arc discharge upstream of a disc shaped body at Mach 10 in a hypersonic shock tunnel. The arc was supplied by a number of lead acid car batteries at low voltage but very high current levels resulting 2.5 to 10kW

of power. The arc created its own shock wave and the drag level was decreased at best by a factor of approximately five and a significant gain was obtained in the total consumption of energy. Additionally they suggested a simple approximate theory to optimise the source power and location. Furthermore, Satheesh and Jagadeesh [82] also carried out experiments in a hypersonic shock tunnel at various Mach numbers, freestream densities with two test gases (air and argon) using an electric arc discharge upstream of a blunt cone model. Schlieren visualisation, accelerometer based one component force measurement and pressure and heat flux measurements were utilised. Their results suggested that low density test conditions resulted in an ineffective interaction and argon was found to be more receptive to energy deposition than air due to lower number of degrees of freedom. The energy spot was not found to be strong enough to produce its own shock, and the shock structure observed was a result of the heated channel formed behind the energy source interacted with the blunt body shock that causes flow alteration which is shown in Fig. 1.18. The amount of power used was around 300-700W showing a significant increase during the test time due to oscillations in the arc as well as the varying flow conditions. A maximum drag reduction of about 50% and 84% reduction in stagnation point heating rate was observed momentarily as a result of energy addition in argon environment. Unnoticeable effect was produced on the flow field when the discharge was located close to the body (0.416 times body diameter). Drag force histories revealed another interesting thing; the drag levels remain nearly unchanged by the presence of the electrode structure even though Schlieren images showed significant amount of waves coming from the upstream of the arc.

Recently Schulein and Zheltovodov [83] investigated the influence of steady energy addition into the flow by a low voltage DC-arc discharge located upstream of the conically nosed and spherically blunted bodies in the Ludwieg tube at Mach 5. The results included drag force measurements (histories not shown) and shadowgraph flow visualizations. They made a clear distinction between the local and global heating as shown in Fig. 1.19. The electrode arrangement was aerodynamically shaped. Large arc to nose distance was used for an increase of the flow heating effect. The amount of power used adds up to 1-3kW. The flow-field structure, arising due to the bow shock/heated wake interaction, as well as the bow shock intensity and the heating power effects on the drag reduction is analyzed in this work. The results demonstrate the existence of an optimum heating

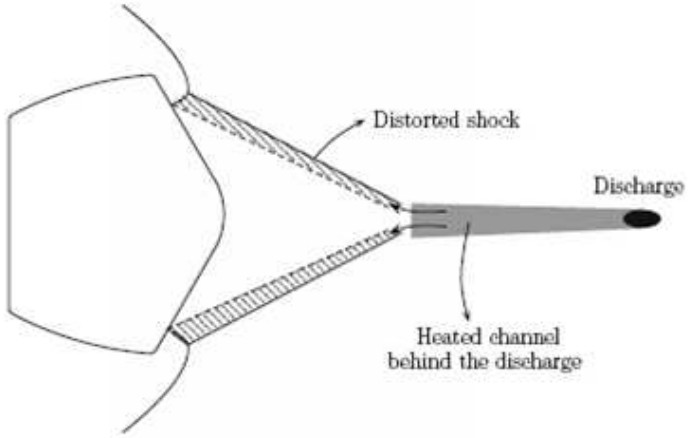

Figure 1.18: The flow model proposed by Satheesh and Jagadeesh [82] showing the interaction between the wake of the heated channel and consequent compression waves.

rate, providing a maximum effectiveness of energy addition and showing distinct drag reductions up to 70% dependent on test conditions and model geometries.

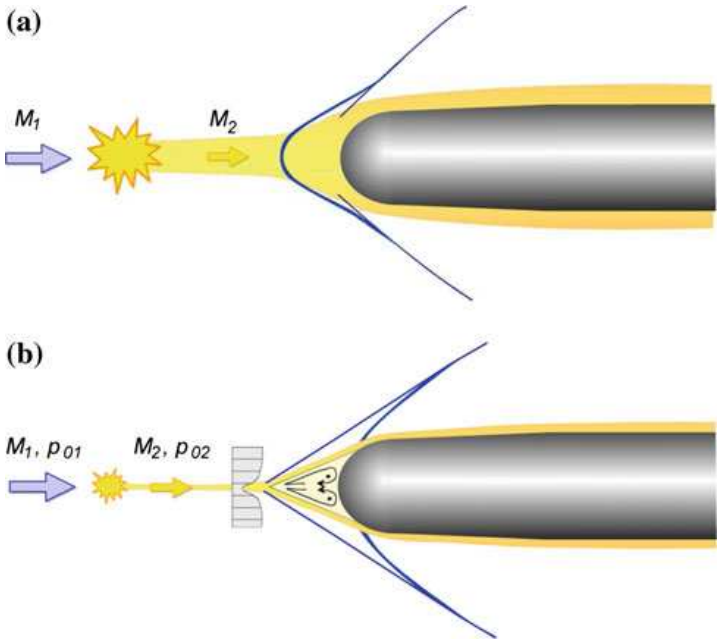

Figure 1.19: Effects of external flow heating upstream of a blunt body; a: global effect, b: localized hot-spike (or thermal-spike) effect by Schulein and Zheltovodov [83].

1.4 Aims and objectives

The main objectives of this thesis are:

- Investigate experimentally the flow physics of the sonic transverse jets at Mach 5 laminar cross flow both in time averaged and time resolved manner to provide reliable experimental data and better understanding at high Mach numbers. The parameters such as momentum flux ratio, incoming Reynolds number, type of the gas and the surface roughness are varied. The size and structures of the upstream and downstream separation regions and jet penetration characteristics together with jet shear layer behaviour are examined. Moreover CFD simulations are conducted on a two dimensional case of Spaid and Zukoski [1] and the numerical solver is validated. Then a three dimensional experimental case is simulated to provide greater understanding on the flow physics as well as to cross check measurements.

- Investigate experimentally the dynamics between the localised energy spot and the blunt body shock for drag reduction at Mach 5 flow. The localised energy spot is created firstly via steady electric arc struck between two electrodes using a small amount of energy and secondly via pulsed laser focusing with a significant amount of energy. In case of electric discharge, the effects of discharge are evaluated in comparison to no discharge case with the electrodes. The unsteady wake/compression structures are examined between the steadily deposited energy spot and the modified bow shock wave. And for the laser focusing unsteady interaction that is happening in a short duration of time is investigated. The effect of the truncation, the distance between the electrodes and the model as well as the type and amount of the energy input on this phenomenon are examined. Moreover CFD simulations are conducted on the baseline cases to cross check measurements together with theoretical estimates.

1.5 Overview of the thesis

This thesis is organized as follows. Chapter 1 deals with introduction and literature survey. In chapter 2, the details of the facility, associated flow diagnostics, the characterisation and calibration of the facility and the details of the experimental setup with models for transverse jets and energy deposition are described

as well as the numerical methodology for CFD simulations.

Chapter 3 presents the results of the transverse jets studies and the main findings of the investigations with different relevant parameters as well as the comparison with numerical results. And Chapter 4 presents the results of the energy deposition studies for drag reduction and the main findings of the investigations as well as the comparison for baseline cases with numerical results.

In Chapter 5, some important conclusions are drawn and future works are recommended.

Chapter 2

Experimental and Numerical Methodologies

All of the experiments regarding transverse jets in high speed cross flow and energy deposition for drag reduction are conducted in the High Supersonic Tunnel (HSST) of the University of Manchester at Mach 5. HSST has arrived in the School of MACE in 2005 without vacuum tanks, it had become partially operational with 2 new vacuum tanks (with a connection of 100mm of diameter pipe as opposed to 200mm diameter of diffuser throat) in July 2007 with incorrect connection between vacuum pumps. The useful running time was around 0.5sec. In March 2008 it had become fully operational with 4.5 sec of useful running time. In July 2009 the connection between vacuum tanks was changed to 325mm diameter pipe and useful running time was increased to 7.5 sec. In summer 2010 new vacuum pump for HSST and new compressor for George Begg building were installed that significantly improved tunnel recharge time to 15 minutes. The author has started his PhD in late 2006 and unfortunately suffered from these setbacks over the years. On the other hand he is grateful and proud to be the first person running the HSST in the University of Manchester. The details of the facility with flow diagnostics, models and experimental setup as well as numerical setup are described below.

2.1 University of Manchester HSST

The tunnel is of the intermediate blowdown (pressure-vacuum) type which uses dry air as working fluid and is shown schematically in Fig. 2.1. Air from high

pressure airline is passed through an Ecoair Series AT 15 adsorption dryer, and stored in a pressure vessel at 16bar. The gas then passes though an infinitely variable pressure reducing regulator where constant gas total pressure is obtained by a power dome controller Type C4 Model 208/3. This is manually preloaded and maintained at a pressure necessary to achieve the required total pressure downstream of the settling chamber using compressed air from a Compair Broomwade Type V85 compressor regulated via a pressure controller Type P.140 Model 133/140A. After passing through a pneumatically operated quick-acting 100mm Worcester Type A45-4466-TT ball valve the gas enters the 24kW electric resistive heater. This consists of a stainless steel tube which has been preheated by passing an electric current through it from a manual remote controlled Lincoln Electric Type SAE 600 welding motor generator. The heater tube, which is 30m long and has an inside diameter of 38mm and a wall thickness of 3.2mm, is formed into a coil of 16 turns of 0.6m diameter. The heater coil is thermally and electrically insulated from the rest of the tunnel and is embedded in a container filled with granules of vermiculite to reduce heat loss. The gas temperature is raised from ambient to temperature between that sufficient to avoid liquefaction on its expansion through the nozzle and that of a maximum enthalpy flow condition of 700K. On leaving the heater the air enters the settling chamber which is downstream of the flow straightener matrix. Immediately downstream of the settling chamber is situated a contoured axisymmetric nozzle. A set of three 150mm exit diameter open jet nozzles with nominal Mach numbers of 4, 5 and 6, and a pair of 170mm exit diameter annular-jet Mach 5 nozzles containing 51mm and 30mm diameter centre-bodies are available. The tunnel working section is an enclosed free-jet design. The working chamber volume assumes the form of a 325mm square cross-section of length 900mm. Its major axis is parallel to both the ground and the direction of flow. A pair of interchangeable hinged access doors located on either side of the working chamber allows the 195mm diameter Quartz windows mounted in them to assume two possible longitudinal positions at right angles to the flow as shown in Fig.2.2.

The test gas passes through an evacuated working section chamber into a diffuser having an entrance diameter of 250mm. Before flow is established in the tunnel a starting shock has to be swallowed and held in the diffuser. In order to accommodate a wide range of model sizes and configurations the diffuser can be moved in the direction of flow such that the distance between the end

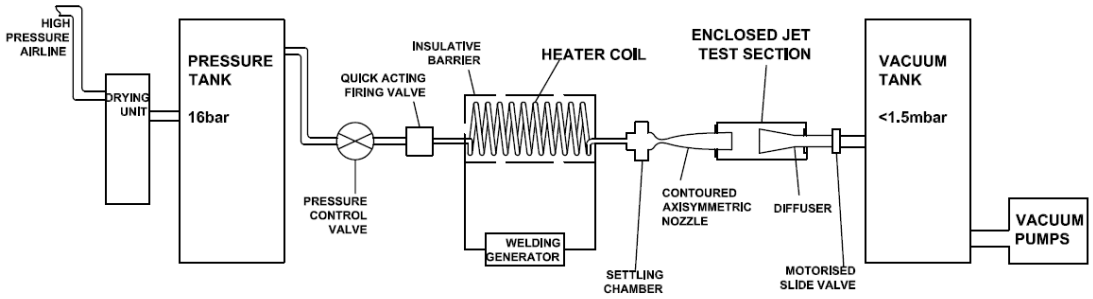

Figure 2.1: University of Manchester HSST schematic layout.

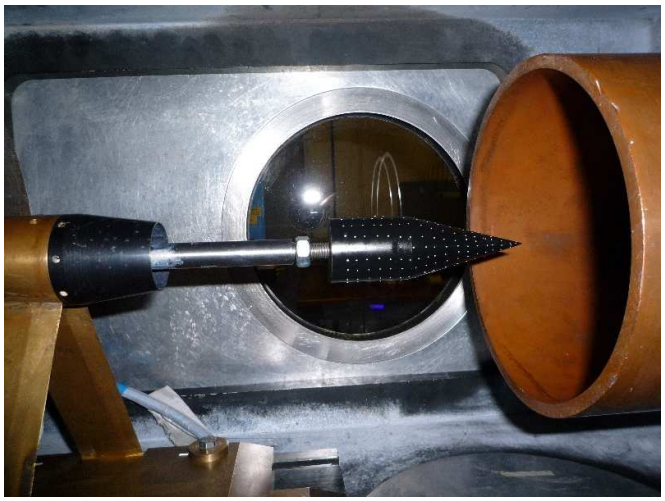

Figure 2.2: Test section of HSST with a cone-cylinder model placed on a sting.

of the nozzle and the start of the diffuser can be between 140mm and 400mm. After diffuser a 200mm diameter motorised slide valve is positioned between the working section and the vacuum tank. This allows access to the working section without pressurising the vacuum tank, between runs whilst the vacuum vessel can be maintained at a pressure of below 1.5mbar. The vacuum vessel is serviced by a set of vacuum pumps. These hydro kinetically driven Edwards EH2600 Roots blower type mechanical booster pump forming the low pressure stage which is backed two rotary piston vacuum pumps, a General Engineering Kinney Size GKD220 and Edwards Model 412J, each placed in series.

Variation of the Reynolds number is accomplished by the setting of different supply pressures and heater temperatures. The envelope of the unit Reynolds numbers, Re/m, achievable with this facility is shown in Fig. 2.3. The range is from $2.5 \cdot 10^6 1/m$ to $26 \cdot 10^6 1/m$. Various curves, which are based on stagnation pressure values of 5, 6, 7 and 8bar for two limiting values of heater supply

temperature settings of 375K and 700K, are drawn. Solid vertical lines represent attainable Re/m values at Mach numbers of 4,5 and 6. For Mach 5 the achievable range unit Reynolds number is from $4 \cdot 10^6 1/m$ to $16 \cdot 10^6 1/m$.

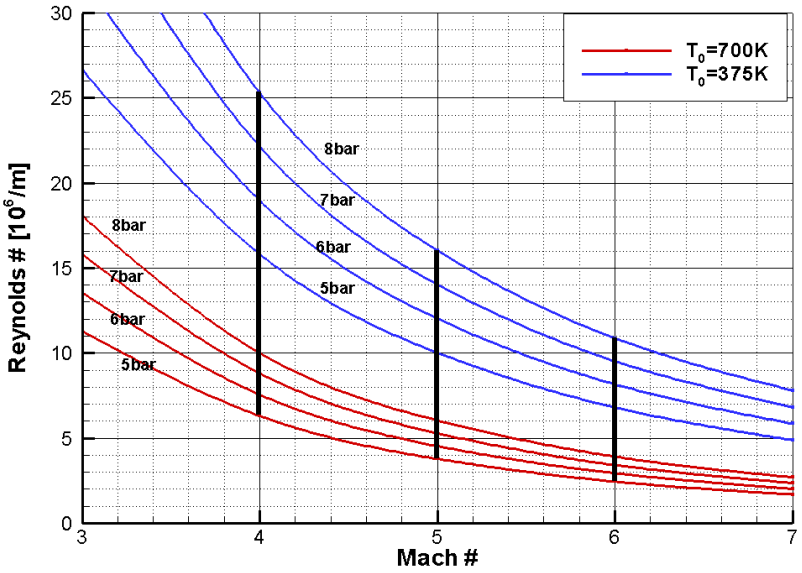

Figure 2.3: Unit Re number variation for different stagnation temperatures and pressures.

The relationship between the unit Reynolds number and Mach number is interesting. For a fixed reservoir conditions of p_0 and T_0 unit Reynolds number starts to increases with increasing Mach number to a point, then decreases from thereon and approaches zero as Mach number goes to infinity provided that the required pressure ratio is maintained by the wind tunnel to have isentropic subsonic/supersonic flow. Maximum unit Reynolds number is achieved at $M_\infty \approx 1.2$ for $\gamma = 1.4$ for a wide range of p_0 and T_0 when $\frac{dRe/m}{dM_\infty} = 0$. Fig. 2.4 shows this relation. It has to be noted that isentropic flow assumption is made from the nozzle settling chamber all throughout the test section up to diffuser where oblique waves form at diffuser walls. Also Sutherland's law of viscosity is employed and the values of $p_0 = 6450mbar$ and $T_0 = 372K$ are used for the plot. It has to be noted that Fig. 2.3 shows this behaviour only from a Mach number of 3 to 7.

The running conditions of the tunnel are limited by the amount of heat which can be supplied by the heater and the mass flow rate the vacuum pumps can remove from the vacuum vessel. The useful steady running time of the facility is terminated when the pressure in the vacuum chamber exceeds the pressure in the downstream end of the diffuser which is of the same order of magnitude as

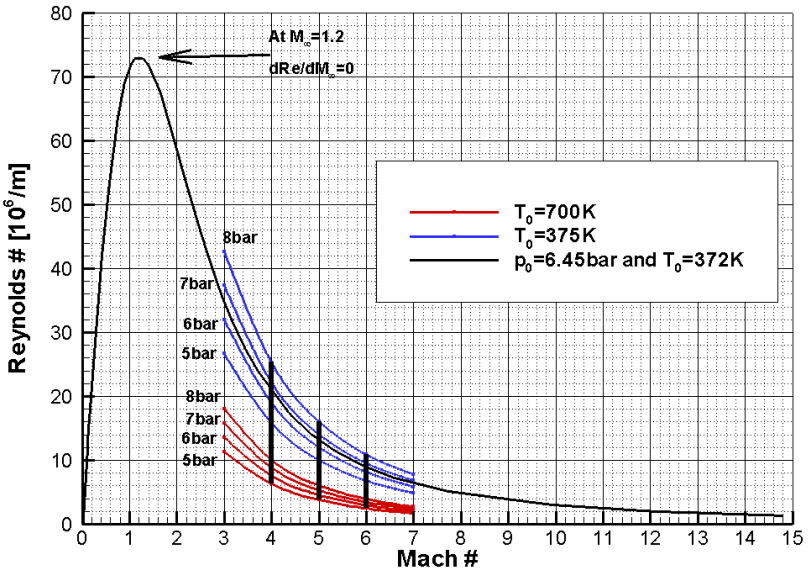

Figure 2.4: Unit Re number variation with freestream Mach number for fixed reservoir conditions.

the pitot pressure in the test section.

2.2 Flow diagnostics

2.2.1 Pressure and temperature measurements

Stagnation, pitot and static pressure measurements are done using high-sensitivity Kulite © pressure transducers. A pitot probe (3mm in diameter) attached to a Kulite pressure transducer (XTE-190M, 0-100psi range) via small chamber and a K type thermocouple probe (3mm in diameter) with a wire diameter of 1.0mm are located at the settling chamber to measure p_0 and T_0 respectively. For pitot pressure measurements, p_{pitot}, a specific pitot rake is designed (see 2.3) and Kulite XTE-190M (0.7bar range) pressure transducers are connected to the rake. For jet stagnation pressure measurements, p_{0pitot} for transverse jets, another Kulite pressure transducer (XTE-190M 0-3.5bar) is connected to the 8mm air pipe via T-junction just before the jet orifice. In case of wall pressure measurements, a housing for pressure transducers is used and pressure 1mm tappings on model (see Section 2.4.1) are connected to this housing via flexible heat resistant tubing with pressure transducers being connected to the other side of the housing. The linearity of transducers are maintained by vacuum calibration using a 0-3bar

range (±6mbar accurate) gauge situated in the test section wall. Analog signals from all the sensors are acquired by a high-speed Data Acquisition (DAQ) card, National Instruments(NI) © PCI-6251, after it has been conditioned by a SXCI-1000 unit. This signal conditioning unit enables various modules to be inserted for different applications. Current modules are SCXI-1520 compatible with pressure or load measurements and SCXI-1112 for temperature measurements. Naturally any sensor is connected to SXCI-1000 unit for conditioning; signals are digitised and acquired by PCI-6251 card. The existing system had the capability of collecting data at a frequency up to 333kSamples/s at 16bit digitisation. The DAQ has a fully programmable environment; it can generate proper digital or analog signals at a precise time by means of software, LABVIEW v.8.

2.2.2 Schlieren photography

Toepler's z-type Schlieren technique [84] is adapted for flow visualisation that consist of a continuous light source of Palflash 501 (Pulse Photonics) with a focusing lens and a 1mm wide slit, two 8inches parabolic mirrors with 6ft focal length, a knife edge, a set of Hoya 49mm close-up lenses and a digital Canon SLR camera, EOS-450D, 12MP. The offset angle of parabolic mirrors with respect to their axis is set to 5 degrees to prevent optical aberrations such as coma and astigmatism [84] as much as possible. Parallel beam of light is passed through test section windows before focusing on the knife edge plane that is placed perpendicular to flow direction and the focused beam is shone on CMOS sensor of the camera. The camera is set to continuous shooting mode at which it can record 3.5fps at full resolution; the shutter speed is adjusted to maximum value of 1/4000sec with an ISO speed of 400 to provide enough detail and appropriate brightness. In addition a high speed Photron SA-1 High Speed Video system is utilised to record time-resolved Schlieren images up to 675000fps at various pixel resolutions and shutter speeds. Optimum frame rate is based on a compromise between adequate temporal resolution and pixel resolution considering the overall running time of the tunnel as well. Shutter speed is set to around 1 to 4μsec to resolve flow features with sharpness. The layout of the optical setup and the DAQ architecture with measurement chain is shown in Fig. 2.5.

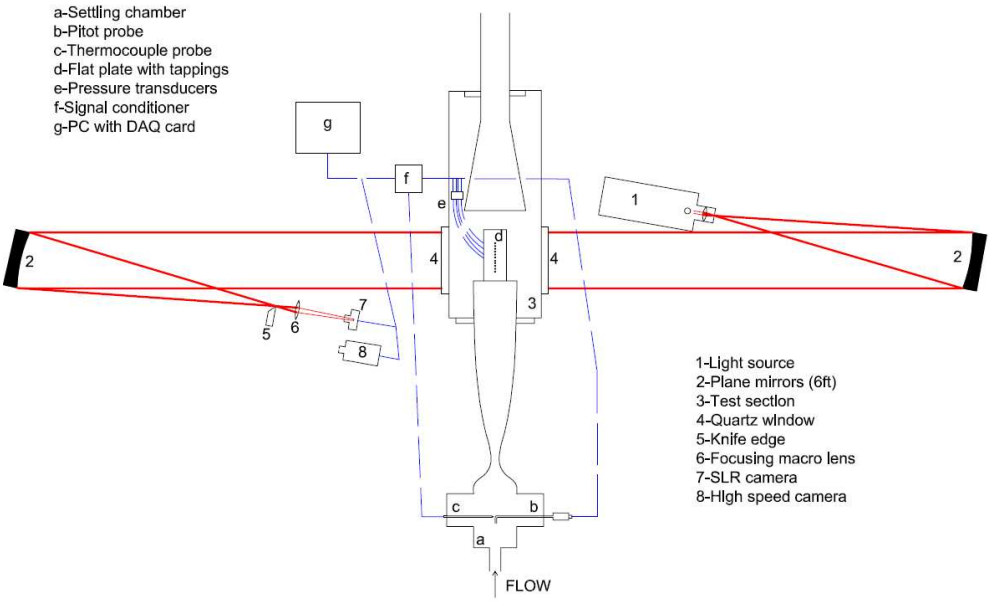

Figure 2.5: Schematic setup of Schlieren visualisation with DAQ architecture.

2.2.3 Oil dot visualisation

Discrete dots composed of linseed oil, silicon 800 oil and titanium dioxide powder with few drops of oleic acid are applied on matt black painted model surfaces to visualise the traces and the extents of flow structures. The following mixture is found to be optimum and suitable for hypersonic wind tunnels and similar facilities; 1.5g of TiO_2 is dissolved in 8.0g of linseed oil. The resulting mixture is mixed with 2.0g of silicone 800 oil afterwards several drops of oleic acid is added. Resulting mixture is applied using a syringe to make 0.5mm blobs on the surface. Silicone oil controls the viscosity of the mixture and makes it thicker while oleic acid controls the surface tension of the blob. During the test run oil dots respond to the levels of surface shear stress, wall pressure and wall temperature through viscosity, therefore the ideal dot should be thin enough to move in the direction of the flow and leave a streak behind it yet should show resistance to spreading. Oil dot pattern can indicate laminar-turbulent transition, separation and reattachment regions [85]. When shear stress on the wall suddenly increases, i.e. transition regions, oil dots show longer streaks, when it changes direction, i.e. separation or reattachment locations, oil dots either do not respond or show signs of reversed flow. Finally at the downstream of the reattachment locations they are wiped away due increased τ_w.

2.2.4 3-component force measurements

Lift, drag and pitching moment measurements are collected by a 3-component Aerotech © Force Balance. The balance consists of a tapered sting at the rear for attachment to the arc system that supports the sting and allows the incidence angle of the model to be adjusted through a $\pm 20^\circ$ range; and the balance sensors themselves, which are dedicated strain gauged bridges as shown in Fig. 2.5 on the left. The data collected by the sensors is sent to a junction box which contains the power supply unit for the force balance and ancillary equipment, the Digital Signal Conditioning Units (DSCUs, shown in Fig. 2.5 on the right), a Digital Signal Conditioning Manager (DSCM) and the interconnecting cables. The box has external connections for the balance leadwire cable, the mains power supply and Ethernet cabling. While data may be sampled by the analogue sensors of the force balance at 4-5kHz, useful converted data stored may only be sampled at 300 Hz by the digital hardware in the junction box. The bias uncertainty of lift and drag measurements are with $\pm$ 0.074N whereas for pithing moment the accuracy it is $\pm$ 0.004N m.

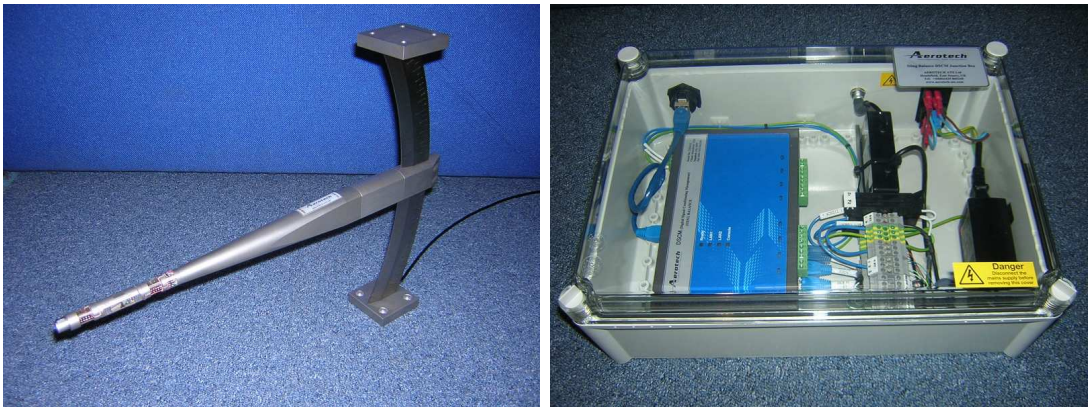

Figure 2.6: Left: the picture of force balance with arc system; right: the picture of DSCU.

2.2.5 Particle image velocimetry (PIV) measurements

Two component PIV measurements are carried out with a dedicated PIV system, which includes a seeding device that discharge particles through an orifice, an illuminating laser with related optics to create a laser sheet and a recording camera. The following subsections describe the sub-systems.

Seeding

The particles seeded into flow field enable to visualize and then to extract the velocity information of fluid motion. As a standard requirement, they should follow the flow in a coherent homogeneous way with minimum velocity lag at the same time providing sufficient illumination to be recorded with adequate contrast. Furthermore they have to withstand the free stream conditions of HSST. For this purpose aluminum oxide powder particles with a nominal crystal size of 300nm are used with a nominal bulk density of $\rho_p = 3970 kg/m^3$. PS-10 powder seeder device is used to generate an airflow seeded with particles. This device consists of a rotating powder containing drum fixed that is controlled by an electronic motor inside a pressure vessel. The drum is rotated about a horizontal axis and at each revolution of the drum ensures a small amount of powder is dispensed through a small opening. Inside the chamber situated six sonic break-up jets to prevent agglomeration of the particles and baffles that are attached to outer perimeter of the drum also help to agitate heavy agglomerates. In order to prevent powder particles leaking back to the upstream half of the chamber and contaminating the region where the electric motor is housed, purge air is continuously supplied. Single exit port of 10mm is located on the side of the chamber to allow seeded airstream flow towards the rig via an air tube. When the drum is not rotated the seeder seizes to dispense particles thus the chamber acts solely as a pressurised vessel, that can be controlled via regulators. A schematic is shown in Fig. 2.7.

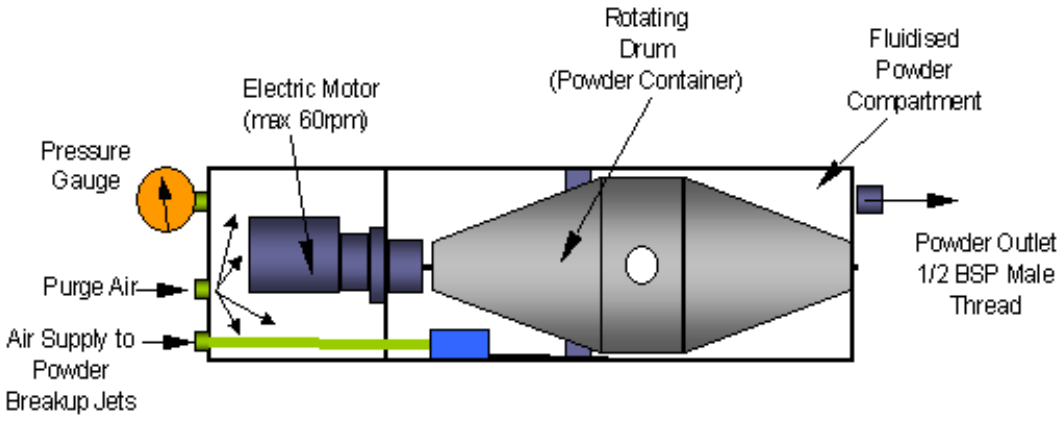

Figure 2.7: Schematic of PS-10 powder seeder device.

The flow tracing capability of particles of diameter d_p and a particle density ρ_p is usually quantified through the particle relaxation time, τ_p. The theoretical

behavior for small spherical particles may be reduced to the modified Stokes drag law defined by Melling [86]. Given the relatively low value of the Mach number and Reynolds number based on the particle diameter, the modified drag relation that takes into account rarefaction effects yields the expression for the relaxation time in Eqn. 2.1, where Kn_d is the Knudsen number, which is defined in Eqn. 2.2. Re_d is the Reynolds number based on the diameter of the particle and M_v is the Mach number both evaluated for the maximum particle slip velocity ΔV [87].

$$\tau_p = \frac{\rho_p d_p^2 \left(1 + 2.7 K n_d\right)}{18\mu} \tag{2.1}$$

where

$$Kn_d = 1.26\sqrt{\gamma}\left(M_v / Re_d\right) \tag{2.2}$$

As suggested by Samimy and Lele [88], the particle dynamic effects may be further parameterized by the Stokes number written in Eqn. 2.3. For accurate flow tracking the time scale of flow has to be bigger than the time response of the particles, i.e. $Sk << 1$. The characteristic jet flow time scale of is found as 70μ sec by assuming ΔV as u_{jet} (see Eqn. 2.3), whereas the particle time response is calculated as 1.6μ sec using typical air jet conditions ($T_{0jet} = 295K, p_{0jet} = 685mbar - 3040mbar, u_{jet} = 315m/s$). Therefore the Stokes number for the current transverse jet tests is found to be as 0.04-0.02, indicating that the particles track the flow with fidelity.

$$Sk = \frac{\tau_p}{\tau_f} \quad where \quad \tau_f = 10\frac{d_{jet}}{\Delta V} \approx 10\frac{d_{jet}}{u_{jet}} \tag{2.3}$$

Illumination

A Litron Nano L series, Nd:Yag Q-switched laser is used for PIV illumination. The laser has the pulse energy of 200mJ at repetition rate of 15Hz. The laser beams are pulsed at the wavelength of 532nm. The pulse width of the light is 6ns and the pulse separation time (the time interval between two consecutive PIV images light pulses, Δt) can be adjusted up to 0.1 μ sec as minimum. A laser sheet of 0.5mm thickness is produced with a series of spherical and cylindrical lenses and routed above the test section via laser guide arm.

Image recording

A LaVision Imager ProX2M CCD camera with $1600 \times 1200 pixel^2$ resolution is used to record scattered light reflecting from particles at 14bit digitisation. The camera is equipped with a Sigma 105mm focal objective lens with f number of 5.6, in combination with a narrow-bandpass 532nm filter in order to minimize ambient light interference. The camera views the laser sheet orthogonally at a desired Field of View (FoV). Whole operation is synchronised and run using DaVis 7.2 software with a Programmable Timing Unit (PTU).

2.3 Calibration of HSST

HSST has become operational recently at full capacity thus a calibration was necessary to check useful running time, flow uniformity and available space for models for Mach 5 non-centrebody nozzle with 152mm exit diameter. A pitot rake, shown in Fig. 2.8, is manufactured and mounted on the sting of the arc system mentioned in Section 2.2.4. The tube outer diameter is 2mm and the tube internal diameter is 1.4mm. The conditions for the calibration are tabulated in Table 2.1. The pitot rake is adjusted vertical and horizontal at 2mm and 62mm from the nozzle exit at a typical unit Reynolds number value of $13.1 \cdot 10^6 1/m$. The streamwise, transverse and spanwise directions are denoted as x, y and z directions respectively.

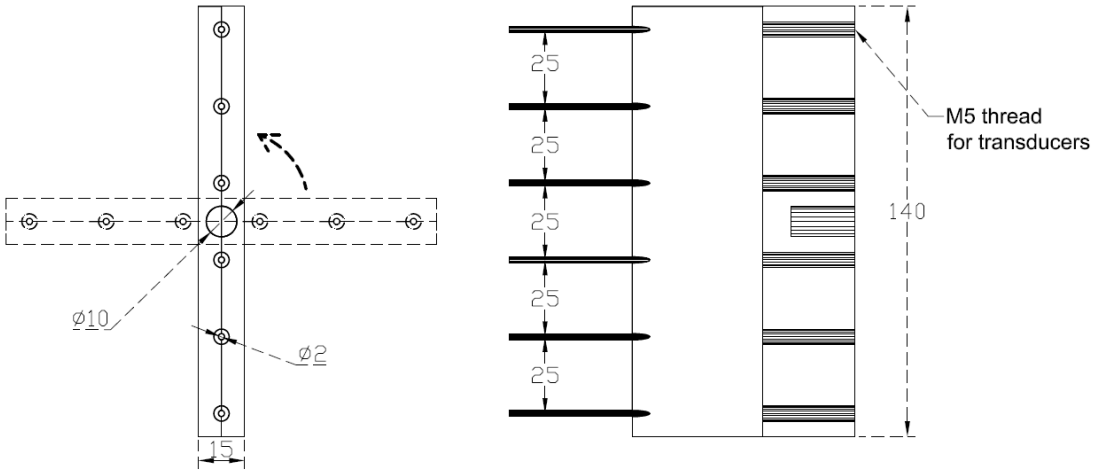

Figure 2.8: Schematic of pitot rake.

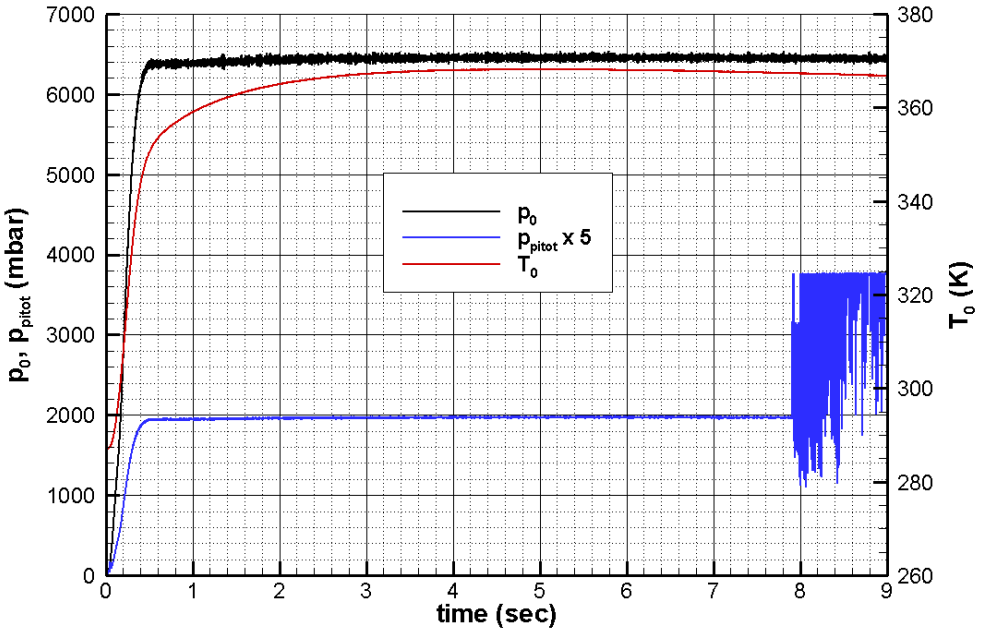

Figure 2.9: Time histories of stagnation pressure and temperature signals with a typical pitot signal, note the right axis for stagnation temperature.

Table 2.1: HSST calibration conditions at Mach 5.

p_{supply} (psi)	T_{supply} (^0K)	M_∞	p_0 $(mbar)$	T_0 (^0K)	Re/m $(\cdot 10^6 1/m)$
175	375	5.0	6450	372	13.1

The time history of stagnation pressure and temperature with pitot pressure history is shown in Fig. 2.9. These signals are recorded at 5kHz (with 10kHz hardware filtering) using instrumentation specified above. Stagnation and pitot pressure signals show a sudden increase due to the initial shock propagating downstream, passing the test section (provided that there is no blockage) and being swallowed by the diffuser. Then a stable plateau is reached for a certain duration of time. Around 8sec from the start pitot pressure signal reveals a sudden jump accompanied by severe oscillations, which corresponds to the passage of a normal shock coming from the diffuser and moving upstream as a result of increased back pressure in the vacuum tanks. This phenomenon indicates the termination of useful running time. Within this plateau stagnation and pitot pressures experience minor variations of less than 1% and remain stable due to stable pressure supply through the dome valve.

If p_{pitot} is non-dimensionalised by p_0, the plateau can be seen even more clearly as shown in Fig. 2.10 (top) and the divided signal is a true indication of useful running time of 7.5sec and Mach number variation. Mach number is deducted from the divided signal using normal shock relations (Rayleigh's pitot tube formula) as specified below in Eq.2.4. MathCad © is utilised to solve this non-linear equation using a root-finding routine since the left hand side of the equation is known. In addition, the frequency content of the stagnation and pitot pressure signals is also examined, as shown in Fig. 2.10 bottom. Both signals are clipped at the region of useful running time and the mean values are subtracted from instantaneous values before applying Fast Fourier Transform (FFT). The biggest peak in stagnation pressure signal is observed at 200Hz, which might be due to the harmonic component of the electronic noise. The other peaks at 900, 1650 and 2000Hz might come from the cavity frequencies as p_0 is measured with a pitot tube connected to a small chamber, where the pressure transducer is attached to the other side. However all these frequencies are smaller than 2.5mbar in magnitude. In case of pitot pressure signal a rather spread out peak is observed at 360Hz, which has a magnitude of 0.06mbar. The reason for that is unknown. These peaks for stagnation pressure and pitot pressure signals are small in magnitude compared to the non-periodic flow signal. Thus there is not a significant frequency that needs to be considered as a result. In addition another p_0 signal is recorded at 50kHz sampling rate without filtering. The frequency content is found to be not considerably different than 5kHz case justifying the sampling rate chosen.

$$\frac{p_{pitot}}{p_0} = \left[\frac{(\gamma+1)\,M_\infty^2}{(\gamma-1)\,M_\infty^2+2}\right]^{\frac{\gamma}{\gamma-1}} \left[\frac{\gamma+1}{2\gamma M_\infty^2-(\gamma-1)}\right]^{\frac{1}{\gamma-1}} \tag{2.4}$$

In case of stagnation temperature history, thermocouple signal shows a continuous rise from the vacuum temperature to a value close to heater temperature (for this run it is 375K) as shown in Fig. 2.9. Although the heater is insulated carefully and heavily there is a slight heat loss. The slow continuous rise of stagnation temperature is associated with the thermal inertia of the thermocouple rather than being physical manifestation of temperature history. Theoretically the thermocouple behaviour is modelled as the solution of a first order ordinary differential equation with a time constant,τ; thus if this theoretical curve with a τ of 0.6sec plotted on top of the experimental T_0 signal in Fig. 2.11 good agreement

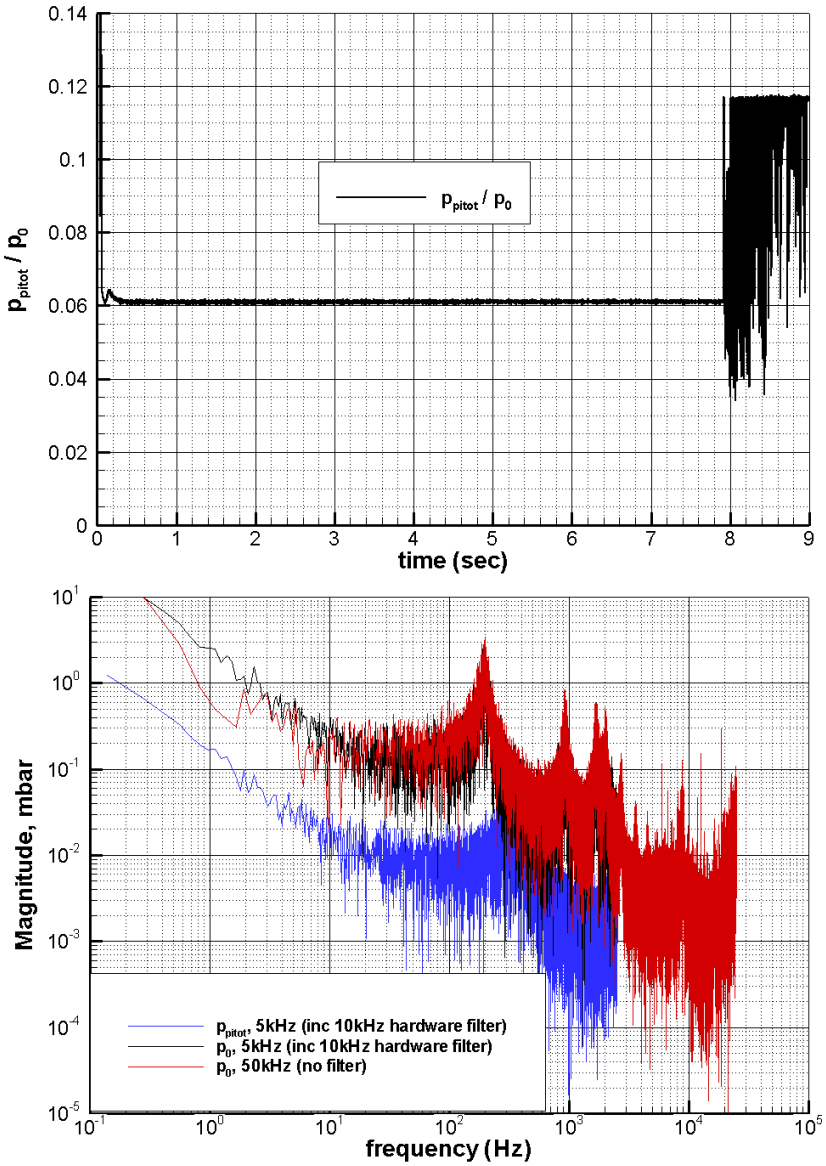

Figure 2.10: Top: time history of p_{pitot} signal non-dimensionalised by p_0, bottom: frequency content of the pitot pressure signal.

around steady state value is obtained. For the plot, the initial temperature value is taken as T_{vac}, and the final temperature value is taken as T_{max} where the temperature gradient becomes practically negligible. The equation of the theoretical behaviour is specified in the Fig. 2.11. There is a considerable difference between the experimental data and theory in the rising period where the initial increase is quite steep (probably due to the passing tunnel start-up shock wave) up to 0.2sec (possible inflection point) and then where the increase is sustained with decreasing slope (i.e. $d^2T/dt^2 < 0$). After 3sec the first order model matches the

physical behaviour. Hence the steady value of 368K is taken as reference when the gradient becomes negligible.

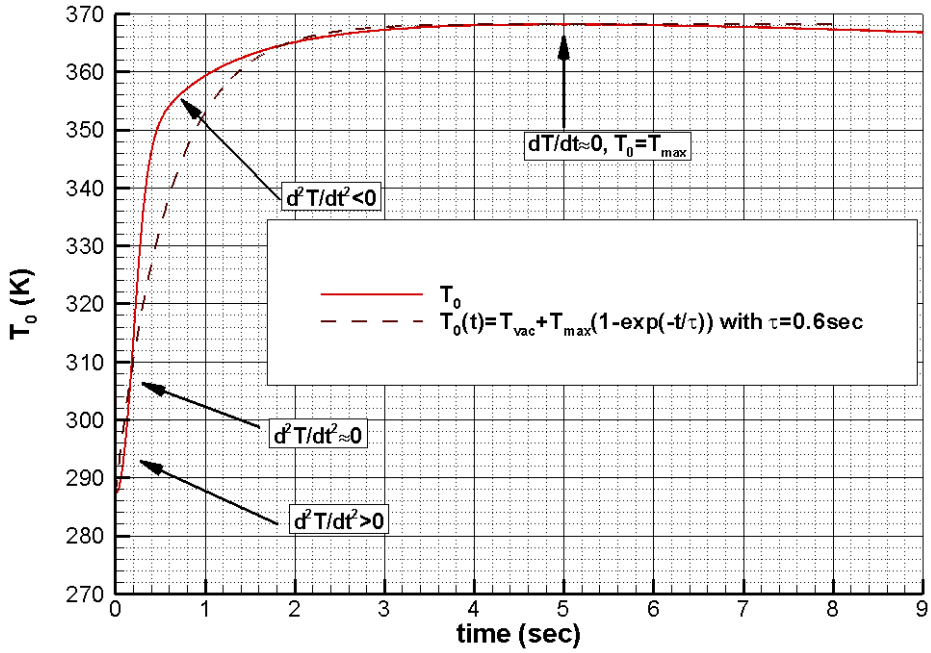

Figure 2.11: Time history of stagnation temperature signal with theoretical first order estimation for a thermocouple behaviour with τ=0.6sec.

From the above discussion it can be concluded that the variations in stagnation and pitot pressure signals are small and hence flowfield can be assumed steady safely, about 7.5 seconds. To further verify this fact, Schlieren pictures (with the SLR camera) spanning the duration of a test are shown in Fig.2.12. These pictures correspond to a vertical configuration of the pitot rake at 2mm from the nozzle exit and show the startup phase, steady phase and the ending phase of the useful running time.

Schlieren visualisation of the flow over the pitot rake at two different locations (2mm and 60mm from nozzle exit) and configurations (vertical and horizontal) are shown below in Fig.2.13. 2mm vertical configuration is not repeated as it is available in Fig. 2.12.

The flowfield does not experience considerable changes during the useful running time concluded from pictures. Stable bow shock waves can be seen very clearly in front of the pitot channels. Furthermore there are Mach waves emanating from the nozzle exit due to pressure difference between nozzle exit and test section (not seen in Schlieren images). These weak waves make a maximum

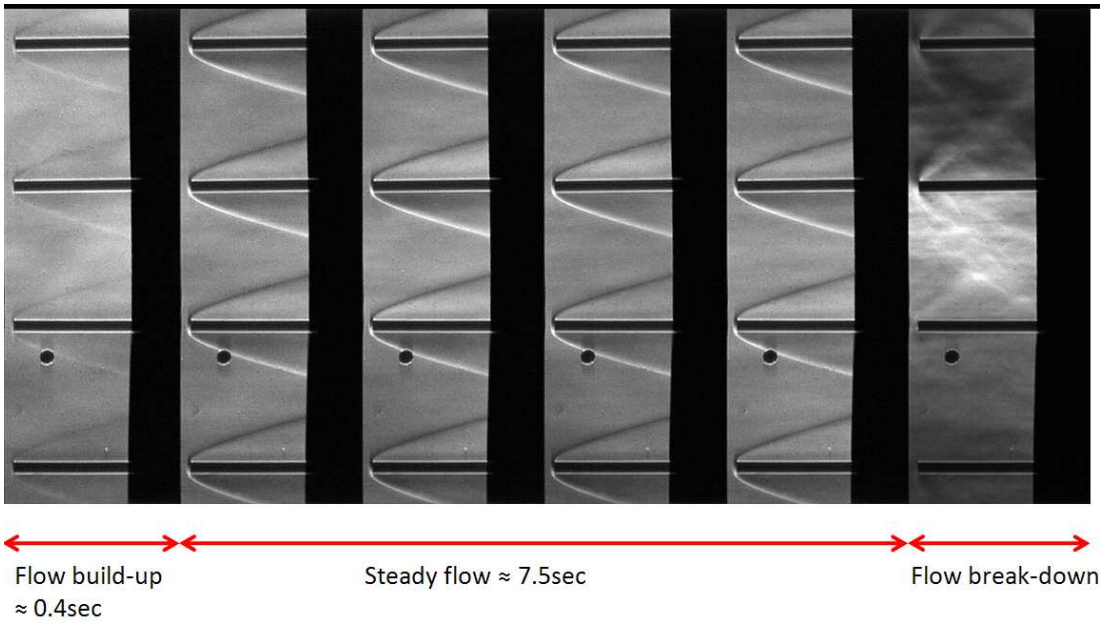

Figure 2.12: Schlieren pictures during the test run, vertical pitot rake at 2mm from the nozzle exit.

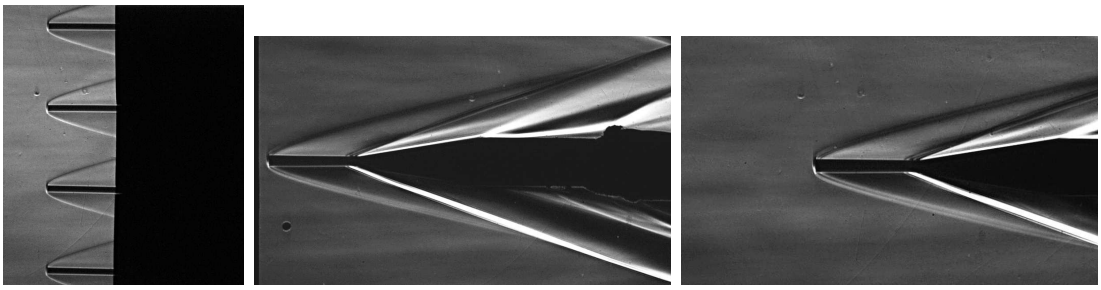

Figure 2.13: Representative Schlieren pictures with different orientations and streamwise locations of the pitot rake; left: horizontal at 2mm from the nozzle exit, middle: vertical 62mm from the nozzle exit, right: horizontal 62mm from the nozzle exit.

of 20degrees with respect to the flow axis as it is shown in Fig. 2.14 for models with big frontal area like the pitot rake for instance. Whereas for models with small frontal area such as a single pitot tube, these waves are aligned at as low as 13degrees from horizontal. The extremities of any model should not intersect with these waves to prevent blockage. As a general rule the bigger the frontal area of the model the more likely the test section is blocked. In fact there is a typical ratio for blockage to start, mentioned by Pope and Goin [89]. It is the ratio model diameter, d_m for blunt bodies divided by the root square of the test section area, A_{sec} (i.e. nozzle exit area for HSST) minus the product of displacement thickness, δ^* and test section perimeter, P, (i.e. nozzle perimeter at the exit

for HSST). This ratio is 0.42 at Mach 5 and it results an allowable blunt body diameter of around 55mm for HSST to ensure tunnel start-up. Maximum model length that can be accommodated inside the test section is 400mm by assuming the symmetric Mach diamond (test rhombus) that is extending 210mm upstream inside the nozzle.

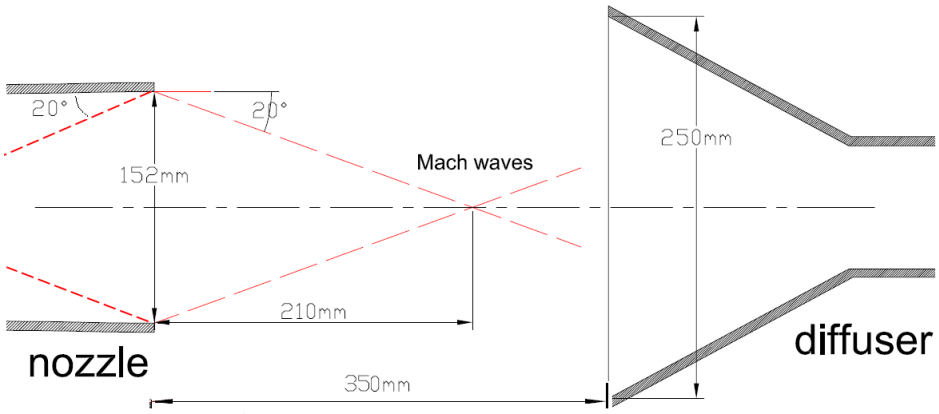

Figure 2.14: Minimum test section available area for models.

Calibration results at two different streamwise stations with both vertical and horizontal configurations are depicted on Table 2.2 below. The flow quality in the test section is found to be very good in terms of symmetry and variations in Mach number that are very small, about 0.4%. The free stream values are calculated using isentropic relations and the associated uncertainties are estimated using standard techniques based on precision and bias calculations described by Moffat [90]. These values are tabulated in Table 2.3. All the uncertainties are based on 95% confidence interval levels. Uncertainties associated with test flow conditions include contributions from uncertainties in supply pressure set by dome valve, supply temperature set by heater, measured outputs from the data acquisition system and the estimated values are given in Table 2.3. The details of the uncertainty calculation is described in Appendix B.

2.4 Experimental setup for transverse jets in high speed cross flow

Following subsections explain the experimental setup for transverse jets in high speed cross flow studies, comprising of flat plate model with jet orifice (without

Table 2.2: Calibration results

x(mm)	y(mm)	z(mm)	Mach no	x(mm)	y(mm)	z(mm)	Mach no
2	62.5	0	4.97	62	62.5	0	4.97
2	37.5	0	4.98	62	37.5	0	4.98
2	12.5	0	5.01	62	12.5	0	5.00
2	-12.5	0	5.01	62	-12.5	0	5.00
2	-37.5	0	4.98	62	-37.5	0	4.98
2	-62.5	0	4.97	62	-62.5	0	4.97
2	0	62.5	4.97	62	0	62.5	4.97
2	0	37.5	4.98	62	0	37.5	4.98
2	0	12.5	5.01	62	0	12.5	5.00
2	0	-12.5	5.01	62	0	-12.5	5.00
2	0	-37.5	4.98	62	0	-37.5	4.98
2	0	-62.5	4.97	62	0	-62.5	4.97

Table 2.3: Free stream conditions at Mach 5.

p_0 $(mbar)$	T_0 (^0K)	Re/m $(\cdot 10^6 1/m)$	p_{pitot} $(mbar)$	p_∞ $(mbar)$	u_∞ (m/s)
6450 ±0.7%	372 ±1.7%	13.1 ±3.7%	396 ±1%	12.18 ±2.4%	790±1.0%

and with rough surface), oil dot visualisation setup and PIV setup.

2.4.1 Model

The model used for this study is a sharp leading edge flat plate with a converging jet hole of 2.2mm, through which a sonic turbulent jet of either air, CO_2 and He is injected after regulation. The flat plate is 155mm long, 68mm wide and 5mm thick as it is shown in Fig. 2.15 and painted with mat black paint. Considering the Mach wave angle of 11.5degrees at Mach 5, the disturbances created at the corners of the flat plate can meet at 166mm downstream of the leading edge, which is longer than the flat plate length. There are 25 pressure tappings (of 1mm in diameter) on the model. The model inside the test section shown in Fig. 2.16 on the left. For the roughness investigation whole flat plate is covered with three different sand papers, P120, P400 and P1000. The sand grain at the leading edge is filed to have a minimal effect on leading edge thickness. The pressure tappings on the surface are punched through the sand paper as well as the jet orifice as shown in Fig. 2.16 on the right. P1000, P400 and P120 have the

manufacturer specified average particle diameters of 18.3μm, 35μm and 125μm respectively.

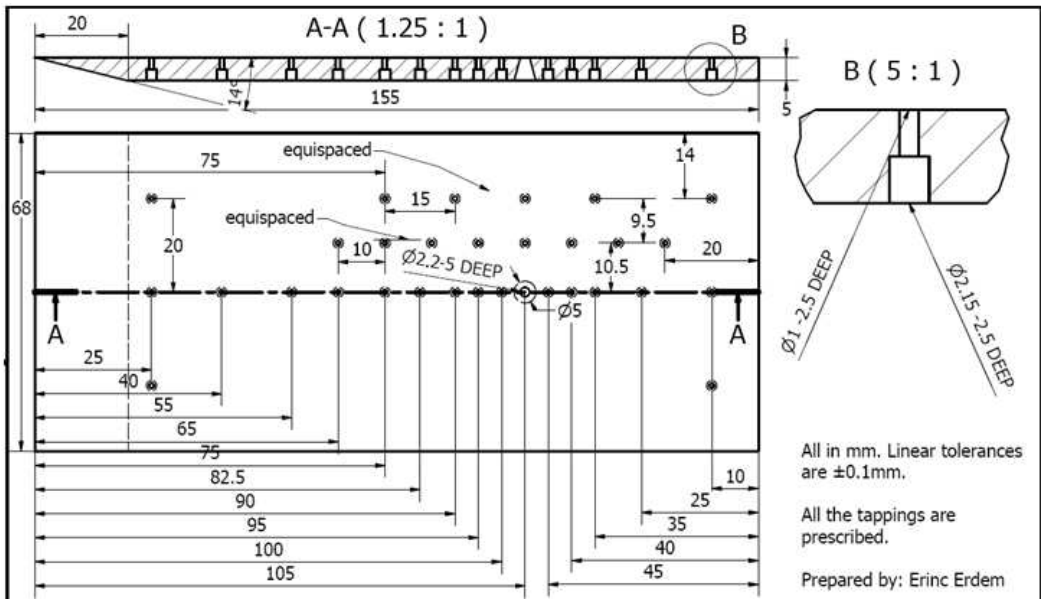

Figure 2.15: Technical drawing of the model specifying dimensions.

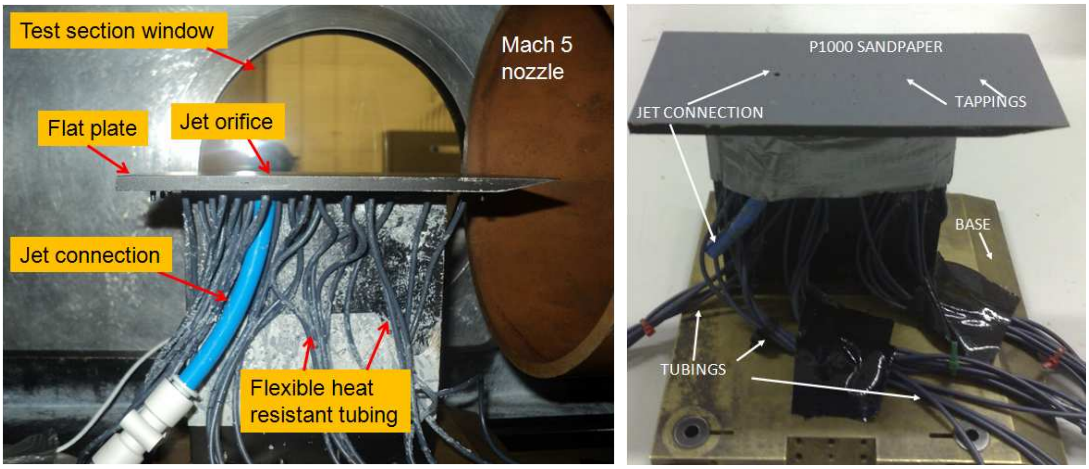

Figure 2.16: Left: flat plate model placed inside test section (smooth case), right: flat plate covered with P1000 sandpaper.

Oil dot visualisation setup

In case oil dot visualisation, two light sources of 500W and 800W power placed on either side of the test section to provide uniform illumination and the LaVision Imager ProX2M CCD camera is placed above the test section with an angle about

45° as shown in Fig. 2.17. During the test camera is run at 30Hz with 0.1msec exposure time.

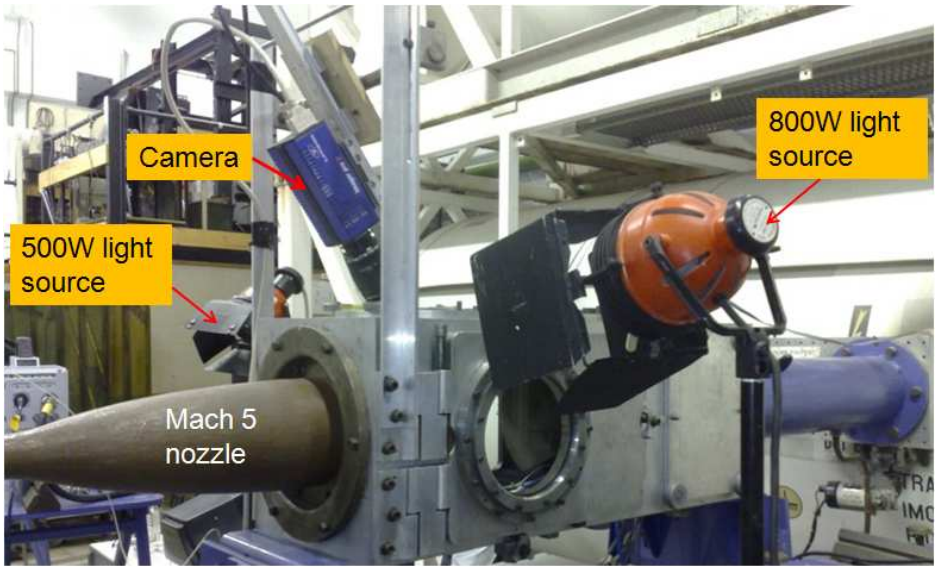

Figure 2.17: Oil dot visualisation setup.

PIV setup

The whole PIV setup is arranged such that it can produce a laser sheet that is tilted at 45° with respect to flat plate as shown in Fig.2.18. The laser sheet is localised at the centreline. The camera sees a FoV orthogonally to laser sheet. In the experiments only the traverse jet is seeded with aluminum oxide powder particles and the jet stagnation pressure is measured on the line just before the jet orifice, prior to experiments with the seeder drum being idle. Whereas during the test run the pressure transducer is removed to avoid deposition of particles inside the diaphragm of the sensor and the seeding density level stays stable. Pulse separation between laser pulses, Δt, is set to 0.6μsec for air and CO_2 and 0.3μsec for Helium so that sufficient displacement for the tracer particles of between 4.5 to 10pixels for the velocity range from 300 to 800m/s.

The flow field is imaged in the streamwise (x) and wall-normal (y) directions over a field of view of approximately $64 \times 48 mm^2$, resulting in a digital resolution of approximately 25 pixels per mm. A dataset of around 100 is acquired during the test time at 15Hz. Recorded images are divided into initial interrogation windows and then processed with a cross correlation algorithm using DaVis 7.2 software. The initial interrogation areas are selected as $32 \times 32 pixel^2$ with 2 passes

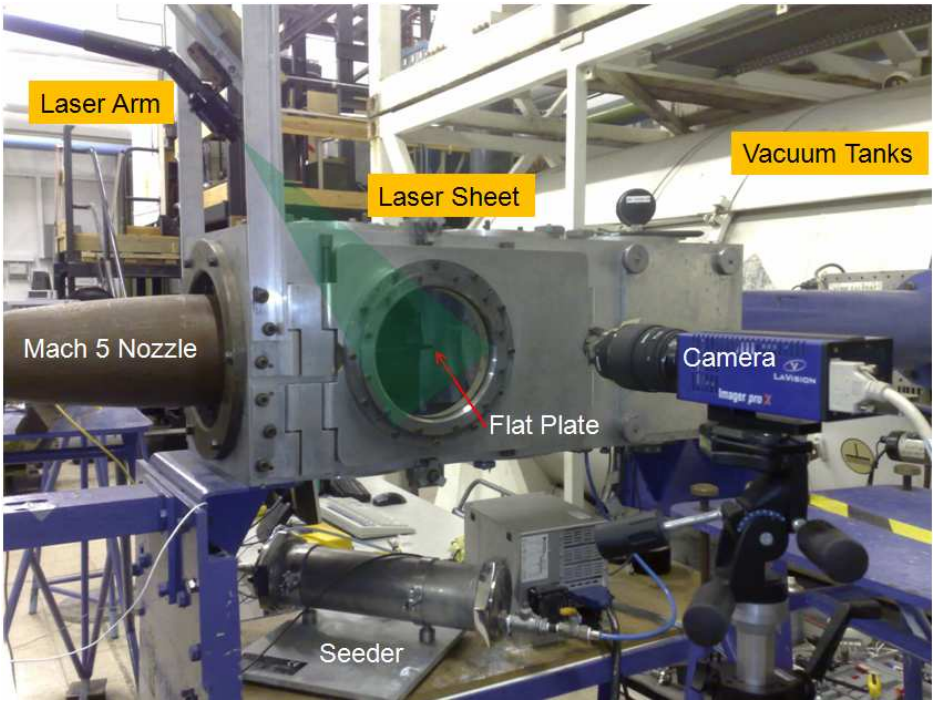

Figure 2.18: PIV setup.

and then refined to $16 \times 16 pixel^2$ with 3 passes. A 75% overlap is employed in order to improve spatial resolution and to prevent the appearance of spurious vectors. With this arrangement, two adjacent velocity vectors are separated by approximately 0.2mm.

2.5 Experimental setup for energy deposition for drag reduction

Following subsections explain the experimental setup for drag reduction studies, comprising of the axisymmetric models, high voltage generation and the electrodes and finally laser focusing equipment.

2.5.1 Axisymmetric models

Test models for the drag reduction studies are an axisymmetric cone-cylinder model of 15degrees half angle with two blunt faced truncated cone-cylinder models, an axisymmetric cone-cylinder with flare model together with a blunt faced truncated cone-cylinder with flare model, as shown in Fig. 2.19. Medium to high

truncation levels are chosen, i.e. $d_t/d_b = 0.5, 0.75$, to increase the interaction time of the energy spot on the frontal face as well as to increase frontal face area to energy spot area ratio. Both would result increased efficiency of the energy deposition. It has to be noted that the dimensions are in mm. These models are placed on a sting using a 20mm long thread from inside and positioned 50mm to 60mm from the nozzle exit.

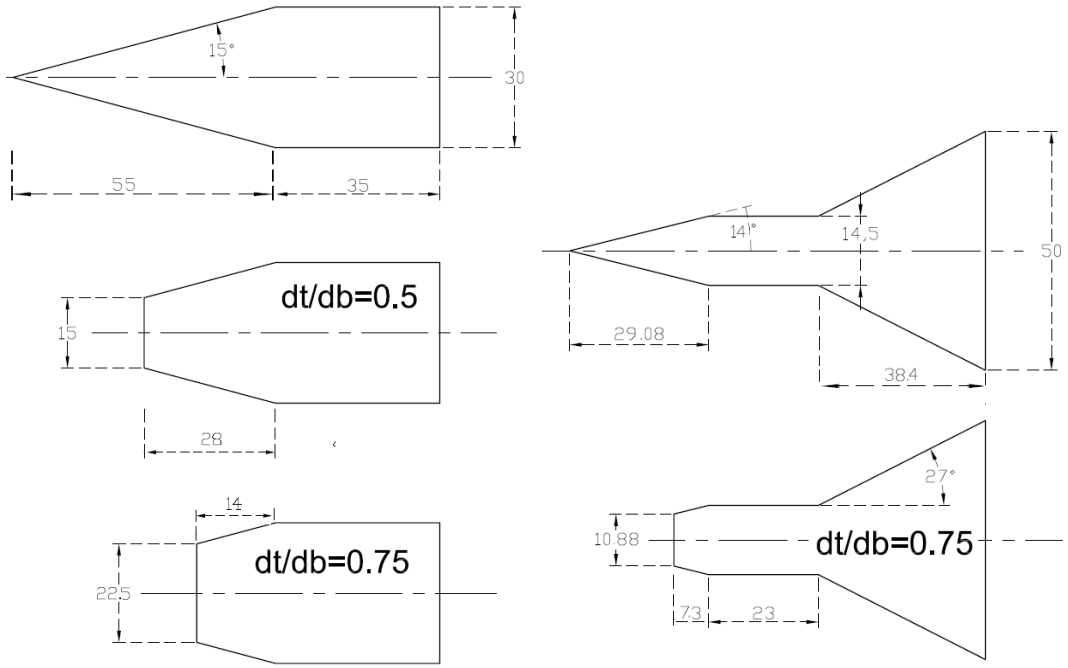

Figure 2.19: Left: axisymmetric cone-cylinder models, right: axisymmetric cone-cylinder models with flare.

2.5.2 High voltage arc discharge generation

High voltage is generated inside an earthed Faraday cage that is positioned just underneath the test section. The cage is powered by an adjustable constant voltage source, Voltcraft VLP3610. The power supply is capable of producing 36volts, 10amperes. The output from the power supply is connected to the DC-30kV high voltage generator from Electrofluidsystems that is used to generate high voltage arc discharges. This unit was developed for aerospace plasma propulsion and optimized for low weight (less than 100g) at highest power and output voltage. The device consists of one integrated board with an onboard low voltage control circuit and a high voltage cascade. First, a small transformer transforms the low

input voltage to 3kV peak to peak. The following voltage multiply cascade generates the output voltage with up to 30kV peak to peak. A signal generator can be used to pulse the high voltage signal as preferable low frequencies at 50% duty cycle. Beyond 60Hz there is a DC bias that reduces the pulsing rate. Therefore for this study it is run at steady actuation mode without pulsing.

2.5.3 Electrode arrangement

The output from the high voltage unit is routed inside the test section with insulating wires and connected to one of the two electrode holders. The other holder is connected to earth. The electrodes are made of tungsten rods of 0.5mm diameter at the tip and the holders are made of brass. The high voltage holder is inserted inside a macor support. A schematic diagram of the electrode arrangement that shows reasonable flow interference with enough structural stability is shown in Fig. 2.20. In this arrangement, the electrodes are an angle of 63° with the flow direction and with their tips at distances of $l/d_t = 1.8, 1.5, 1.3$ and 0.9 from the model, where d_t is diameter of the truncated face encountering the flow. The distance over which the arc is created is kept around 2mm as it has been suggested by Knight [71] and Kolesnichenko [67] as the most efficient energy addition processes with very thin channels.

The voltage output is monitored using a LeCroy PPE-20kV high voltage probe and the current is monitored using a Tectronix current probe. These output signals are connected to a Picoscope 3201 250MHz oscilloscope.

2.5.4 Laser focusing arrangement

The Nd:Yag laser mentioned in Section 2.2.5 is used to focus the energy on a concentrated volume in front the models. To achieve a higher perturbation of laser energy deposition, the laser system is run at the maximum power. The diameter of output laser beam is 6mm as quoted by the manufacturer. Laser energy deposition is obtained by focusing the laser beam using concave convex lens system. A combination of three lens is adapted; the first 25.4mm concave lens with focal length of f=-100 mm expands the laser beam and a following 50mm diameter convex lens with 250mm focal length then collimates or converges the beam expansion slightly. Finally, the laser beam is focused to the wind tunnel test section through the top Quartz window by a third convex lens as shown

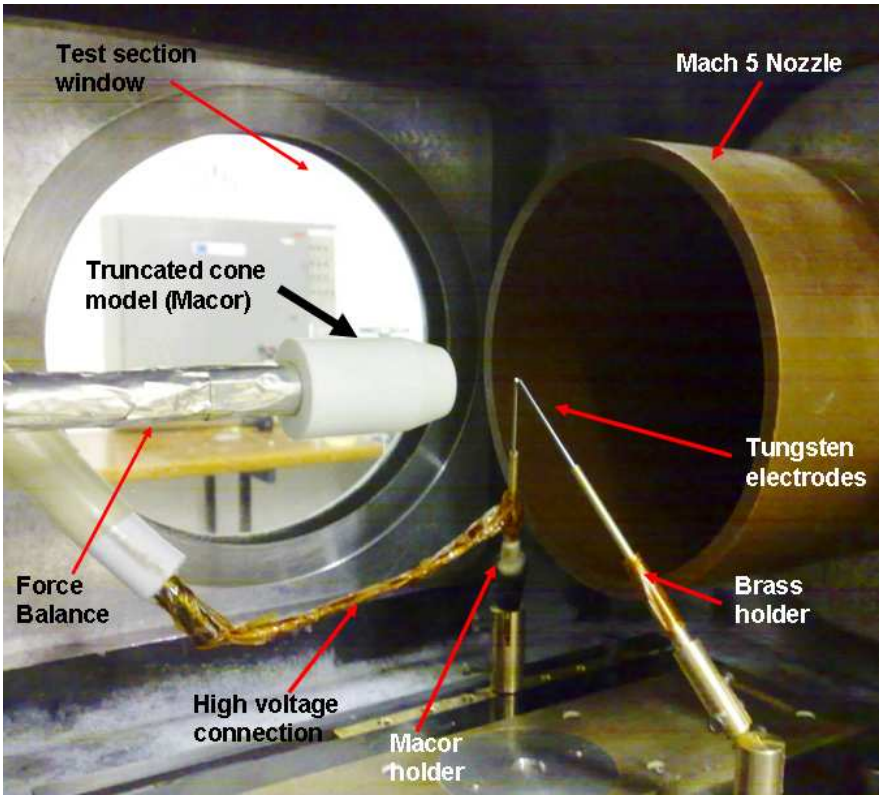

Figure 2.20: Electrodes arrangement inside test section.

in Fig. 2.21. The set up of laser beam is inclined at a small angle respect to the normal direction of top window with aim of avoiding the risk of unexpected focusing of the beam from reflection of test section window. The benefit of using combination lens to focus is that laser beam can be focused into a smaller spot to obtain higher energy density. The distance between the laser spot and the models is set to $l/d_t = 1.4$.

2.6 Numerical considerations

Following subsections explain the common numerical setup for simulations of the transverse jets in high speed crossflow and axisymmetric cone-cylinder models (baseline tests). The details of the computational grid and boundary conditions for individual simulations are specified in Chapters 3 and 4.

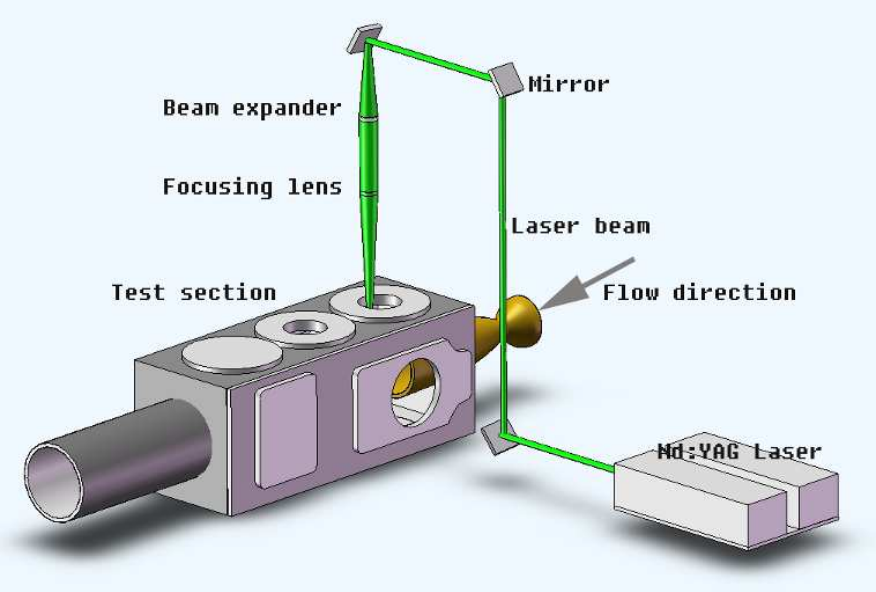

Figure 2.21: Laser deposition arrangement inside test section.

2.6.1 Numerical solver

In the current numerical studies Favre Averaged Navier-Stokes (FANS) equations are solved with density based (coupled) double precision solver of FLUENT®. Second order spatially accurate upwind scheme (SOU) with Roe's Flux-Difference Splitting is utilised. In this scheme formulation second-order accuracy is achieved at cell faces through a Taylor series expansion of the cell-centred solution about the cell centroid. Therefore the face value of a flow variable, ϕ_f is computed using the following equation [91]:

$$\phi_{f,SOU} = \phi_c + \nabla\phi_c \cdot \Delta\vec{s} \tag{2.5}$$

where ϕ and $\nabla\phi$ are the cell-centred value and its gradient in the upstream cell, and $\Delta\vec{s}$ is the displacement vector from the upstream cell centroid to the face centroid as shown clearly in Figure 2.22.

This formulation requires the determination of the gradient in each cell centre. For this purpose, $\nabla\phi_c$ is expressed as a summation of values at the cell faces using Green-Gauss theorem shown below.

$$\nabla\phi_c = \frac{1}{\mathcal{V}} \sum_f \overline{\phi}_f \, \vec{A}_f \tag{2.6}$$

where ϕ_f is the value of ϕ at the cell face centroid. Consequently for the

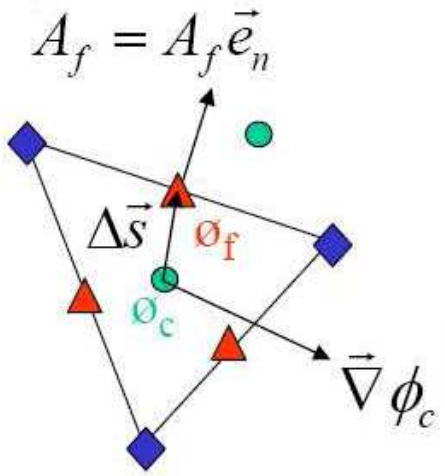

Figure 2.22: Cell nomenclature

evaluation of face values, the arithmetic average of the nodal values on the face is computed as expressed in Equation 2.7.

$$\overline{\phi}_f = \frac{1}{N_f} \sum_{n}^{N_f} \overline{\phi}_n \tag{2.7}$$

where N_f is the number of nodes on the face. The nodal values, $\overline{\phi}_n$ are constructed from the weighted average of the cell values surrounding the nodes in an unstructured manner in Figure 2.23. In structured meshes the weighted average is the average of four cells surrounding the node in two dimensions.

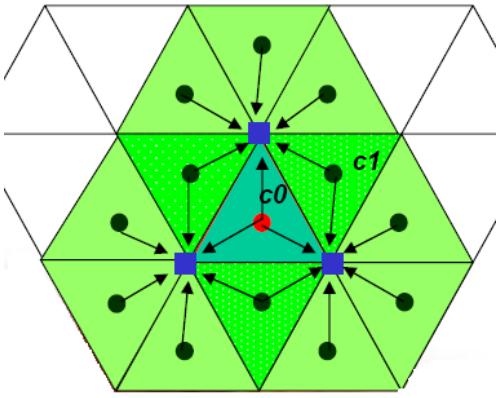

Figure 2.23: Green-Gauss node based gradient evaluation stencil

Finally the gradient of ϕ is limited with ψ in the second term of Equation 2.8 so that no spurious wiggles are introduced; the limiter adapted is the one

from Venkatakrishnan [91]. It is based on a comparison of the actual ϕ value at the adjacent cell, $c1$, with the one estimated by evaluating $\nabla\phi_c$ and $\Delta\vec{s}_{0-1}$ at $c0$ (see Figure 2.23) using Equation 2.5. If the estimated value is much larger in magnitude, an extremum is detected and the gradient is limited by a scale factor.

$$\phi_f = \phi_c + \psi\nabla\phi_c \cdot \Delta\vec{s} \tag{2.8}$$

2.6.2 Turbulence Model and solver parameters

For the range of Reynolds number attainable and for the flat plate for jet studies, the axisymmetric models for drag reduction studies, the high speed boundary layer developing on the surfaces is laminar unless tripped (see Section 3.1.1 for verification). Nevertheless adverse pressure gradients inherent in the flowfields due to either the presence of the jet or the flare, cause the boundary layer to separate and trigger transition. Therefore a turbulence model has to be employed in simulations to take the transition into account. Shear-Stress Transport (SST) $\kappa - \omega$ model of Menter is adapted for jet studies and for the flared truncated cone-cylinder models. For the simple cone-cylinder models laminar simulations are conducted naturally. SST performs well in the presence of adverse pressure gradients and consequent separations noted in user documentation [91]. In this model, $\kappa - \omega$ at near wall region is blended with $\kappa - \epsilon$ outside boundary layer. The transport equations for κ and ω are specified below in Equations 2.9 and 2.10. Moreover the corrections for compressibility and transition are applied. The correction for transition is nothing but a low Reynolds number modification to the turbulent viscosity.

$$\frac{\partial}{\partial t}(\rho k) + \frac{\partial}{\partial x_i}(\rho k u_i) = \frac{\partial}{\partial x_j}\left(\Gamma_k \frac{\partial k}{\partial x_j}\right) + \tilde{G}_k - Y_k + S_k \tag{2.9}$$

and

$$\frac{\partial}{\partial t}(\rho \omega) + \frac{\partial}{\partial x_i}(\rho \omega u_i) = \frac{\partial}{\partial x_j}\left(\Gamma_\omega \frac{\partial \omega}{\partial x_j}\right) + G_\omega - Y_\omega + D_\omega + S_\omega \tag{2.10}$$

In case of compressibility correction, compressibility affects turbulence through so-called "dilatation dissipation", which accounts for the decrease in spreading or growing rate of mixing layers or free shear layers with increasing convective Mach number that is well documented by Smits and Dussuage [92]. Specifically

for this model compressibility takes part in dissipation terms such as Y_k and Y_ω and partially in the production of turbulence kinetic energy as defined below.

$$Y_k = \rho\beta^* k\omega \text{ and } Y_\omega = \rho\beta\omega^2$$

where β^* and β are expressed below as functions of $F(M_t)$;

$$\beta^* = \beta_i^* \left[1 + \zeta^* F(M_t)\right] \tag{2.11}$$

$$\beta = \beta_i \left[1 - \frac{\beta_i^*}{\beta_i}\zeta^* F(M_t)\right] \tag{2.12}$$

$\zeta^* = 1.5$ and other parameters are defined in user documentation [91]. The compressibility function, $F(M_t)$, is given by following conditional expression.

$$F(M_t) = \begin{cases} 0 & M_t \leq M_{t0} \\ M_t^2 - M_{t0}^2 & M_t > M_{t0} \end{cases}$$

where

$$M_t^2 = \frac{2k}{a^2} M_{t0} = 0.25a = \sqrt{\gamma RT}$$

Lastly the term $\tilde{G}_k$ represents the production of turbulence kinetic energy which involves β^*, and is affected by compressibility as well, as shown below.

$$\tilde{G}_k = \min(G_k, 10\rho\beta^* k\omega)$$

where G_k is defined in the same manner as in the standard k-ω model as with other constants [91].

For the wall boundary condition in SST model, following equation is used for ω in FLUENT®[91]. The homogeneous turbulence condition applies to the stresses at the wall such that $k = 0$.

$$\omega_{wall} = \frac{\rho u_\tau^2}{\mu}\omega^+ \quad where \quad \omega^+ = \min(2500, \frac{6}{B_i \left(y^+\right)^2})$$

where the expressions for friction velocity and wall shear stress are defined below:

$$u_\tau = \sqrt{\tau_w/\rho} \quad \tau_w = \mu \left(\frac{\partial u}{\partial y}\right)_w \quad and \quad y^+ = y u_\tau/\nu$$

In case of solver parameters Courant-Friedrichs-Lewy (CFL) condition is kept at 0.5 with proper under-relaxation factors to ensure stability. Full-multi grid initialization technique that solves Euler equations at a certain number of temporary grid levels starting from coarse to fine and then sets the fine grid level solution as an initial solution, is employed rather than providing constant initial conditions to start simulation with. The benefit of this technique is accelerated convergence.

Chapter 3

Transverse Jets at Mach 5 Cross Flow

In this chapter the results of the transverse jets at Mach 5 cross flow are presented; the effects of incoming unit Reynolds number, injectant gas and surface roughness are investigated with three different values of momentum flux ratio, J. The tests include conventional/high speed schlieren photography, wall pressure measurements, oil dot visualisation and PIV measurements. CFD simulations are also carried out, firstly the solver is validated for this type of problems in a two-dimensional case of Spaid and Zukoski [1]. Then a three dimensional case replicating an experimental case is simulated to provide greater understanding on the flow physics. Theoretical estimates are also utilised to further build confidence on the test campaign.

3.1 Experimental test campaign

In the experimental test campaign the transverse jet is started just before the test gas arrival; and due to low pressure in the test section the jet spreads out quite significantly in all directions with a huge Mach disc (30mm in length, top boundary not shown). Afterwards with the arrival of the test gas Mach disc gets suppressed due to higher effective back pressure caused by the bow shock and rotates towards the main direction of the flow, in the horizontal direction, x. The start up behaviour is visualised using schlieren photography at 3kfps with 20μsec exposure in Fig. 3.1 for test 3 in Table 3.1.

The Mach disc height, h, extends 8.2mm above the wall (measured as the

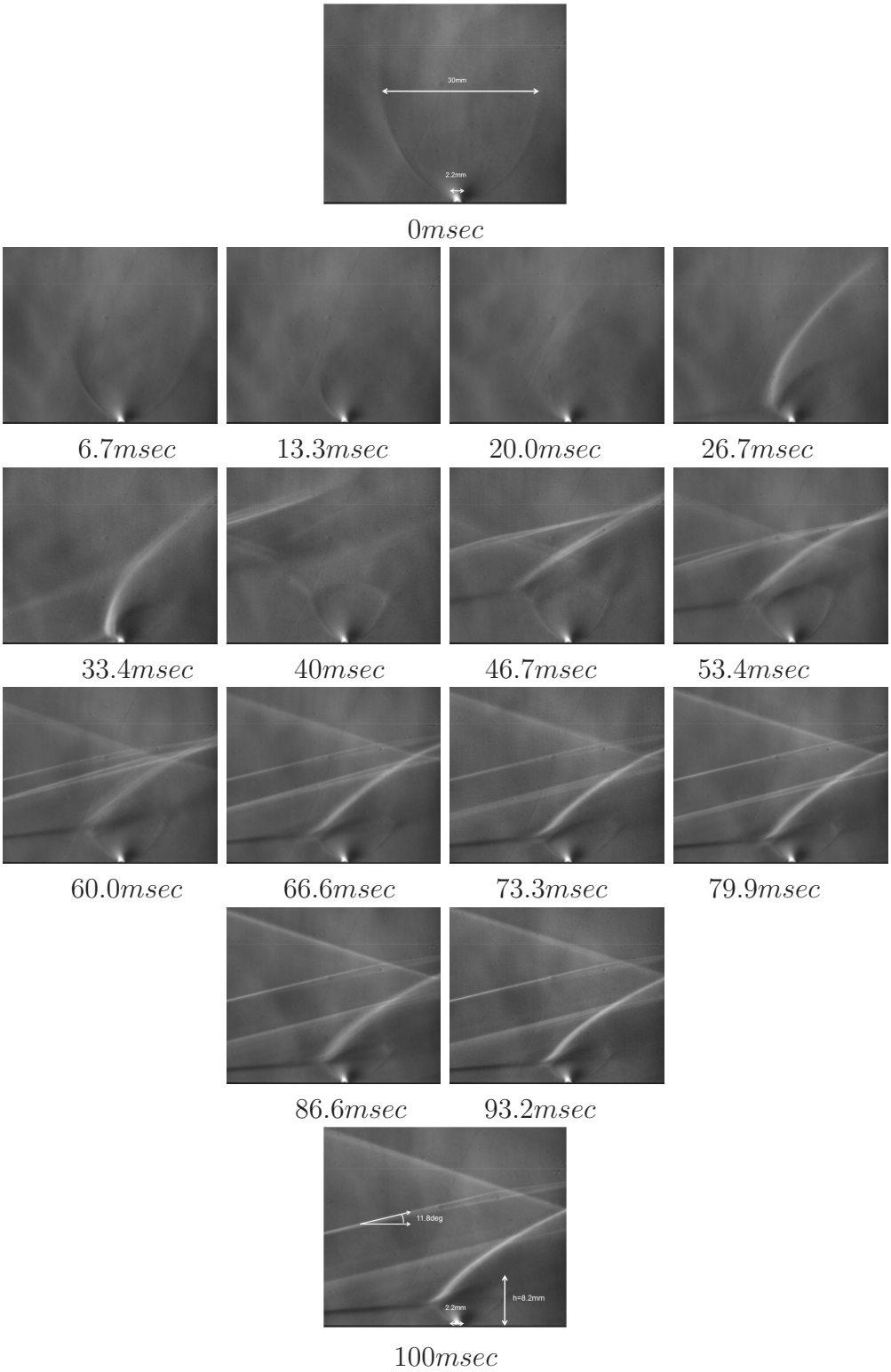

Figure 3.1: High speed schlieren visualisation of the sonic transverse jet captured at 3000fps with 20μsec exposure time.

maximum height from the wall) and the separation shock hits the bow shock causing oscillatory behaviour in addition to inherent jet shear layer instabilities. Another thing to note is the leading edge shock makes 11.8° with the horizontal at downstream region, which is consistent with the theoretical Mach angle of 11.5° at Mach 5. The flowfield nearly stabilises in 100msec with the bow and separation shocks oscillating.

Table 3.1 shows all the cases tested. It has to be noted that schlieren visualisations and surface pressure measurements are conducted as a standard for each test. Tests 1-3, tests 10-12 and tests 13-15 utilised oil dot visualisation and PIV as additional flow diagnostics. Tests 16-24 include rough surfaces, whose specifications are depicted under jet gas type. The uncertainties in experimental values are calculated using an approach mentioned in Appendix B.

3.1.1 Baseline tests

Schlieren visualisation

Baseline tests consist of the first three tests, tests 1-3 in Table 3.1, at a typical high unit Reynolds number with the smooth plate configuration and three different momentum flux ratios. Fig. 3.2 shows the long exposure ($250\mu sec$) schlieren images of the flowfield for the baseline case. The following flow structures can be observed; a leading edge shock due to viscous interaction at the leading edge and following laminar boundary layer growth up to the separation point accompanied by diversion in upward direction thereafter. Separation shock emanates around the separation point and intersects the jet induced bow shock; sonic jet expands suddenly and aligns itself backwards, afterwards its expansion is terminated by the Mach disc. The boundaries of the jet is confined with barrel shocks around it. Separation region, separation shock and bow shock are three dimensional curved flow structures around the transverse jet. Curved recompression shock has occurred just above the separation region downstream of the jet. These three dimensional flow structures are superimposed on schlieren images as expected. Finally the Mach waves coming from the pressure tappings are apparent. These flow structures are well reported in literature and mentioned in Chapter 1. Transverse jet penetrates further for higher values of J, the bow shock moves away from the surface and the separation region extends in both upstream and downstream directions.

Table 3.1: Experimental test conditions.

Test No	Jet Gas	p_0 $(mbar)$	T_0 (^0K)	Re/m $\cdot 10^6(1/m)$	p_{0jet}/p_∞	Re_{djet} $\cdot 10^3$	J
1		6460	372	13.11	55	19.6	1.16
2	*Air*	6490	375	13.0	130	46.5	2.75
3	*Smooth*	6390	375	12.81	251	88.5	5.30
4		5874	469	8.20	60	19.5	1.26
5	*Air*	5911	473	8.15	143	46.7	3.02
6	*Smooth*	5927	477	8.07	273	89.7	5.77
7		5471	571	5.62	65	20.1	1.37
8	*Air*	5548	571	5.70	152	47.3	3.21
9	*Smooth*	5577	576	5.65	293	90.6	6.18
10		6450	366	13.42	57	8.1	1.33
11	*He*	6520	373	13.17	114	16.0	2.65
12	*Smooth*	6512	377	12.95	171	23.9	3.96
13		6452	374	12.96	56	32.7	1.13
14	CO_2	6468	374	13.00	130	75.8	2.64
15	*Smooth*	6488	379	12.78	178	104	3.61
16		6438	378	12.73	55	19.4	1.17
17	*Air*	6439	375	12.91	132	47.1	2.78
18	*P*1000	6431	364	13.53	248	89	5.25
19		6442	374	12.98	56	19.8	1.19
20	*Air*	6453	373	13.07	131	47.5	2.77
21	*P*400	6388	366	13.30	251	88.8	5.30
22		6398	374	12.88	57	19.7	1.20
23	*Air*	6458	377	12.82	131	47.3	2.76
24	*P*120	6422	375	12.90	249	88.7	5.26
	Unc.	±0.7%	±2.0%	±3.5%	±2.2%	±2.8%	±4%

The high speed boundary layer developing on the flat plate before the jet induced separation within the achievable range of unit Reynolds numbers is laminar unless tripped. To verify this fact an approach on transition by Simeonides [93] is employed. In his approach flat plate transition data from several different facilities are collected and a unique way is proposed to correlate this data with characteristic parameters such as leading edge thickness, viscous interaction parameter, etc. Transition phenomenon is classified into two major categories;

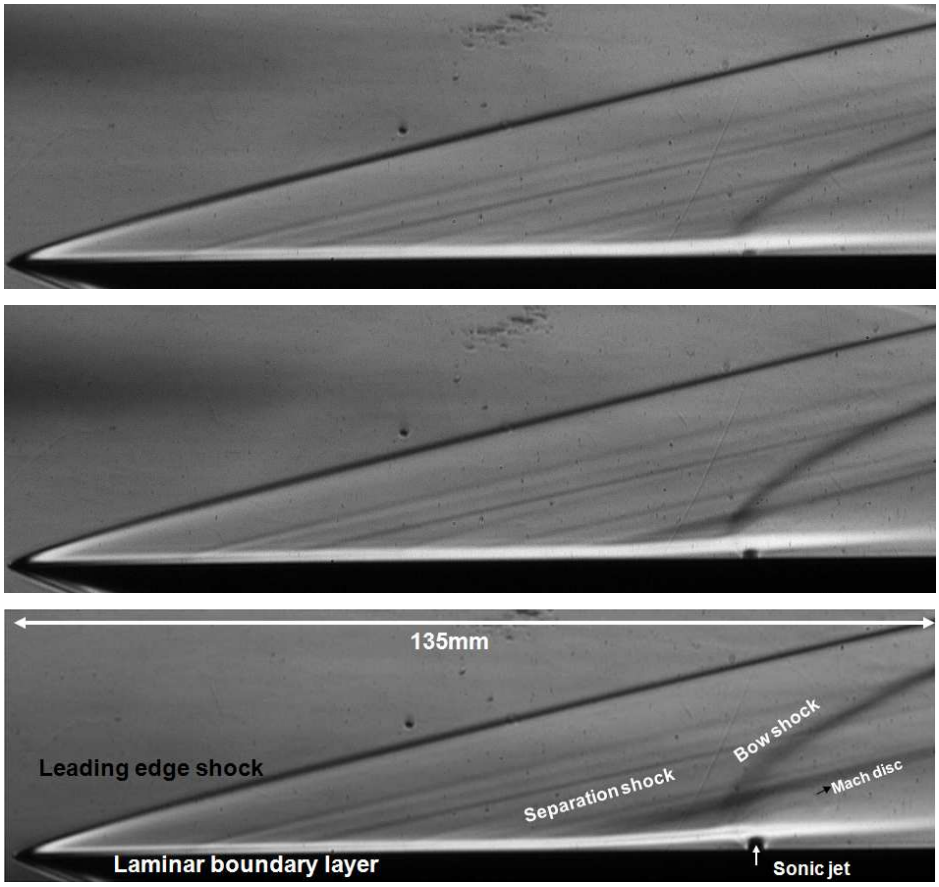

Figure 3.2: Schlieren visualisation of the flowfield in the presence of the sonic transverse jet with three different momentum flux ratios; top: test 1, middle: test 2, bottom: test 3 with annotated flow structures.

viscous dominated transition and bluntness dominated transition. The parameter defining this classification is simply the ratio of a bluntness parameter, β, to viscous interaction parameter, $\bar{\chi}$ at the transition location. If $\beta/\bar{\chi}$ is greater than 1.9 then the transition is bluntness dominated transition otherwise it is viscous dominated transition. When data is separated, two very good correlation plots can be drawn as shown in Fig. 3.3, Re_{tr} against $Re/m/M$ for viscous dominated transition, Mx_{tr}/b against Re_b/M^2 for bluntness dominated transition, where b is leading edge thickness. Therefore x_{tr} is estimated as $200mm$ from the leading edge for the current sharp flat plate from the viscous dominated transition plot for the highest attainable unit Reynolds number at Mach 5 (i.e. $16 \cdot 10^6 1/m$). Considering the length of the plate being $155mm$, the incoming boundary layer is laminar. Another estimate is available from Anderson [94] based on cone data, expressed in Eqn. 3.1. Remembering a cone has a shorter transition length than

a flat plate because of the curved nature of streamlines due to three dimensional effects, this estimate can be utilised for checking the transition location on the flat plate. Thus x_{tr} is estimated as $200mm$ again proving laminar flow developing on the plate. However around the first upstream separation region there is a strong probability of transition phenomenon to take place due to the fact that at high Reynolds numbers the laminar reattachment does not occur.

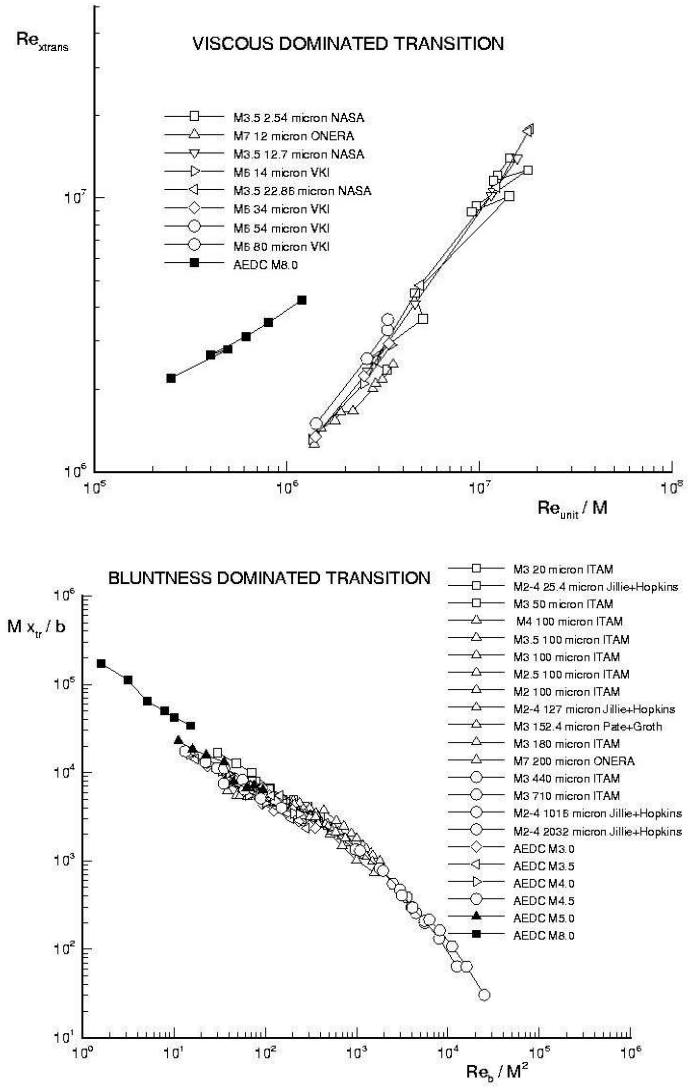

Figure 3.3: Top: Correlation of viscous-dominated supersonic/hypersonic flat plate transition data: transition Reynolds number, Re_{tr} versus unit Reynolds number by Mach number, $Re/m/M$; bottom: Correlation of leading edge bluntness-dominated supersonic/hypersonic flat plate transition data: Mx_{tr}/b against Re_b/M^2 by Simeonides [93].

$$log_{10}(Re_{tr}) = 6.421exp\left[1.209 \times 10^{-4} M_e^{2.641}\right] \tag{3.1}$$

The boundary layer thickness, δ is measured utilising the fact that there is a significant density gradient along compressible boundary layers, gradually increasing away from the wall and becoming minimum at the boundary layer edge as noted by Smits and Dussuage [92]. Depending on the wall temperature and assuming constant pressure along the compressible boundary layer; the density locally at the vicinity of the wall can be constant if the wall is adiabatic or it can be decreasing towards the wall if the wall is heated or it can be increasing if the wall is cooled. In the current experimental programme the wall is always cooler than the adiabatic wall temperature, T_{aw} $(= T_\infty\,(1 + r((\gamma - 1)/2)M_\infty^2))$ of 335K based on the free stream flow conditions at $13.1 \cdot 10^6 1/m$ specified in Table 3.1. Therefore the density is increasing towards the wall as well as increasing towards the edge as well. As a consequence there should be an inflexion point inside the boundary layer for a continuous behaviour of density. Needham [95] had shown that the outer edge of dark line in the schlieren pictures is very close to the boundary layer edge, hence it can be taken as a measure of boundary layer thickness. Nevertheless in the current configuration knife edge is positioned in a horizontal way that any gradient in positive y direction appears as a bright region, hence the end of the bright line is taken as a reference. Thus the boundary layer thicknesses are found to be about 1.7-2.1mm $\pm 0.1mm$ just upstream of the separation region from Fig. 3.2. The result is compared with the theoretical estimate from Popinski and Ehrlich [96] using Eckert's reference temperature method [97]. The details of the calculation are mentioned in Appendix A. The theoretical estimates give δ values around 1.3-1.4mm. The discrepancies might be attributed to the presence of tappings disturbing the boundary layer flow via creating weak Mach waves, inherent roughness on the plate, adverse pressure gradient due to jet and the accuracy of the reference temperature method. Mach disc height, the incoming boundary layer thickness at the upstream of the separation region and the extent of the separation region can be extracted from schlieren images using digital image processing. The Mach disc height is compared to a theoretical estimate from Cassell [40] as it is shown below in Eqn. 3.2. c_d is the discharge coefficient of the sonic jet with values around 0.96-0.98 for the range of jet Reynolds numbers considered. The agreement is found to be satisfactory since jet penetration is governed heavily by J, and the stagnation conditions for both jet and the tunnel

are known accurately. In terms of the extent of the separation region, it is taken as the distance between where boundary layer starts to deviate from the main flow direction and the centre of the jet orifice. These values are tabulated in Table 3.2.

$$\frac{h}{d_{jet}} = \frac{1}{M_\infty}\sqrt{\frac{2p_{0jet}\gamma_{jet}}{c_d p_\infty \gamma_\infty}}\left[\frac{2}{\gamma_{jet}-1}\frac{2}{\gamma_{jet}+1}^{(\gamma_{jet}+1/\gamma_{jet}-1)}\left\{1-\frac{p_\infty}{p_{0jet}}^{(\gamma_{jet}-1/\gamma_{jet})}\right\}\right]^{1/4} \tag{3.2}$$

Table 3.2: Experimental boundary layer thicknesses (δ), Mach disc heights (h) and separation lengths (x_{sep}) tests 1-3.

Test No	δ (mm)	δ_{theo} (mm)	h (mm)	h_{theo} (mm)	x_{sep} (mm)
1	2.1 ±0.1	1.4	4.2 ±0.15	4.1	15.9 ±0.3
2	1.9 ±0.1	1.3	6.2 ±0.15	6.3	30.2 ±0.3
3	1.7 ±0.1	1.3	8.2 ±0.15	8.7	44.1 ±0.3

Mach disc height non-dimensionalised by jet orifice diameter, h/d_{jet} against momentum flux ratio, J, and the separation distance against Mach disc height are plotted in Fig. 3.4. A very good power law fit is applied for Mach disc height and the resultant equation is shown in the figure. The penetration increases with increasing momentum flux ratio however the trend is nonlinear. This finding is consistent with the results obtained by Papamoschou and Roshko [11]. Their results show that the penetration behaviour of a sonic/supersonic jet through a circular hole into high speed crossflow is not dramatically different than the subsonic jet penetration into subsonic cross flow. A power law fit can be applied when penetration height over jet diameter is drawn against momentum flux ratio. In case of separation distance against Mach disc height, a nearly linear behaviour is obtained with a slope of around 3.5. The extent of the separation region is strongly governed by the state of the incoming boundary layer as the bow shock induces adverse pressure gradient and causes it to separate. Generally for three dimensional jet interactions the separation region is closer to the injection port due to three dimensional relieving effect. But in this case the boundary layer is laminar thus it is less resistant to adverse pressure gradients and it separates earlier than a turbulent boundary layer.

Fig. 3.5 shows the measured time histories of tunnel stagnation pressure,

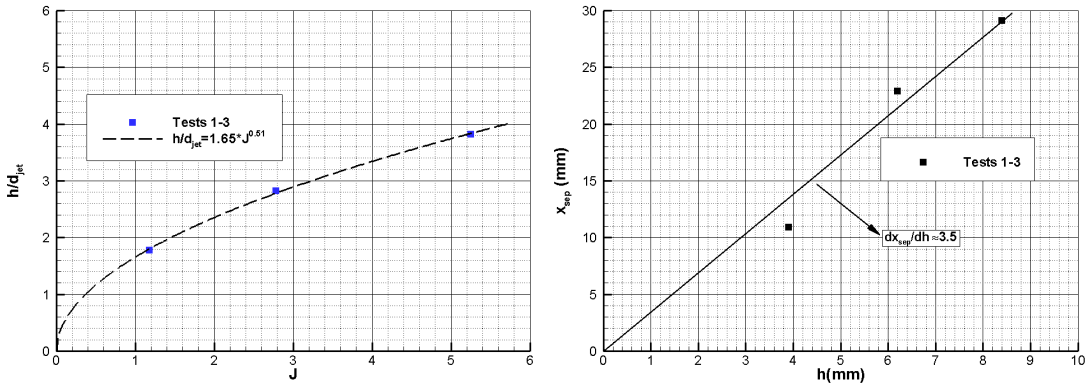

Figure 3.4: Left: Mach disc height non-dimensionalised by jet diameter versus momentum flux ratio; right: separation distance non-dimensionalised by jet diameter versus momentum flux ratio for tests1-3.

$p_0(t)$ for test 3, jet stagnation pressure, $p_{0jet}(t)$ for tests 1-3 and wall pressure, $p_w(t)$ at the first tapping in the centre again for test 3. Also the variations of the pressure values are depicted proving quite steady conditions prevailed during the tests. However, as mentioned above, the interaction of the transverse jet with the incoming flow is unsteady owing to jet shear layer instabilities coupled with incoming boundary layer. In the region near the injector exit, the injectant fluid moves with a higher velocity tangent to the interface than the incoming flow. As a result, large vortices are periodically formed engulfing large quantities of free stream fluid and drawing it into the jet shear layer and then are convected downstream at high speeds. These large scale coherent structures are dominant in the jet shear layer and their structural evolution might have a big influence on the jet near field [18]. It is therefore important to understand how these structures and their growth rates change in time as the crossflow and jet conditions are changed.

These structures are visualised using schlieren photography at 16kfps with 1μsec exposure as they are shown in Fig. 3.6 for test 3. Several interesting features, such as the large scale structures at the jet periphery and the bow shock are very apparent in those images. The large scale vortices are periodically generated in the early stages of the jet free stream interaction. Therefore the bow shock is affected by these vortices and is oscillatory in nature. The stand off distance is very small, almost merged within the jet, and curves sharply downstream. The local shape of the bow shock appears to depend strongly on the large scale shear layer structures, especially close to the jet exit where the free stream behind the

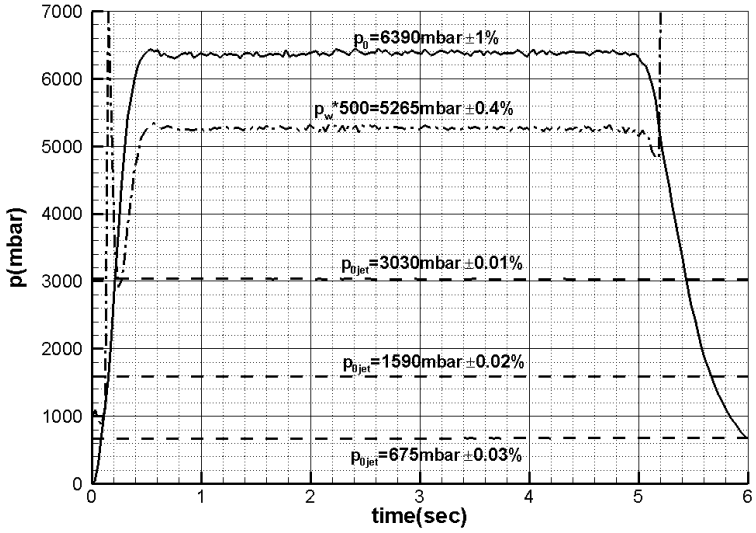

Figure 3.5: Time histories of tunnel and jet stagnation pressure signals with a representative wall static pressure signal.

steep bow shock is subsonic. Furthermore separation shock is unsteady as well due to the disturbances in the injection vicinity that are fed upstream through the boundary layer. The barrel shock and the Mach disk are, however, not very clear in the short exposure schlieren images, due to the unsteadiness of the jet. Although the jet shear layer eddies seem to be two-dimensional, it has to be recalled that they are part of the unsteady Kelvin-Helmholtz spanwise rollers wrapping around the jet. They are only the traces of three-dimensional transverse vortex tubes whose cores coiled up around the jet with their legs connected downstream of the jet exit [18].

Three instantaneous schlieren images for each J value together with Root Mean Square (RMS) of the fluctuations in the light intensity based on 1000 schlieren images show different levels of penetration and signify the high levels of unsteadiness respectively as they are shown in Figures 3.7 and 3.8 for tests 1-3. The jet upper boundary can be easily seen from the RMS images and high amplitudes in RMS are observed to occur in the flow domain occupied by the fluctuating bow shock and the separation shock. As the momentum flux ratio is increased the jet boundary and the bow shock shift in transverse direction. It has to be noted that the evolution of coherent jet shear layer vortical structures can not be discussed because of the long interframe time of schlieren recording, which is $62.5\mu sec$. The leading edge shock is observed as a very thin line (the unsteadiness is minimal), which demonstrates the good flow quality at the upstream

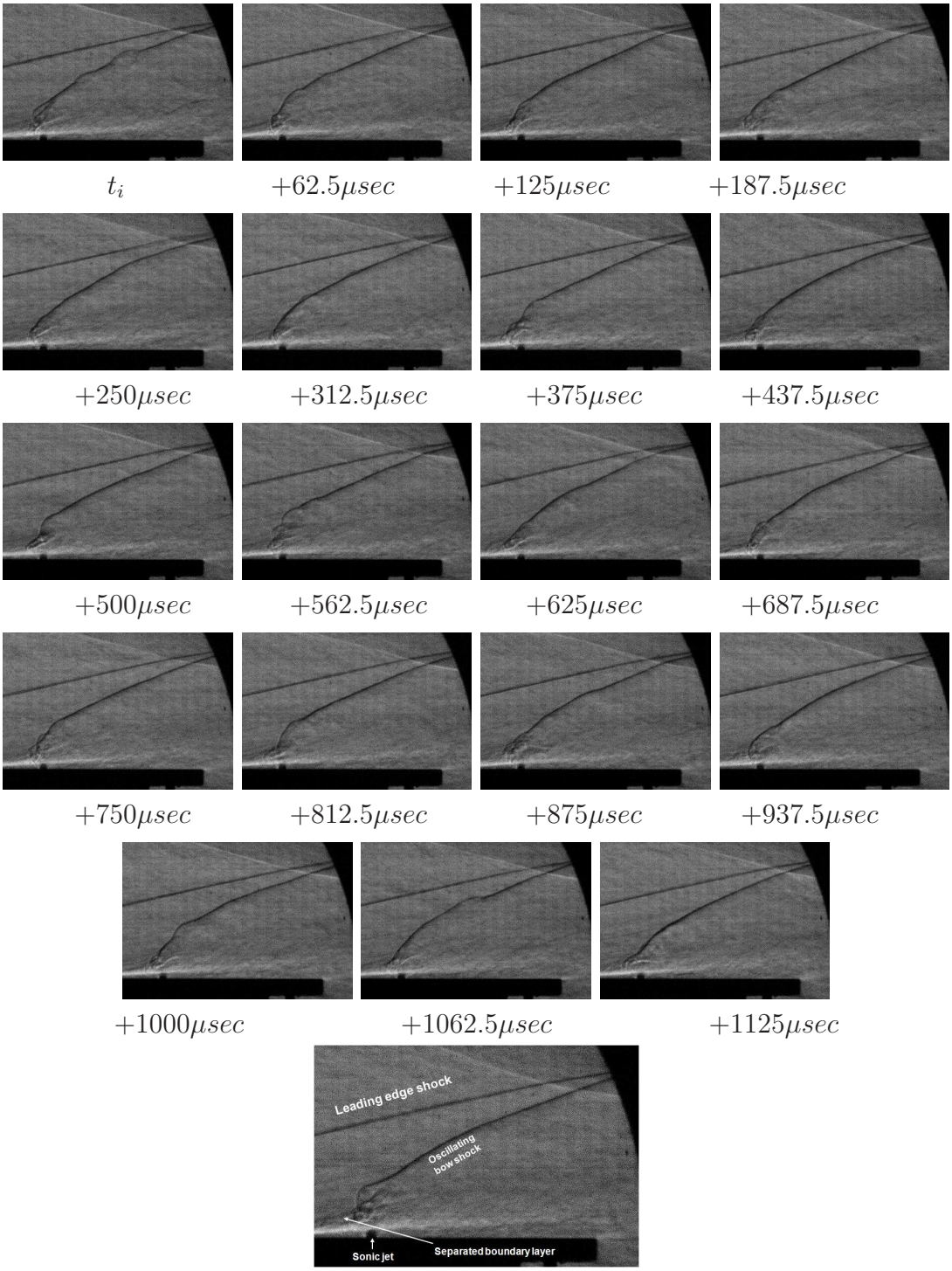

Figure 3.6: High speed schlieren visualisation of the sonic transverse jet captured at 16000fps with 1 μsec exposure time and annotated flow structures.

conditions.

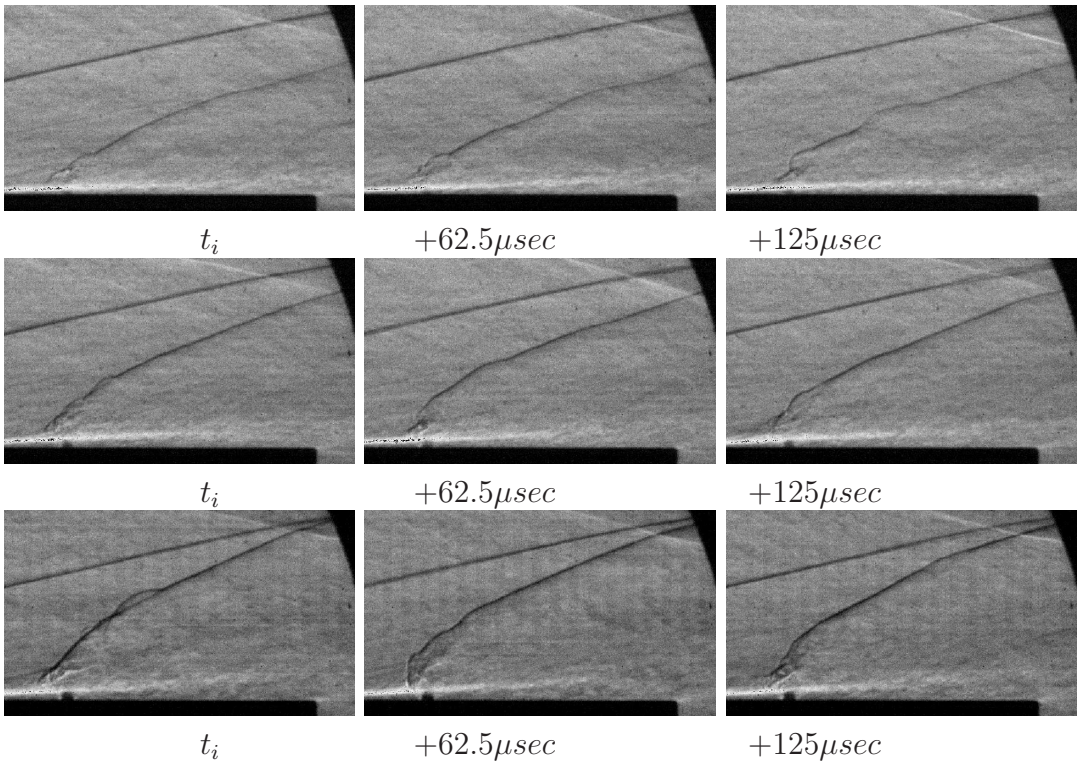

Figure 3.7: Three instantaneous schlieren images of air injection; top: test 1, middle: test 2, bottom: test 3.

PIV

To assess the jet penetration characteristics and trajectories PIV investigation is carried out. Only the transverse jet is seeded and regulated, measurements are done at the centreline where the flow field can be safely assumed two dimensional. However the laser sheet thickness of 0.5mm compared to 2.2mm jet orifice diameter will include some extent of unavoidable out of plane motion. To avoid excessive deposition of seeded particle (aluminium oxide) inside the test section the drum inside the seeder is initiated right after the tunnel start even though the transverse jet is started with air only (few amount of particles that are on the line are carried with the jet). Figure 3.9 shows raw PIV images captured throughout the test run. Unsteadiness of the jet trajectory and jet shear layer instabilities are observed clearly. Periodically formed large vortices are engulfing large quantities of incoming air, drawing it into the jet shear layer, and then are convected downstream at high speeds. After the useful running time has passed

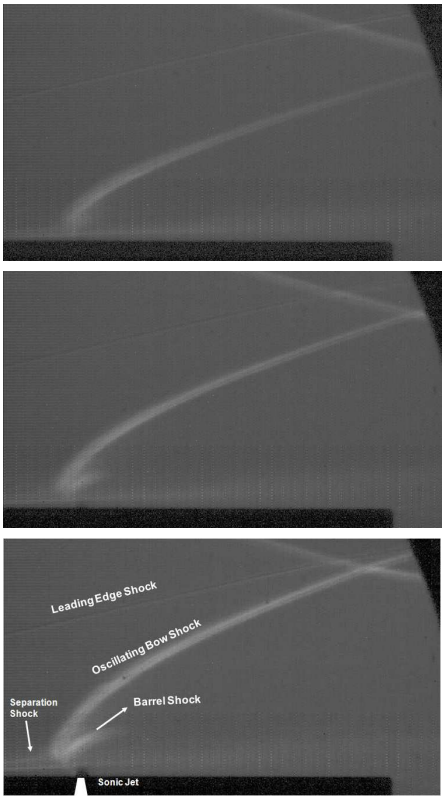

Figure 3.8: RMS of instantaneous schlieren images of air injection of a time series of 1000 samples; top: test 1, middle: test 2, bottom: test 3 with annotated flow structures.

(around 7.2sec), severe oscillations start to occur and Mach 5 flow no longer exists and when the firing valve is closed (when there is no cross flow) the jet discharges nearly vertically.

Figures 3.10 to 3.12 show selective raw PIV images and associated vector fields for tests 1-3 with increasing J value. As the jet is discharged from the orifice at a velocity around 315m/s, acceleration in the transverse direction is observed and terminated by the Mach disc which bends the jet towards the main flow direction. After the normal shock the jet velocity is reduced following an acceleration reaching values of 750m/s, which is close to the free stream velocity but slightly lower due to the presence of the bow shock. With increasing momentum flux ratio, higher levels of penetration and thicker jet affected area are observed as expected.

Figures 3.13 and 3.14 show averaged flow fields and Turbulence Intensity (TI) ($\sqrt{\overline{U'^2}}/U_{jet}$ in %) contours over 100 vector fields for tests 1-3 during the useful running time. Averaged streamlines are also visualised in Fig. 3.13. The spatial coordinates are normalized with the jet diameter, d_{jet}. The main flow

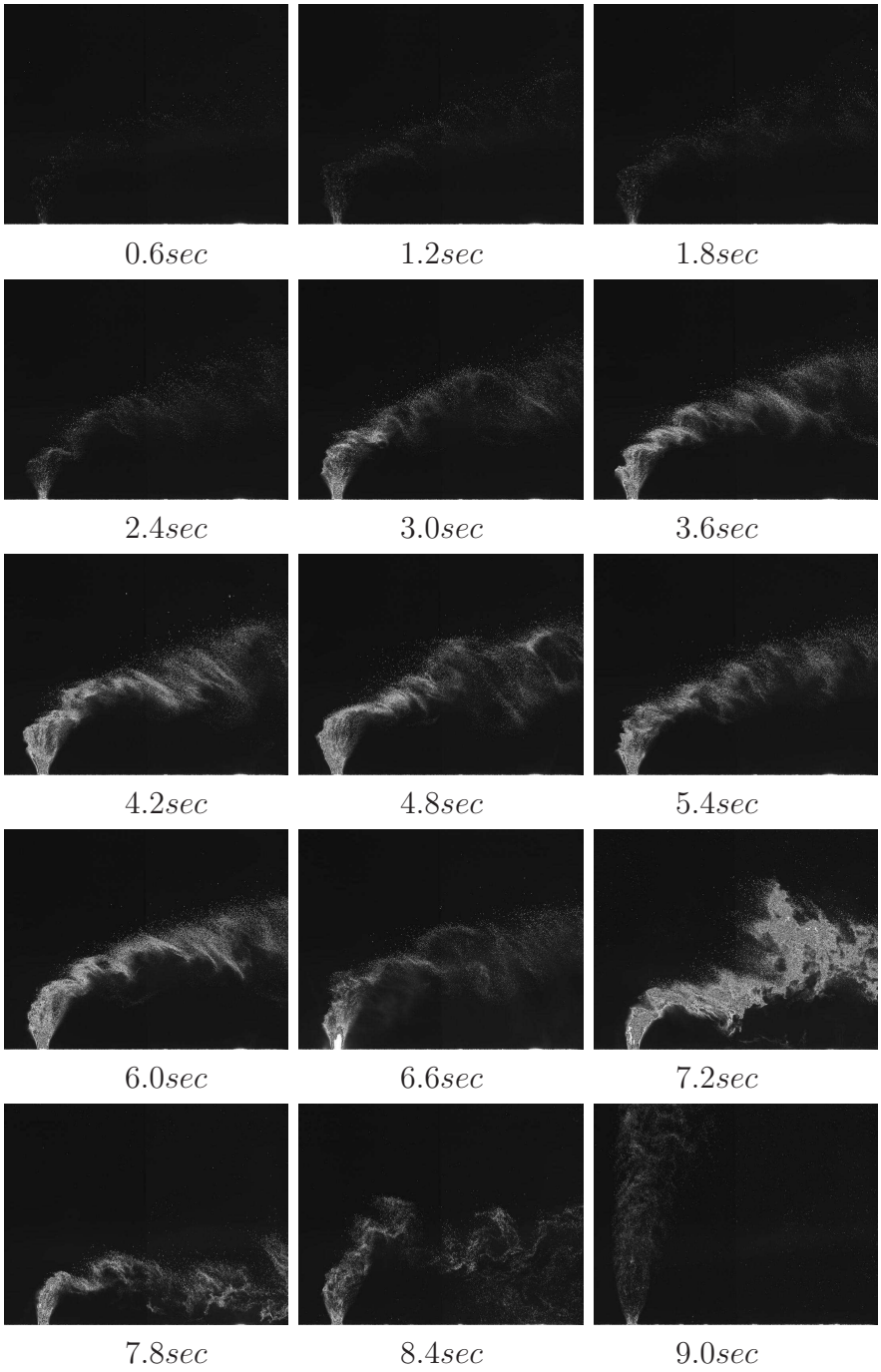

Figure 3.9: PIV raw image visualisation of the sonic transverse jet captured at 15fps. Only first frames of the PIV recording are shown.

is in the x direction. One interesting thing to note is on the windward side of the jet (upstream side), the flow turns fairly quickly towards the main flows direction whereas for the leeward side (downstream side), the turning behaviour is

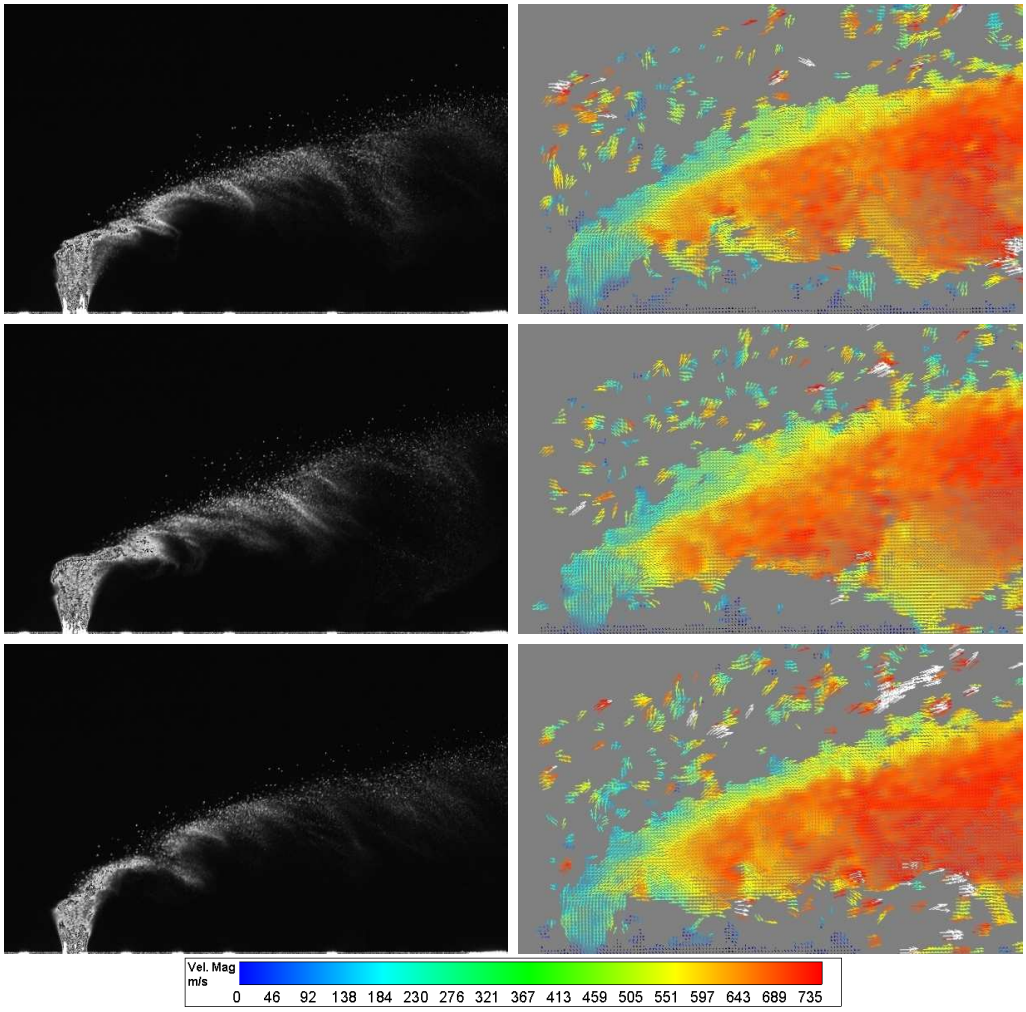

Figure 3.10: Three instantaneous raw PIV images and associated vector fields for test 1.

rather gradual. The unsteady jet shear layer structures do not appear in averaged velocity contours as it is expected. In case of TI contours (Fig. 3.14), the jet boundaries and the associated penetration characteristics are demonstrated. The barrel shocks and the Mach disc forming the jet boundary can be easily seen and are visualised/quantified for the first time in open literature. As J is increased the extent of the local jet boundary (drawn in black dotted lines) composed of barrel shocks and Mach disc, and the extent of jet spreading (drawn in black dashed lines) are increasing. The upper boundary of the jet spreading is defined by the maximum penetration of its shear layer vortices. While the penetration bandwidth can be related to the difference between the extents of the jet spreading boundary. For test 1 the Mach disc height and penetration height at $x = 20d_{jet}$

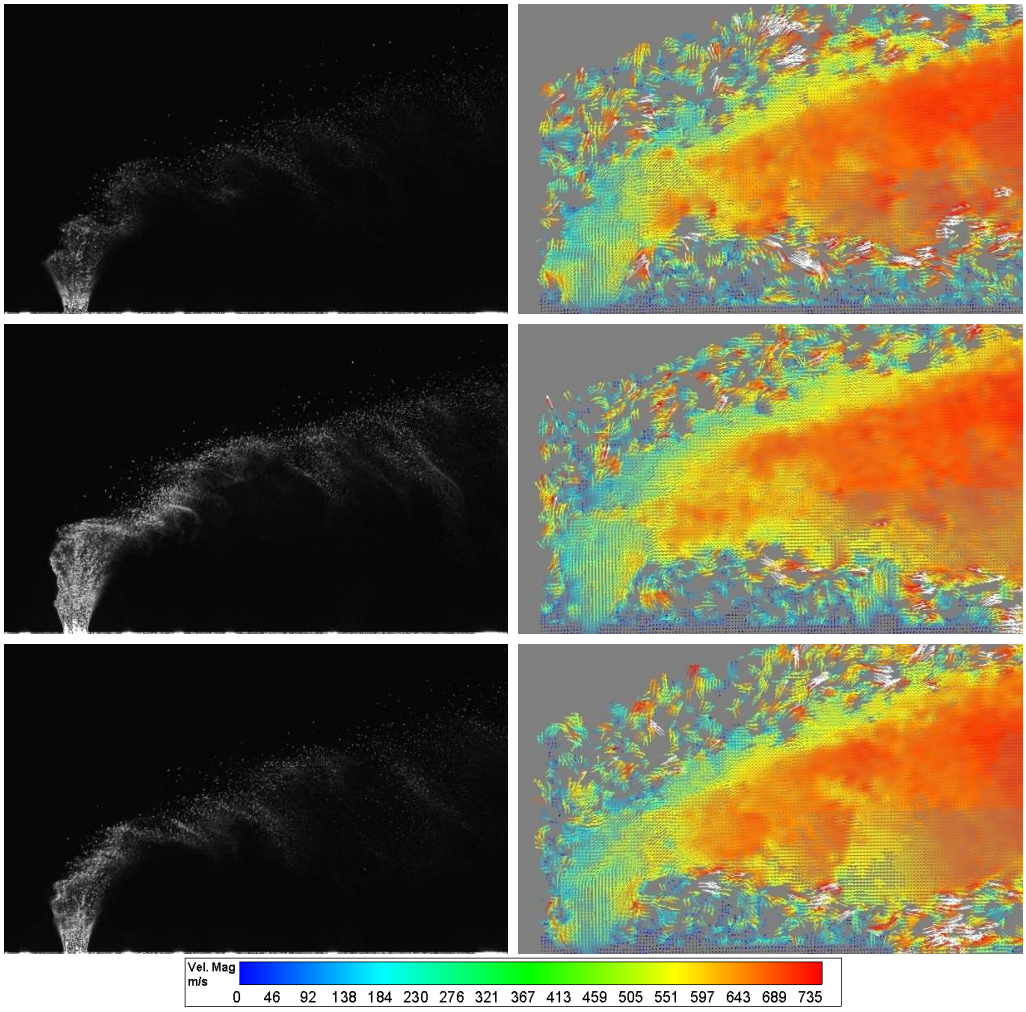

Figure 3.11: Three instantaneous raw PIV images and associated vector fields for test 2.

are found as 4.4mm and 16.5mm respectively. For test 2 these values are 6.4mm and 22mm whereas for test 3 they are found as 6.4mm and 22mm. The Mach disc height values are in very good agreement with the values found from schlieren images. However the uncertainty in h is found to be $\pm$0.3mm. This uncertainty is mainly due to the finite response time of the particle in transverse air jet flow, which is found to be 3-1.6 μsec for tests 1-3 respectively as shown in Table 3.5. As there is significant deceleration through the Mach disc, the particles can not adjust themselves as quick as the flow hence blurring around the disc occurs for each instantaneous velocity vector field. Individual vector fields are statistically avaraged to get the averaged flow field, therefore the blurring is added to the summation.

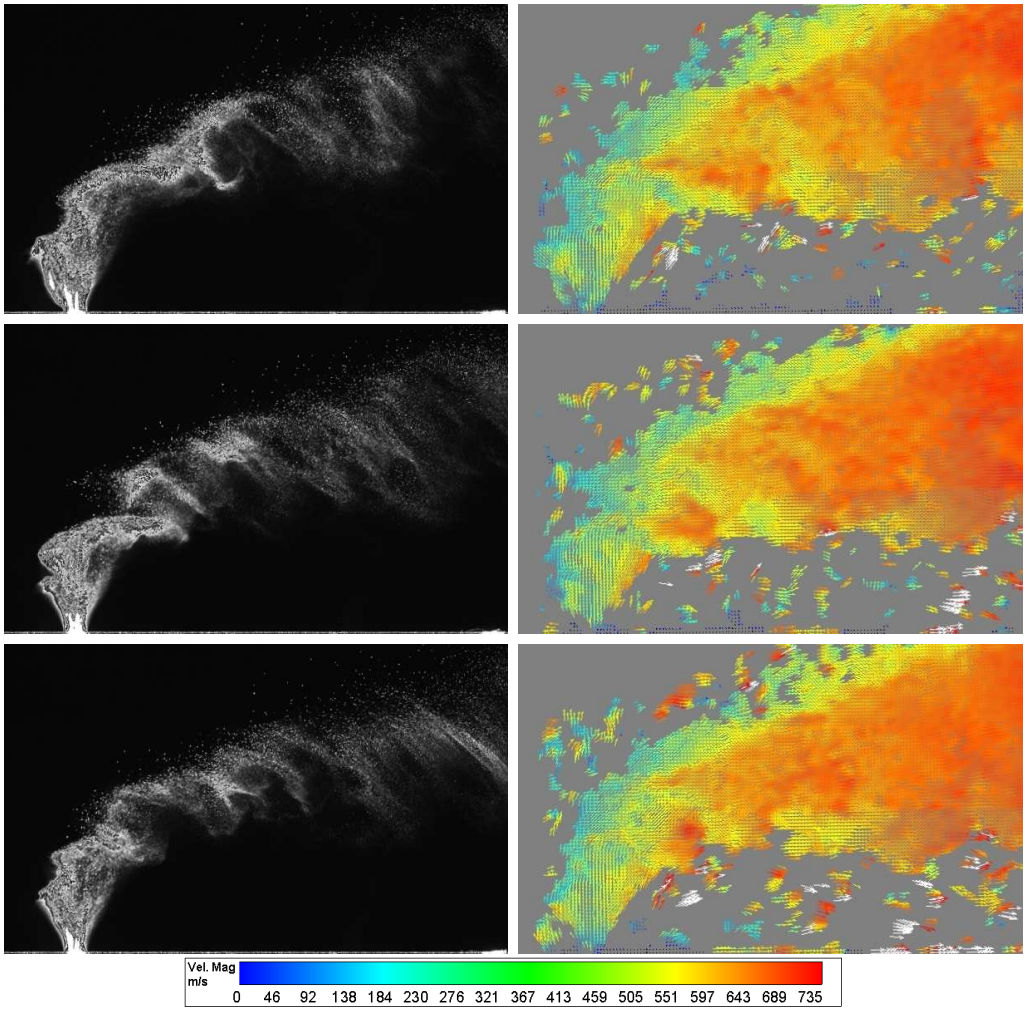

Figure 3.12: Three instantaneous raw PIV images and associated vector fields for test 3.

In addition Perurena et al. [98] has come up with a formula based on the penetration height of water injected into Mach 6 cross flow using image processing as depicted in Eqn. 3.3. They found out that this equation for Mach 6 presented a less inclined slope for the jet trajectory, showing the higher pressure distribution exerted by the hypersonic cross flow on the jet surface compared to supersonic cross flows. This equation is also plotted in Fig. 3.14. The agreement in the farfield beyond $x = 8d_{jet}$ is found to be reasonable within 10%.

$$\frac{h(x)}{d_{jet}} = 3.5J^{0.3}\left[\frac{x}{d_{jet}}\right]^{0.38} \tag{3.3}$$

The cross-check between PIV results and schlieren can be done in RMS terms.

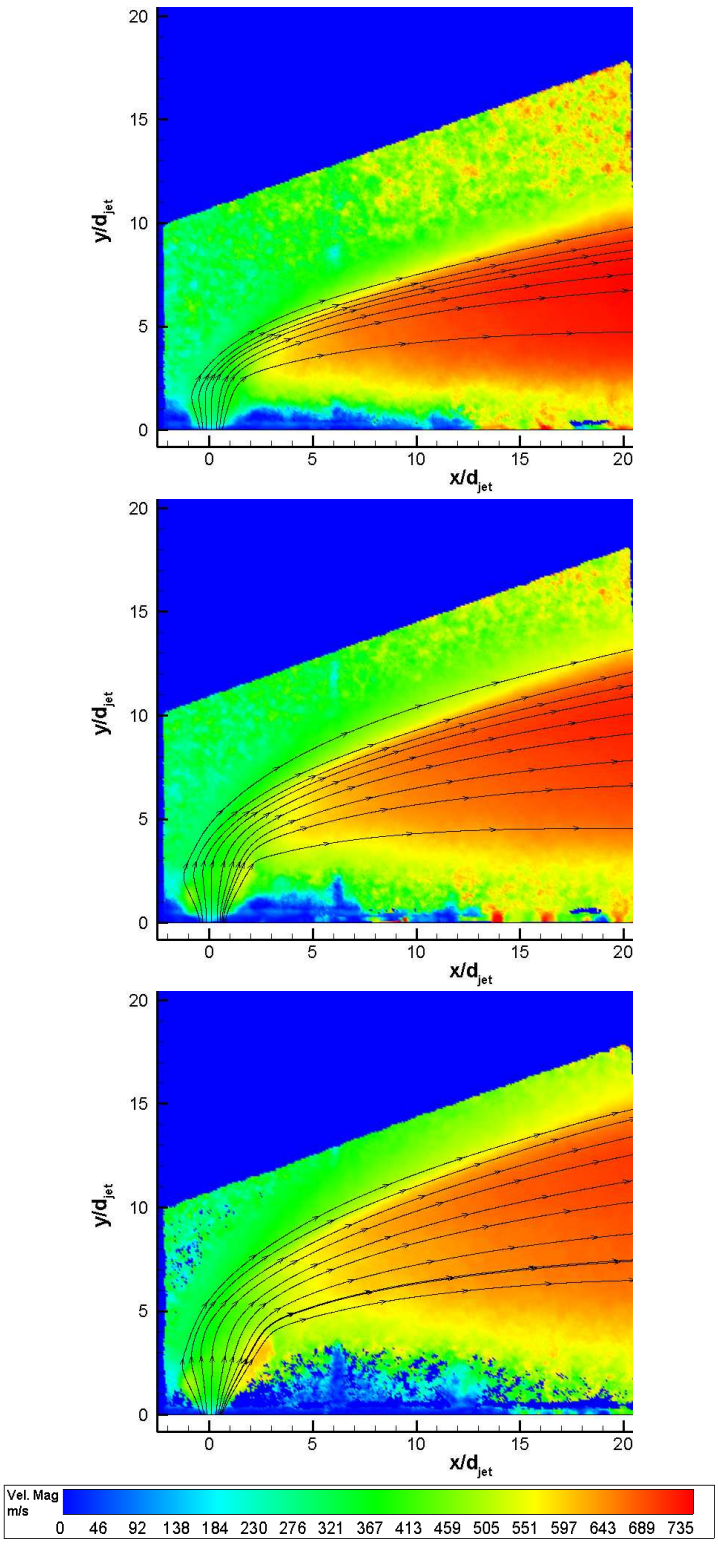

Figure 3.13: Averaged flow field velocity magnitude contours; top: test 1, middle: test 2, bottom: test 3.

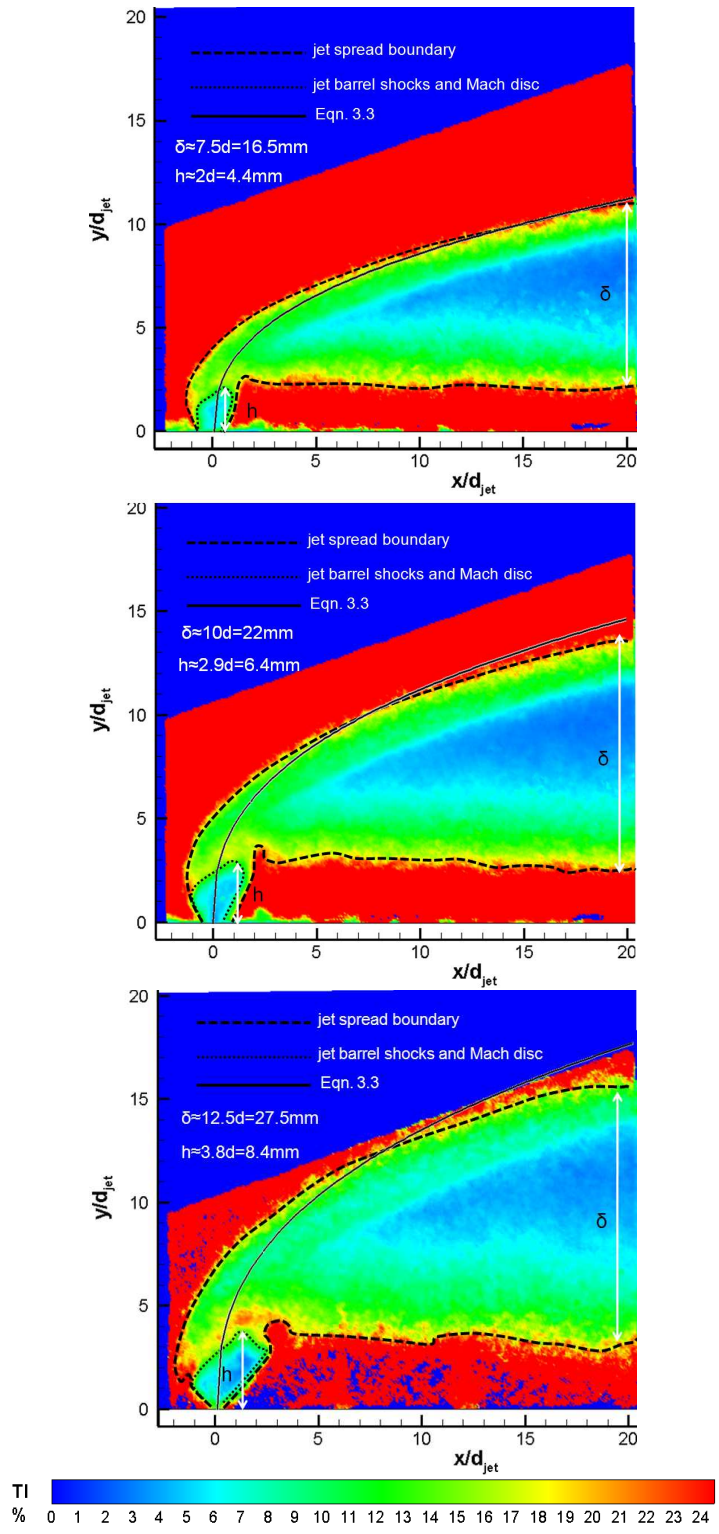

Figure 3.14: Averaged flow field turbulence intensity (TI) contours; top: test 1, middle: test 2, bottom: test 3.

Figure 3.15 shows overlaid schlieren RMS pictures shown in Fig. 3.8 on PIV results shown in Fig. 3.14. The barrel shocks and the Mach disc shape found from PIV results are in line with schlieren images building further confidence on the experimental campaign. Furthermore another important fact is deduced from the Fig. 3.15 that the mutual interaction between the jet and the decelerated air stream behind the bow shock is responsible for particles entrained into the free stream and vice versa. However it should also be kept in mind that the finite response time of particles spreads the jet boundaries outwards even though the final interrogation area size is $16 \times 16 pixel^2$ ($0.64 \times 0.64 mm^2$) with 75% overlap.

Wall pressure measurements

In terms of non dimensional surface pressure values, the data reduction procedure for surface pressure measurements is as follows; $p_\infty(t)$ is calculated using isentropic relations from $p_0(t)$, i.e. $(= p_0/\left(1 + ((\gamma - 1)/2)M_\infty^2\right)^{(\gamma-1)/\gamma})$. Then the divided signals of $p_w(t)/p_\infty(t)$ and $p_{0jet}(t)/p_\infty(t)$ signals are obtained. These signals are integrated and averaged over the duration of the stagnation pressure plateau of a test run . Figure 3.16 shows non-dimensional wall pressure distributions against non dimensional distance, i.e $(x - x_{jet})/d_{jet}$, for different momentum flux ratios at centreline, z/d_{jet}=4.77 and z/d_{jet}=9.1 for tests 1-3. The theoretical estimate using viscous interaction for cold wall (i.e. $T_w << T_{aw}$) is also shown in Fig. 3.16. The details of theoretical estimate are in Appendix A. In addition the data without the jet is also plotted.

$$\begin{aligned} \overline{p_w/p_\infty} &= \frac{1}{t_f - t_i} \int_{t_i}^{t_f} p_w(t)/p_\infty(t) dt \\ \overline{p_{0jet}/p_\infty} &= \frac{1}{t_f - t_i} \int_{t_i}^{t_f} p_{0jet}(t)/p_\infty(t) dt \end{aligned} \tag{3.4}$$

In theory the wall pressure along at the leading edge is slightly higher than the free stream pressure reaching 1.1 times p_∞ due to viscous interaction and gradually decreases to free stream value. This behaviour is also observed in experiments with slight overshoot which might be due to experimental uncertainty. The non-dimensional pressure values are found to be accurate within 5% using the procedure specified in Appendix B. After the gradual decrease, the wall pressure starts to increase from the point at which the flow separates, and then there

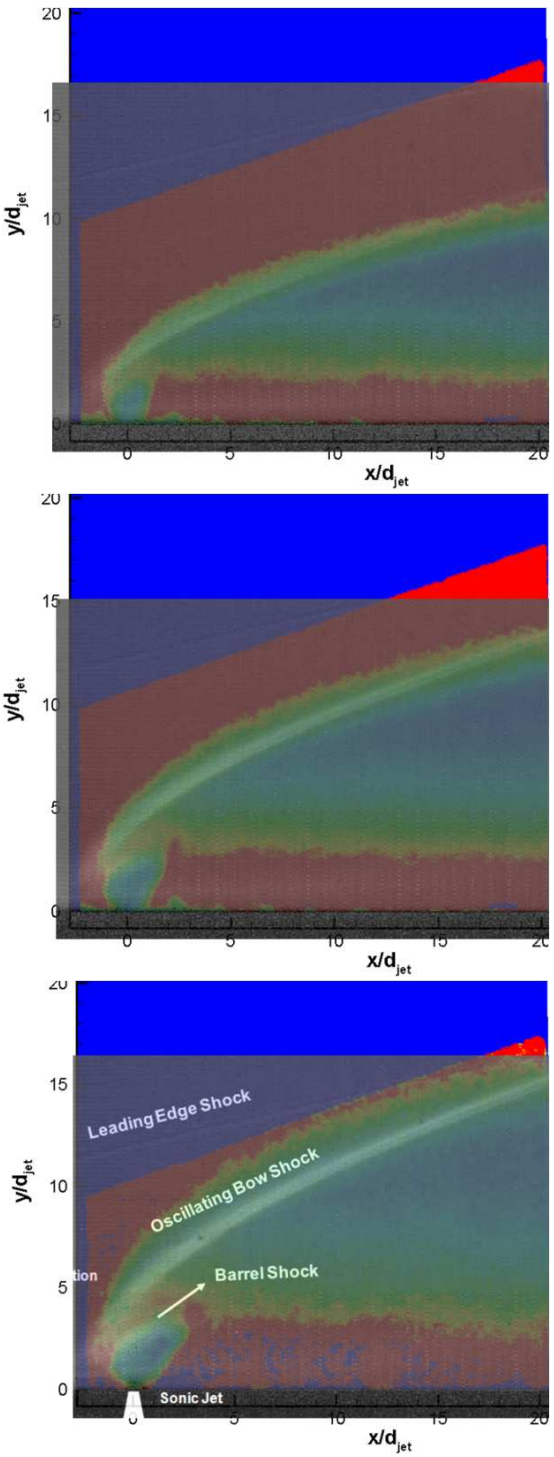

Figure 3.15: Overlaid RMS images of 1000 instantaneous schlieren images on PIV turbulence intensity (TI) contours; top: test 1, middle: test 2, bottom: test 3.

is further rise to a pressure plateau. The pressure rise due to the injection does not become apparent until a $(x - x_{jet})/d_{jet}$ value of -20 for test 3, afterwards it

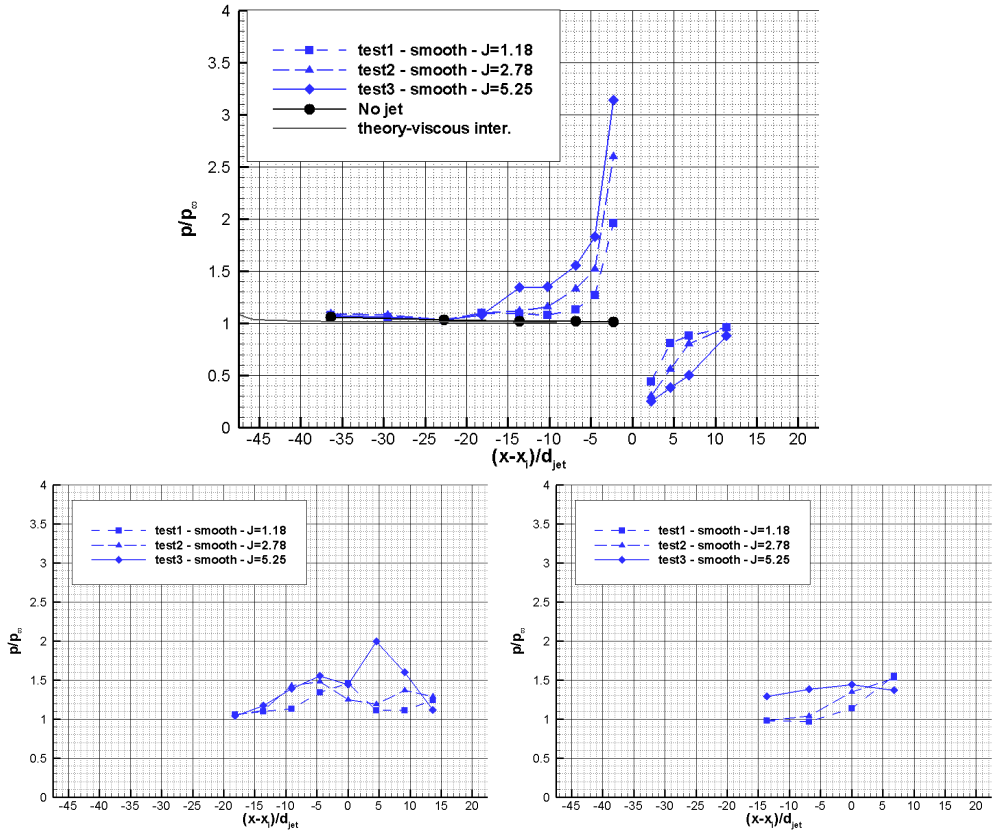

Figure 3.16: Non dimensional wall pressure distribution against non dimensional distance at the centreline (top), $z/djet$=4.77 (bottom left) and $z/djet$=9.1 (bottom right) for test 1-3.

rises gradually implying laminar separation. The rise is rather abrupt for turbulent boundary layers, thus proof of the existence of laminar boundary layer. Generally, for a laminar boundary layer, the separation region due to adverse pressure gradient is larger than the one for a turbulent boundary layer due to its less resistive nature; hence it separates earlier than a turbulent boundary layer. This rise is followed by the peak at the upstream of the jet reaching nearly 3.2 for highest J value. Downstream of the jet the pressure well is apparent that is accompanied by a rise due to recompression shock. The non dimensional pressure in the downstream of the jet does not exceed 1 for hypersonic interactions. Each plot exhibits the effect of increasing jet to free stream momentum flux ratio which leads to increase in the wall static pressure values at both upstream and downstream regions. The size of upstream and downstream flow structures extent not only in streamwise direction but also in the spanwise direction, spreading laterally with higher J values. The magnitude of the peak pressure on the z/d_{jet}=4.77

off-centreline is found to be around 2 at x/d_{jet}=5.

Oil dot visualisation

To visualise the lateral spreading of the jet, oil dot visualisation is carried out with setup defined in Section 2.4.1. The image distortion due the tilted camera setup is corrected using DaVis 7.2 software utilising the fact that the oil dots that are separated 5mm apart constitute a marked pattern to transform the oblique FoV to a normal one. It has to be noted that only the half of the plate is marked with oil dots as the pressure tappings are situated on the other half. Figure 3.17 shows the time history of the oil movement captured at 30fps with 0.1msec exposure time. After 4.2sec the oil movement is come to an end. Therefore for the comparison of different J values and gases this final image is taken into account.

Figure 3.18 shows the difference in oil dot patterns with increasing momentum flux ratio. The footprint of the bow shock attachment region, horseshoe vortex core and jet plume separation region can be identified. Oil dots before the attachment of the bow shock (i.e. λ separation shock) move minimally, however, just downstream of the attachment region they move outwards significantly and bend towards the main stream direction. The horseshoe vortex spreads the oil dots away from its core and the separation region behind the jet plume keeps the oil dots away from itself causing deposition on the separation line. The lateral extent of the interaction is influenced by the momentum flux ratio as it is expected, however Joshi and Schetz [99] arrived to a conclusion that lateral dimension of the jet depends more on the lateral extension of the injector than the momentum flux ratio. The injector shape is circular for all cases thus the effect of J can be assessed. The interaction region extends to 5, 9 and 14 times d_{jet} in lateral direction at x/d_{jet}=0 for tests 1, 2 and 3 respectively.

As a summary the test campaign for the baseline tests serve as a means to get fundamental insight about the physical behaviour of the interaction between the transverse jets and Mach 5 cross flow, furthermore to build up confidence in experimental results to further examine the effects of different parameters on the interaction.

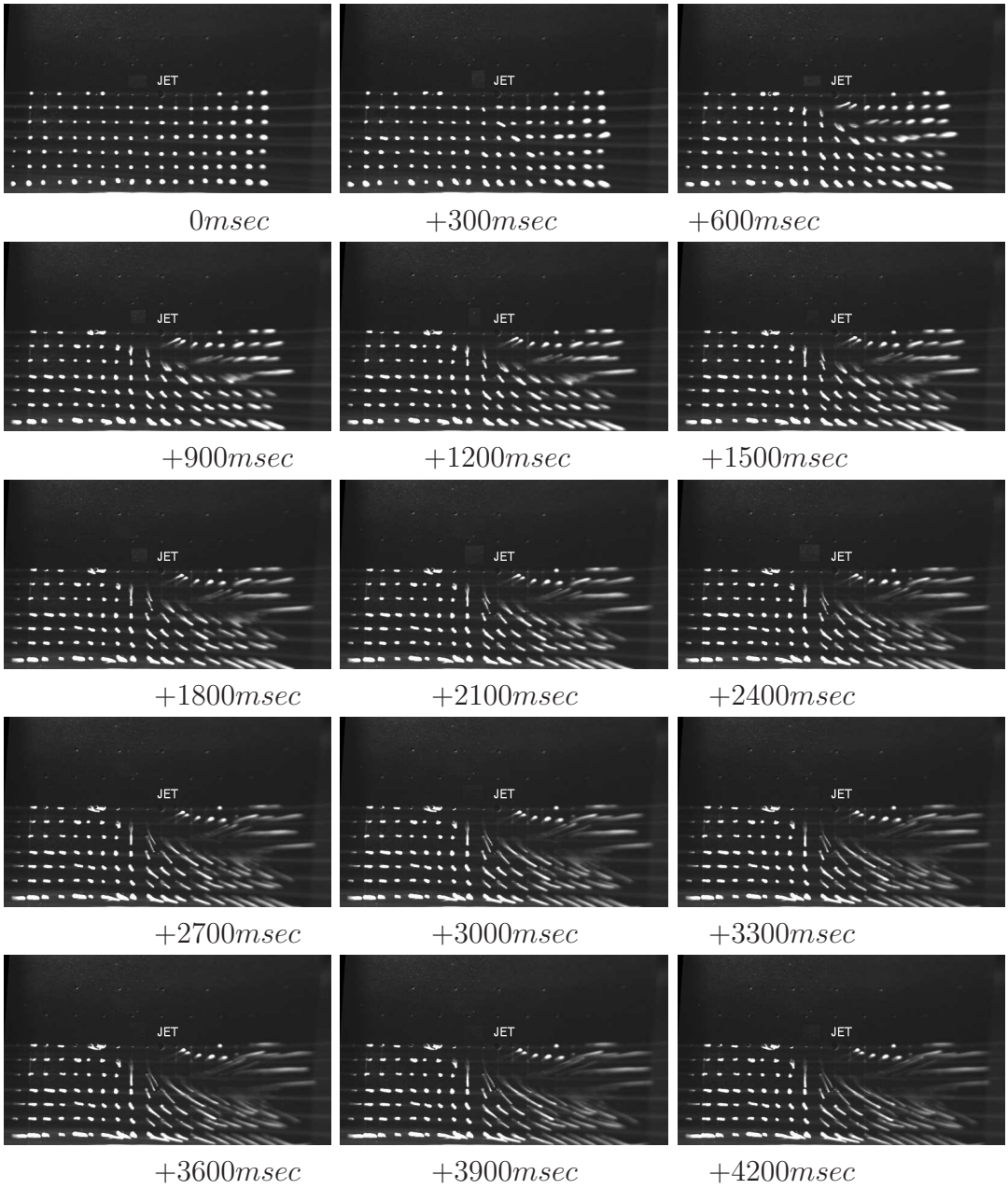

Figure 3.17: Oil dot visualisation of the sonic transverse jet captured at 30fps with 0.1msec exposure time for test 3.

3.1.2 Effect of unit Reynolds number

The effect of unit Reynolds number, hence the effect of incoming boundary layer developing on the flat plate, on the interaction phenomenon is examined for air injection at two other incoming flow conditions in addition to baseline tests. These conditions are specified in Table 3.1. Tests 4-6 have a unit Reynolds number of

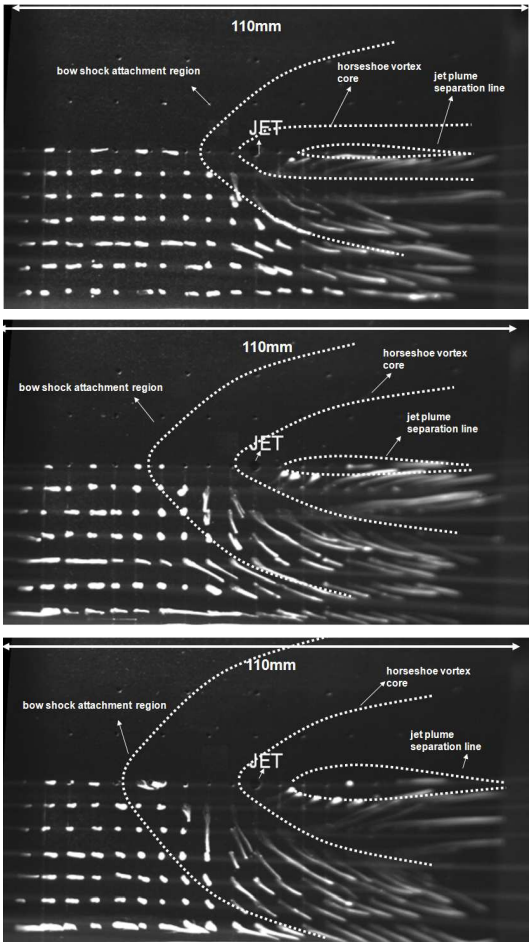

Figure 3.18: Oil dot visualisation of the sonic transverse air jet; top: test 1, middle: test 2, bottom: test 3.

$8.1 \cdot 10^6 1/m$ and Tests 7-9 have a value of $5.7 \cdot 10^6 1/m$. Stagnation temperature is increased and stagnation pressure is decreased to have a smaller unit Reynolds number, nevertheless this results in bigger J values compared to baseline values. This however does not alter the findings of the comparisons done from hereon.

Schlieren visualisation

Figures 3.19 and 3.20 show the long exposure (250μsec) schlieren images of the flowfield for the tests 4-6 and tests 7-9. Due to lower incoming unit Reynolds numbers compared to baseline tests the boundary layer developing on the plate is again laminar. The flow structures mentioned in Section 3.1.1 are also observed: a leading edge shock due to viscous interaction at the leading edge and

following laminar boundary layer growth up to the separation point accompanied by diversion in upward direction thereafter, separation shock that emanates around the separation point and intersects the jet induced bow shock, and finally sonic jet barrel shocks with the Mach disc.

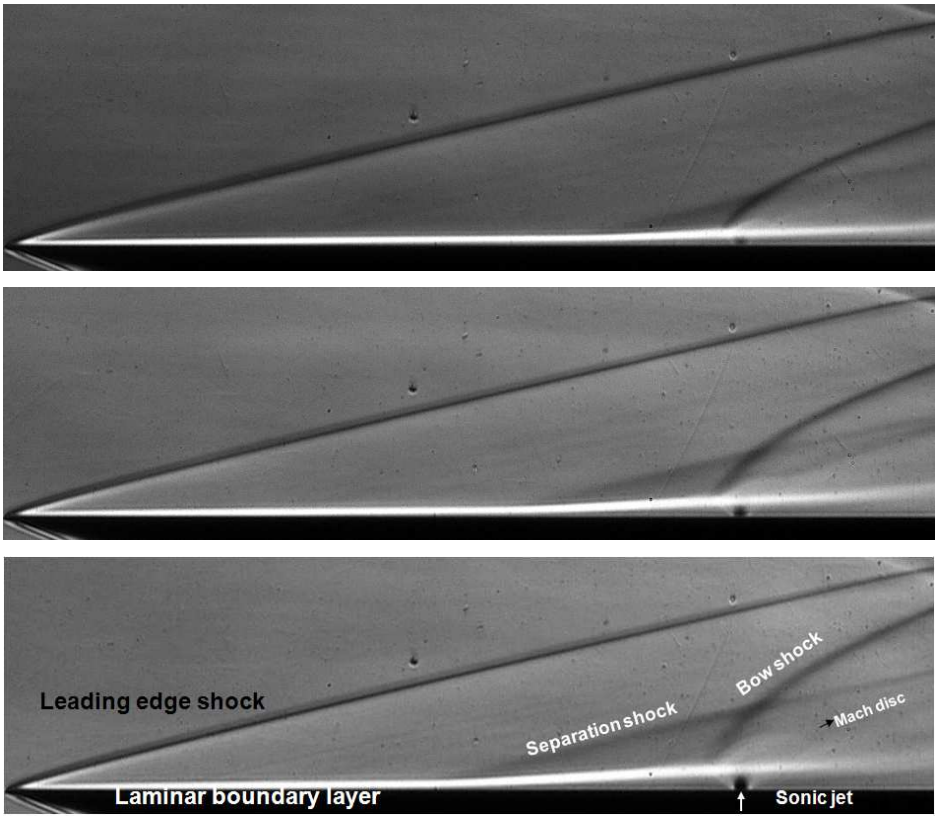

Figure 3.19: Schlieren visualisation of the flowfield in the presence of the sonic transverse jet with three different momentum flux ratios; top: test 4, middle: test 5, bottom: test 6 with annotated flow structures with J values of 1.26, 3.02 and 5.77 respectively.

As utilised in Section 3.1.1 the thickness of the boundary layer upstream of the separation region, Mach disc height and the separation length can be extracted from schlieren images using image processing. These values are tabulated in Table 3.3 with theoretical estimates mentioned in Section 3.1.1. At lower Reynolds number results in a thicker boundary layer, as the boundary layer thickness is inversely proportional to $\sqrt{Re_x}$ for laminar flows. A thicker boundary layer has a reduced value of wall shear stress and hence is less resistant to adverse pressure gradients compared to thin boundary layers. That is the reason for bigger separation regions for tests 4-9 compared to baseline tests. Therefore the boundary layer thickness just before the separation depends on the running length of

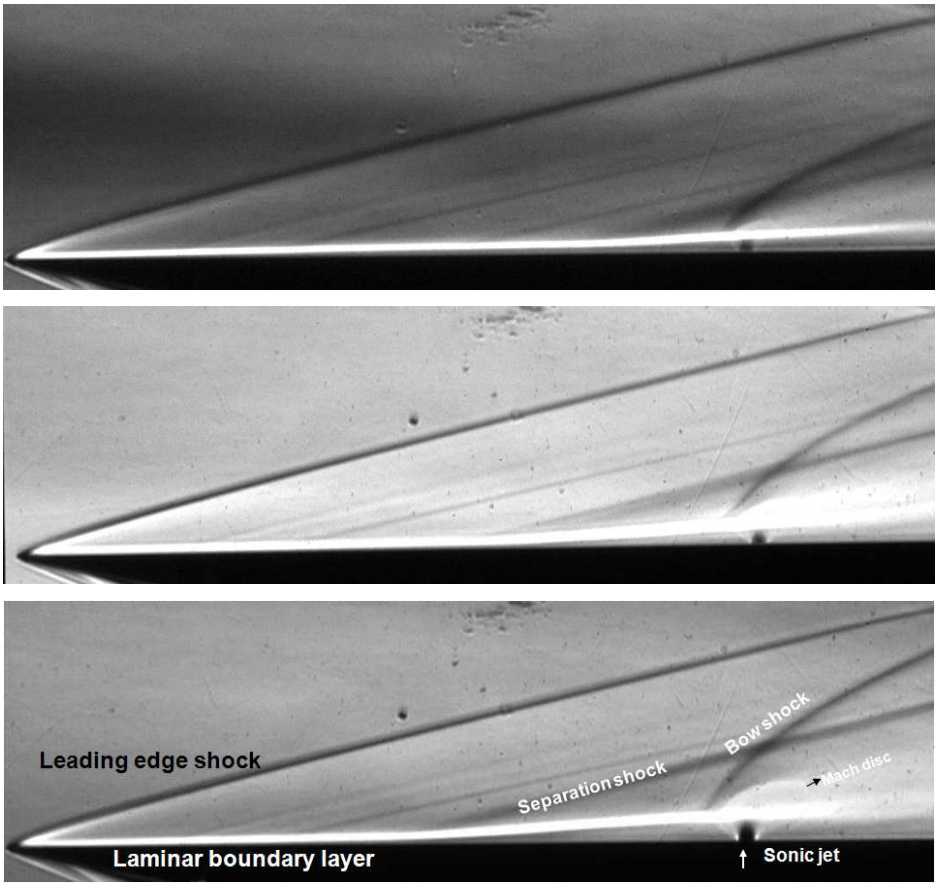

Figure 3.20: Schlieren visualisation of the flowfield in the presence of the sonic transverse jet with three different momentum flux ratios; top: test 7, middle: test 8, bottom: test 9 with annotated flow structures with J values of 1.37, 3.21 and 6.18 respectively.

the plate up to the onset of separation location. Regarding the comparison with theoretical estimates for boundary layer thickness, the agreement is found to be fairly good compared to big differences observed for baseline tests (which have a longer running length due to smaller separation regions). For the Mach disc height the agreement is deteriorated at high momentum flux ratios (test 6 and test 9) whereas for the other tests the agreement is satisfactory. The slight increase in h is expected due to the increase in J values compared to baseline tests.

Mach disc height non-dimensionalised by jet orifice diameter, h/d_{jet} against momentum flux ratio, J, and the separation distance, x_{sep} against Mach disc height are plotted in Fig. 3.21. These results are compared to baseline tests. Another power law fit is applied for Mach disc height in addition to the one deducted from baseline tests and the resultant equation is shown in the figure. General behaviour of fits well on a power law fit with a square root dependence

Table 3.3: Experimental boundary layer thicknesses (δ), Mach disc heights (h) and separation lengths (x_{sep}) for tests 4-9.

Test No	δ (mm)	δ_{theo} (mm)	h (mm)	h_{theo} (mm)	x_{sep} (mm)
4	1.9±0.1	1.7	4.6±0.15	4.3	23.8±0.3
5	1.8±0.1	1.6	6.3±0.15	6.6	27.5±0.3
6	1.7±0.1	1.5	8.3±0.15	9.1	32.7±0.3
7	2.2±0.1	1.6	4.3±0.15	4.4	20.4±0.3
8	2.1±0.1	1.5	6.5±0.15	6.8	37.3±0.3
9	1.8±0.1	1.4	8.2±0.15	9.4	47.0±0.3

on J. However the lower values penetration at the highest momentum flux ratio is apparent; the reason for that is unknown. In terms of separation length steeper slopes are observed for lower Reynolds numbers which justify the presence of the thicker boundary layers that are less resistant to adverse pressure gradients. The slope has increased from 3.5 to 5.6 by reducing the unit Reynolds number from $13.1 \cdot 10^6 1/m$ to $5.7 \cdot 10^6 1/m$.

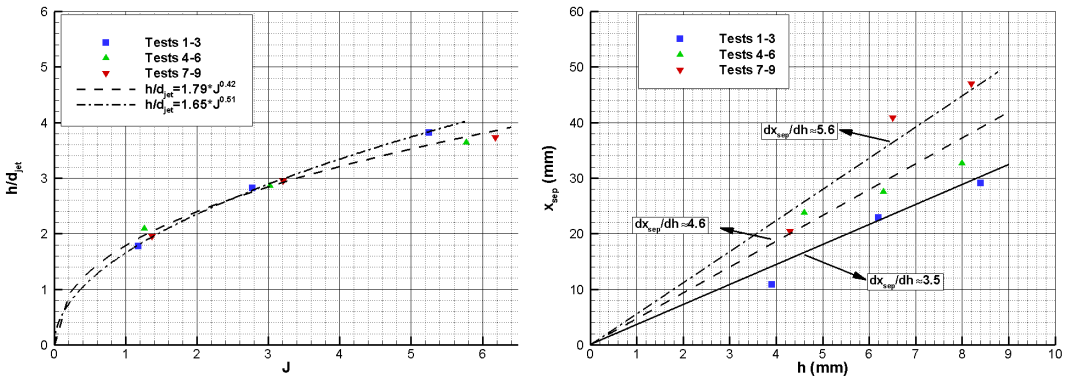

Figure 3.21: Left: Mach disc height non-dimensionalised by jet diameter versus momentum flux ratio; right: separation distance versus Mach disc height for tests 1-9.

Wall pressure measurements

Figures 3.22 and 3.23 show non-dimensional wall pressure distributions, p/p_∞, against non dimensional distance, i.e $(x - x_{jet})/d_{jet}$, for different momentum flux ratios at centreline, z/d_{jet}=4.77 and z/d_{jet}=9.1 for tests 4-6 and tests 7-9 respectively. The theoretical estimate using viscous interaction for cold wall is also shown for the centreline plots. The details of theoretical estimate are in Appendix A. In addition the data without the jet are also plotted in the

centreline plots in Figures 3.22 and 3.23. The wall pressure along the flat plate is slightly high at the leading edge due to viscous interaction and it gradually decreases to free stream value along the plate. This behaviour is also observed in experiments in fact the induced pressure rise due to viscous interaction is even more pronounced for lower Reynolds numbers. After the gradual decrease wall pressure starts to increase from the point at which the flow separates, and then there is further rise to a pressure plateau. The pressure rise due to the injection does not become apparent until a $(x - x_{jet})/d_{jet}$ value of -22 for test 6 and -27 for test 9, afterwards it rises gradually implying laminar separation. This rise is followed by the peak at the upstream of the jet reaching nearly 3.1 for test 6 and 3.4 for test 9. Downstream of the jet the pressure well, the increase in pressure is apparent due to the recompression shock. Each plot exhibits the effect of increasing jet to free stream momentum flux ratio which leads to increase in the wall static pressure values at both upstream and downstream regions. The size of upstream and downstream flow structures extents not only in streamwise direction but also in spanwise direction, spreading laterally with higher J values. The pressure plateau on the centreline and the pressure distribution on the z/d_{jet}=4.77 line of tests 4-6 are slightly higher compared to the baseline tests. One of the reason for that is the slightly increased J value. However for tests 7-9, the plateau is much more extended and gradual with a small dip before the pressure peak, which is surpassing the effect of the increase in J. The magnitude of the peak pressure on the z/d_{jet}=4.77 off-centreline is found to be around 2.1 at slightly downstream of the jet orifice, i.e. x/d_{jet}=5 for test 6 and 2.5 at the jet location for test 9 respectively.

Figure 3.24 compares the effects of incoming Reynolds number with variation in J on non dimensional pressure distribution at the centreline with increasing momentum flux ratio from top to bottom. Baseline tests are shown for comparison. An interesting thing to note is that the downstream pressure distribution in all cases are not affected by the developing boundary layer on the flat plate. In case of upstream pressure distribution, as the unit Reynolds number is decreased the jet affected area grows, the pressure peaks are increased and possibly leading to the net force on the plate to be modified favourably. For the design of injection systems for hypersonic vehicles flying at different altitudes, this phenomenon has to be taken into account. The interaction force is bigger at high altitudes due to lower unit Reynolds number.

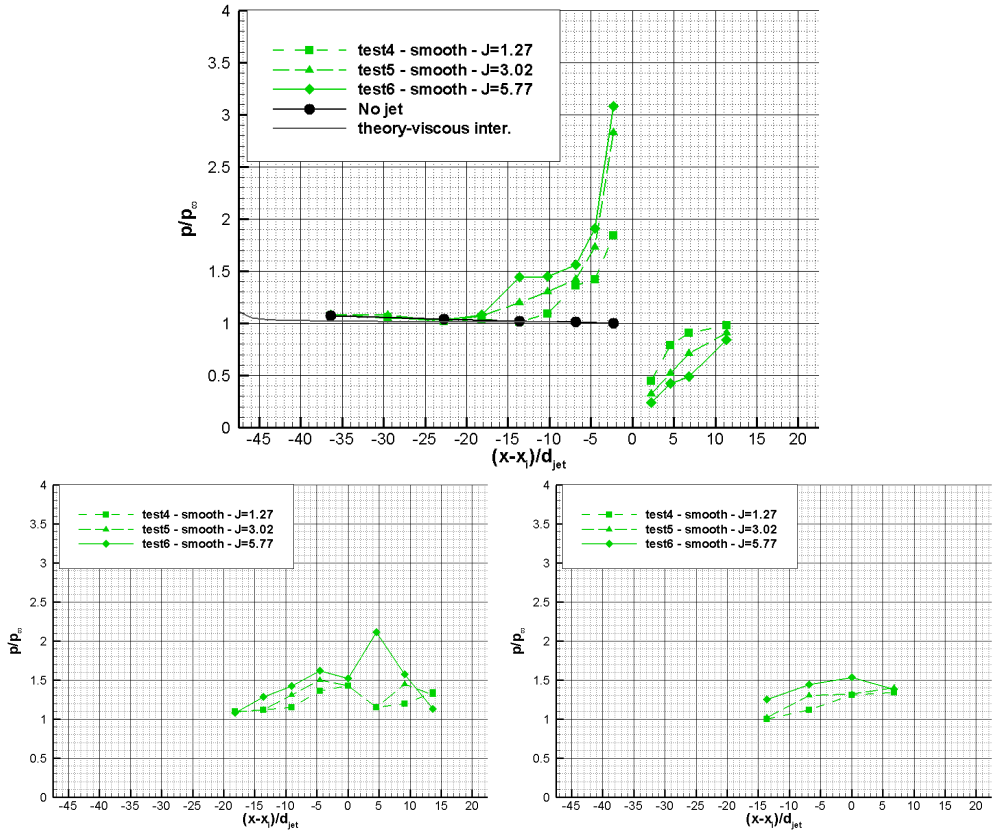

Figure 3.22: Non dimensional wall pressure distribution against non dimensional distance at the centreline (top), $z/djet$=4.77 (bottom left) and $z/djet$=9.1 (bottom right) for tests 4-6.

3.1.3 Effect of injectant gas

The effect of the type of the injectant gas on the interaction phenomenon is examined for HE and CO_2 injection at a typical high unit Reynolds number in addition to baseline tests. These conditions are specified in Table 3.1. Tests 10-12 have HE as injectant gas and tests 13-15 have CO_2 as injectant gas. Since Helium is lighter than air and CO_2 is heavier than air in terms of molecular weight, it would be worthwhile to investigate the associated interaction dynamics of these with incoming Mach 5 flow. Moreover the specific heat ratio, γ of HE is 1.667 whereas it is 1.304 for CO_2. Especially tests 11 and 14 can be directly compared to test 3 as they have nearly the same J and Re/m value and the differences or similarities in their penetration characteristics can be assessed.

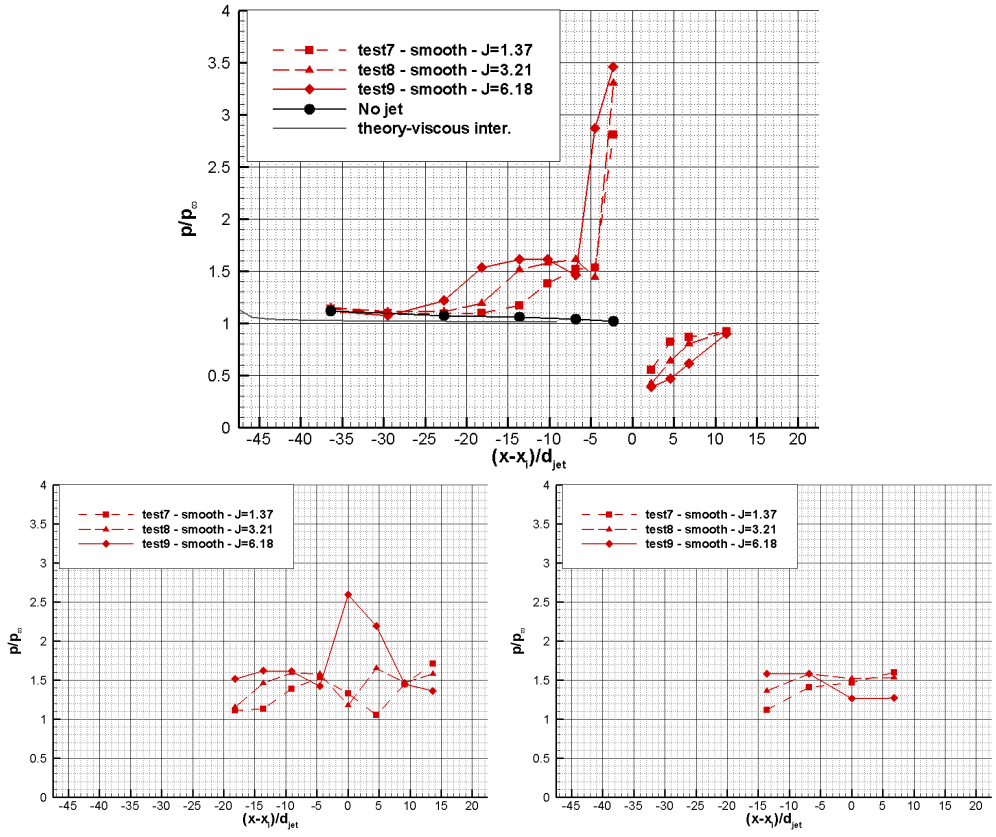

Figure 3.23: Non dimensional wall pressure distribution against non dimensional distance at the centreline (top), $z/djet$=4.77 (bottom left) and $z/djet$=9.1 (bottom right) for tests 7-9.

Schlieren visualisation

Figures 3.25 and 3.26 show the long exposure ($250\mu sec$) schlieren images of the flowfield for the tests 10-12 and tests 13-15. Due to nearly the same incoming unit Reynolds numbers compared to baseline tests the boundary layer developing on the plate is again laminar. The flow structures mentioned in Section 3.1.1 are also observed in here: a leading edge shock due to viscous interaction at the leading edge and following laminar boundary layer growth up to the separation point accompanied by diversion in upward direction thereafter, separation shock that emanates around the separation point and intersects the jet induced bow shock and sonic jet barrel shocks with the Mach disc. The tests involving Helium injection do not include Mach disc height data as it is not possible to deduct it from schlieren images.

As utilised in Section 3.1.1, the thickness of the boundary layer upstream of

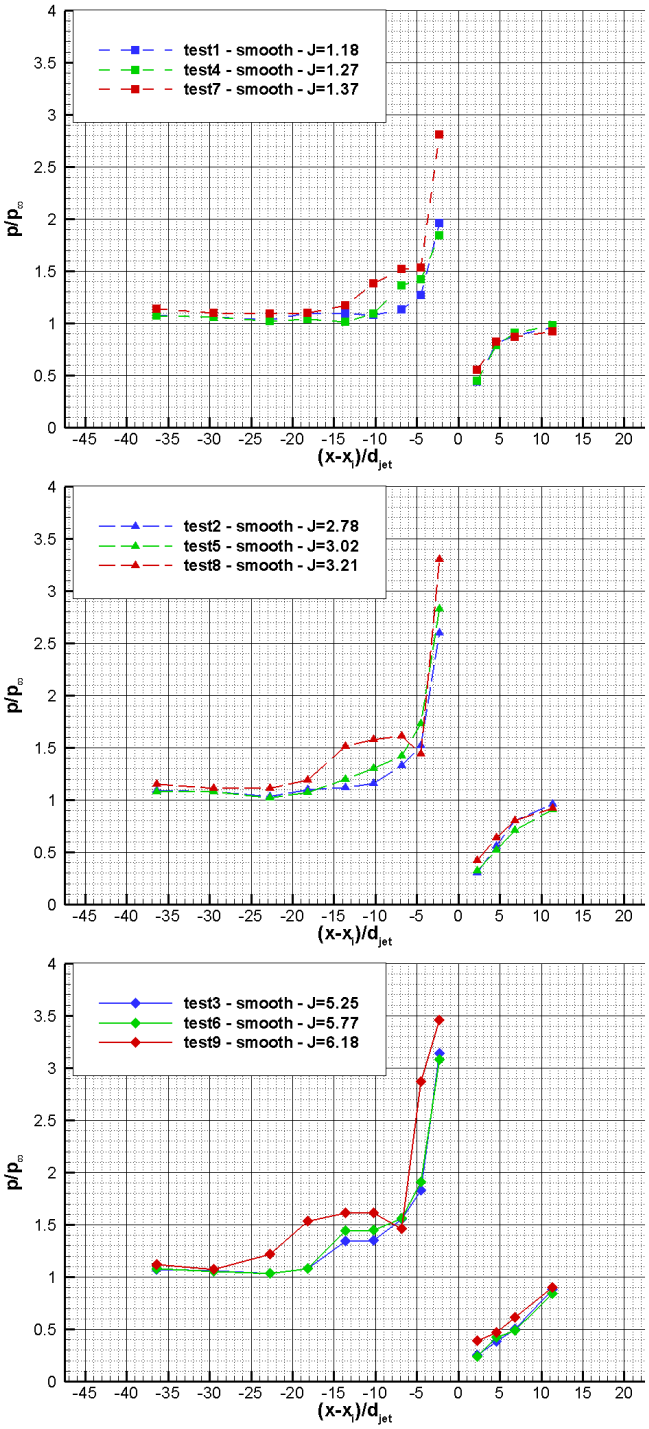

Figure 3.24: Non dimensional wall pressure distribution against non dimensional distance for different unit Reynolds numbers at the centreline with increasing momentum flux ratio from top to bottom.

the separation region, Mach disc height (only for tests 13-15) and the separation

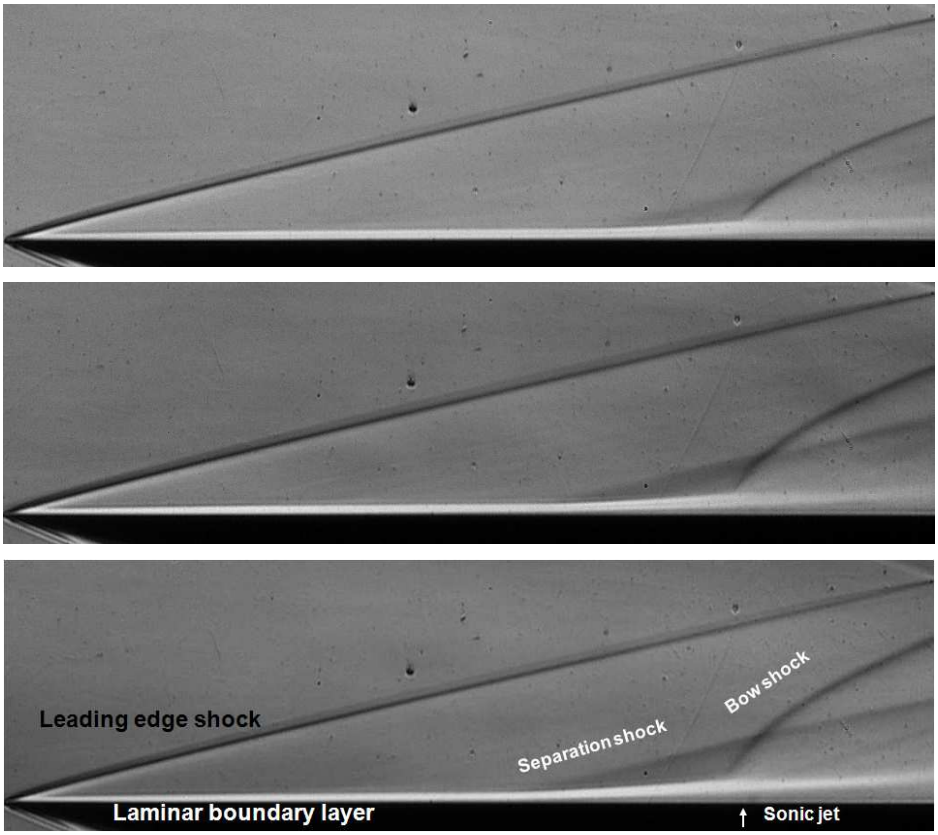

Figure 3.25: Schlieren visualisation of the flowfield in the presence of the Helium sonic transverse jet with three different momentum flux ratios; top: test 10, middle: test 11, bottom: test 12 with annotated flow structures with J values of 1.33, 2.65 and 3.96 respectively.

length can be extracted from schlieren images using image processing. These values are tabulated in Table 3.4 with theoretical Mach disc height estimates mentioned in Section 3.1.1. The effect of the injectant gas on the size of separation is remarkable. Carbon Dioxide tests result a significantly larger separation lengths compared to Helium. The reason for that might be the deposition of the heavy gas around the upstream jet periphery and the creation of an obstacle staying inside the boundary layer like in the case of wall cooling. From the Table 3.4 it can be easily concluded that the Mach disc height for CO_2 tests are close to theoretical estimates and the separation region is significantly influenced by type of the injectant gas. The agreement between the experimental and the theoretical Mach disc heights is good. Regarding the comparison with theoretical estimates for boundary layer thickness the agreement is found to be reasonable.

Mach disc height non-dimensionalised by jet diameter, h/d_{jet}, is plotted against

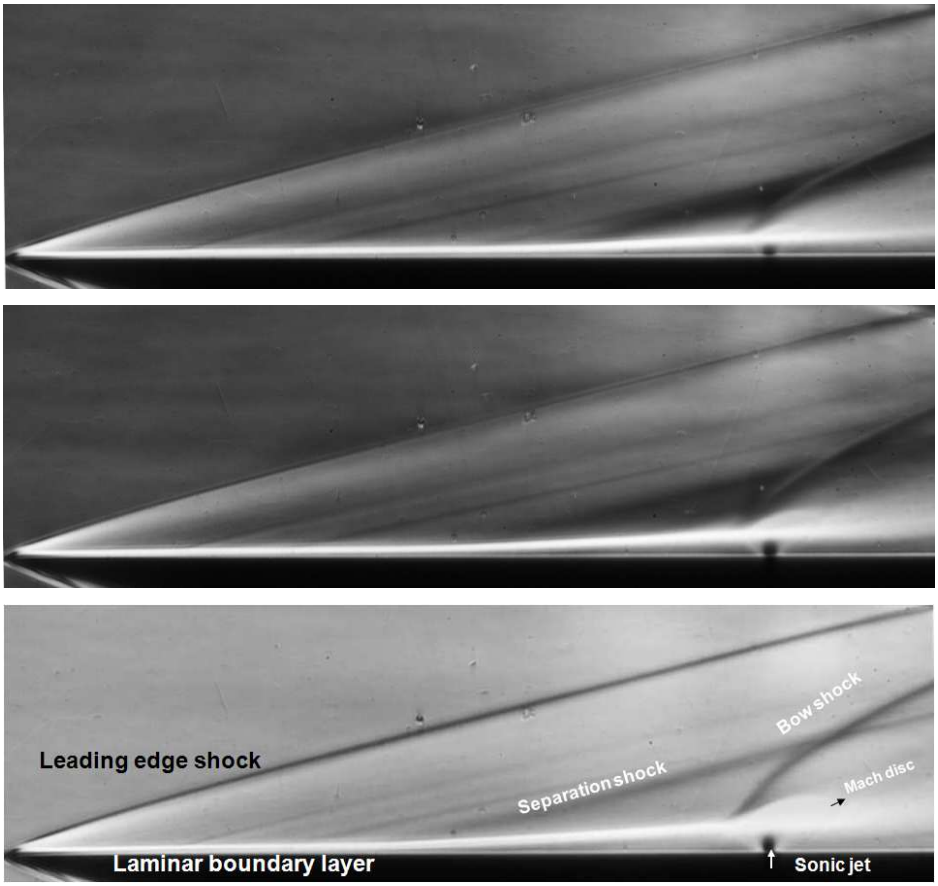

Figure 3.26: Schlieren visualisation of the flowfield in the presence of the Carbon Dioxide sonic transverse jet with three different momentum flux ratios; top: test 13, middle: test 14, bottom: test 15 with annotated flow structures with J values of 1.13, 2.64 and 3.61 respectively.

Table 3.4: Experimental boundary layer thicknesses (δ), Mach disc heights (h) and separation lengths (x_{sep}) for tests 10-15.

Test No	δ (mm)	δ_{theo} (mm)	h (mm)	h_{theo} (mm)	x_{sep} (mm)
10	1.8±0.1	1.4	–	3.9	11.5±0.3
11	1.6±0.1	1.3	–	5.5	22.9±0.3
12	1.5±0.1	1.3	–	6.8	26.0±0.3
13	1.7±0.1	1.3	4.2±0.15	4.3	30.4±0.3
14	1.4±0.1	1.2	6.5±0.15	6.5	44.4±0.3
15	1.3±0.1	1.1	8.0±0.15	7.6	52.8±0.3

momentum flux ratio, J in Fig. 3.27 (left) for CO_2 tests. These results are compared to baseline tests. Another power law fit is applied for Mach disc height in

addition to the one deducted from baseline tests and the resultant equation is shown in Fig. 3.27 (left). The general behaviour fits well on a power law fit with a square root dependence on J. In case of separation length, x_{sep}, against Mach disc height, h (Fig. 3.27 right), the slope has increased from 3.5 to 7 by using Carbon Dioxide and the reason for that might be the penetration path close to the surface and imposing a bigger obstacle to incoming flow.

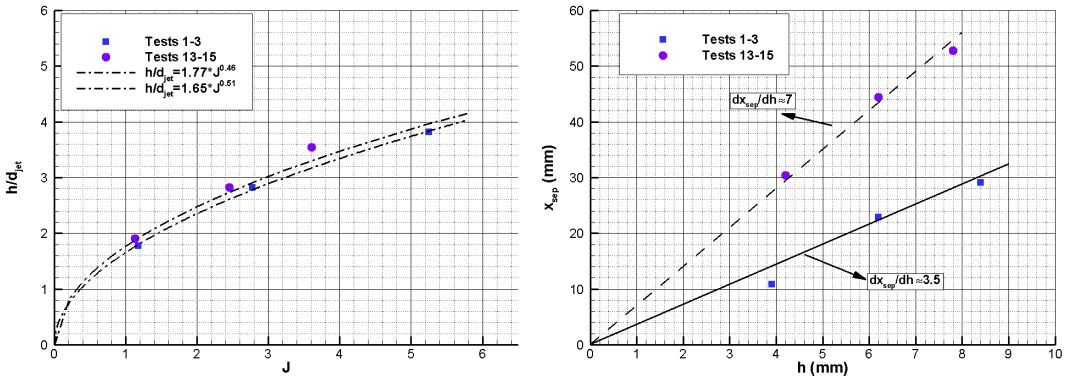

Figure 3.27: Left: Mach disc height non-dimensionalised by jet diameter versus momentum flux ratio; right: separation distance versus Mach disc height for tests 1-3 and tests 13-15.

Three instantaneous schlieren images for tests 10-15 together with RMS of a time series of 1000 schlieren images show different levels and characteristics of penetration and signify the high levels of unsteadiness respectively as shown in Figures 3.28, 3.29 and 3.30 3.31. The jet upper boundary can be easily seen from the RMS images and high amplitudes in RMS are observed to occur in the flow domain occupied by the fluctuating bow shock and separation shock. As the momentum flux ratio is increased the jet boundary and the bow shock shift in transverse direction. The characteristics of Helium injection is different than CO_2 injection even though the momentum flux ratio is kept the same, for instance tests 11 and 14. As a lighter gas Helium discharges spreads less due to its high velocity on the other hand CO_2 spreads and mixes significantly with the surrounding air stream.

PIV

As different gases are injected with particles for PIV investigation, the flow tracing capability of particles has to be assessed using Stokes number, Sk. using modified Stokes drag law that includes Knudsen number based on the diameter of the

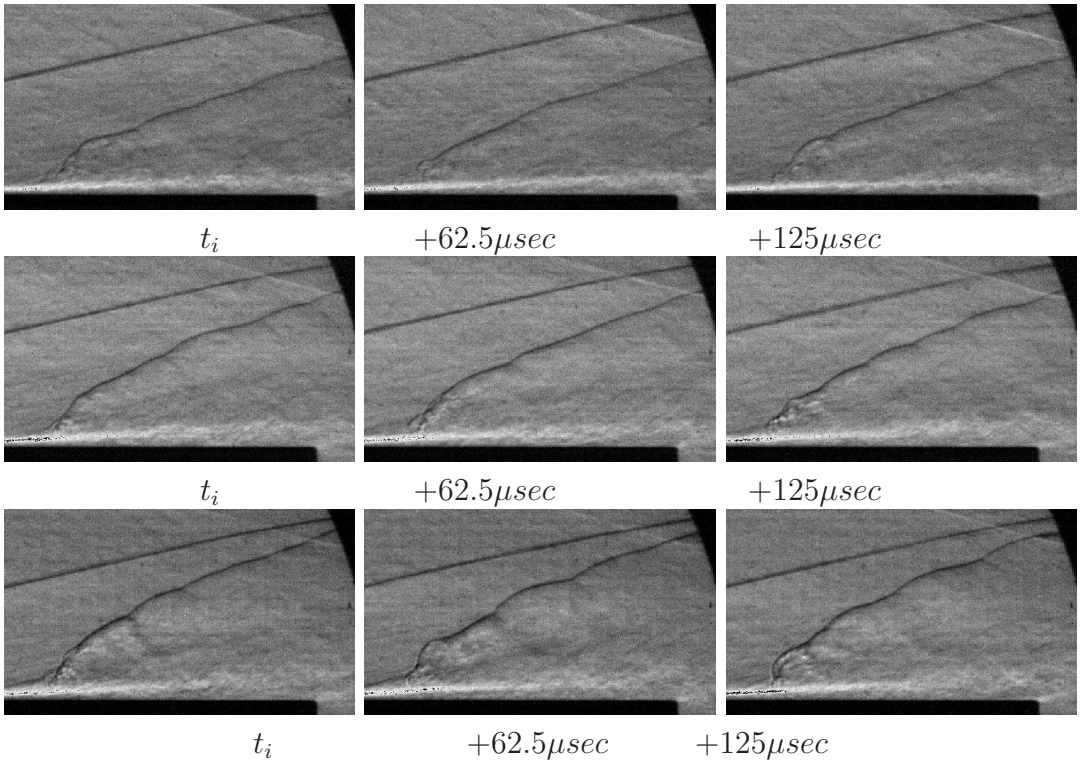

Figure 3.28: Three instantaneous schlieren images of Helium injection; top: test 10, middle: test 11, bottom: test 12.

particle, Kn_d, Reynolds number based on the diameter of the particle, Re_d and Mach number, M_v, both evaluated for the maximum particle slip velocity ΔV as explained in Section 2.2.5. The slip velocity is assumed as jet velocity and the related characteristics are tabulated in Table 3.5. The flow following capability of aluminum oxide particles for Helium injection is the most critical one due to its high jet velocity and biggest particle relaxation time. In this case Sk is around 0.23-0.11 for test 10-12 respectively. However it should always kept in mind that the finite response time of particles spreads the jet boundaries and Mach disc through blurring mechanism described in Section 3.1.1 even though the final interrogation area size is $16 \times 16 pixel^2$ ($0.64 \times 0.64 mm^2$) with 75% overlap.

Figures 3.32 to 3.34 show selective raw PIV images and associated vector fields for tests 10-12 with increasing J value. As the Helium jet is discharged from the orifice at a velocity around 875m/s, it spreads minimal and accelerates in the transverse direction. Then it is bent very abruptly towards the main flow direction. The nearfield spreading rate is very small however as its velocity is reduced to around 750m/s in the mid/farfield it starts to mix with the surrounding

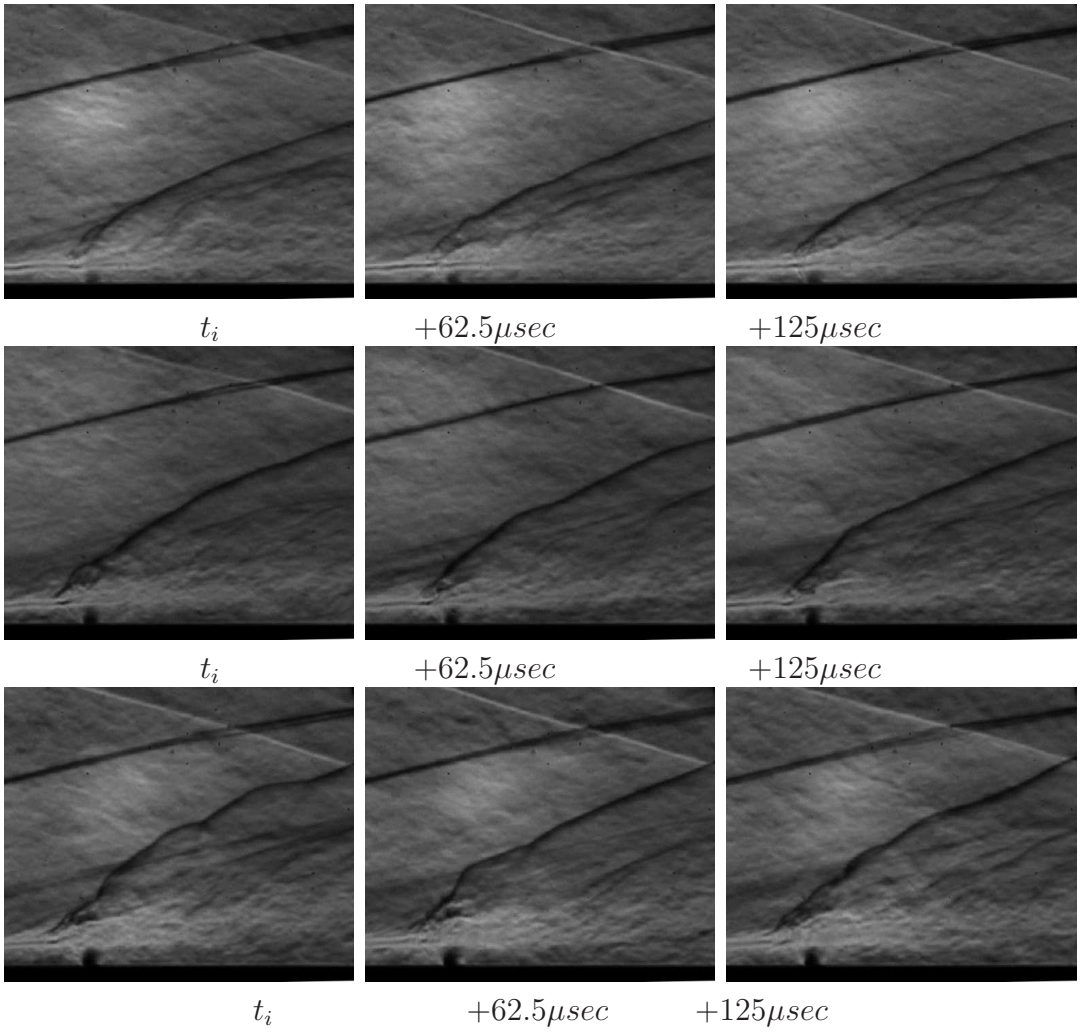

Figure 3.29: Three instantaneous schlieren of CO_2 injection; top: test 13, middle: test 14, bottom: test 15.

air flow and get dispersed. This penetration behaviour is very different compared to air injection (see Section 3.1.1, especially test 2). With increasing momentum flux ratio, higher levels of penetration and thicker jet affected area are observed as expected.

Figures 3.35 to 3.37 show selective raw PIV images and associated vector fields for tests 13-15 with increasing J value. As the CO_2 jet is discharged from the orifice at a velocity around 250m/s, acceleration in the transverse direction is observed and terminated by the Mach disc which bends the jet towards the main flow direction. After the normal shock the jet velocity is reduced following an acceleration reaching values of 750m/s, which is close to the free stream velocity but slightly lower due to the presence of the bow shock. The spreading of the

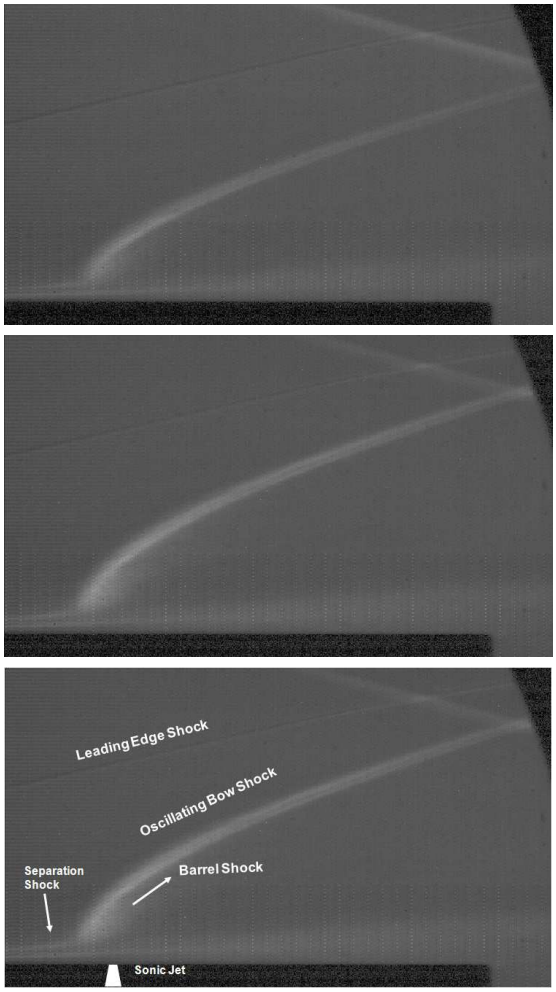

Figure 3.30: RMS of instantaneous schlieren images of Helium injection of a time series of 1000 samples; top: test 10, middle: test 11, bottom: test 12 with annotated flow structures.

CO_2 jet in the farfield is less than air due to its heaviness in terms of molecular weight, and it stays closer to the wall compared to air injection (see Section 3.1.1, especially test 2). With increasing momentum flux ratio, higher levels of penetration and thicker jet affected area are observed as expected.

Figures 3.38 and 3.39 show averaged flow fields and TI contours over 100 vector fields for tests 10-12 during the useful running time. Averaged streamlines are also visualised in Fig. 3.38. The spatial coordinates are normalized with the jet diameter, d_{jet}. The main flow is in the x direction. The unsteady jet shear layer structures do not appear in averaged velocity contours. However averaged jet streamlines show high penetration and consequent convection with the main flow. In case of TI contours (Fig. 3.39), the jet boundaries and the associated

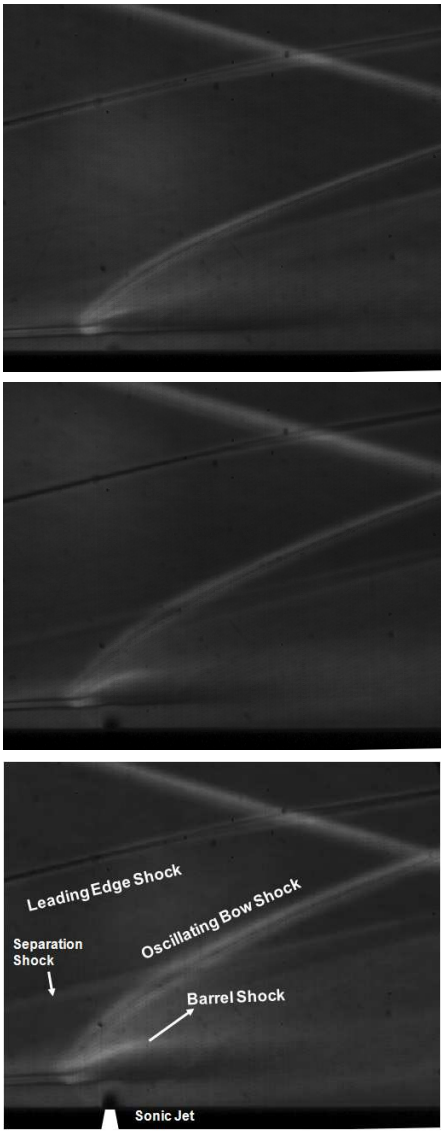

Figure 3.31: RMS of instantaneous schlieren images of CO_2 injection of a time series of 1000 samples; top: test 13, middle: test 14, bottom: test 15 with annotated flow structures.

penetration characteristics are demonstrated. The barrel shocks can be seen easily however the Mach disc forming the jet boundary can not be visualised like in schlieren images (see Fig. 3.25). As J is increased the extent of the local jet boundary (drawn in black dotted lines) composed of barrel shocks and Mach disc, and the extent of jet spreading (drawn in black dashed lines) are increasing. For tests 10-13 the penetration height values at $x = 20d_jet$ are found as 20.9mm, 28.6mm and 30.8mm respectively. The theoretical Eqn. 3.3 underestimates the jet boundary in all cases by 15-20%.

Table 3.5: Particle characteristics for transverse jets for tests 1-3 and tests 10-15.

Jet Gas	Test No	u_{jet} (m/s)	Kn_d	τ_p μsec	τ_f μsec	Sk
	1	315	0.50	2.95	70	0.04
AIR	2	315	0.21	1.97	70	0.03
	3	315	0.11	1.63	70	0.02
	10	875	1.36	5.7	25	0.23
HE	11	875	0.68	3.5	25	0.14
	12	875	0.45	2.7	25	0.11
	13	250	0.32	2.9	88	0.03
CO_2	14	250	0.14	2.1	88	0.02
	15	250	0.10	2.0	88	0.02

Figures 3.40 and 3.41 show averaged flow fields and Turbulence Intensity contours over 100 vector fields for tests 13-15 during the useful running time. Averaged streamlines are also visualised in Fig. 3.40. The spatial coordinates are normalized with the jet diameter, d_{jet}. The main flow is in the x direction. Averaged jet streamlines show low penetration and consequent convection with the main flow closer to the wall with small amount of spreading. In case of TI contours (Fig. 3.41), the jet boundaries and the associated penetration characteristics are demonstrated. The barrel shocks and the Mach disc forming the jet boundary can be easily seen. As J is increased the extent of the local jet boundary (drawn in black dotted lines) composed of barrel shocks and Mach disc, and the extent of jet spreading (drawn in black dashed lines) are increasing. For test 1 the Mach disc height and penetration height at $x = 20d_{jet}$ are found as 4.2mm and 11mm respectively. For test 2 these values are 6.4mm and 21.2mm whereas for test 3 they are found as 8.1mm and 22.9mm. The Mach disc height values are in very good agreement with the values found from schlieren images. However the uncertainty in h is found to be $\pm$0.3mm. The theoretical Eqn. 3.3 significantly overestimates the lowest J case (test13) however it performs fairly good for tests 14 and 15.

For the similar values of J (tests 2, 11 and 14) three different gases, air, Helium and Carbon Dioxide exhibits very different penetration and mixing behaviour. This is a clear demonstration of the complexity of jet interaction phenomenon, which can not be oversimplified to momentum flux ratio.

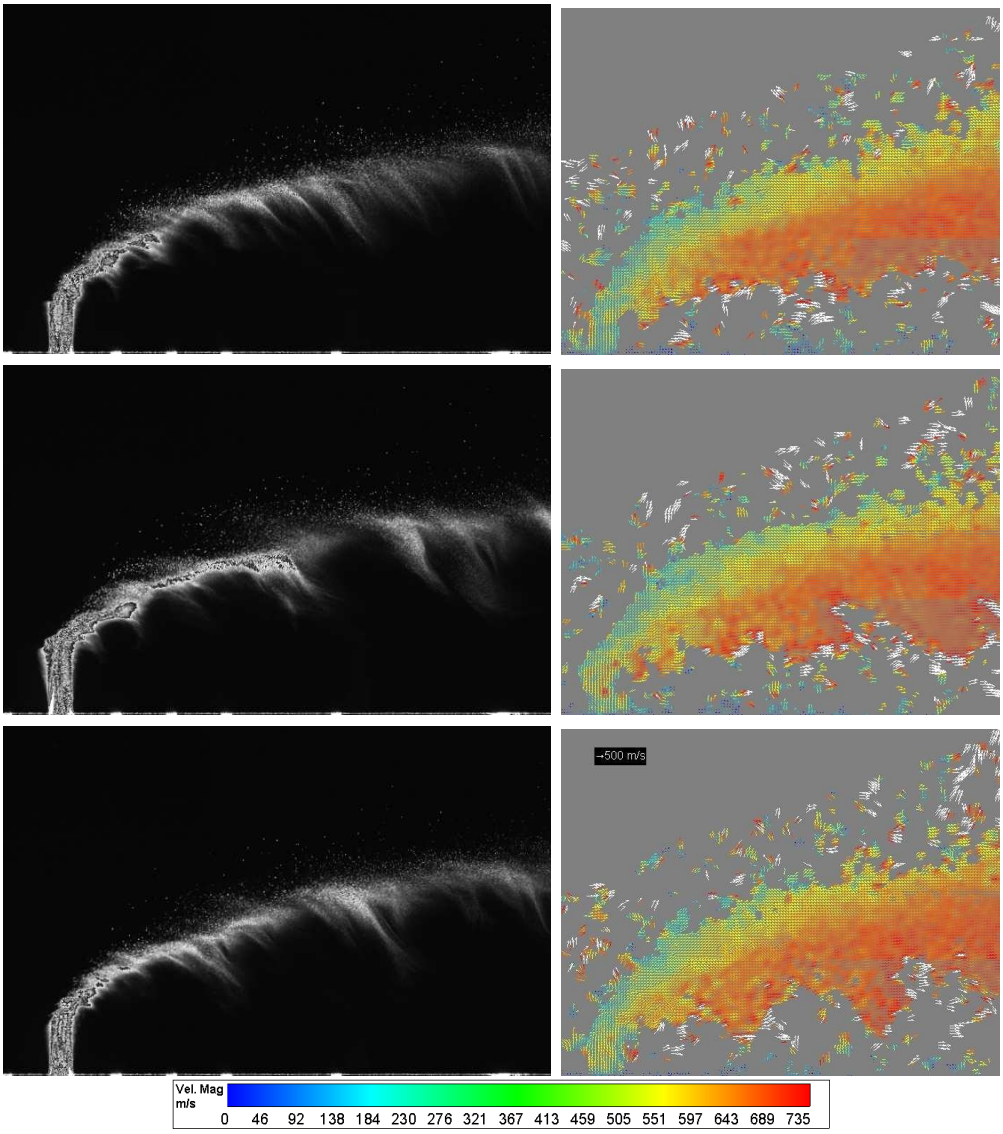

Figure 3.32: Three instantaneous raw PIV images and associated vector fields for test 10.

Wall pressure measurements

Figures 3.42 and 3.43 show non-dimensional wall pressure distributions, p/p_∞, against non dimensional distance, i.e $(x - x_{jet})/d_{jet}$, for different momentum flux ratios at centreline, z/d_{jet}=4.77 and z/d_{jet}=9.1 for tests 10-12 and tests 13-15 respectively. The theoretical estimate using viscous interaction for cold wall is also shown on the centreline plots. The details of theoretical estimate are in Appendix A. In addition the data without the jet are also plotted on the centreline plots in Figures 3.42 and 3.43. The wall pressure along the flat plate is considerably

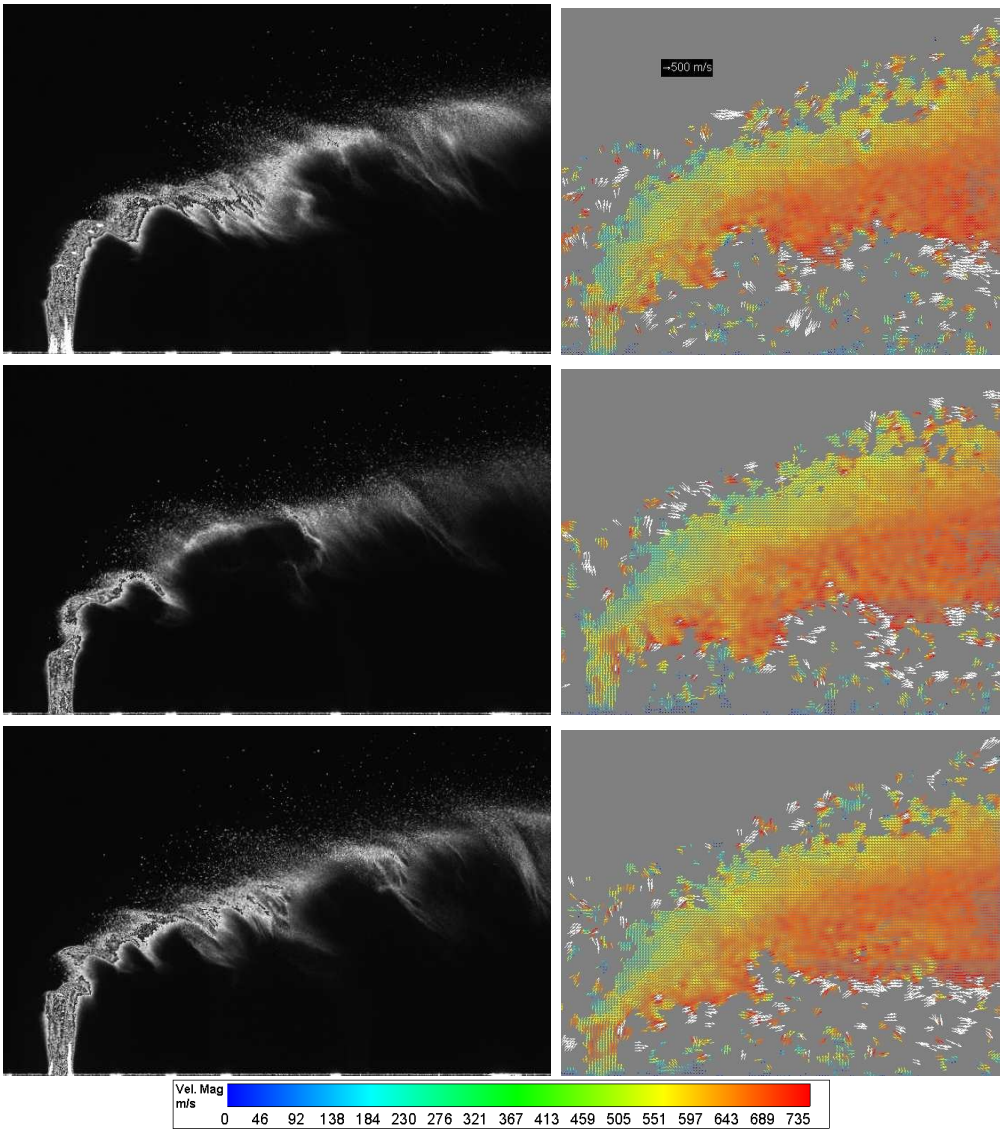

Figure 3.33: Three instantaneous raw PIV images and associated vector fields for test 11.

high at the leading edge due to viscous interaction and it gradually decreases to free stream value along the plate. After the gradual decrease wall pressure starts to increase from the point at which the flow separates, and then there is further rise to a pressure plateau. The pressure rise due to the injection does not become apparent until a $(x - x_{jet})/d_{jet}$ value of -12 for test 12 and -27 for test 15, afterwards it rises gradually implying laminar separation. This rise is followed by the peak at the upstream of the jet reaching nearly 3 for test 12 and test 15. Downstream of the jet the pressure well is apparent that is accompanied by a rise due to recompression shock. Each plot exhibits the effect of increasing

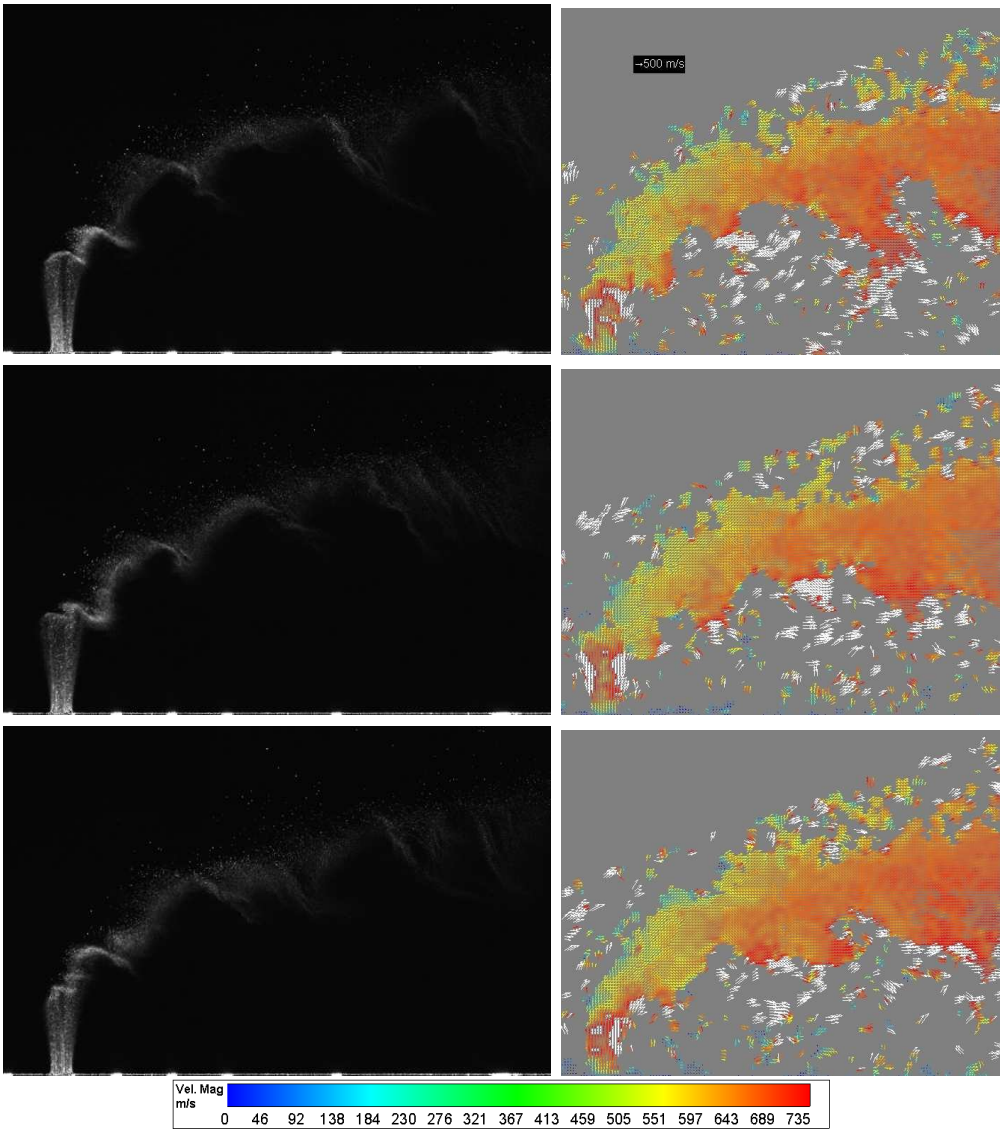

Figure 3.34: Three instantaneous raw PIV images and associated vector fields for test 12.

jet to free stream momentum flux ratio which leads to increase in the wall static pressure values at both upstream and downstream regions. The size of upstream and downstream flow structures extents not only in streamwise direction but also in spanwise direction, spreading laterally with higher J values. The pressure plateau on the centreline for tests 10-12 is not very different from the baseline tests yet the pressure distribution on the z/d_{jet}=4.77 is more evenly distributed compared to the baseline tests. However for tests 13-15 the plateau is much more extended and gradual with a small dip before the pressure peak. The magnitude of the peak pressure on the z/d_{jet}=4.77 off-centreline is found to be 2 at the jet

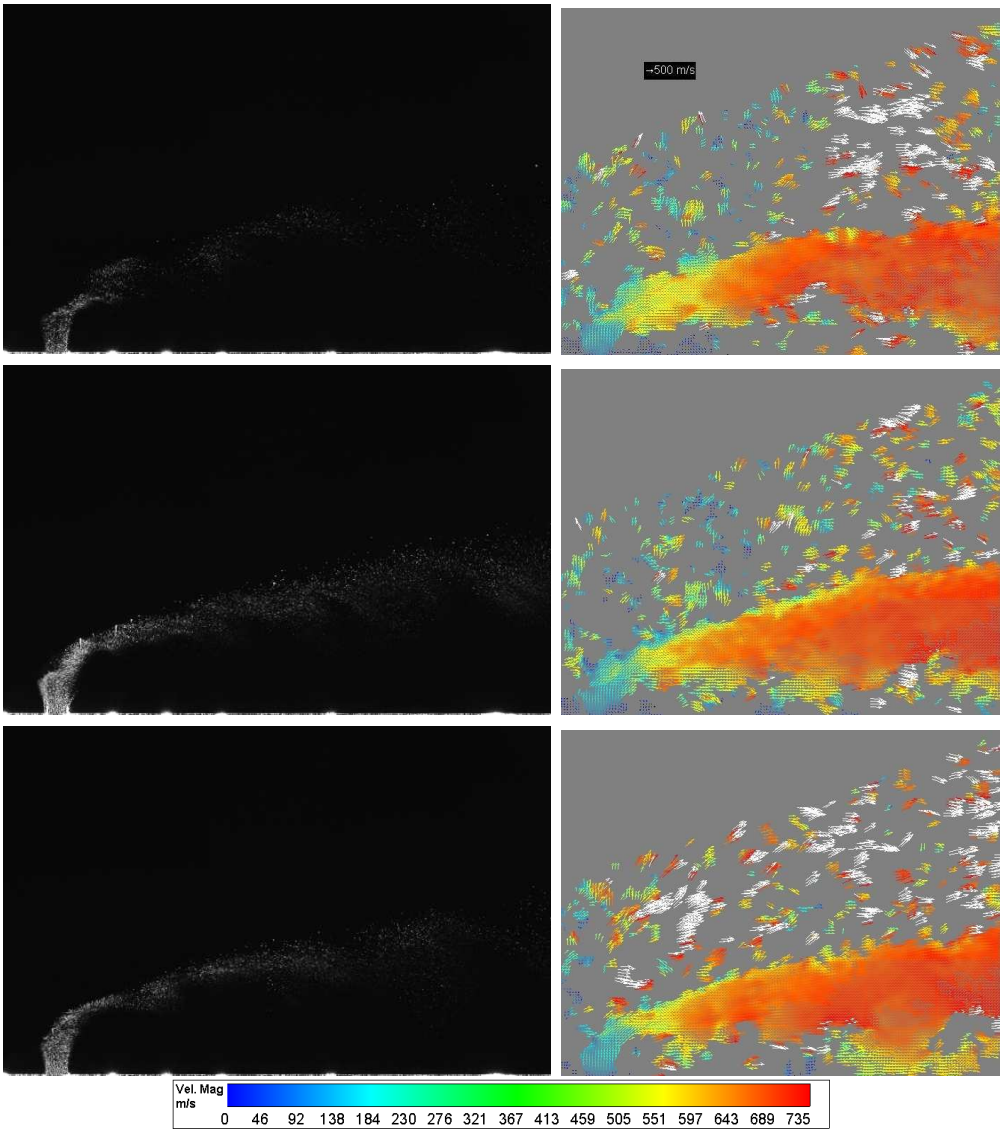

Figure 3.35: Three instantaneous raw PIV images and associated vector fields for test 13.

orifice for test 15.

Figure 3.44 compares the sole effect of injectant gas non dimensional pressure distribution at the centreline with increasing momentum flux ratio from top to bottom. All these tests have similar unit Reynolds numbers and smooth surfaces. Similar J values for low and medium cases are attained, however for high J case air injection has a considerably bigger value. It can be clearly observed hat the injectant gas is affecting wall pressure distribution in the upstream and downstream region even though the jet penetration and free stream Reynolds number are roughly the same. Carbon Dioxide injection has significantly bigger

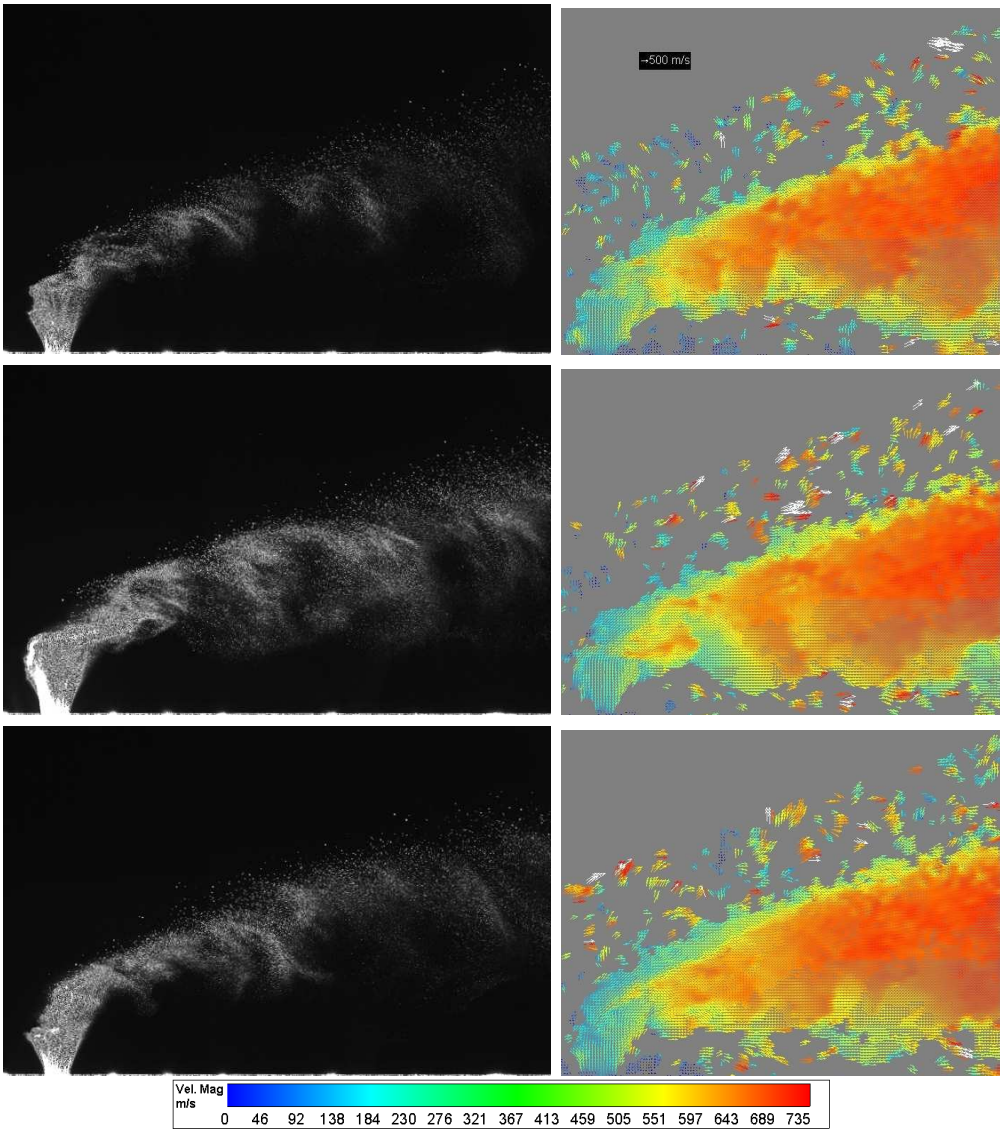

Figure 3.36: Three instantaneous raw PIV images and associated vector fields for test 14.

upstream interaction region for all J values, the reason for that might be due to the deposition of the injectant gas around the jet surrounding and creating a bigger blockage compared to other gases. In the downstream region the difference between air and CO_2 injection is small except right downstream of the jet orifice where slightly higher pressure are observed but with a less steep increase in x direction. In case of Helium injection, it does not cause significant upstream modification compared to air injection except for the highest J case in Figure 3.44 (bottom), where the upstream pressure plateau is smaller. It might be attributed to lower J value. On the other hand the magnitude of downstream pressure well

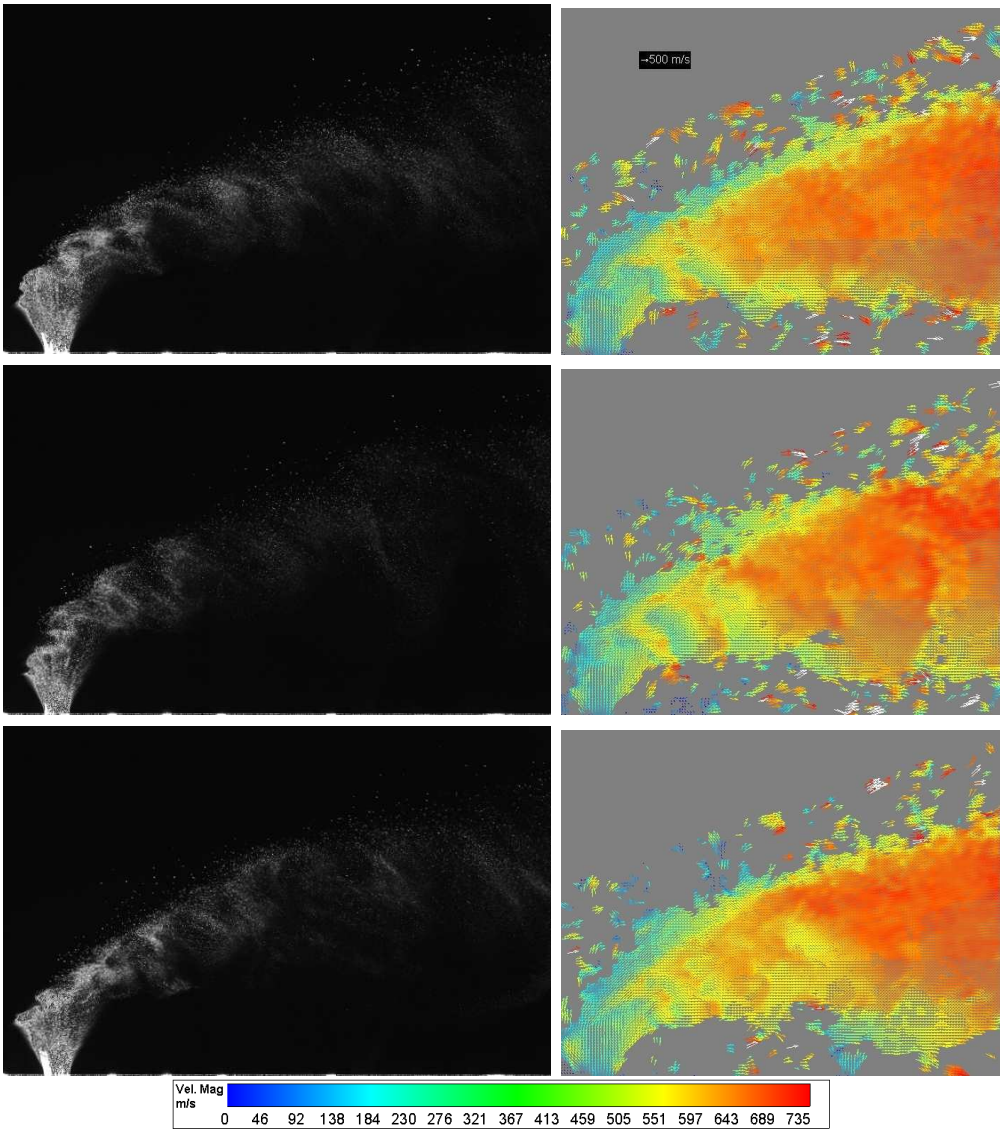

Figure 3.37: Three instantaneous raw PIV images and associated vector fields for test 15.

is more pronounced even exceeding one, which is unusual for transverse jets in hypersonic cross flow.

Oil dot visualisation

Figures 3.45 and 3.46 show the difference in oil dot patterns with increasing momentum flux ratio for Helium and Carbon Dioxide injections respectively. The footprint of the bow shock attachment region, horseshoe vortex core and jet plume separation region can be identified. Oil dots before the attachment of the bow

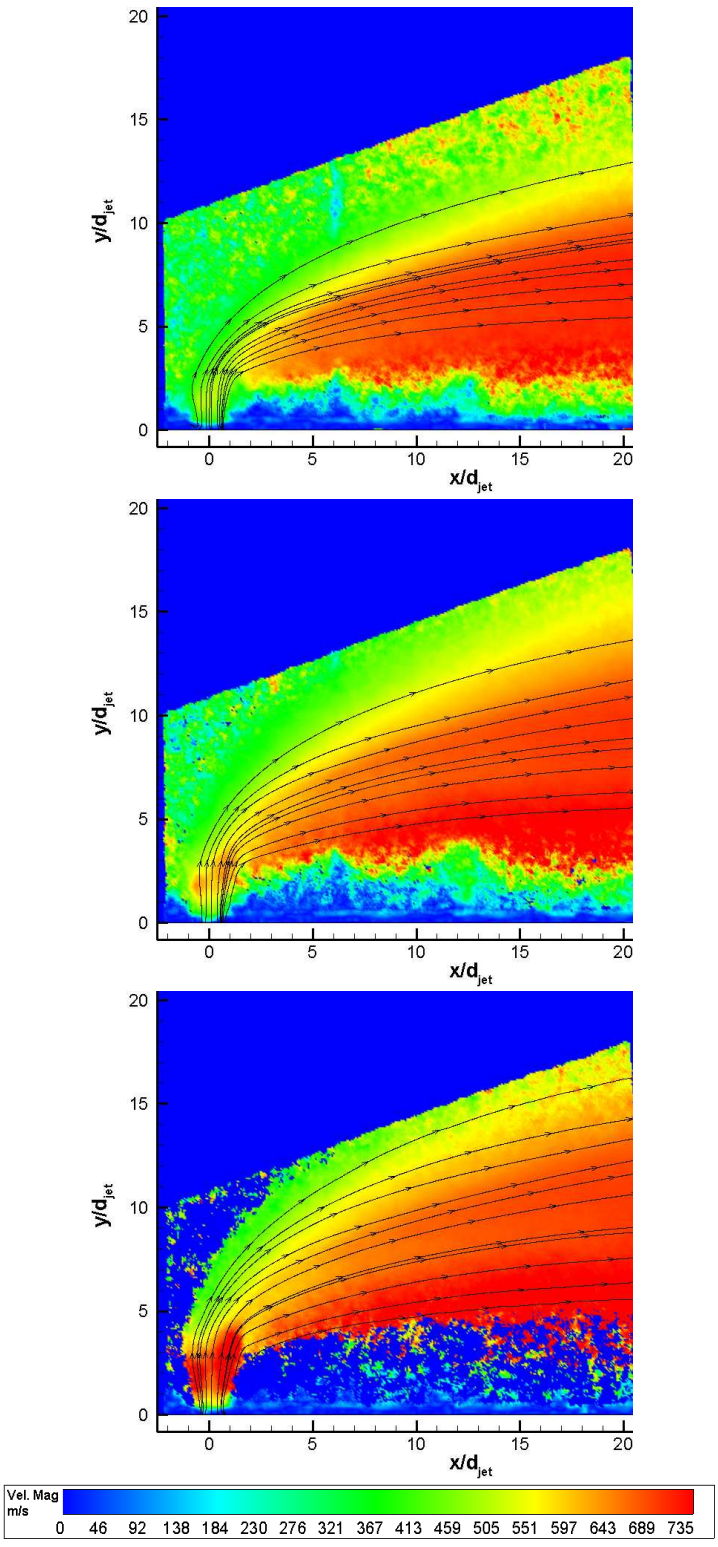

Figure 3.38: Averaged flow field velocity magnitude contours; top: test 10, middle: test 11, bottom: test 12.

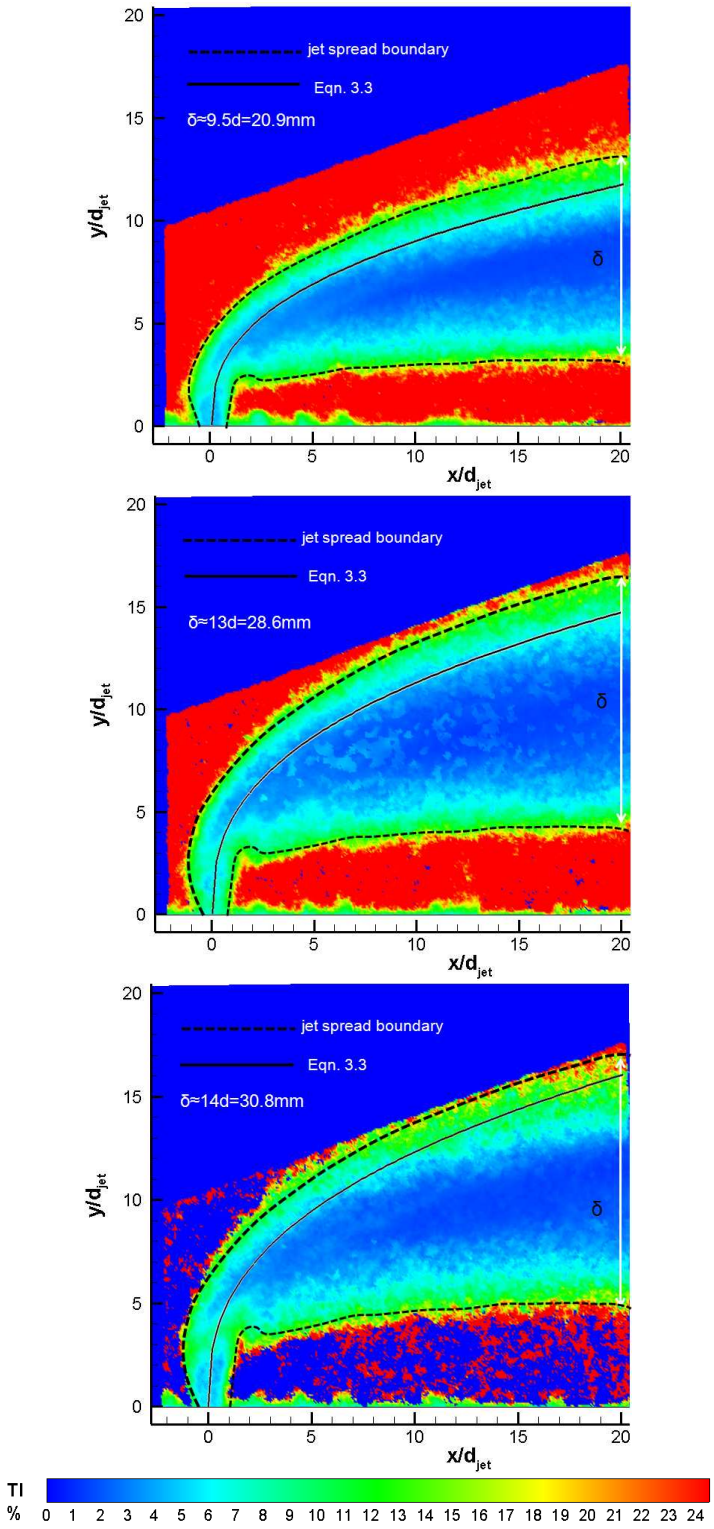

Figure 3.39: Averaged flow field turbulence intensity (TI) contours; top: test 10, middle: test 11, bottom: test 12.

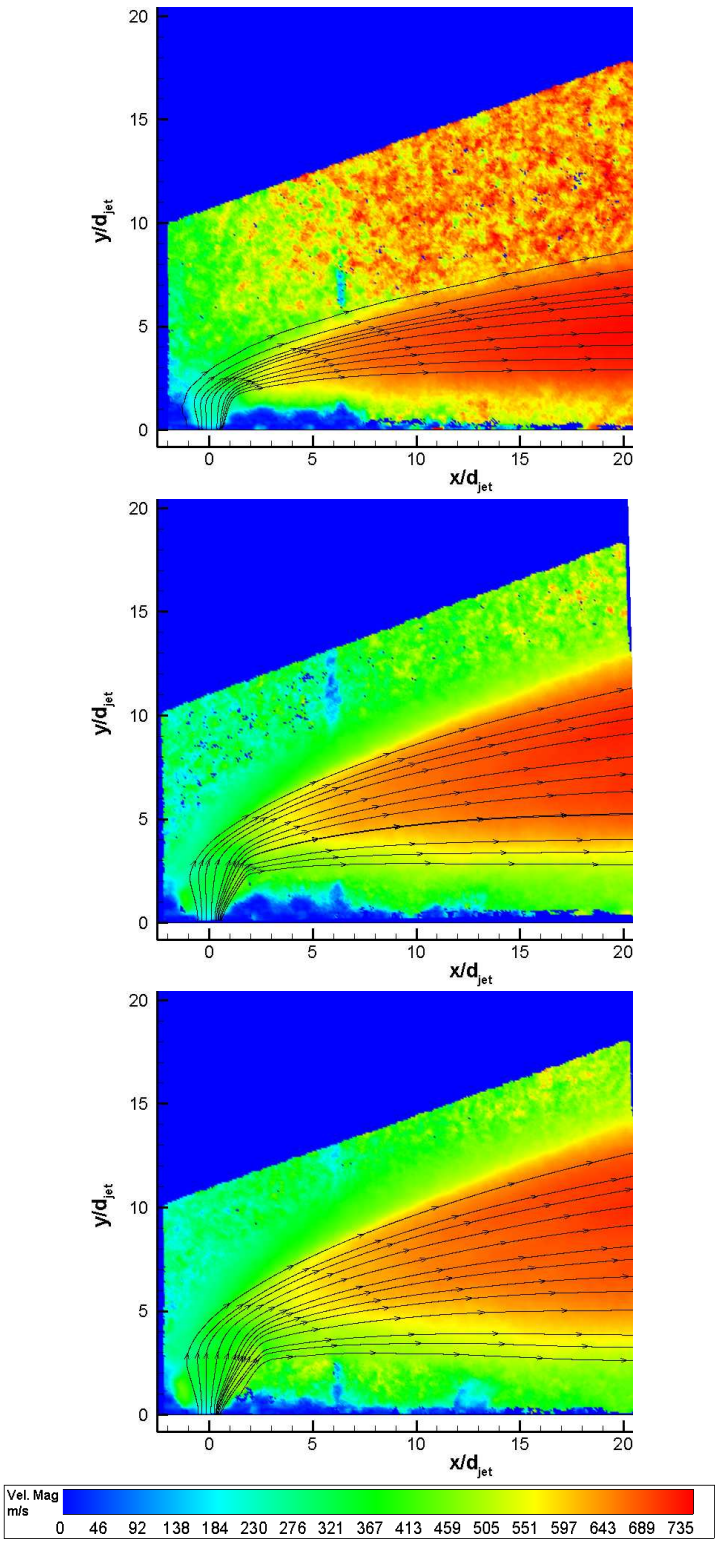

Figure 3.40: Averaged flow field velocity magnitude contours; top: test 13, middle: test 14, bottom: test 15.

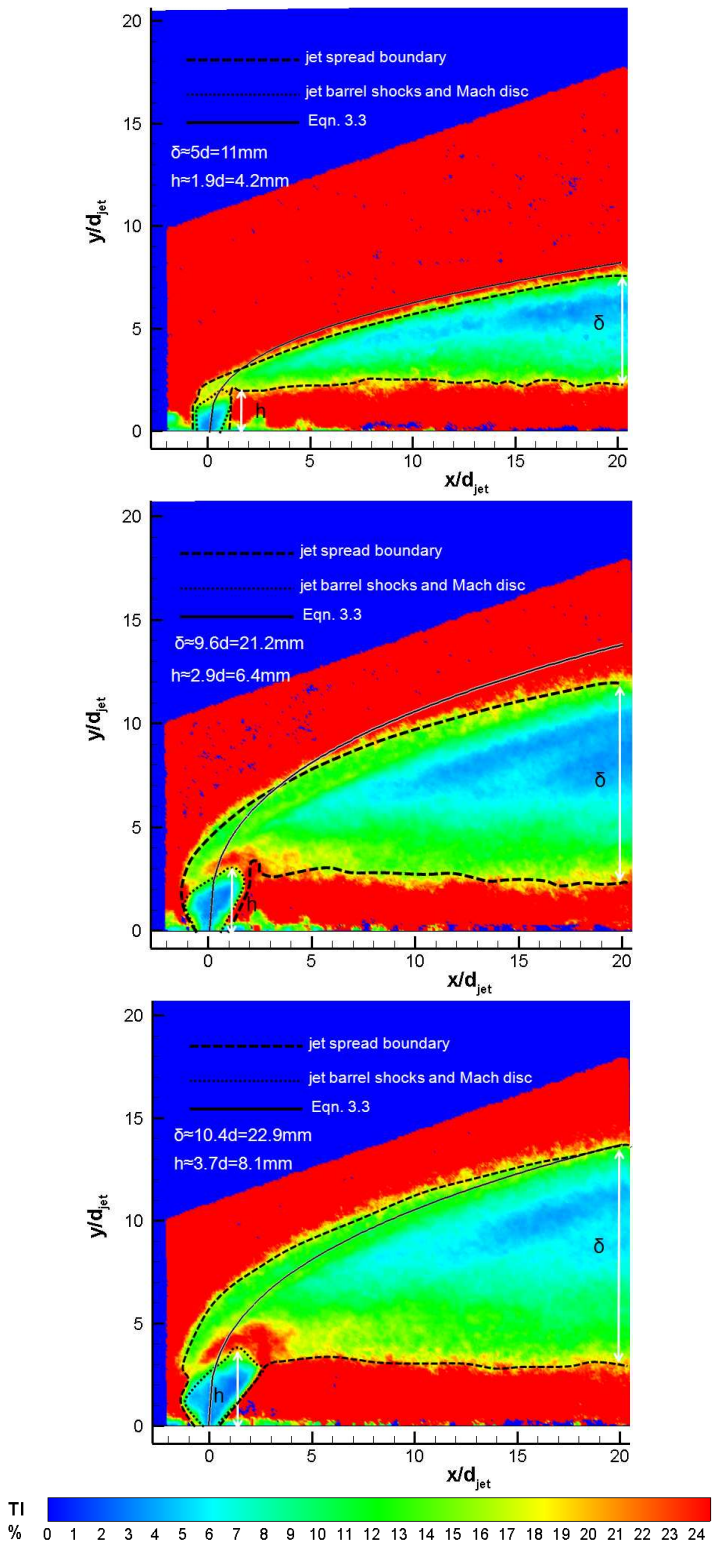

Figure 3.41: Averaged flow field turbulence intensity (TI) contours; top: test 13, middle: test 14, bottom: test 15.

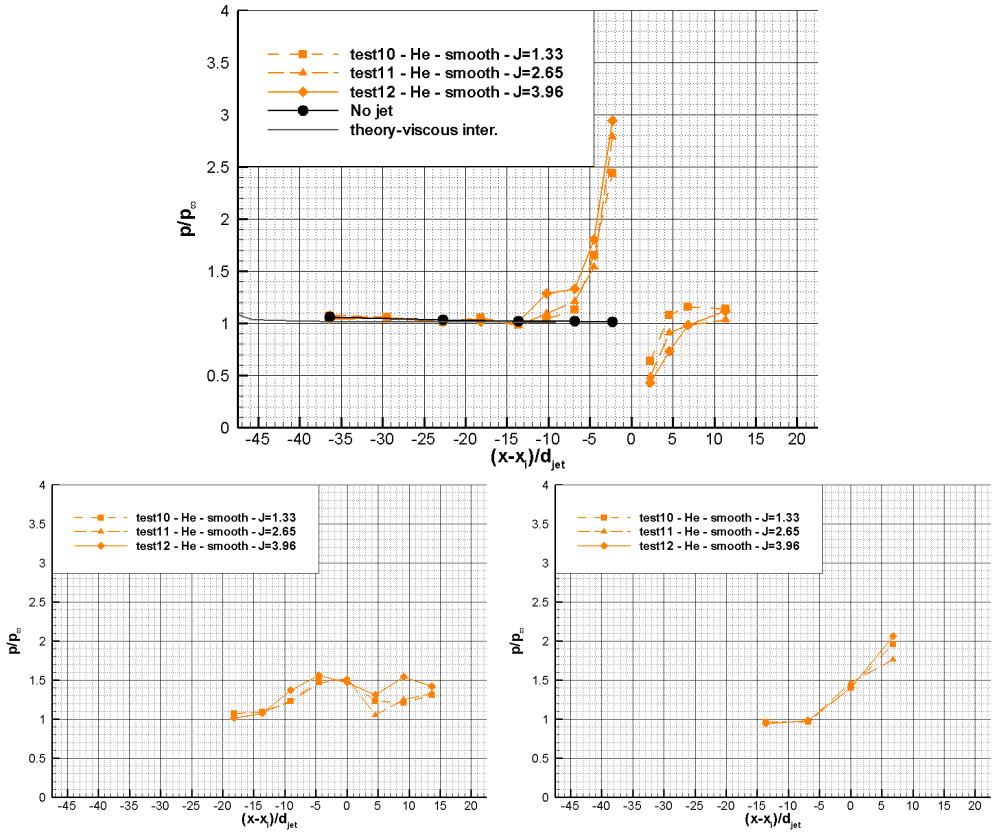

Figure 3.42: Non dimensional wall pressure distribution against non dimensional distance at the centreline (top), $z/djet$=4.77 (bottom left) and $z/djet$=9.1 (bottom right) for tests 10-12.

shock (i.e. λ separation shock) move minimally, however, just downstream of the attachment region they move outwards significantly and bend towards the main stream direction. The horseshoe vortex spreads the oil dots away from its core and the separation region behind the jet plume keeps the oil dots away from itself causing deposition on the separation line. The interaction region for Helium injection is quite small even for the highest J value and stays close to the jet orifice whereas the affected area is significantly larger for CO_2 injection. In fact the bow shock attachment region can be visualised only for the smallest J value. The interaction region extends to 6.8, 7.7 and 8.6 times d_{jet} in lateral direction at x/d_{jet}=0 for tests 10, 11 and 12 respectively. on the other hand for Carbon Dioxide, the interaction region extends to 9.1, 13.6 times d_{jet} in lateral direction at x/d_{jet}=0 for tests 13, 14 respectively. The affected area reaches the side of the plate for test 15.

As a conclusion it is believed that the type of injectant gas is clearly a case

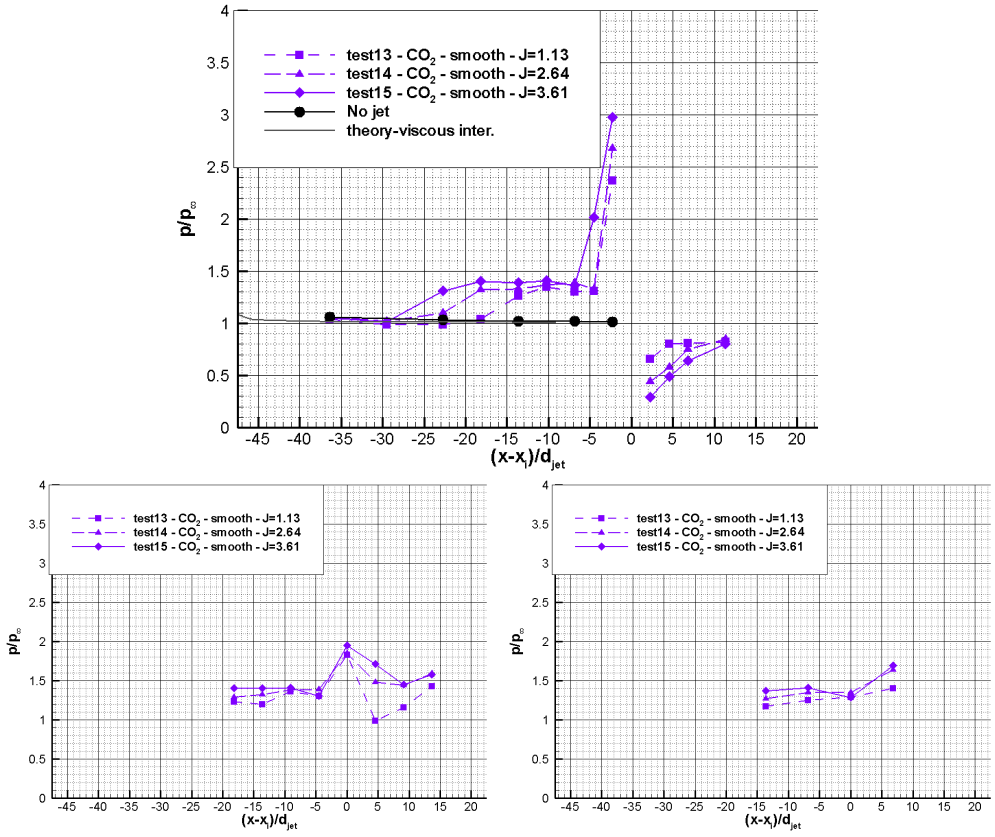

Figure 3.43: Non dimensional wall pressure distribution against non dimensional distance at the centreline (top), $z/djet$=4.77 (bottom left) and $z/djet$=9.1 (bottom right) for tests 13-15.

changing paramater in terms of penetration and spreading behaviour in near and farfield. The injectant gas definitely influences the pressure distribution and the size of upstream and downstream flow structures with lateral extent in spanwise direction. Carbon Dioxide provides smaller penetration but favourable interaction at the upstream region and Helium provides great penetration and favourable interaction at the downstream region compared to air. Considering the upstream region is much more critical for the creation of aerodynamics forces and moments, Helium or an alternative lighter gas is mainly beneficial for deep penetration and mixing in the farfield for scramjet applications rather than the creation of necessary side forces. On the other hand Carbon Dioxide is more useful for aerodynamic steering and also flame holding in the near field of the jet where it suspends dominantly. For the design of injection systems for hypersonic vehicles flying at different altitudes, this characteristics have to be taken into account.

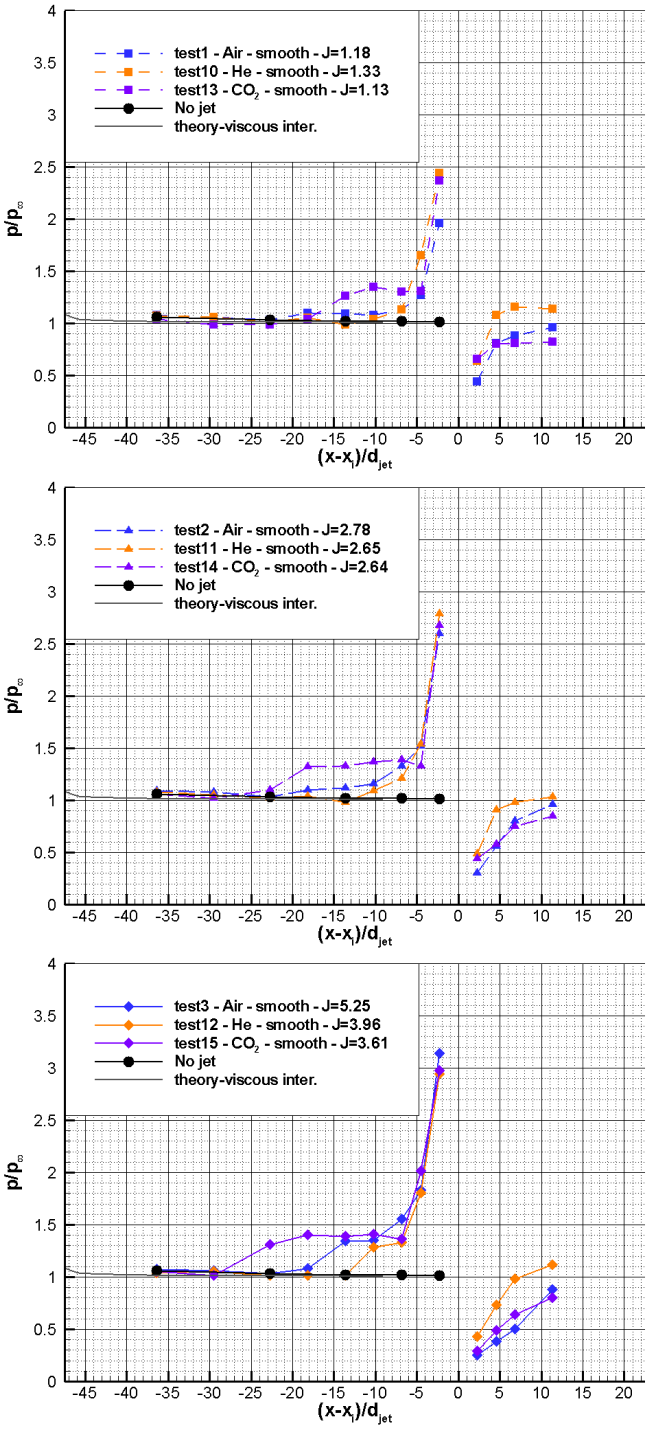

Figure 3.44: Non dimensional wall pressure distribution against non dimensional distance for air, *Helium* and CO_2 injections at the centreline with increasing momentum flux ratio from top to bottom.

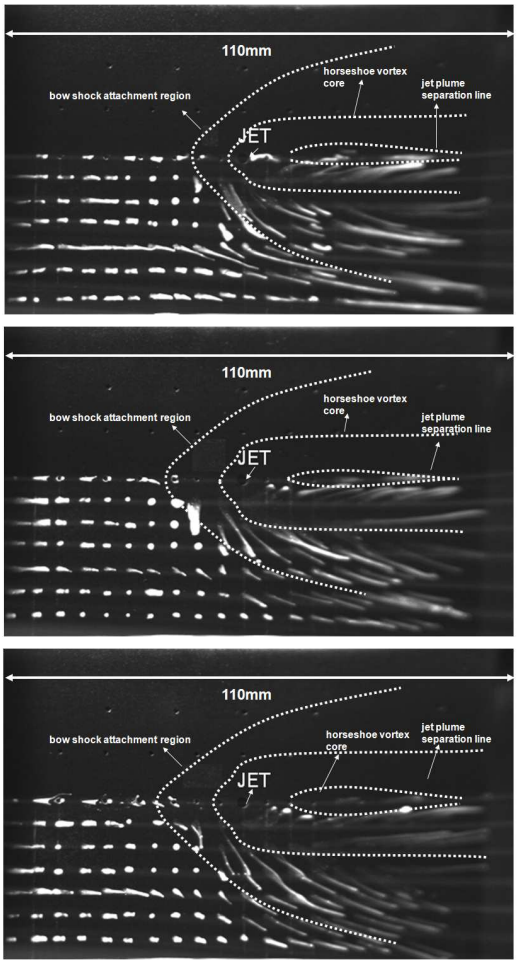

Figure 3.45: Oil dot visualisation of the sonic transverse Helium jet; top: test 10, middle: test 11, bottom: test 12.

3.1.4 Effect of roughness

The effect of surface roughness, hence the development of incoming boundary layer on the flat plate, on the interaction phenomenon is examined with air injection for three different rough surfaces in addition to baseline tests. These conditions are specified in Table 3.1. Tests 16-18 have a P1000 sandpaper covering the flat plate, tests 19-21 use medium roughness P400 sandpaper and tests 22-24 utilise high roughness P120 sandpaper. All these surfaces include sub-boundary layer scale roughnesses, that are small compared to the boundary layer thickness of 2.5mm at the injection location (no jet case) of 105mm from the leading edge. Furthermore an attempt to avoid the transition mechanism due to roughness is made to assess the effect of the roughness on laminar boundary layers. Nonetheless P120 surface has resulted in a transitional interaction as it will be explained

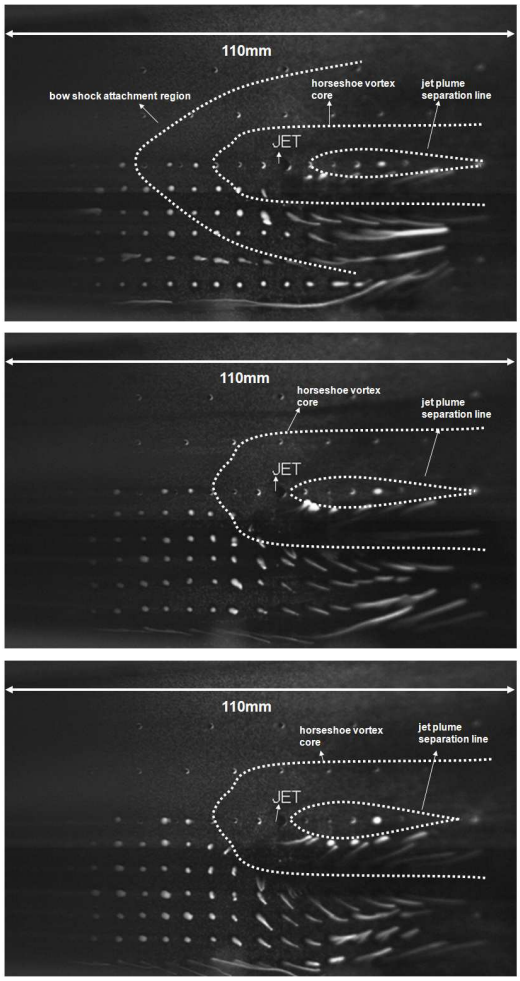

Figure 3.46: Oil dot visualisation of the sonic transverse Carbon Dioxide jet; top: test 13, middle: test 14, bottom: test 15.

the results of this Section 3.1.4. In the transitional interaction the pressure rise on the upstream separation regions due to the jet injection is not as gradual as in laminar separation as explained in Section 3.1.1. Transitional interactions have smaller upstream separation regions compared to laminar interactions and bigger upstream separation regions than the turbulent interactions. The leading edge of the flat plates are filed to have a minimal effect on the leading edge bluntness, nevertheless it is not possible to completely avoid bluntness effects although the effects are limited to the area around the leading edge. The spanwise averaged leading edge thickness is less than 0.1mm, with the roughest sand paper, i.e. P120, the averaged value of the leading edge thickness is found to be less than 0.7mm. The effect of bluntness delays transition according to the findings of Simeonides [93] for flat plates, hence the boundary layers developing on the

rough surfaces can be safely assumed laminar with the exception of P120.

Schlieren visualisation

Figures 3.47 to 3.49 show the long exposure ($250\mu sec$) schlieren images of the flowfield for the tests 16-18, 19-21 and tests 22-24. The flow structures mentioned in Section 3.1.1 are also observed: a leading edge shock due to viscous interaction at the leading edge following a laminar boundary layer growth up to the separation point accompanied by diversion in upward direction thereafter, separation shock that emanates around the separation point and intersects the jet induced bow shock and sonic jet barrel shocks with the Mach disc.

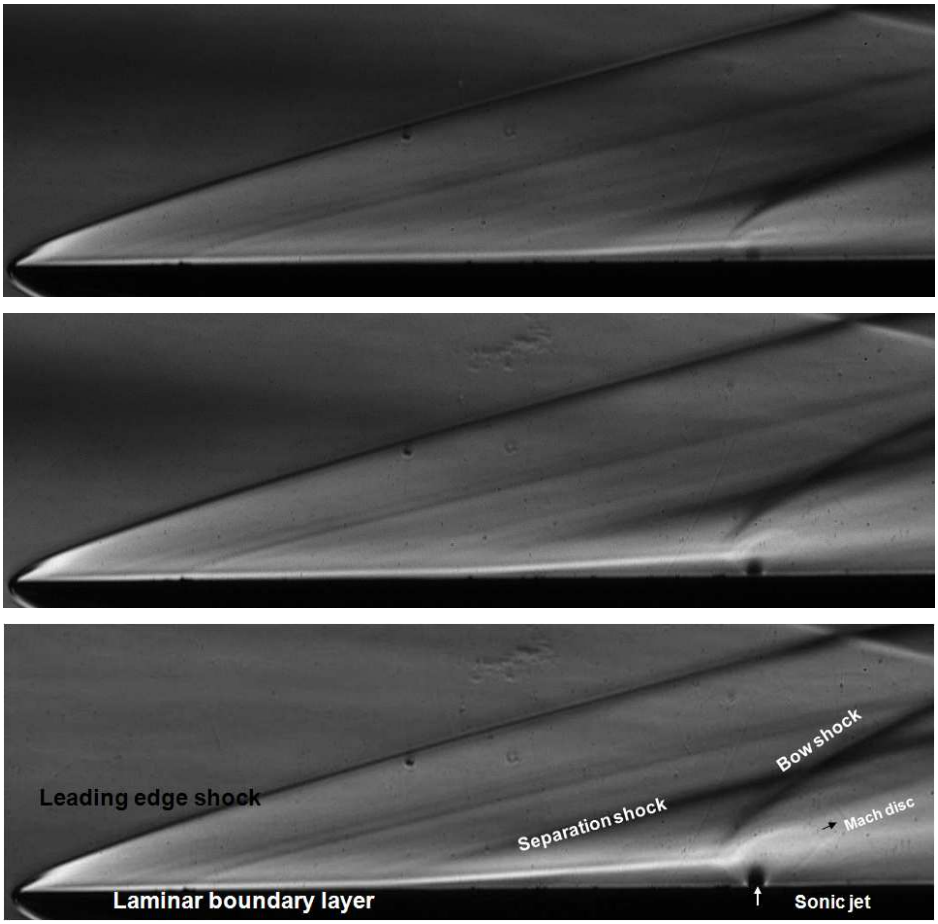

Figure 3.47: Schlieren visualisation of the flowfield in the presence of the sonic transverse jet with P1000 sand paper and three different momentum flux ratios; top: test 16, middle: test 17, bottom: test 18 with annotated flow structures with J values of 1.17, 2.78 and 5.25 respectively.

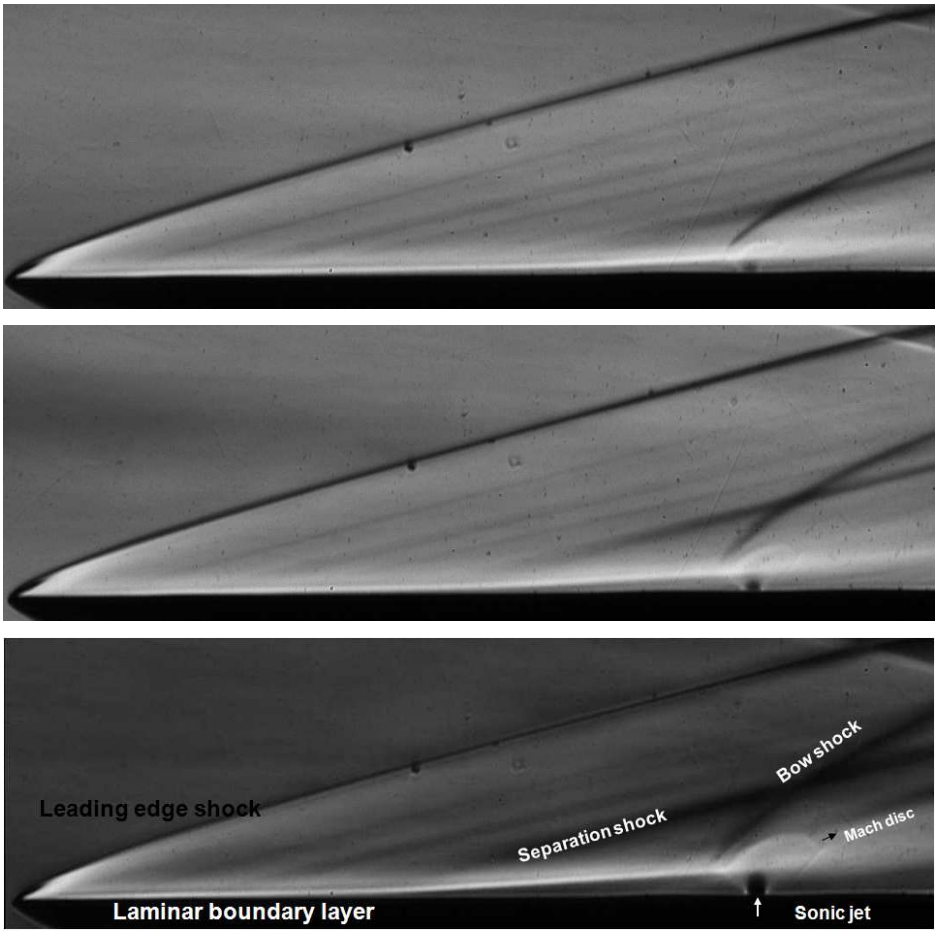

Figure 3.48: Schlieren visualisation of the flowfield in the presence of the sonic transverse jet with P400 sand paper and three different momentum flux ratios; top: test 19, middle: test 20, bottom: test 21 with annotated flow structures with J values of 1.19, 2.77 and 5.30 respectively.

As utilised in Section 3.1.1, the thickness of the boundary layer upstream of the separation region, Mach disc height and the separation length can be extracted from schlieren images using image processing. These values are tabulated in Table 3.6 with theoretical Mach disc height estimates mentioned in Section 3.1.1. The main influence of roughness on laminar/turbulent boundary layer is to dissipate the boundary layer via friction and to create momentum deficit. This, as also in the case of Reynolds number effect, results in a thicker boundary layer but with less full profile, which is also less resistant to adverse pressure gradients [56]. That is the reason for bigger separation regions for all rough tests. Mach waves coming from the rough surface and the tappings are apparent as well. For tests 22-24 the boundary layer developing on the plate is blurred even partially

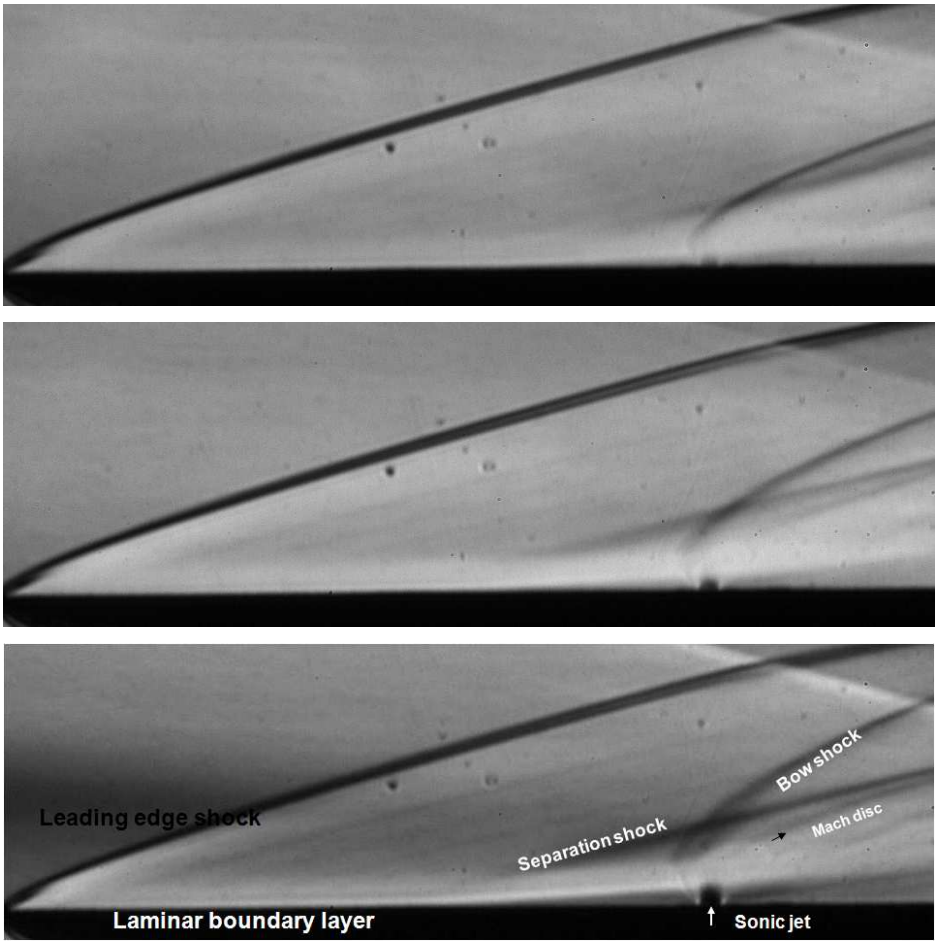

Figure 3.49: Schlieren visualisation of the flowfield in the presence of the sonic transverse jet with P120 sand paper and three different momentum flux ratios; top: test 22, middle: test 23, bottom: test 24 with annotated flow structures with J values of 1.20, 2.76 and 5.26 respectively.

masking the Mach disc whereas for tests 16-21 a bright line on the wall is clearly demonstrated. This is the first indication of transition. The boundary layer thickness just before the separation can not be deducted for tests 22-24 because of this blurring phenomenon. From the Table 3.6 it can be easily concluded that the Mach disc height is barely affected by the state of the incoming rough boundary layer, yet the separation region is heavily influenced by roughness. The agreement between the experimental and the theoretical Mach disc heights is good.

Mach disc height non-dimensionalised by jet diameter, h/d_{jet}, is plotted against momentum flux ratio, J in Fig. 3.50 (left) for all rough tests. These results are compared to baseline tests. The trends show that as the momentum flux ratio is

Table 3.6: Experimental boundary layer thicknesses (δ), Mach disc heights (h) and separation lengths (x_{sep}) for tests 16-24.

Test No	δ (mm)	h (mm)	h_{theo} (mm)	x_{sep} (mm)
16	2.0±0.1	4.2±0.15	4.1	22.9±0.3
17	1.7±0.1	6.3±0.15	6.3	38.3±0.3
18	1.4±0.1	8.3±0.15	8.7	51.9±0.3
19	2.0±0.1	4.3±0.15	4.1	27.2±0.3
20	1.8±0.1	6.2±0.15	6.3	37.0±0.3
21	1.6±0.1	8.3±0.15	8.7	53.1±0.3
22	-	4.4±0.15	4.1	17.3±0.3
23	-	6.2±0.15	6.3	28.4±0.3
24	-	8.5±0.15	8.7	37.3±0.3

increased higher penetration into the main crossing flow is observed as expected. The relation is nonlinear, roughly proportional with root square of J, which is deducted from power law fit applied accurately in addition to the one deducted from baseline tests and the resultant equation is shown in Fig. 3.50 (left). The general behaviour fits well on a power law fit with a square root dependence on J. This proves that the Mach disc height is only dependent on momentum flux ratio, upstream boundary layer has very little influence. In case of separation length, x_{sep}, against Mach disc height, h (Fig. 3.50 (right), the slope has increased from 3.5 to 6 by using a rough surface. However using a quite aggressive rough surface can trigger transition that can reduce the interaction area. The difference between P1000 and P400 surfaces is not discernible.

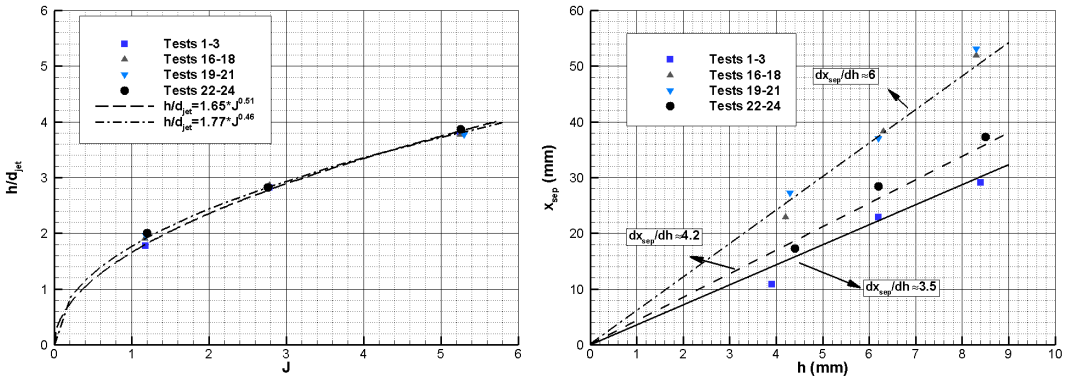

Figure 3.50: Left: Mach disc height non-dimensionalised by jet diameter versus momentum flux ratio; right: separation distance versus Mach disc height for tests 1-3 and tests 16-24.

Wall pressure measurements

Figures 3.51, 3.52 and 3.53 show non-dimensional wall pressure distributions, p/p_∞, against non dimensional distance, i.e $(x-x_{jet})/d_{jet}$, for different momentum flux ratios at centreline, z/d_{jet}=4.77 and z/d_{jet}=9.1 for tests 16-18, tests 19-21 and tests 22-24 respectively. The wall pressure along the flat plate is quite big at the leading edge due to viscous interaction and it gradually decreases to free stream value along the plate. This behaviour is also observed in experiments in fact the induced pressure rise due to viscous interaction is even more pronounced in the presence of roughness. After the gradual decrease wall pressure starts to increase from the point at which the flow separates, and then there is further rise to a pressure plateau. The pressure rise due to the injection does not become apparent until a $(x - x_{jet})/d_{jet}$ value of -27 for tests 18 and 21 and -22 for test 24, afterwards it rises gradually implying laminar separation except for tests 22-24, where the increase is constant without a plateau. The reason for that might be the transition phenomenon occurring before the jet induced separation. The pressure rise is followed by the peak at the upstream of the jet reaching nearly 3.4 for test 18 and 3.8 for tests 21 and 24. The influence of roughness is heavily felt on the extend of upstream separation region, the magnitude of the pressure peak and the extend of the downstream reattachment region as well as the laterally affected area. Spanwise pressure distribution is also augmented by roughness with values reaching up to 2.5 times free stream pressure for z/d_{jet} of 4.77 and up to 1.8 times free stream pressure for z/d_{jet} of 9.1 respectively which are considerably higher than baseline smooth case.

Figure 3.54 compares the sole effect of roughness with different surfaces on non dimensional pressure distribution at the centreline with increasing momentum flux ratio from top to bottom. Firstly in all these plots the differences between P1000 and P400 is hardly distinguishable as confirmed by Figures 3.51 and 3.52. Secondly rough surfaces experience longer separation regions and gradual pressure rises followed a plateau except P120. The pressure peak is magnified yet the downstream separation region is not significantly altered.

As a conclusion the magnitudes of the upstream pressure distributions and pressure peak are incremented by the presence of roughness. Hence the effectiveness of jet interaction is increased. P1000 and P400 are found to be favourable surfaces due to their ability to augment pressure distribution without significantly modifying the state of the upstream boundary layer. However one important fact

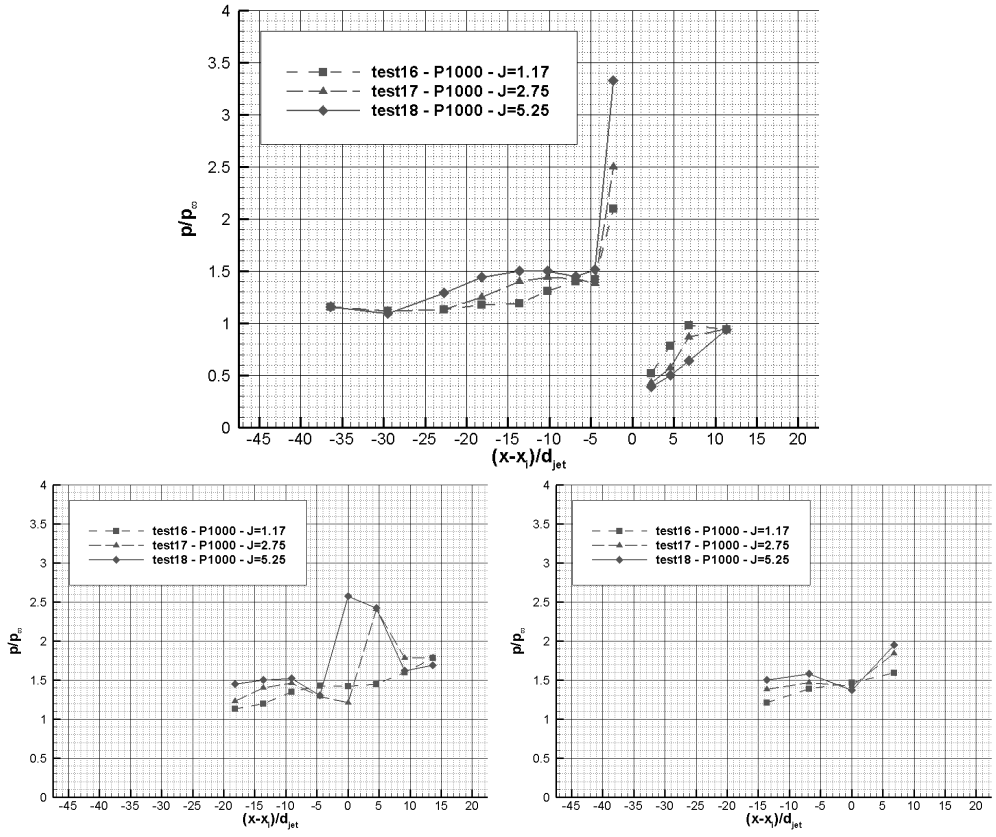

Figure 3.51: Non dimensional wall pressure distribution against non dimensional distance at the centreline (top), z/d_{jet}=4.77 (bottom left) and z/d_{jet}=9.1 (bottom right) for tests 16-18.

to be aware of is that roughness also augments the heat transfer rate. For the design of injection systems for hypersonic vehicles flying through harsh environments and subjecting to ablation, collective augmentation of pressure and heat transfer distribution has to be considered.

3.2 Numerical campaign

3.2.1 Spaid and Zukoski Case

Experimental data description for slot jet injection

In the experimental data set of Spaid and Zukoski [1], jet was injected through a converging slot of 0.2667mm wide across the spanwise direction at a station of 228.6mm from the leading edge of the plate. The injectant gases were N_2 and He. A series of free stream Mach and unit Reynolds numbers were tested such as 2.61

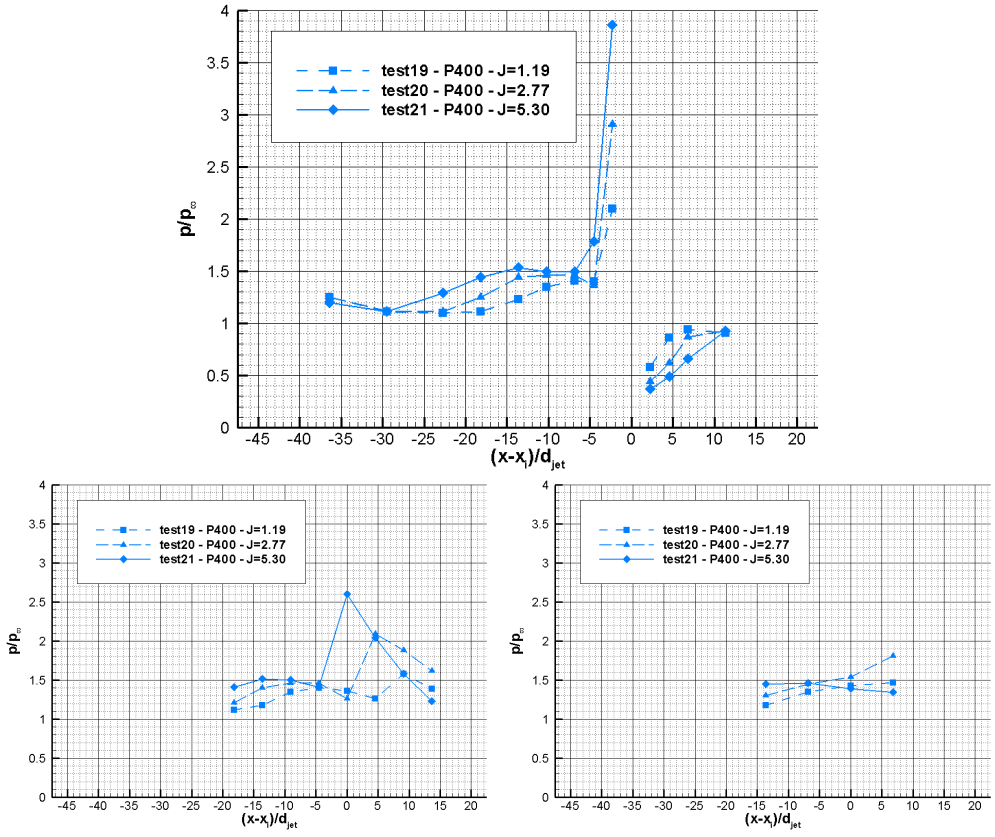

Figure 3.52: Non dimensional wall pressure distribution against non dimensional distance at the centreline (top), z/d_{jet}=4.77 (bottom left) and z/d_{jet}=9.1 (bottom right) for tests 19-21.

and 11.48×10^6 1/m, 3.5 and 13.12×10^6 1/m, 4.54 and 12.8×10^6 1/m respectively. The measured quantities were reservoir conditions for both free stream and the jet, and wall pressures on the flat plate. It is a commonly used test case for under expanded injection flows into supersonic cross flows due to its coverage of a wide range of jet to free stream pressure ratios (p_{jet}/p_∞) from 8.79 to 63.61 and jet to free stream momentum flux ratios from 0.72 to 6.77 in a well documented systematic way. Precaution was taken to ensure two dimensionality by the use of side plates, i.e. the leakage from the bottom of the flat plate to the top is prevented with this precaution; three dimensional complications were reported as separation region extends to the forward of side plates especially at highest Mach number case. Extensive amount of pressure tappings were used and nicely spread providing good spatial accuracy and gradually changing wall pressure plots. Boundary layer is tripped at the leading edge by a trip wire, but transition was reported to occur 50.8mm to 76.2mm from the leading edge by shadowgraph

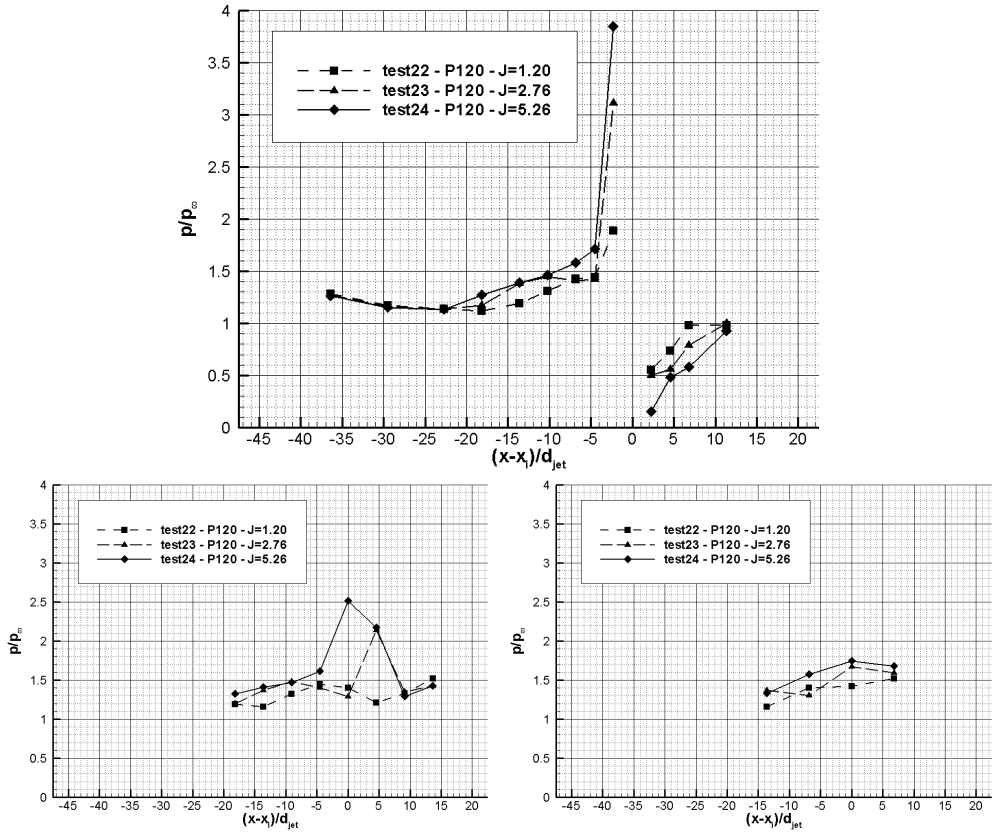

Figure 3.53: Non dimensional wall pressure distribution against non dimensional distance at the centreline (top), $z/djet$=4.77 (bottom left) and $z/djet$=9.1 (bottom right) for tests 22-24.

photography for M_∞ of 2.61 and 3.50. At M_∞ of 4.54 the interaction between jet and the cross flow was reported to be transitional based on wall pressure distribution and shadowgraph images; moreover the loss of two dimensionality was mentioned. Among different cases, following ones are chosen for comparison in this study as shown in Table 3.7. M_1 and p_1 are the upstream Mach number and pressure respectively just at the upstream of separated region outside of the boundary layer. Whereas p_2 is the plateau pressure at the downstream of separation shock, at the edge of shear layer. The data was presented in terms of p/p_1 against distance from the leading edge of the flat plate, not in terms of p/p_∞. The reason for that might have been the need to assess the jet interaction phenomenon with respect to undisturbed boundary layer flow developed on the flat plate rather than with respect to freestream conditions. One important thing to note is that p_1 is greater than p_∞ due to the leading edge shock wave which is associated with viscous interaction as explained in detail in Appendix A.

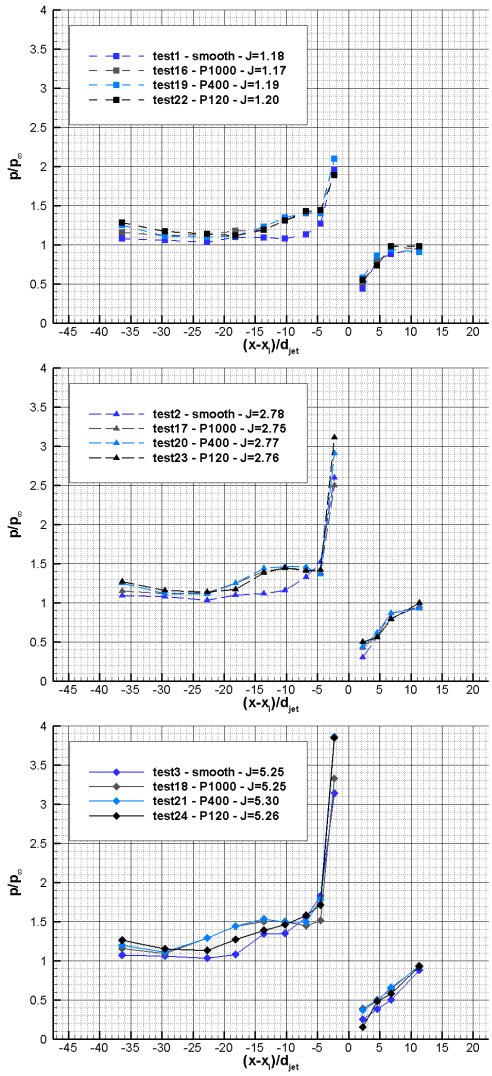

Figure 3.54: Non dimensional wall pressure distribution against non dimensional distance for different rough surfaces at the centreline with increasing momentum flux ratio from top to bottom.

Grid sensitivity and the effects of inlet and jet turbulence levels

Case 7 from Table 3.7 is selected as the test case (the one with highest p_{0jet}/p_1 ratio) to critically assess grid requirements and to study the effect of inlet and injection turbulence levels on results. For the incoming turbulent boundary layer developing on the flat plate at the upstream of the separated region; the definitions of boundary layer thickness, displacement and momentum thicknesses with the shape factor are expressed below, and computed using numerical integration. Their values are shown in Table 3.8. u_e and ρ_e are velocity and density at the

Table 3.7: Flow conditions by Spaid and Zukoski [1].

Case	$p_0(bar)$	$T_0(^0K)$	$p_{0_{jet}}(bar)$	$T_{0_{jet}}(^0K)$
1	1.34	318	1.59	298
2	1.32	318	3.00	294
3	1.33	318	5.73	291
4	2.40	309	0.52	292
5	2.41	311	1.02	293
6	2.41	313	1.94	293
7	2.41	314	3.80	292

for cases 1-3
$M_\infty = 2.61$ and Re/m=$11.48 \times 10^6(1/m)$
p_{0jet}/p_1=23.5, 44.5 and 82.9
J=1.87, 3.57 and 6.77

for cases 4-7
$M_\infty = 3.50$ and Re/m=$13.12 \times 10^6(1/m)$
p_{0jet}/p_1=16.55, 32.4, 61.3 and 120.2
J=0.72, 1.4, 2.65 and 5.19

boundary layer edge respectively. High H value clearly indicates separating flow.

$$\delta = y|_{u=0.99u_e} \tag{3.5}$$

$$\delta^* = \int_0^\delta \left(1 - \frac{\rho u}{\rho_e u_e}\right) dy \tag{3.6}$$

$$\theta = \int_0^\delta \frac{\rho}{\rho_e}\frac{u}{u_e}\left(1 - \frac{u}{u_e}\right) dy \tag{3.7}$$

$$H = \frac{\delta^*}{\theta} \tag{3.8}$$

Table 3.8: M_1 and p_1 values with boundary layer properties for Case 7.

M_1	$p_1(mbar)$	$\delta(mm)$	$\delta^*(mm)$	$\theta(mm)$	$H = \delta^*/\theta$
3.48	32.5	2.28	1.09	0.15	7.34

Figures 3.55 and 3.56 show the comparison of computed non-dimensional wall pressure distributions (p/p_1) with experimental data and the skin friction coefficient ($c_f = 2\tau_w/\rho_\infty u_\infty^2$) plots for five computational grids with moderate TI

level. The horizontal axis is non-dimensionalised by injection location, X_i. All grids captured upstream and downstream prominent flow features; the agreement with the experimental data is good. Nevertheless computations slightly overpredict the extent of upstream separation region and the downstream pressure well. From Figure 3.55 it can be observed that the difference between 482×190 and 482×260 is insignificant in terms of wall pressure distribution and skin friction coefficient. Only the coarse grid, 482×150, deviates from the solution with the finest grid in the upstream and downstream regions, thus number of grid points in y direction is selected as 190. In case of grid resolution in x direction, 397 grid points are enough to obtain a grid independent solution as shown from Fig. 3.56. Hence numerical solution turned out to be grid independent beyond a computational grid of 397×190. For this grid; wall y^+ values less than 0.5 for almost everywhere in the upstream and downstream regions and a maximum of 2.5 at upstream injection port vicinity are obtained as shown in Fig. 3.55 bottom plot; suggesting compatibility of this grid with a low Reynolds number turbulence model.

Figure 3.57 shows the comparison of computed non-dimensional wall pressure distribution with experimental data and the skin friction coefficient plot for four injection turbulence intensities with a computational grid of 397×190. Jet TI values of 0.5, 2.5 and 5% are tested with proposed κ and ω values of $100m^2/s^2$ and $5 \times 10^5 s^{-1}$ from Sriram and Mathew [46] respectively. It can be clearly deducted that the results are independent of the jet turbulence. Only small deviation in the downstream pressure hump is observed with TI of 0.5%. Therefore a TI of 2.5% is selected as the jet turbulence intensity.

Figure 3.58 shows the comparison of computed non-dimensional wall pressure distribution with experimental data and the skin friction coefficient plot for five inlet turbulence intensities with a computational grid of 397×190. There is not any discernible difference between different inlet turbulence levels in terms of wall pressure distribution, however transition location is found to be dependent on incoming flow turbulence. In the experimental data description, transition was reported to take place at 50.8mm to 76.2mm from the leading edge. Moderate turbulence levels such as 5% and 10% result quite early transition, whereas for 0.5% of TI transition occurs at 41.15mm and for 0.05% and 0.005% of TI it takes place at 55.37mm, compatible with experimental findings. Therefore a TI of 0.05% is selected as the inlet turbulence intensity.

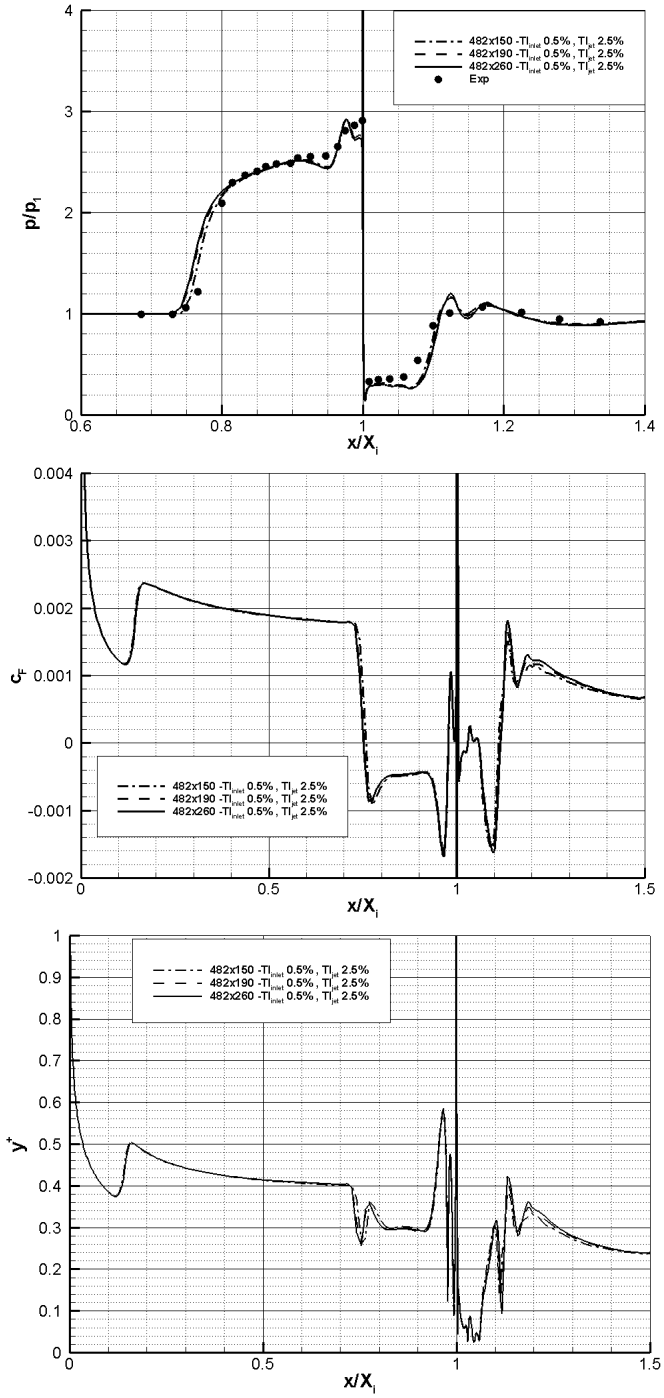

Figure 3.55: Non-dimensional pressure (top), skin friction coefficient (middle) and wall y^+ (bottom) distributions at the wall for successive grid refinement in y direction.

Finally a computational grid of 397×190 on a domain of $365.6mm \times 100mm$ with inlet TI of 0.05% and jet TI of 2.5% is adapted for the rest of the numerical

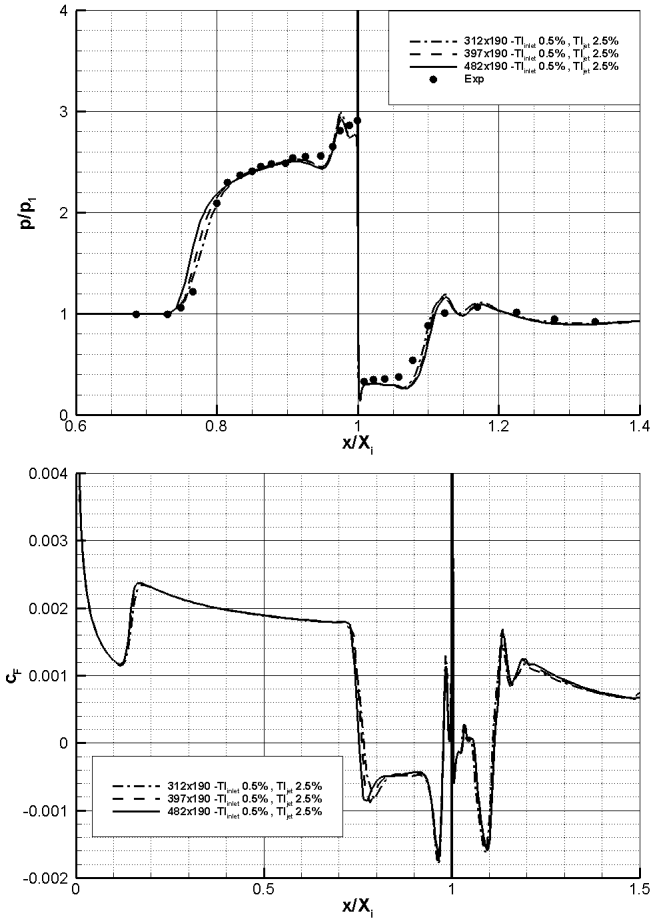

Figure 3.56: Non-dimensional pressure (top) and skin friction coefficient (bottom) distributions at the wall for successive grid refinement in x direction.

simulations. Figures 3.59 and 3.60 present Mach number contours and streamlines at the proximity of the injection location for case 7 with this grid and these turbulence intensity values. All the upstream and downstream circulation flow structures are resolved clearly. Mach disc is captured in detail as well. Incoming flow changes its direction and becomes parallel to the sonic surface on top of PUV and PDV via a separation shock. Then another change in direction occurs around above the Mach disc via a jet induced bow shock; streamlines become curved. Consequently incoming free stream moves over the injection plume. Finally curved streamlines that are passing over PDV and SDV are diverted parallel to the wall via a recompression shock at the downstream of PDV.

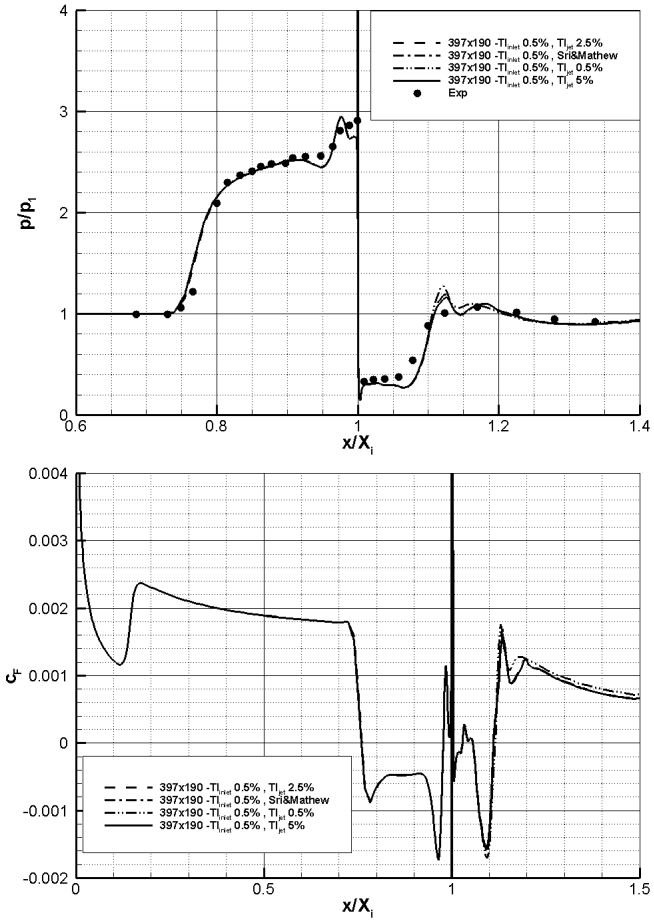

Figure 3.57: Non-dimensional pressure (top) and skin friction coefficient (bottom) distributions at the wall for different jet turbulence intensities.

Wall pressure distributions

Figures 3.61 and 3.62 represent the comparison of computed non-dimensional wall pressure distribution with experimental data of Spaid et al. [1] for cases 1-3 and cases 4-7. Computed non-dimensional wall pressure distributions show good agreement with experimental data in all cases for all pressure ratios on the contrary to findings from other authors referenced. The extents of the separation regions in cases 1-3 are estimated quite accurately and for cases 4-7 they are predicted within 5% error. The slope of the pressure rise before plateau is predicted very closely to the experimental values for cases 1-3 and within a small error margin for cases 4-7. The magnitude of the pressure spike (region 3) for all cases is found accurately. Although previous studies from Chenault and Beran [43], Sriram and Mathew [46] predicted steeper upstream pressure rises

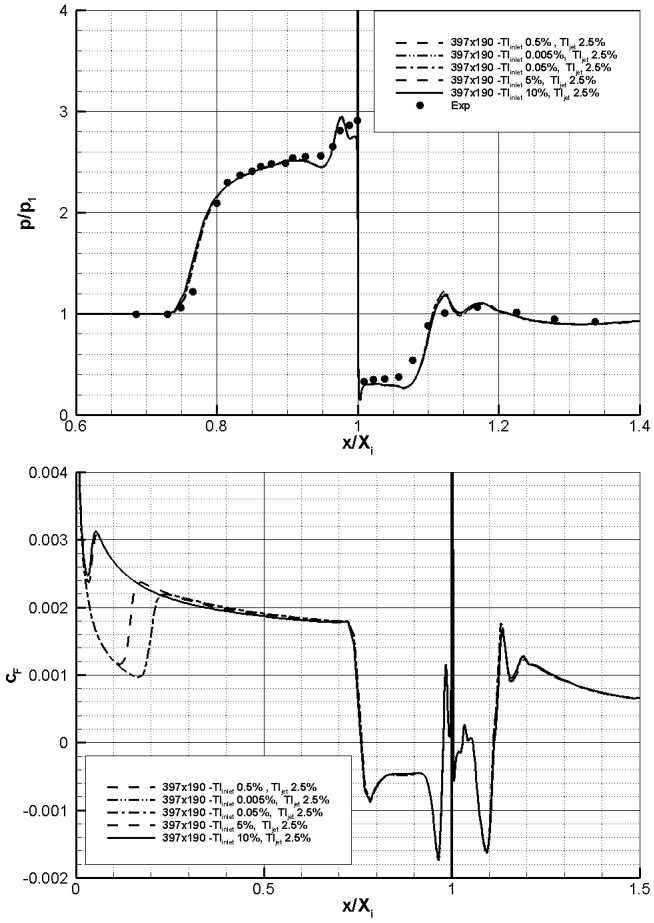

Figure 3.58: Non-dimensional pressure (top) and skin friction coefficient (bottom) distributions at the wall for different inlet turbulence intensities.

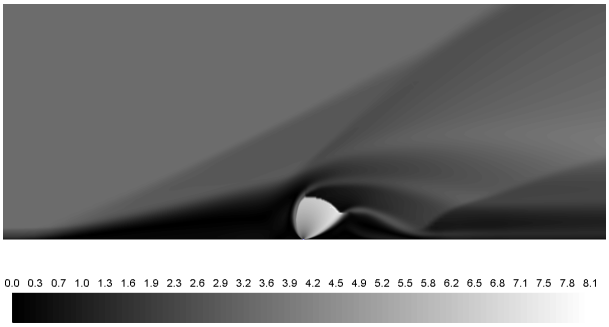

Figure 3.59: Mach number contours for case 7.

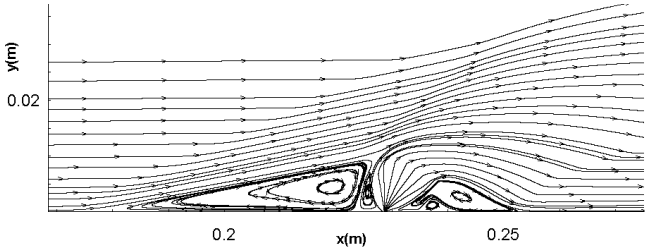

Figure 3.60: Streamlines around the jet injection port for case 7.

and more accurate separation lengths for cases 4-5, they significantly underpredicted pressure spike at especially high pressure ratios (cases 6-7). Nevertheless; the authors not only predict the upstream pressure rise, the separation length accurately for cases 1-3 and within good accuracy range for cases 4-7 but the magnitude of pressure spikes are very accurately estimated for all cases as well. At the downstream side the length of the pressure well (region 4) is predicted closely to the experimental results except for cases 3 and 7 (high pressure ratio cases) where there is a little discrepancy, which is acceptable. As expected, as the pressure ratio increases (thus J), transverse jets penetrates further into the main stream, upstream and downstream circulation regions extend further upstream and downstream respectively, the pressure plateau and subsequent pressure rise become clearer.

Skin friction coefficient distributions

Skin friction coefficient is plotted in Figures 3.63 and 3.64 that specify the extent of the upstream separation zones and the approximate location for transition to turbulence. Transition locations are found to comply fairly well with experimental findings.

For cases 1-3 laminar boundary layer undergoes transition about 21.72mm to

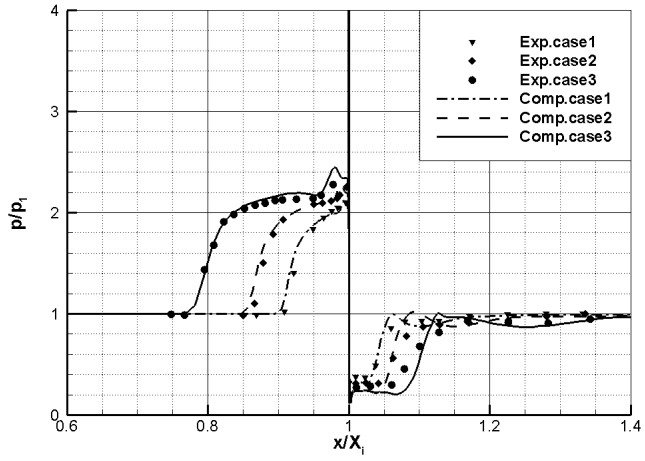

Figure 3.61: Comparison of non-dimensional wall pressure distributions for cases 1-3.

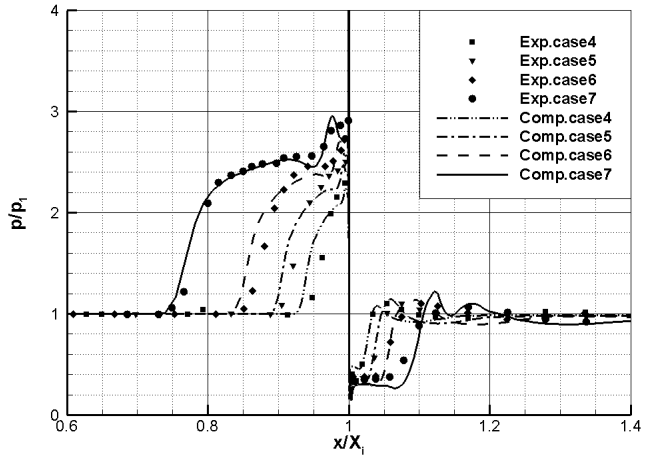

Figure 3.62: Comparison of non-dimensional wall pressure distributions for cases 4-7.

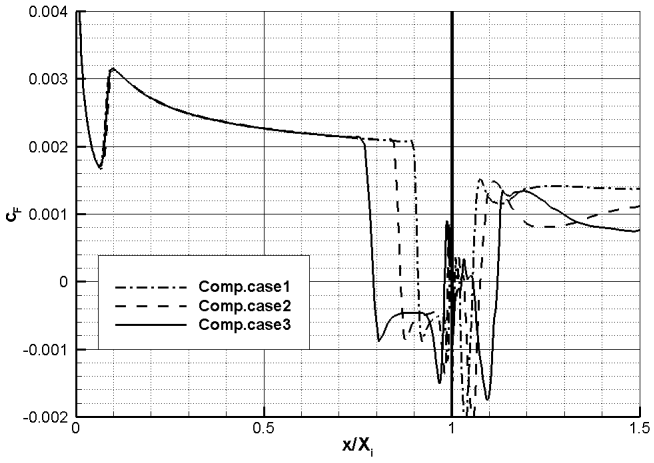

Figure 3.63: Skin friction coefficient distributions for cases 1-3.

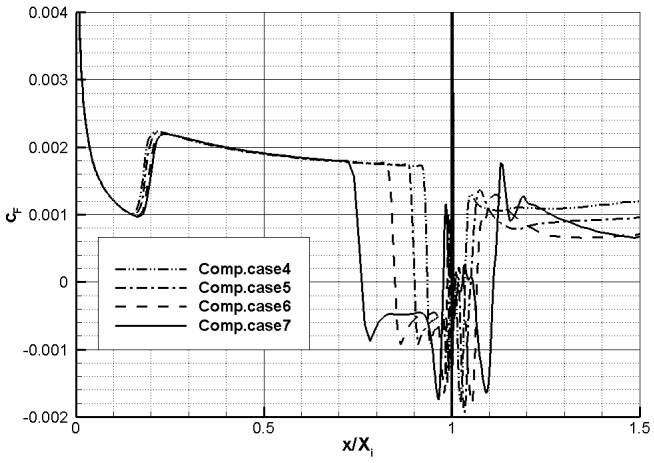

Figure 3.64: Skin friction coefficient distributions for cases 4-7.

23.77mm from the tip of the plate, which is underpredicted. Whereas for cases 4-7 it is found to be between 49.15mm and 55.32mm, which is well predicted. Considering the fact that experimental transition locations were determined using schlieren/ shadowgraph photography techniques, they inherently include uncertainty due to old film recording techniques, in addition the other factors such as bluntness, roughness, acoustic radiation from wind tunnel walls can significantly affect transition, which were not reported in data set. On the numerical side the uncertainty in turbulence modelling plays a major role in capturing transition as RANS/FANS models depend on the modelling of whole range of the scales of turbulence rather than resolving. Moreover they employ Boussinesq hypothesis that assumes eddy viscosity is an isotropic scalar quantity, which is not necessarily true for many flowfields involving secondary flows. Thus the simulated range of transition locations is acceptable.

Table 3.9 summarizes upstream flow conditions with Mach disc height or plume height, h, and transition and separation locations non-dimensionalised by injection location for all cases.

Jet penetration and separation region

For jet penetration; Mach disc height non-dimensionalised by undisturbed boundary layer thickness just at the upstream of separation region, h/δ, is plotted against momentum flux ratio, J for all cases in Figure 3.65. Almost perfectly linear fits are applied and equations with R^2 values (a measure of how good the fit is; 1 for perfect fit), are shown. h/δ is particularly important in scramjet

Table 3.9: Upstream flow conditions, Mach disc height and non-dimensional transition locations and separation lengths.

Case	M_1	$p_1(mbar)$	$\delta(mm)$	$h(mm)$	$\frac{x_{tr}}{X_i}$	$\frac{x_{sep}}{X_i}$
1	2.6	67.09	2.91	3.30	0.095	0.089
2	2.6	66.29	2.76	5.90	0.099	0.136
3	2.6	66.88	2.51	10.0	0.104	0.209
4	3.48	32.35	2.91	1.93	0.215	0.065
5	3.48	32.44	2.76	3.50	0.224	0.99
6	3.48	32.47	2.55	5.90	0.233	0.15
7	3.48	32.50	2.28	10.0	0.242	0.239

applications as it represents the ability of fuel to penetrate over the boundary layer and mix with denser air rather high temperature low density flow near the wall. The trends show that as the momentum flux ratio is increased higher penetration into the main crossing flow is observed. For the same J value, cases 4-7 ($M_1 = 3.48$) provide deeper penetration compared to cases 1-3 ($M_1 = 2.6$). This can be explained by the increased jet pressure ratio to have the same J value.

In case of the extent of separation region; separation location, x_{sep}, is plotted against Mach disc height in Fig. 3.66 for all cases. Perfectly linear fits are again applied with equations and R^2 values. Separation location is found to be a linear function of plume height and as the jet pressure ratio is increased separation region extended upstream, which is observed naturally in the experiments as well. The slope of the fits are 4.93 and 4.09 for $M_1 = 3.48$ and $M_1 = 2.6$ respectively. Spaid and Zukoski [1] observed the separation region being around four times the plume height in their experiments. Therefore above findings are also compatible with experimental observations.

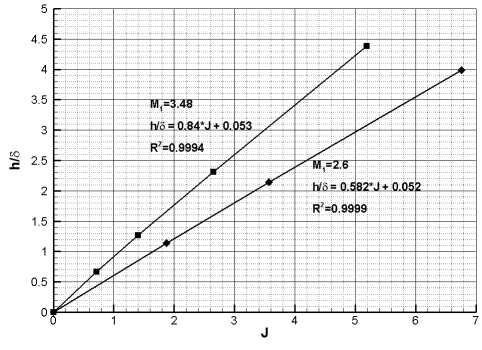

Figure 3.65: Mach disc height non-dimensionalised by undisturbed boundary layer thickness versus momentum flux ratio.

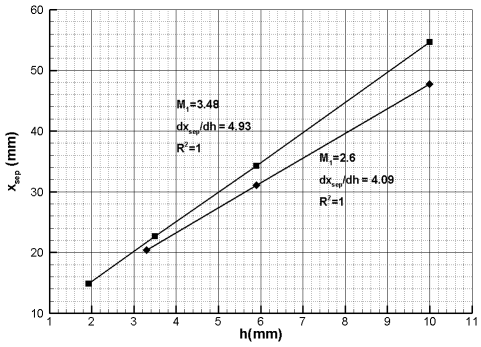

Figure 3.66: Separation location versus Mach disc height.

Present investigation aimed mainly to validate the numerical solver and gain confidence in numerical procedure with the data set of Spaid and Zukoski [1] for a wide range of pressure ratios including capturing transition locations and to study the effect of incoming flow and jet turbulence levels on jet interaction phenomenon. This set of experiments is of greater value because of good spatial resolution around the injection port. Sidewalls ensured two dimensionality and the cases where three dimensional effects started to appear were clearly documented. Computed non-dimensional wall pressure distributions showed very good agreement with experimental data for cases 1-3 and good agreement for cases 4-7. In addition transition locations were captured with acceptable accuracy. The results are found to be insensitive to jet turbulence intensity however transition location is strongly influenced by inlet turbulent intensity. $\kappa - \omega$ SST model provided quite accurate results over a wide range of pressure ratios for such a complex flow field.

3.2.2 Three dimensional case

Steady axisymmetric turbulent simulations with $\kappa - \omega$ SST model with compressibility and transition corrections for the transverse injection on a flat plate for tests 3 (see Table 3.1) are carried out.

Computational domain and boundary conditions

The computational domain is simply formed by rectangular block with adiabatic wall on the bottom surface with a small injection orifice, left inlet boundary, right outlet boundary, top and side farfield walls. Only half of the flat plate is modelled

utilising symmetry at the centreline plane as shown in Fig. 3.67. The domain has the size of 160mm×40mm×35mm.

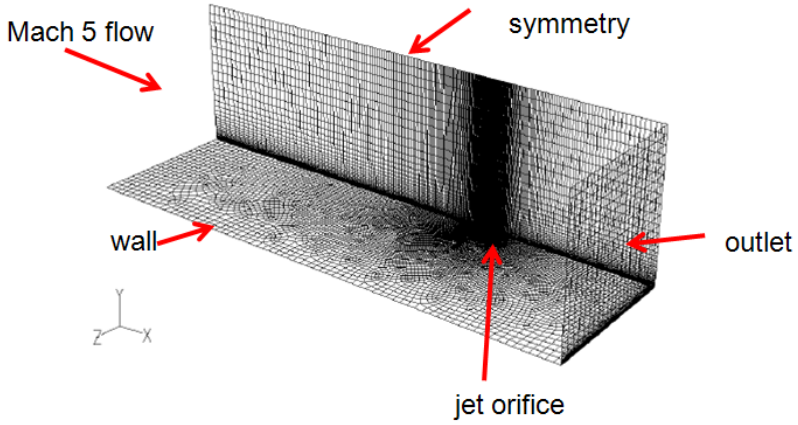

Figure 3.67: Computational domain and mesh for transverse injection on a flat plate.

In case of boundary conditions at the far-field boundary, Mach number and free stream conditions (p_∞ and T_∞) are specified together (see Section 2.3). Turbulence intensity value of 0.1 and a turbulent viscosity ratio, (μ_t/μ), of 1 are chosen for simulations. Air is assumed to be a thermally and calorically perfect gas; Sutherlands law of viscosity is employed. For the jet, sonic conditions are simply prescribed. TI value of 5% and a hydraulic diameter (d_h) is assigned to the radius of the jet orifice.

Grid sensitivity analysis

Grid sensitivity analysis is conducted for test 3 condition; three different computational meshes at different resolutions are created using the multi-block grid strategy. The domain is divided into blocks and in each block, grid points are clustered towards the regions of high gradients. The continuity between the blocks is ensured. The wall computational grid is created with unstructured quadrilateral pave elements and these elements are extruded in wall normal direction to create the volume mesh. Table 3.10 shows the relevant parameters for each computational grid such as the number of mesh points at the wall and at the wall normal and y^+ range. The values of the normal spacing have been chosen to ensure that the separation regions are captured accurately as close to experiments.

Figure 3.68 shows the computed non-dimensional wall pressure distributions,

Table 3.10: Computational grid parameters.

Grid Name	# mesh points wall	# mesh points normal	y^+ range
Coarse	8435	66	0.08-3.5
Medium	10479	79	0.02-1.7
Fine	11973	85	0.008-0.7

p/p_∞, (top) with the axial skin friction coefficient c_f plot (bottom) for three computational grids. The results are compared with the experiments. The agreement in the upstream and downstream separation regions is found to be fairly good. CFD is overestimating the pressure plateau. In terms of upstream separation region CFD results 36mm whereas experiments result around 29mm as deducted from skin friction plots. The oscillations especially in the skin friction coefficient plot might come from the fact that there are two upstream separation regions in between which flow reattaches and separates afterwards as well as the instabilities in the numerical scheme causing wiggles even though a limiter is applied as mentioned in Section 2.6.

Medium computational grid of 10479×79 is chosen as the grid adapted for the rest of the numerical simulations. Figure 3.69 presents Mach number and density gradient contours at the centreline. All the upstream and downstream circulation flow structures are resolved clearly. Mach disc is captured in detail as well. Incoming flow changes its direction due to the presence of PUV and PDV via a separation shock. Then another change in direction occurs around above the Mach disc via a jet induced bow shock. Consequently incoming free stream moves over the injection plume. Finally main flow that is passing over PDV and SDV are diverted parallel to the wall via a recompression shock at the downstream of PDV.

Figure 3.70 shows the comparison the density gradient in vertical direction, y, with the experimental schlieren image focused at the jet surroundings. The agreement between numerical simulations and experiments is found to be good.

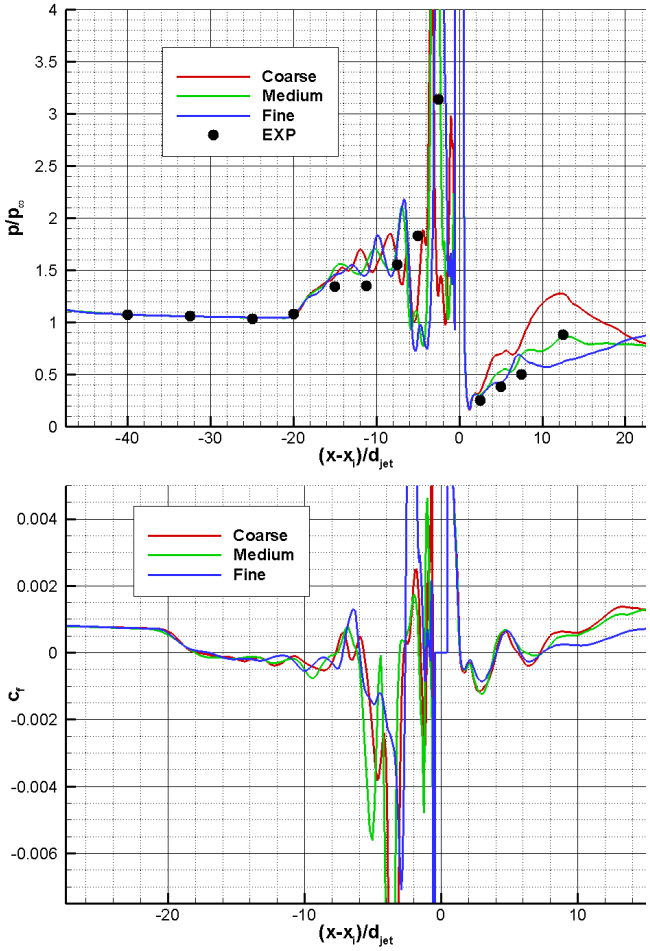

Figure 3.68: Non-dimensional pressure (top) and skin friction coefficient (bottom) distributions at the centreline for successive grid refinement.

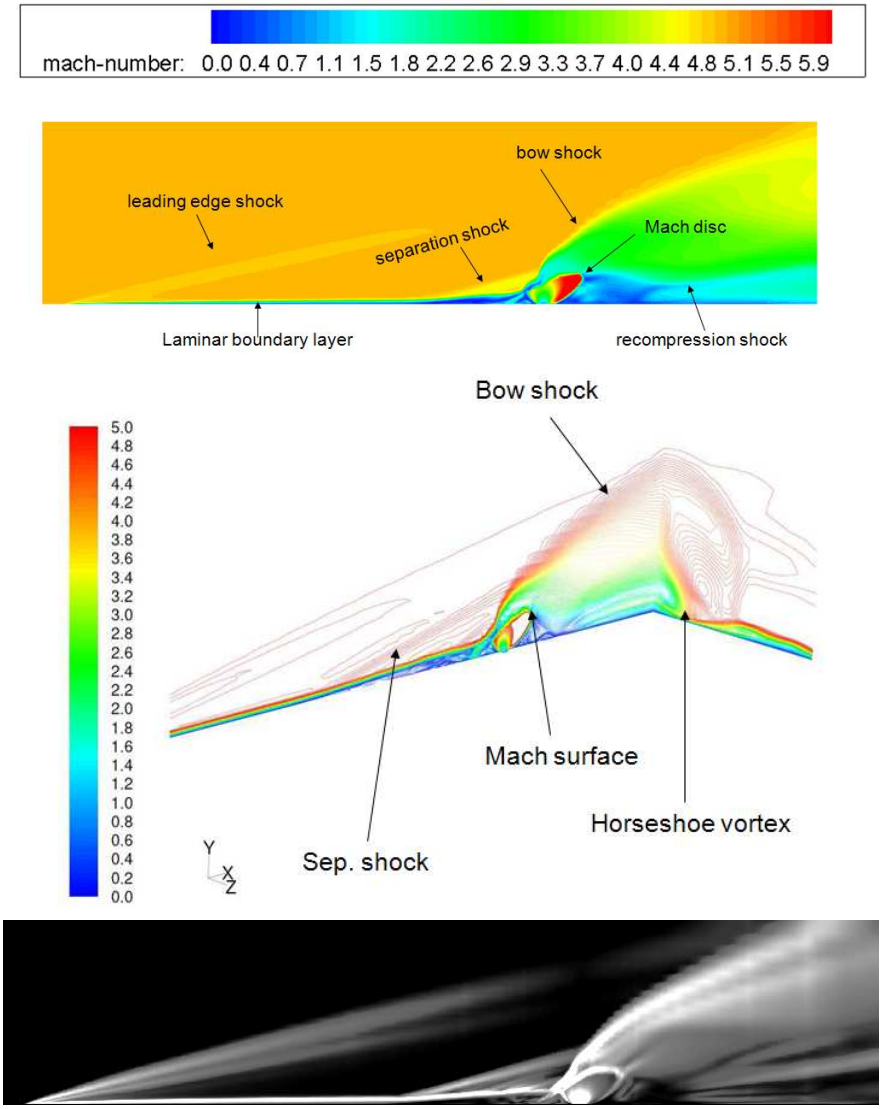

Figure 3.69: Computed Mach number contours on the centreline (top), isometric view of Mach number contours (middle) and density gradient contours in vertical direction, $\partial\rho/\partial y$, on the centreline (bottom) for medium grid.

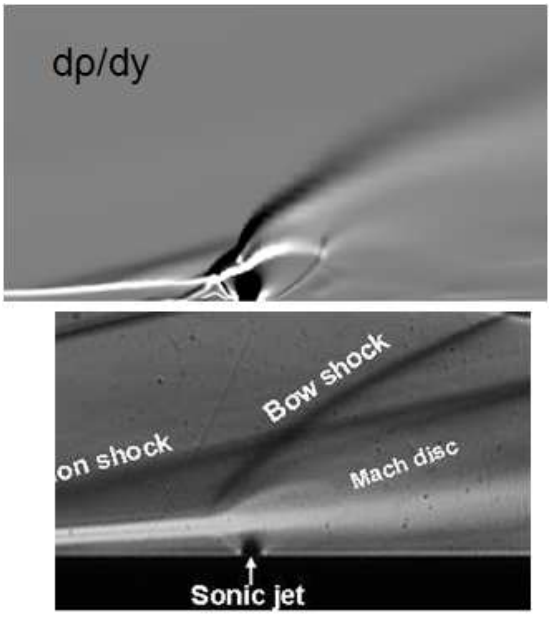

Figure 3.70: Computed density gradient contours in vertical direction, $\partial\rho/\partial y$, (top) and experimental schlieren image (bottom).

Chapter 4

Energy Deposition Studies

In this chapter the results of the energy deposition campaign are presented; firstly baseline tests are conducted to map and understand the flow field over the cone-cylinder models at Mach 5. The tests include conventional/high speed schlieren photography, oil dot visualisation and force measurements; and the results are compared to CFD results and theoretical estimates to build confidence on the campaign. Secondly tests addressing the effect of energy deposition via arc discharge are presented. The electrodes are placed in front of truncated models and the aerodynamic interference is assessed and tried to be minimised without the arc discharge. Then the electric arc is steadily discharged and localised at different distances from the models. Discharge-on cases are compared to discharge-off to evaluate the net effect of small amount energy deposition on drag reduction. The diagnostics include high speed schlieren photography and visual observations as well as force measurements. Finally a brief campaign examining the effect of pulsed laser deposition on blunt body drag reduction is carried out using only high speed schlieren photography .

4.1 Baseline tests

4.1.1 Experimental test campaign

Conventional/high speed schlieren photography

The flowfield pictures are shown in Figures 4.1 and 4.2 for cone-cylinder and 4.2 respectively for cone-cylinder-flare models. These pictures are the representative figures of steady flowfields (with long exposure times of $250\mu sec$) during a test

run. The prominent flow structures such as oblique or bow shock waves at the front of the models with expansion fans at the second shoulder can be easily seen for the sharp cone-cylinder model. Truncated cone-cylinder models also include additional expansion fans emerging on the first shoulder before the small separation region due to the severe flow diversion of 75.5 degrees (buried inside the expansion fan however clearly observed in CFD). The boundary layer developing on straight segments is very thin and can be hardly seen before it forms the shear layer and the wake. The angle of the conical shock for cone-cylinder model is 19.8° with 14° cone half angle and 19.1° for flared model with 14° cone half angle. Both are matching the conical flow theory very well, which are deducted from tables in NACA Report 1135 [100] as 20° and 19.2° respectively. The bow shock stand-off distance is found as 0.275 d_t from experiments and 0.28 d_t from Ref. [101] in shock wave detachment distance for plane and axisymmetric flow plot for Mach 5. Thus these are further cross-checks of HSST calibration proving Mach 5 flow.

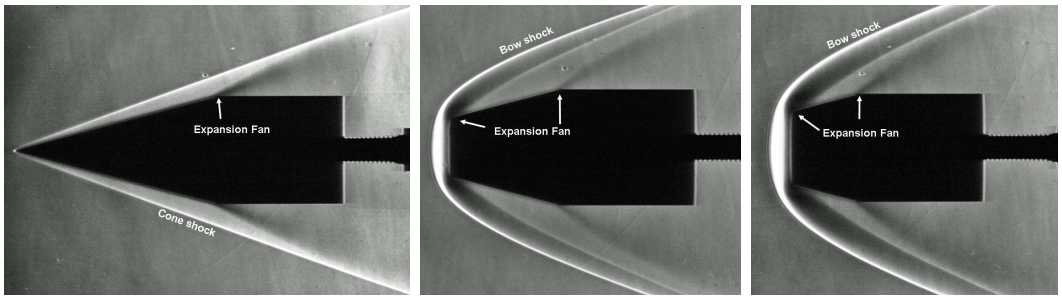

Figure 4.1: Schlieren visualisation of cone-cylinder models, left: no truncation, middle: $d_t/d_b = 0.5$, right: $d_t/d_b = 0.75$.

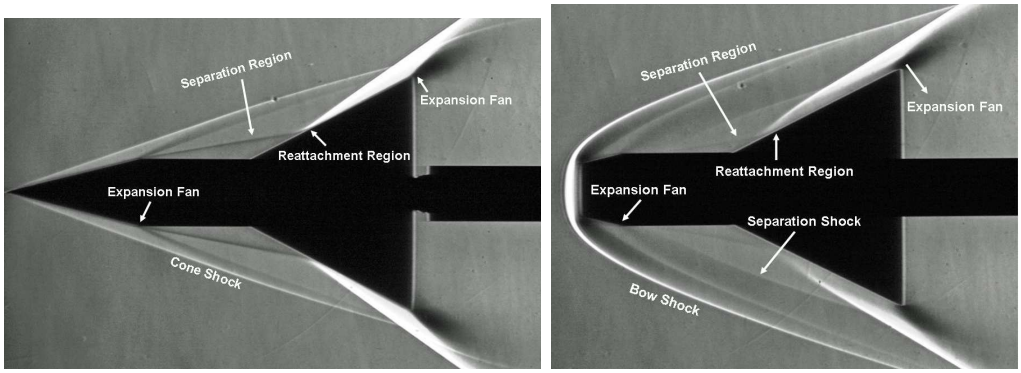

Figure 4.2: Schlieren visualisation of cone-cylinder models with flare, left: no truncation, right: $(d_t/d_b = 0.75)$

.

In case of cone-cylinder models with flare, additional flow patterns appear such as shock wave laminar boundary layer interaction leading to separation around the corner just before the flare. The adverse pressure gradient due to the compression corner causes the upstream laminar boundary layer to separate and to form a circulation region over the straight segment and the flare as a bridging mechanism. Consequent separation shock on the straight segment on the flare is evident. A separated free-shear layer impinges on the ramp, reattaching and turning through a recompression shock wave system. Flow separation impinging on the flap surface is a highly disturbing process which may cause transition of the free shear layer [102]. The schematic of this compression corner interaction is shown schematically in Fig. 4.3 (top left). It is also shown by Simeonides and Haase [103] for laminar compression corner flows as it is shown schematically in Fig. 4.3 (top right) and observed by Yang et al. [104] with Pressure Sensitive Paints (PSP) for the truncated model as shown in Fig. 4.3 (bottom). The necking region formed due the high pressure exerted at the reattachment location, is believed to be a transition mechanism as the subsequent streaks formed on the flare indicate Goertler vortices and these vortices amplify disturbances in the boundary layer promoting transition. The size of separation region is affected by the magnitude of the adverse pressure gradient (closely related to the ramp angle), bluntness, state of the boundary layer, surface roughness, surface temperature and incoming turbulent intensity [102]. The circulation region is more apparent and bigger in size for the sharp model compared to truncated model, in fact it starts from the shoulder and extends over the flare. The separation length, x_{sep} is 23mm and 12.7mm; and the reattachment length, $x_{reattach}$ is 11.8mm and 5.9mm for the sharp and truncated models respectively. These values are measured from the corner with an uncertainty of $\pm$0.25mm. Finally at the end of the flare, an expansion fan is followed by the wake for both models.

Conventional schlieren images with long exposure time (250μsec) only provide averaged flowfields whereas high speed imaging reveals the unsteadiness present in the flowfield owing to the unsteady nature of the laminar boundary layer shock wave interaction as shown in Figures 4.4 and 4.6. Only ten images are shown for each case due to size restrictions, and the final ones for ach case are annotated in Figures 4.5 and 4.7 .

RMS of the fluctuations in the light intensity based on 100 schlieren images are shown in Fig. 4.8 for both models indicating the locations of unsteadiness due

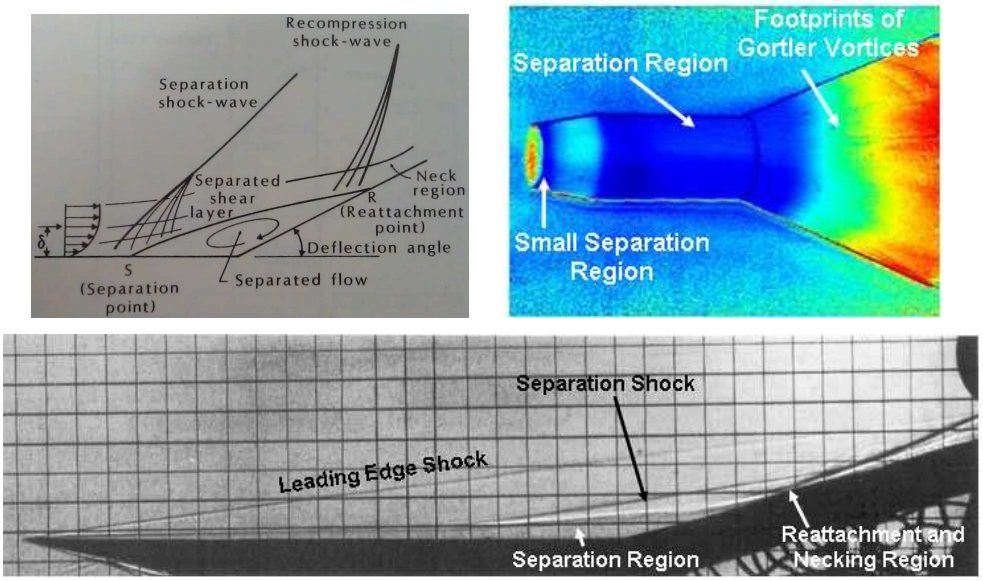

Figure 4.3: Top left: Schematic of a separated-flow pattern for a shock wave boundary layer interaction at a ramp by Bertin [102], top right: PSP visualisation of a truncated cone-cylinder model with flare by Yang et al. [104], bottom: schlieren visualisation of a compression corner in hypersonic flow by Simeonides and Haase [103].

to the forward-backward motion of the reattachment. High levels unsteadiness (bright regions) is observed around the reattachment region as expected.

Oil dot visualisation

Figure 4.9 shows the oil dot visualisation over flared models; around the corner region the oil dot movement is small whereas on the flare they extend considerably due to higher levels of shear. For the sharp model whole straight segment experiences elongated streaks just upstream of the corner where oil deposits and forms a clear line. This line corresponds to a smaller circulation region that is not observed in schlieren images but in CFD discussed in Section 4.1.2. In case of the truncated model oil streaks decrease in length along the straight segment and they start moving upstream at the upstream of the corner.

Force measurements

The drag measurements using 3-component force balance are conducted and the time histories are shown in Fig. 4.10. It can be easily observed from the Fig. 4.10 that there is a direct correlation between the signal of a pitot probe inside the test section (see Section 2.3) and the drag signal measured by the force balance.

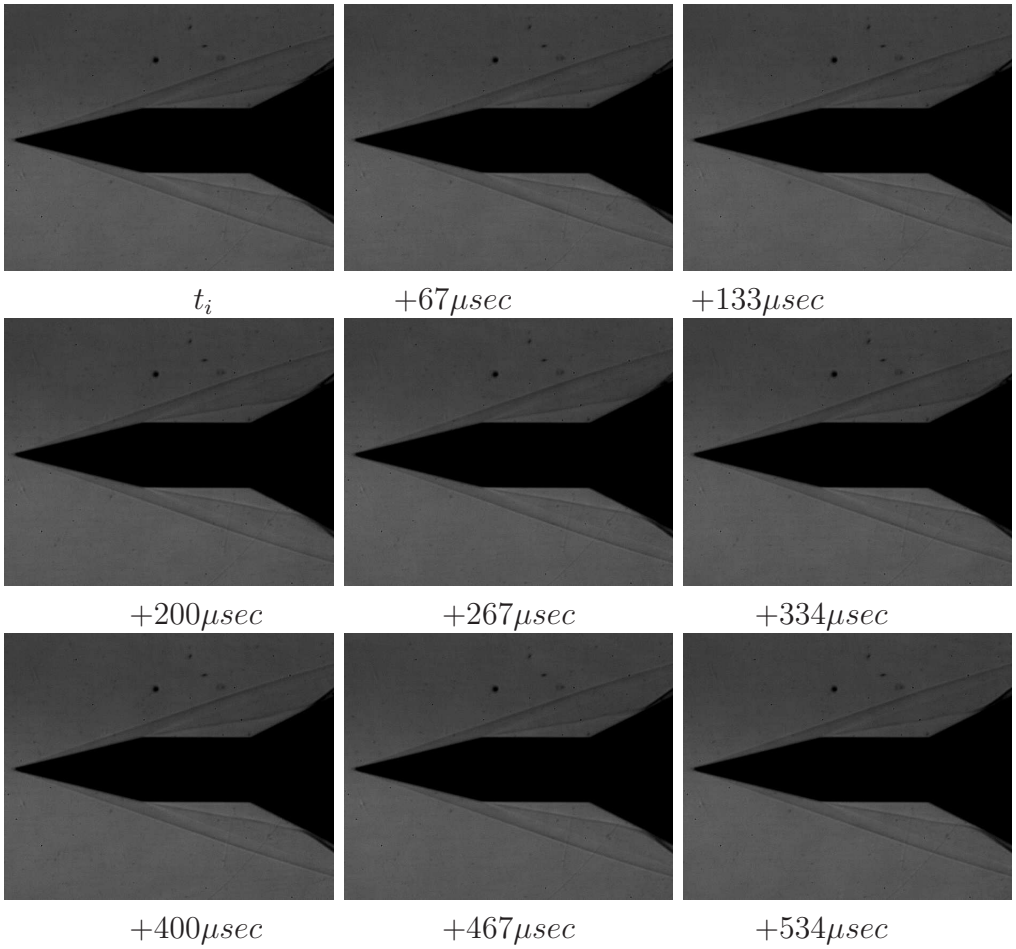

Figure 4.4: High speed schlieren visualisation of cone-cylinder model with flare captured at 15000fps with 4μsec exposure time.

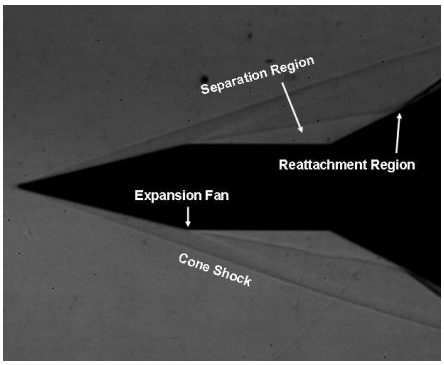

Figure 4.5: High speed schlieren visualisation of cone-cylinder model with flare captured at 15000fps with 4μsec exposure time, annotated flow structures.

Initial normal shock wave that is travelling downstream at the start of the tunnel is projected by an early spike in the drag history and then a continuous rise to a

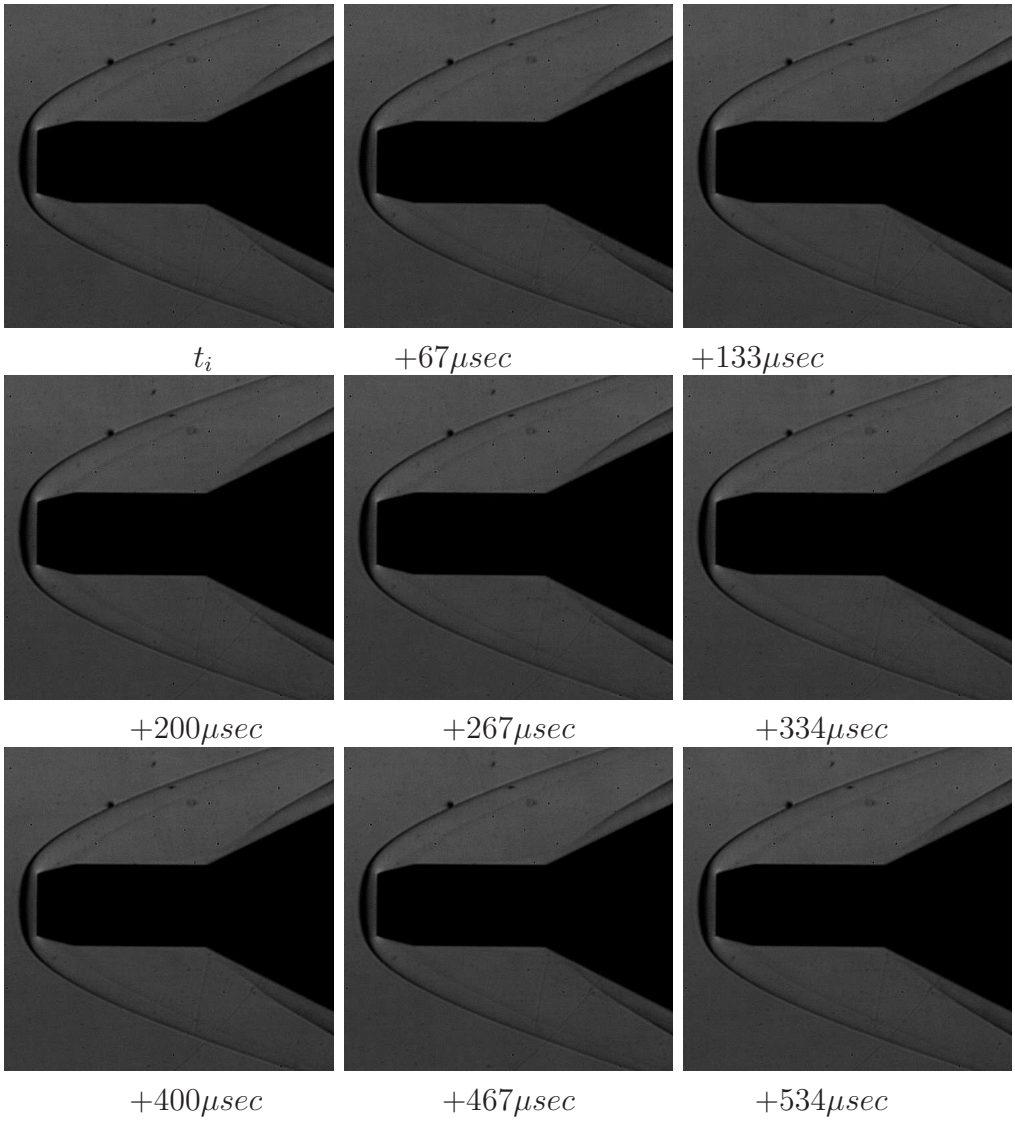

Figure 4.6: High speed schlieren visualisation of truncated cone-cylinder model with flare captured at 15000fps with 4μsec exposure time.

steady plateau is followed after a small dip. From thereon steady flow conditions are sustained for certain amount of time and terminated by the shutting valve which results in an upstream travelling normal shock wave. Simple time averaging is applied over the period of steady flow to get drag force values as shown in Eqn. 4.1. These values are tabulated at Table 4.2.

$$\overline{D} = \frac{1}{t_f - t_i} \int_{t_i}^{t_f} D(t)dt \tag{4.1}$$

Additionally analytical estimates using Newtonian theory are utilised. For

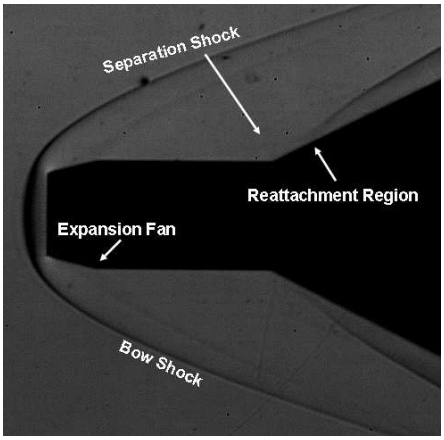

Figure 4.7: High speed schlieren visualisation of truncated cone-cylinder model with flare captured at 15000fps with 4μsec exposure time, annotated flow structures.

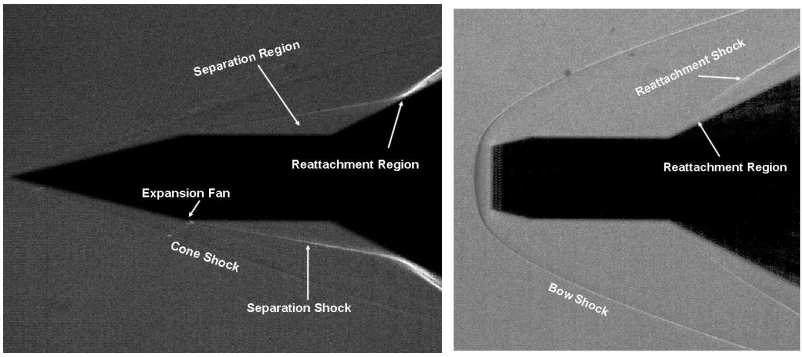

Figure 4.8: RMS of 100 schlieren images of cone-cylinder models with flare, left: no truncation, right: $(d_t/d_b = 0.75)$; white regions indicate higher rms levels.

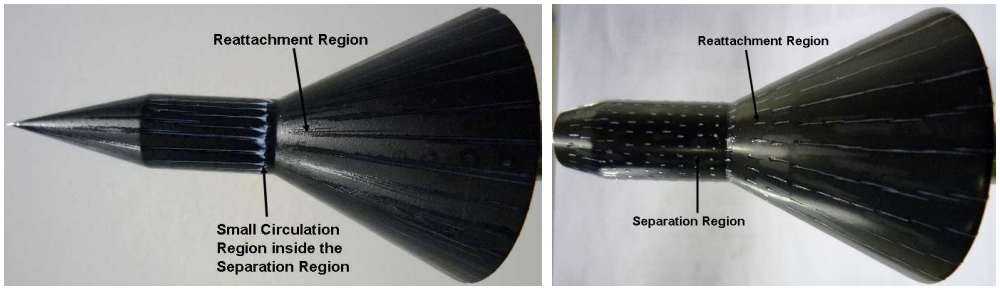

Figure 4.9: Oil dot visualisation of cone-cylinder models with flare, left: no truncation, right: $(d_t/d_b = 0.75)$

.

the cone-cylinder models, only the front and the shoulder regions are taken into account, naturally omitting the contributions from straight and base sections. For the cone-cylinder models with flare, the contribution of the flare is irrespective of the flowfield developing after the shoulder. As a matter of fact the pressure

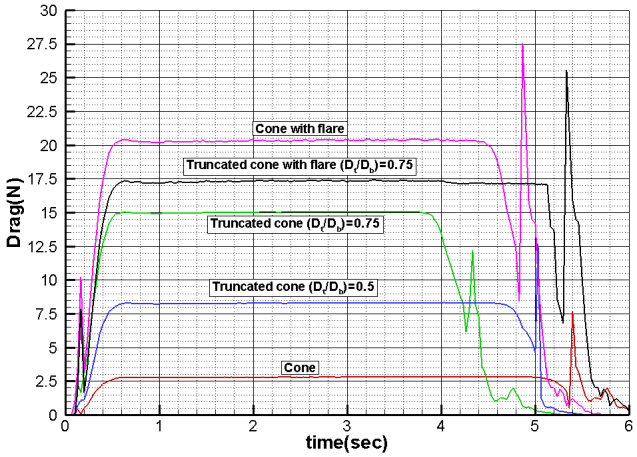

Figure 4.10: Drag force histories of all models during the test runs.

coefficient, c_p, solely depends on the local inclination angle, θ for Newtonian theory and θ, γ and M_∞ for modified Newtonian theory (see below) [102] and the drag force is the integrated effect of the pressure distribution. The values are tabulated at Table 4.2 as well.

$$c_p = 2sin^2\theta \qquad c_p = c_{p_{max}} sin^2\theta$$

where

$$c_{p_{max}} = \frac{2}{\gamma M_\infty^2}\left\{\left[\frac{(\gamma+1)^2 M_\infty^2}{4\gamma M_\infty^2 - 2(\gamma-1)}\right]^{\gamma/(\gamma-1)}\left[\frac{1-\gamma+2\gamma M_\infty^2}{\gamma+1}\right] - 1\right\}$$

4.1.2 Numerical simulations

Steady axisymmetric laminar simulations for the cone-cylinder models and turbulent simulations with $\kappa - \omega$ SST model with compressibility and transition corrections for the cone-cylinder models with flare are carried out.

Computational grid and boundary conditions

The computational domain is formed by a quarter circle followed by a straight line as farfield boundary, straight line at the right boundary as outlet, solid walls on the models and an axis at the bottom as shown in Fig. 4.11. For the computational grid, a multi block structured grid approach is adopted; the domain is divided into blocks and in each block, grid points are clustered towards

the regions of high gradients as shown in Fig. 4.11. The continuity between the blocks is ensured. The same meshing strategy is utilised for the other models as well.

In case of boundary conditions at the far-field boundary, Mach number and free stream conditions (p_∞ and T_∞) are specified together (see Section 2.3). Turbulence intensity values of 0.05, 0.1 and 0.5% are tested with a turbulent viscosity ratio, (μ_t/μ), of 1 for turbulent simulations. Air is assumed to be a thermally and calorically perfect gas; Sutherlands law of viscosity is employed.

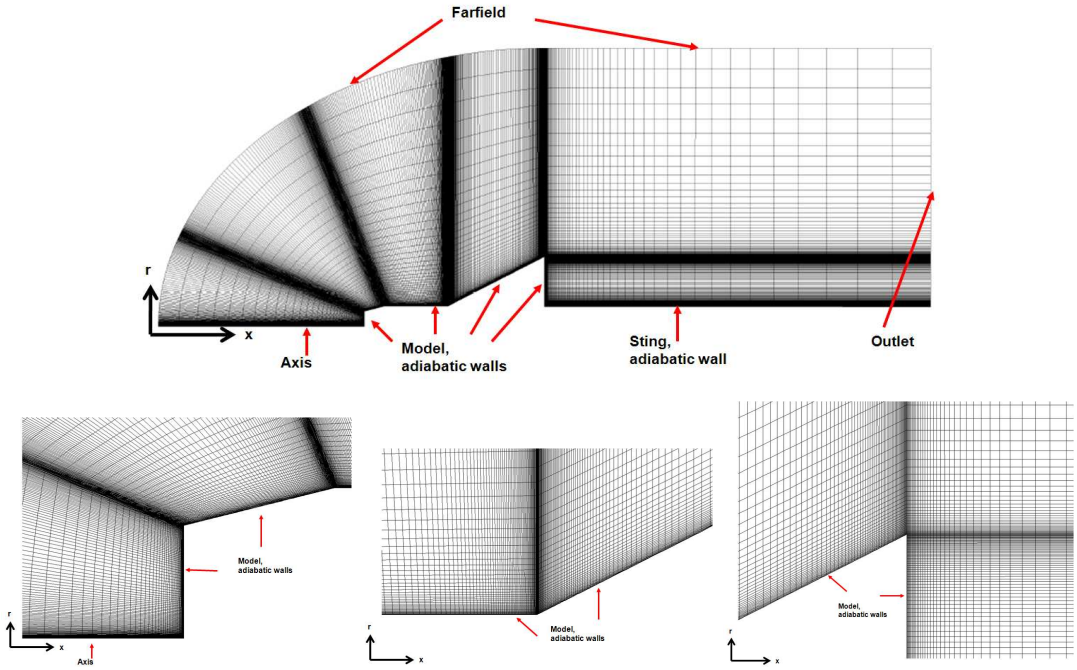

Figure 4.11: Computational domain and mesh for truncated cone-cylinder with flare model (top), mesh distributions in nose region (bottom left), flare junction region (bottom middle) and base region (bottom right).

Grid sensitivity analysis and the effects of incoming TI and wall temperature

Grid sensitivity analysis is conducted for all the models, however only the results from flared models are presented due to the non-trivial flowfield compared to cone-cylinder models and conciseness. Three different computational meshes at different resolutions are created using the multi-block grid strategy. Table 4.1 shows the relevant parameters for each computational grid such as the overall number of mesh points, minimum cell size at nose and cylinder flare junction

regions and y^+ range. The values of the normal spacing have been chosen to ensure that the separation regions are captured accurately as close to experiments. Truncated cone-cylinder model with flare is selected as the test case to critically assess the effect of incoming TI and wall temperature boundary condition in addition. Similar grid distribution is employed for cone-cylinder models.

Table 4.1: Computational grid parameters.

Model Name	# mesh points	# points wall normal	min. cell size nose (μm)	min. cell size junc. (μm)	y^+ range
Cone with flare	42878	59	12.4	13	0.03-2.8
	56124	66	6	6.2	0.012-1.7
	86400	80	1.4	1.3	0.003-0.7
Truncated cone	39872	58	19.4	19.5	0.05-6
with flare	63596	69	6.1	6.4	0.0015-2.4
($d_t/d_b = 0.75$)	93600	80	1.9	1.7	0.0015-1

Truncated cone-cylinder with flare

Figure 4.12 (top) shows the computed non-dimensional wall pressure distributions (p/p_∞) with the axial and radial skin friction coefficients c_f plots (middle and bottom ones) for three computational grids with moderate TI level of 0.1% for truncated cone-cylinder model with flare. The horizontal axis is non-dimensionalized by the length of the model. In Figures 4.12 to 4.17 the geometry is divided into regions with black dashed lines as nose, shoulder, straight segment, flare and base. The plots do not include values from nose and base regions as they are vertical. Grey dashed lines specify experimental separation and reattachment points. The pressure rise in the shoulder region suggests the flow to be supersonic due to the fact that the decrease in streamtube area results an increase in pressure. As a matter of fact the sonic line is coinciding with the corner point between the truncated nose and the shoulder. Then a sudden drop due to expansion fan at the end of the shoulder is observed. On the straight segment pressure is decreasing gradually until the separation region is encountered and the effect of the compression corner shock is felt. From thereon, the gradual rise and the so called the plateau of the bridging region at the corner are indicative of laminar boundary layer separation. On the flare, very steep increase in pressure is observed initially; then the slope is slightly reduced and become nearly linear

up to the base where there is a massive change in streamtube area and hence an immense expansion region responsible for sudden drop in pressure.

In case of skin friction plots in Fig. 4.12 (medium and bottom plots) there is a small separation region right after and extends about 0.03 of x/L (2mm). The coarse grid does not capture the separation the region. Similar rising behaviour is observed on the shoulder for c_f as the pressure is maximised at the shoulder end. On the straight segment the drop is prominent for axial component (obviously zero for radial component) due to boundary layer growth. Skin friction becomes negative and the separation region is slightly underpredicted compared to the experiments (difference is 0.02 of x/L =1.3mm). On this segment c_f nearly exhibits a plateau for medium and fine grids whereas the coarse grid significantly underpredicts the separation region and shows an oscillatory behaviour. At the junction, c_f locally becomes zero and drops further on until the reattachment point on the flare. Reattachment point is captured accurately in simulations compared experimental data even with the coarse grid, the difference is less than 0.7 mm. From thereon steep rise up to 0.6 x/L is observed as in Figure 4.12 top plot. Then the slope is slightly reduced and became oscillatory towards the base.

All the computational grids captured the physical phenomena represented by pressure and skin friction distributions on the model, however the coarse grid significantly underpredicts the extent of the separation region and the consequent steepness of the pressure rise. The extent the separation and reattachment regions are strongly influenced by the grid density in axial direction [105, 106].

For the stagnation region examination, non dimensional pressure distribution at the axis line (up to the nose of the model) and at the nose are plotted in Fig. 4.13. r_t is radius of the truncated frontal face. The theoretical pressure ratio of the bow shock is obtained for medium and fine meshes whereas coarse mesh first overshoots and then undershoots around the desired value due to mesh inadequacy (the numerical scheme is of second order upwinding for all). A slight overshoot for medium grid is also observed. The bow shock stand off distance is $0.55r_t$ from the model, which is very close to experimental observations. After the bow shock, the deceleration is continued up to the model and the pressure is reached around 32.85 times the free stream pressure on the model observed for medium and fine grids (around 33.3 for coarse grid). This value is clearly manifested in the nose region (Fig. 4.13 the right plot). Considering the theoretical pressure ratio value being 32.65, the difference is negligible. The bow shock wave

is progressively weakened above the stagnation region in vertical direction thus the non dimensional pressure is decreasing slowly up to 0.4 r_t and afterwards aggressively dropping to 7.5 times the free stream pressure. The curvature of the shock wave produces an entropy layer where vorticity is present, and where the variation of the flow variables with the distance from the body cannot be neglected, even out of the boundary layer [105]. Mach number contours for medium and fine meshes are presented in Fig. 4.14.

From the Figs. 4.12 to 4.14, it can be observed that the difference between medium and fine grids is insignificant in terms of wall pressure distributions and Mach number contours and very small in terms of skin friction coefficient distributions only in shoulder and flare regions. Hence numerical solution turns out to be grid independent beyond a medium computational grid of 63596 mesh points, which is adapted for the rest of the simulations.

Figure 4.15 shows the computed non-dimensional wall pressure and the skin friction coefficient distributions for three inlet turbulence intensities with a medium grid. There is not any discernible difference between inlet turbulence levels below 0.1%; however higher incoming turbulence intensity of 0.5% results considerably smaller separation and reattachment regions compared to experiments. Skin friction distributions also exhibit a shift in curves between the highest TI and the remaining ones. Thus an incoming TI of 0.1% is selected for the numerical campaign.

Figure 4.16 shows the computed non-dimensional wall pressure and the skin friction coefficient distributions for two different wall boundary conditions for temperature specification, one of them is adiabatic and the other one is constant wall temperature of 295K. There are minimal discrepancies on pressure and skin friction coefficient distributions between these two solutions except on the separation and reattachment regions where constant temperature solution results a slightly smaller separation but a slightly bigger reattachment region compared to adiabatic case. Furthermore on the flare where flow reattaches and possibly transits to turbulence, an incremental shift in skin friction is observed. Considering the adiabatic wall temperature of 335K based on the free stream flow conditions specified in Section 2.3, the effect of constant wall temperature of 295K is small. However heat transfer coefficient, c_H (or Stanton number, see Eqn. 4.2), which can only be displayed for non-adiabatic wall temperature simulations, provides

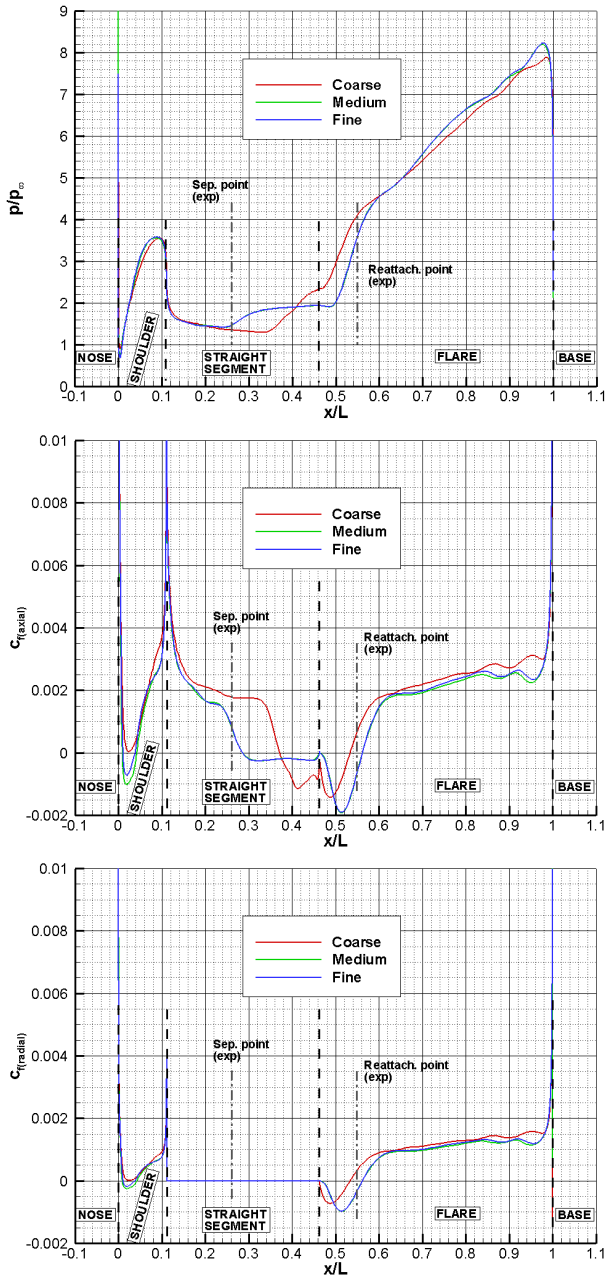

Figure 4.12: Non-dimensional pressure (top), axial (middle) and radial (bottom) skin friction coefficient distributions at the wall of the truncated cone-cylinder model with flare for successive grid refinement.

additional insight into the flowfield description as explained as follows in the following paragraph. Laminar flows exhibit a smoothly decreasing Stanton number trend yet in this case the trend is disturbed by the separation point that reduces

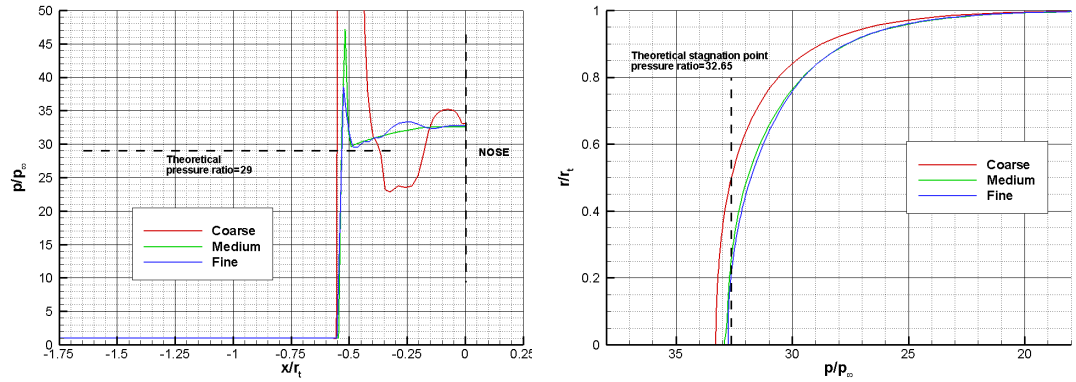

Figure 4.13: Non-dimensional pressure distributions at the axis (left) and at the nose (right) of the truncated cone-cylinder model with flare for successive grid refinement.

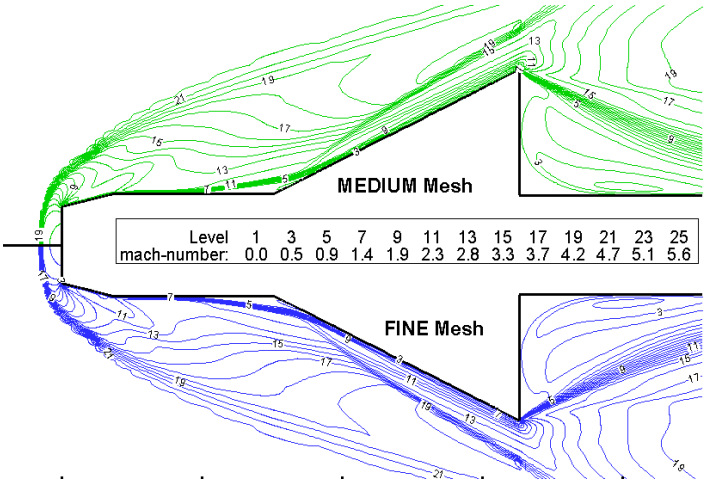

Figure 4.14: Mach number contours for medium and fine computational grids.

heat transfer rather abruptly as it is shown in Fig. 4.17. This behaviour is continued until a local minimum and thereon it starts to increase slowly again up to the corner. After the corner, an abrupt increase in heating rate is observed until a peak is reached slightly downstream of the reattachment. This increase is related to high local pressure and the thinning of the boundary layer caused by the reattachment process, which is followed by streaks promoting transition. The adverse pressure gradient and effective flow concavity in the reattachment area are highly effective in promoting laminar turbulent transition. The process is accompanied by the formation of steady streamwise Goertler type vortical structures as it mentioned by Simeonides and Haase [103]. TI contours shown in Fig. 4.18 further validate the transition postulate. 10% TI is observed inside the separation region on the flare, which is significantly higher than the incoming turbulence level of

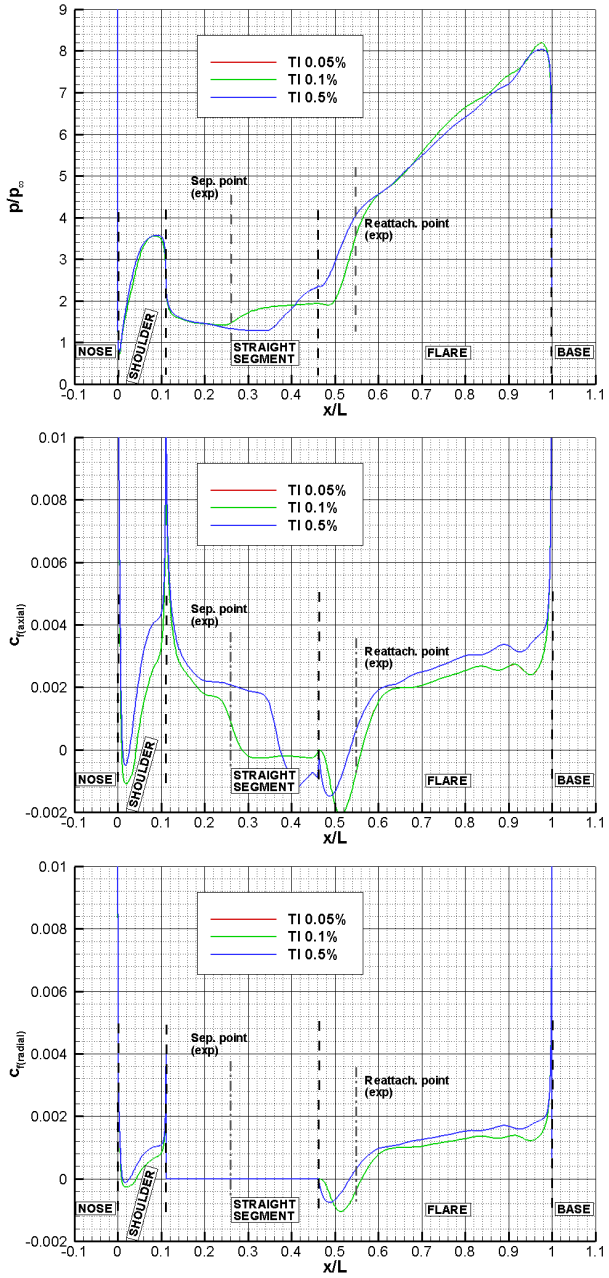

Figure 4.15: Non-dimensional pressure (top), axial (middle) and radial (bottom) skin friction coefficient distributions at the wall of truncated cone-cylinder model with flare for different incoming turbulence intensities.

0.1%. A further rise of from the peak heating is observed at around 0.66 of x/L due to the impingement of the separation shock on the compression shock. This is obviously consistent with the skin friction distribution. In terms of stagnation point heating, the value is found to be around $70kW/m^2$.

As a conclusion both of the temperature boundary conditions are adapted for flared models.

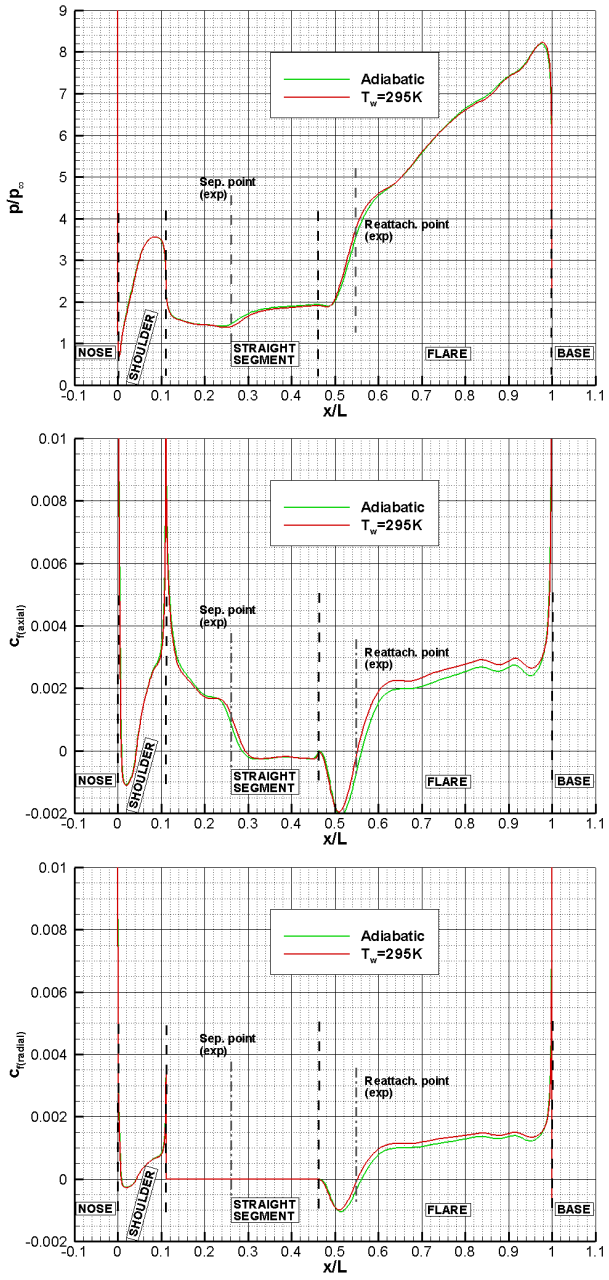

Figure 4.16: Non-dimensional pressure (top), axial (middle) and radial (bottom) skin friction coefficient distributions at the wall of truncated cone-cylinder model with flare for two different wall temperature boundary conditions.

$$c_H = \frac{q}{\rho_\infty u_\infty cp\,(T_{aw} - T_w)} \tag{4.2}$$

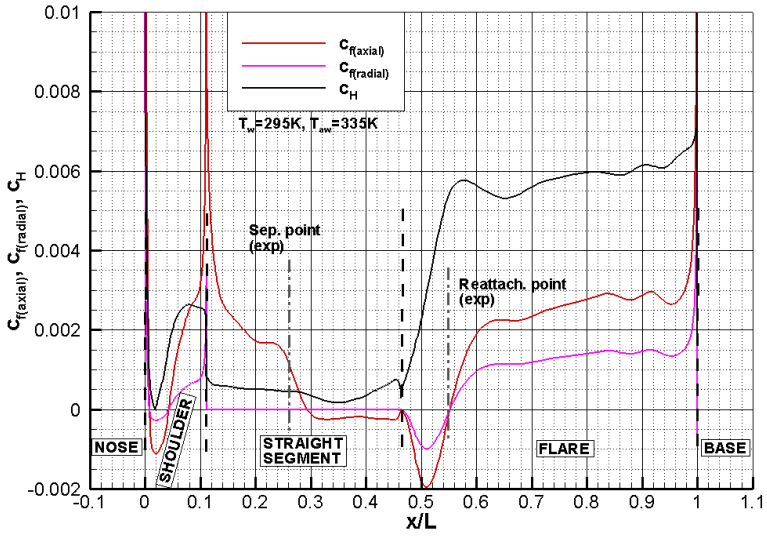

Figure 4.17: Skin friction (axial and radial) coefficient and Stanton number distributions at the wall of truncated cone-cylinder model with flare for 295K wall temperature.

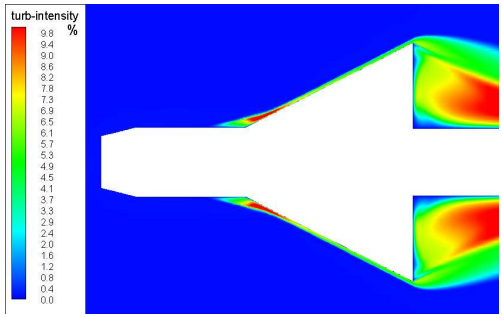

Figure 4.18: Turbulence intensity contours of truncated cone-cylinder model with flare.

Cone-cylinder with flare

Figure 4.19 (top) shows the computed non-dimensional wall pressure distributions with the axial and radial skin friction coefficients plots (middle and bottom ones) for three computational grids with moderate TI level of 0.1% for cone-cylinder model with flare. The horizontal axis is non-dimensionalized by the length of the model. In Figures 4.19 to 4.21 the geometry is divided into regions with black dashed lines such as nose, shoulder, straight segment, flare and base. Grey dashed lines specify experimental separation and reattachment points as for the truncated cone-cylinder model with flare. Right after the tip of the model pressure level decreases slowly and settles to a constant theoretical value of 3.4 for Mach 5(see NACA Report 1135 [100]) after 0.12 of x/L (10.5mm). This initial induced pressure is due viscous interaction explained in detail in Appendix

A. After the end of the conical region the expansion fan creates a drop and on the straight segment pressure levels nearly stays constant inside the separation region. Downstream of the corner there is a huge jump in pressure from 1.8 to about 9.5 times the free stream pressure due to combined separation and compression shock waves. Further downstream on the flare, high pressures are maintained and slightly increased towards the base where there is a huge drop due to massive expansion.

In case of skin friction coefficient, after the tip there is a sudden drop in skin friction where it becomes negative. The upstream extent separation region is slightly underpredicted compared to the experiments (difference is 0.02 of x/L =1.8mm). In the experiments the separation starts right after the corner. Inside the separation region there are actually two small separation bubbles found from simulations. Right after the compression corner c_f shows an oscillatory behaviour followed by a drop and an accompanying rise indicating reattachment and transition. The reattachment point is captured almost perfectly as in experiments at 0.12 of x/L (10.45mm from the corner). Then a plateau is followed on the flare.

All the computational grids captured the physical phenomena represented by pressure and skin friction distributions on the model, however the coarse grid exhibits some variations around the initial corner, at the compression corner and on the flare. The difference between medium and fine grids is insignificant in terms of wall pressure distributions and very small in terms of skin friction coefficient distributions. Hence numerical solution turns out to be grid independent beyond a medium computational grid of 56124 mesh points.

Figure 4.20 shows the computed non-dimensional wall pressure and the skin friction coefficient distributions for two different wall temperature boundary conditions, the first one of is adiabatic and the second one is constant wall temperature of 295K. There are very small discrepancies on pressure and skin friction coefficient distributions between these two solutions except on the straight segment where the separation and reattachment regions coexist. Constant wall temperature solution results a slightly smaller reattachment region compared to adiabatic simulation. Furthermore on the flare where flow reattaches, an incremental shift in skin friction is observed.

Figure 4.21 shows the heat transfer coefficient, c_H, together with skin friction coefficients. In the cone region smoothly decreasing Stanton number trend is observed like in c_f as expected for laminar flows. However departure from this

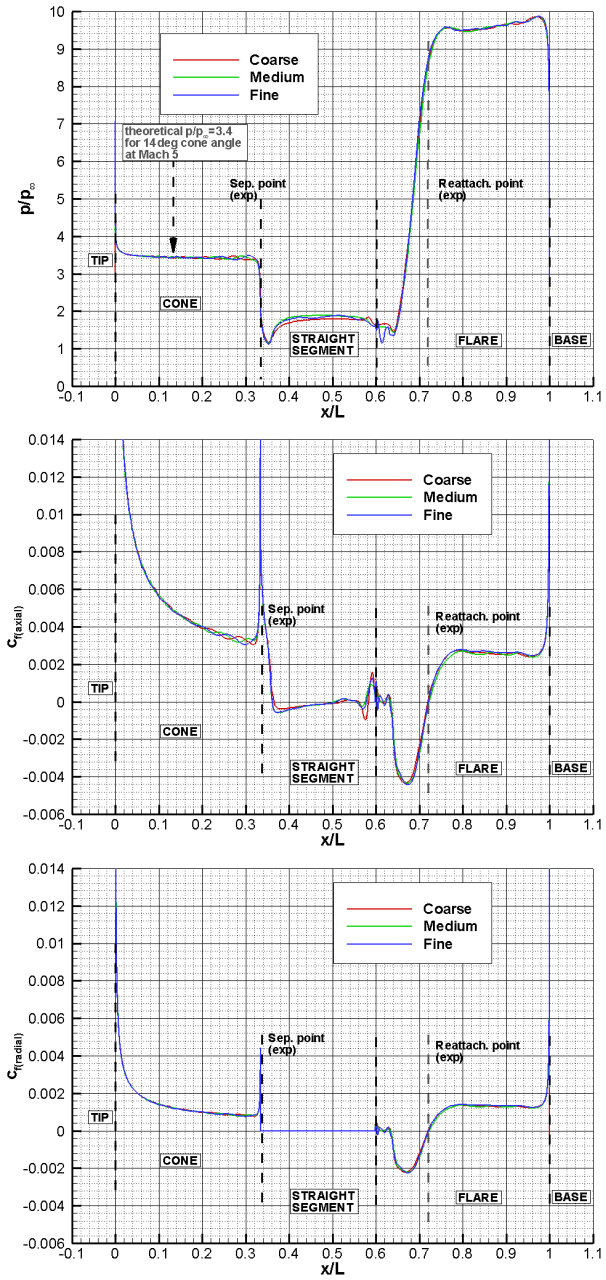

Figure 4.19: Non-dimensional pressure (top), axial (middle) and radial (bottom) skin friction coefficient distributions at the wall for successive grid refinement.

behaviour is imminently apparent on the straight segment where there is a drop and subsequent oscillatory pattern up to nearly the compression corner. There is a peak around the corner signifying the reattachment of the small circulation region and it is followed by a drop on the flare. From thereon the rise and the local maximum in c_H shows the reattachment point. This is obviously consistent

with the skin friction distribution. Afterwards a smooth decrease is observed towards the base. TI contours shown in Fig. 4.22 indicate very small levels of turbulence around the corner nearly the same as the incoming turbulence level of 0.1%. Therefore a definitive conclusion about transition can not be made.

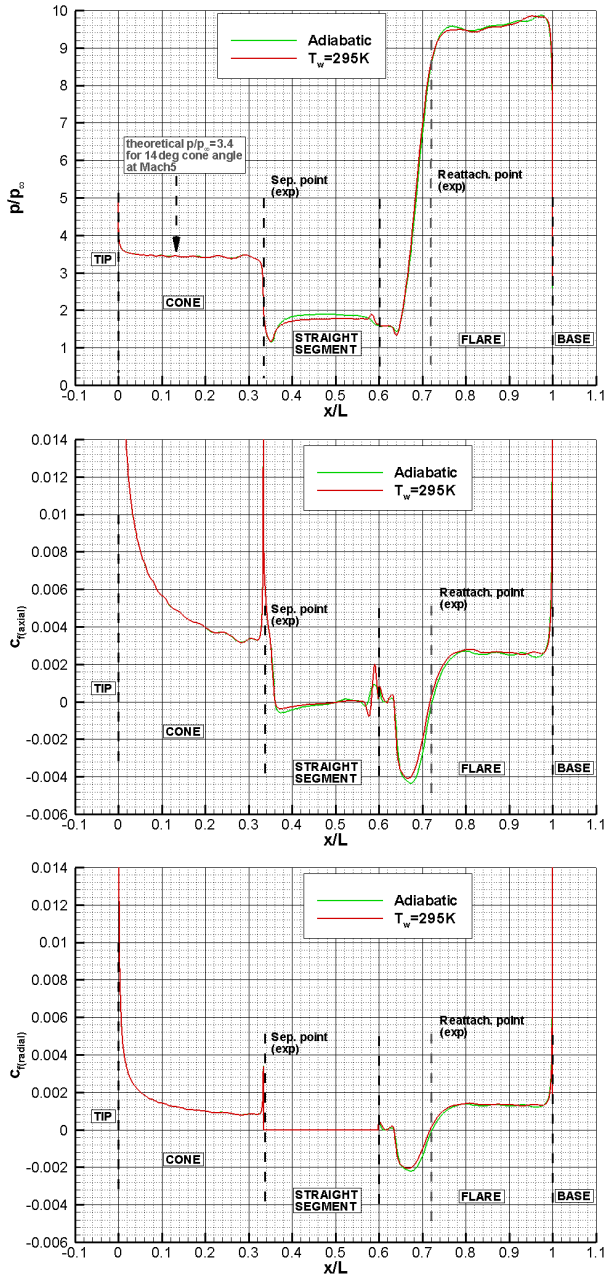

Figure 4.20: Non-dimensional pressure (top), axial (middle) and radial (bottom) skin friction coefficient distributions at the wall of cone-cylinder model with flare for two different wall temperature boundary conditions.

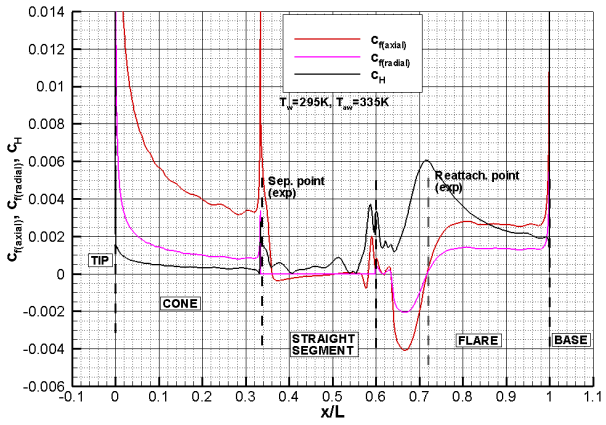

Figure 4.21: Skin friction (axial and radial) coefficient and Stanton number distributions at the wall of cone-cylinder model with flare for 295K wall temperature.

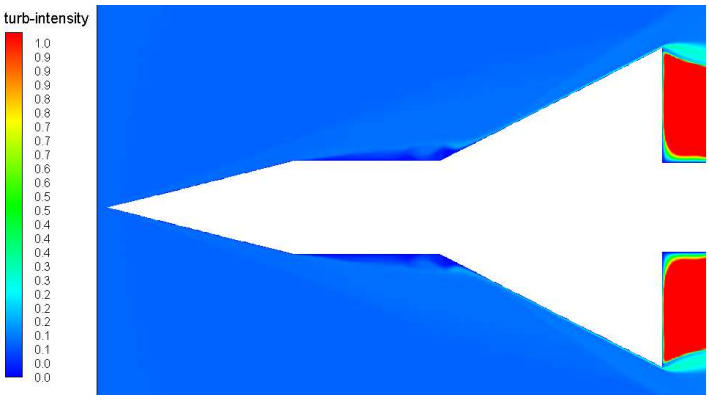

Figure 4.22: Turbulence intensity contours of cone-cylinder model with flare.

In addition theoretical distributions of skin friction and heat transfer coefficients are plotted on top of the computational ones for comparison. The comparison is done only on the conical region because of the applicability of the hypersonic flat plate theory. Firstly c_f and c_H distributions are extracted from Van Driest's solutions of boundary layer equations over a flat plate. The values at Mach 5 and wall to freestream temperature ratio of $T_w/T_e \approx 4.8$ (see flow conditions specified in Section 2.3 are deducted and then multiplied by $\sqrt{3}$ for extension of the flat plate values to the cone. The Van Driest solutions of the boundary layer equations are presented in Appendix A. Furthermore reference temperature method is utilised to estimate c_f and c_H distributions with Eckert's reference temperature formula. The mathematical details of the method are also explained in Appendix A. The comparison is presented in Fig. 4.23. Van Driest's solutions significantly underestimate c_f and overestimate c_H. However the

agreement between reference temperature method and CFD is satisfactory.

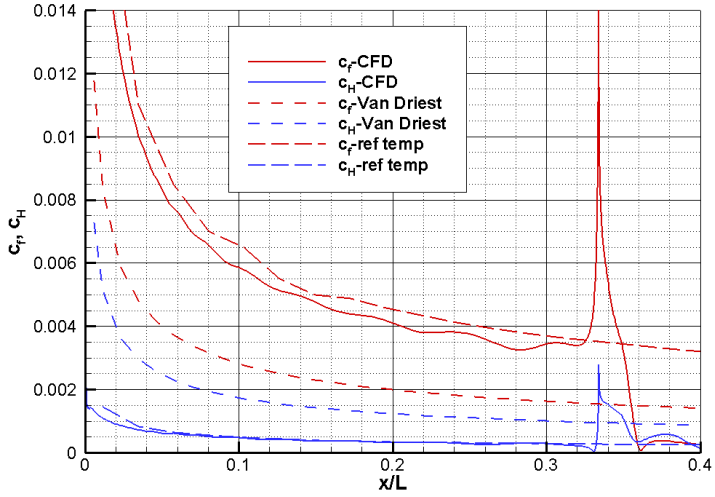

Figure 4.23: Numerical and theoretical skin friction coefficient and Stanton number distributions at the wall of cone-cylinder model with flare for 295K wall temperature.

4.1.3 Comparison of experiments with CFD

Figure 4.24 shows the density gradient field of flared models for comparison. The prominent flow structures and their respective sizes are captured quite close to experiments validating the numerical simulations further. Initial comparison is done on the extents of separation and reattachment regions on skin friction plots mentioned in Section 4.1.2 in detail.

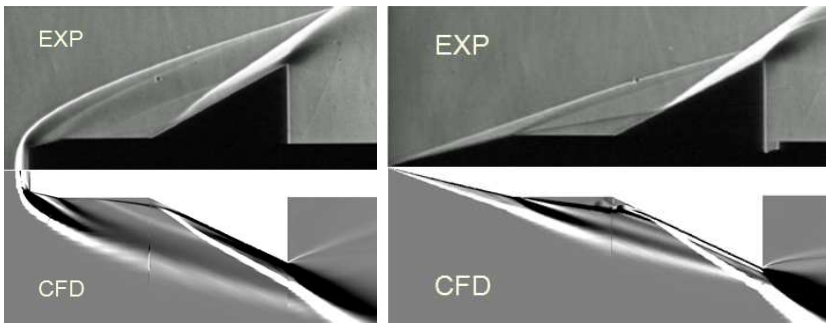

Figure 4.24: Non-dimensional pressure (top) and skin friction coefficient (bottom) distributions at the wall for successive grid refinement in x direction.

Furthermore contours of Mach number from all the numerical simulations for cone-cylinders models are shown in Fig. 4.25, which clearly renders significant flow structures captured quite close to experiments.

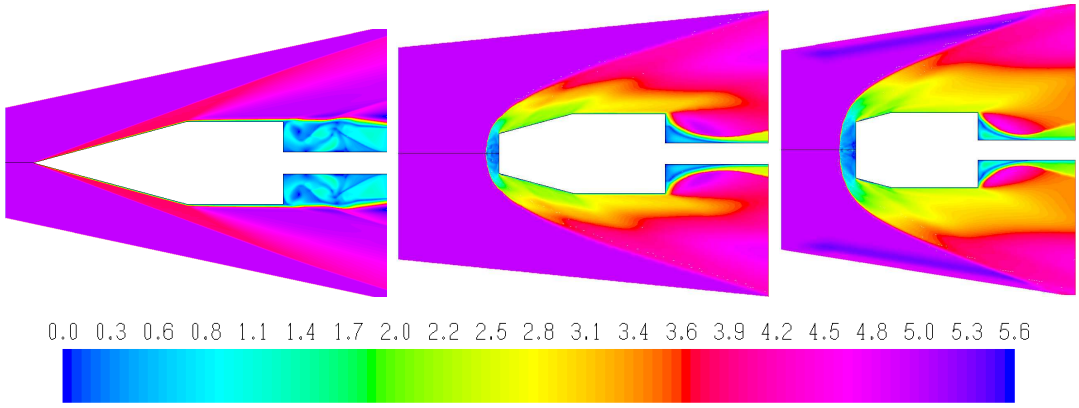

Figure 4.25: Mach contours of cone models, left: no truncation, middle: $d_t/d_b = 0.5$, right: $d_t/d_b = 0.75$.

In terms of drag force comparisons, all the measured, theoretically calculated (using Newtonian/modified Newtonian theory) and simulated drag force values are tabulated in Table 4.2.

Table 4.2: Drag force comparison of the models (Baseline configuration). All the values are in N.

Model Name	Experiment	CFD	Newtonian Method	Mod. Newtonian Method
Cone	2.79 ±0.2%	2.78	2.88	2.69
Truncated cone ($d_t/d_b = 0.5$)	7.99 ±0.25%	8.09	9.93	9.06
Truncated cone ($d_t/d_b = 0.75$)	14.74±0.53%	14.86	18.73	17.02
Cone with flare	18.49±0.64%	18.57	18.53	16.99
Truncated cone with flare($d_t/d_b = 0.75$)	16.44±0.21%	16.66	22.27	20.36

The agreement of experiments with CFD is very good as expected for cone models, however there are slight discrepancies for flared models, which are mainly associated with the shock wave laminar boundary layer interaction and the consequent separation region occurring at the corner explained in Section 4.1.2. The difference is about 1.3% for the truncated cone-cylinder with $d_t/d_b = 0.5$, 0.8% for the truncated cone-cylinder with $d_t/d_b = 0.75$ and nearly negligible for the cone-cylinder. The discrepancy is around 0.4% for the cone-cylinder with flare

and 1.3% for the truncated cone-cylinder with flare. On the other hand, theoretical values differ significantly from the experiments. For sharp models (i.e. all cone models) Newtonian theory gives better results, and for blunt models modified Newtonian theory is better as it is expected. One interesting aspect to note is the fact that truncated cone-cylinder with flare has a smaller drag value than the cone with flare. It is related with the size of the separation region at the corner and the strength of the compression shock over the flare; in the sharp case Mach number upstream of the flare is higher, the compression shock is stronger and consequently the separation region is bigger thus resulting in a bigger pressure distribution on the flare whereas for the blunt case the separation region is smaller and Mach number upstream of the flare is lower hence relatively weaker compression shock is formed consequently reducing drag on the flare. In addition the contribution of the flare to overall drag is bigger than the contribution from the nose region, therefore truncated model has less drag than sharp model. CFD results also confirm these findings yet Newtonian theory does not take these aspects into account; it only relies on the local inclination of the surface, hence an opposite behaviour is observed. The uncertainties in experimental values are calculated using an approach mentioned in Appendix B.

In essence after the baseline campaign, the quality and the credibility of the measurements and simulations are well ensured.

4.2 Energy deposition via electric arc discharge

4.2.1 Tests without discharge

Tests without discharge are conducted to examine the effects of the presence of electrodes. The flow interference and stability of the electrodes are investigated. The setup of the electrode arrangement is shown in Section 2.5. The truncated cone-cylinder with $d_t/d_b = 0.75$ is chosen to assess the interference of the electrodes due to its greater frontal area compared to electrode diameters and the size of the arc of 2mm. The efficiency of the energy deposition is proportional to the ratio of the cross sectional area of the aerodynamic body to the cross sectional area of the energy deposition and free stream Mach number as reported by Knight [71] and mentioned in Section 1.3. The distance between the electrodes and the truncated face is set to 1.3 times the truncation diameter. Figure 4.26

shows schlieren visualisation of the flowfield of the truncated cone-cylinder with $d_t/d_b = 0.75$ at 20000 fps with 3.25μsec exposure around 0.45sec after the firing valve is opened (corresponding to the peak in stagnation pressure). Initially the electrodes move upwards due to aerodynamic force up to 0.45sec and then stabilise for the rest of the run. The main effect of the electrodes is the destruction of the strong bow shock in front of the model and the formation of relatively weak axisymmetric oblique shocks instead, sitting on top of the wake of the electrodes. This wake is causing low frequency oscillatory behaviour of the oblique shocks. Moreover the electrodes induce a rather weak bow shock as well.

4.2.2 Tests with discharge

Visual observations and high speed schlieren photography

In the tests with discharge, the truncated cone-cylinder with $d_t/d_b = 0.75$ is again chosen as the starting point and is compared to without discharge case obviously. The distance between the electrodes and truncated face is set to 1.3 times the truncation diameter. The arc is discharged steadily. The measured voltage history during the tests is shown in Fig. 4.27 with the subfigures showing the physical phenomena. Before the test, vacuum conditions are present with $p_{vac} = 1mbar$, the arc is glowing over a big region on the earthed electrode. The voltage is around 0.9kV over that duration and when the test gas arrives, the glow discharge transforms into an arc discharge that sustains steadily and convects downstream about $5.0mm$. This distance is named as the relaxation distance by Satheesh and Jagadeesh [82]. The voltage level is around 0.6kV during the steady period and showing small variations as opposed to any short duration facility. The current in this period is about 0.011A making the consumed power around 7W; thus considering the flow energy passing through the frontal face of the cylindrical energy spot of 0.5mm in diameter and 2mm in width is around 20.3W for the flow condition specified in Section 2.3), the corresponding heating power ratio is 0.35 (see Eqn. 4.3).

$$\eta = \frac{Q}{\dot{m_{spot}} c p T_0} \tag{4.3}$$

Figure 4.28 shows schlieren visualisation of the flowfield of the truncated cone-cylinder with $d_t/d_b = 0.75$ at 20000 fps with 3.25μsec exposure after the electordes are stabilised. The immediate effect of focused upstream energy addition is to

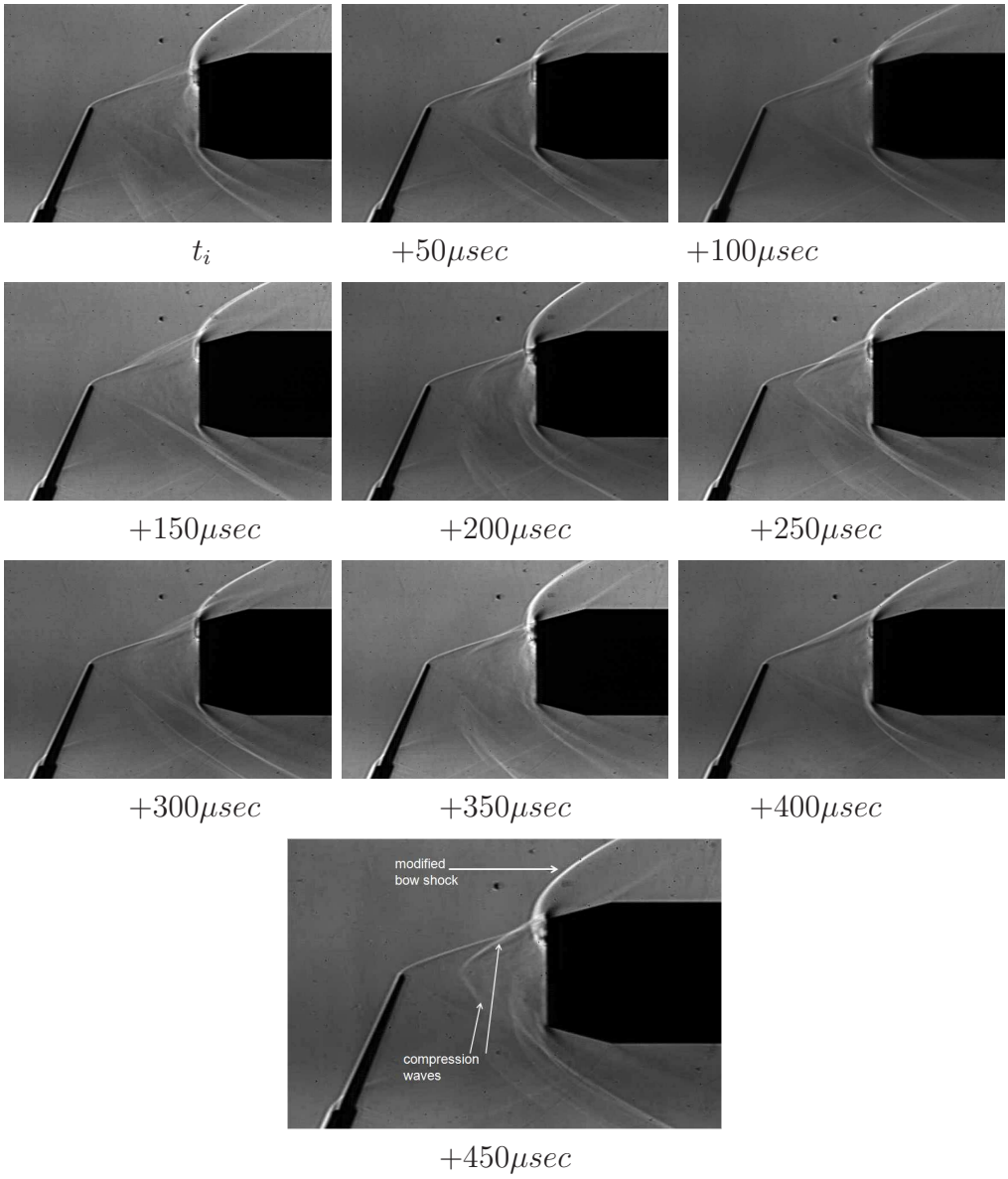

Figure 4.26: Schlieren visualisation of the effect of electrodes on the flow over the truncated cone-cylinder with $d_t/d_b = 0.75$ during the test.

heat, pressurize, and slow the energized fluid; if sufficient energy is provided, weak adjacent compression waves are observed forming around the energized region. However, it is the strong coupling between the energized region and the (downstream) blunt-body nose that dominates the change in flow structure; the blunt body normal shock weakens and moves far upstream toward the energized region, thus resulting in very rapid lateral transition of this shock into oblique waves. These oblique shock waves are coupled with the weaker compression

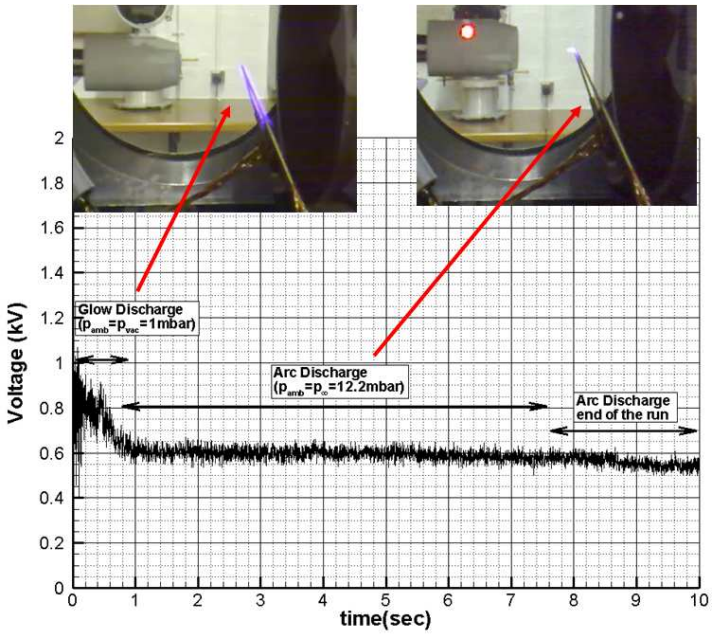

Figure 4.27: Voltage history during a test run with discharge over a truncated cone-cylinder with $d_t/d_b = 0.75$.

waves emanating from the energized region. The finding is consistent with the flow model proposed by Satheesh and Jagadeesh [82], which is shown in Fig. 1.18, when the energy spot not found to be strong enough to produce its own shock. Therefore the shock structure observed is a result of the heated channel formed behind the energy source interacted with the blunt body shock that causes flow alteration. To verify this fact, one dimensional steady flow with heat addition equation (Rayleigh flow) is utilised. The heat addition per unit mass required to choke the flow is specified in Eqn. 4.4 by Knight [71]. It is calculated as 16.2W for the cylindrical energy spot of size of 0.5mm in diameter and 2mm in width, which is bigger than 7W, therefore the localised heating is not powerful enough to create its own shock wave.

$$\Delta q = \frac{cpT_0 \left(M_\infty^2 - 1\right)^2}{(\gamma + 1) M_\infty^2 \left[(\gamma - 1) M_\infty^2 + 2\right]} \tag{4.4}$$

Nevertheless the influence of discharge is barely distinguishable from the discharge-off case for truncation cone-cylinder with $d_t/d_b = 0.75$. The reason for that might be the strong dominant wake of the electrode resulting unsteady behaviour at the nose of the model. Thus the influence of arc becomes small, yet in both cases the bow shock in front of the model is "'killed"' and upstream flow

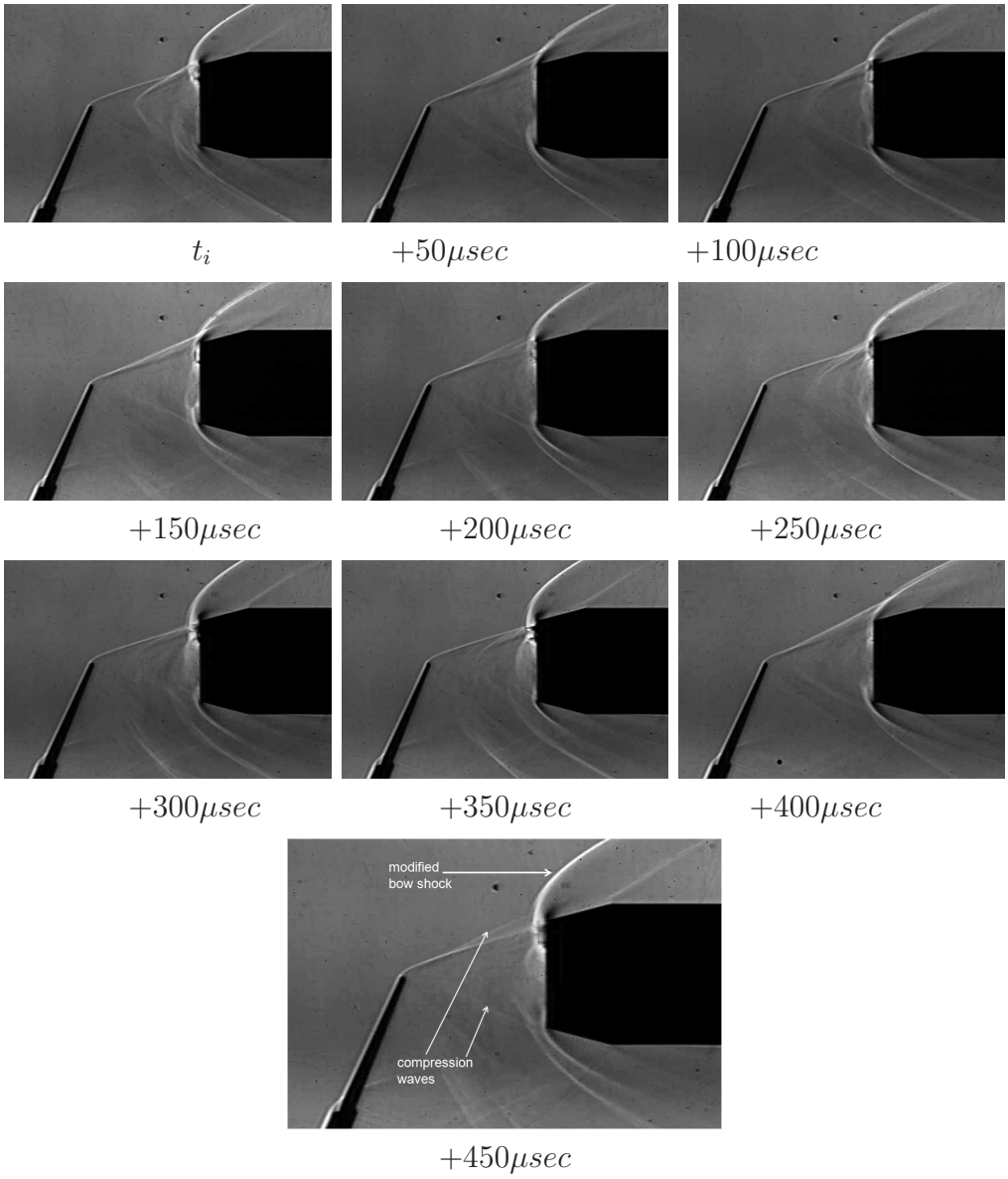

Figure 4.28: Schlieren visualisation of the effect of arc discharge on the flow over the truncated cone-cylinder with $d_t/d_b = 0.75$ during the test.

structure is altered. As a consequence the reduction in drag force on the frontal area is accomplished. The statistical analysis from schlieren images is conducted based on 1000 images during the period when the electrodes are stabilised. In order to quantify the shock wave positions, a number of image processing algorithms are used to extract the required information from the images. Firstly the sharpening and edge detection filtering are applied and then averaged and root mean square images are obtained as it is shown in Fig. 4.29. For the discharge-on

case the compression wave structure has further moved about 1mm downstream with discharge, resulting a slightly longer wake. However considering the flow velocity as 700m/s (slightly less than free stream value due to the wake of the electrodes) and exposure time of 3.25μsec, the image blur due to shock movement is 2.75mm, which is bigger than the difference between the "'on"' and the "'off"' case. Although longer and thicker wake due to energy addition is believed to be the cause of reduced stagnation pressure on the frontal area, as the stagnation pressure reduction varies with the length of the thermal spot and the density in the heated zone, a definitive conclusion can not be made. On the other hand the reasoning can not be linked to plasma effects due to the fact that the plasma effects die off after 5mm from the electrodes (relaxation distance). The cause of such dramatic interaction with the wake and the distorted bow shock wave in front of the model (in addition to wake of the electrodes) could be the coupling of disturbances in arc power or freestream conditions with the blunt body flowfield. Such disturbances can be held responsible for total pressure variation along the heated wake axis [83].

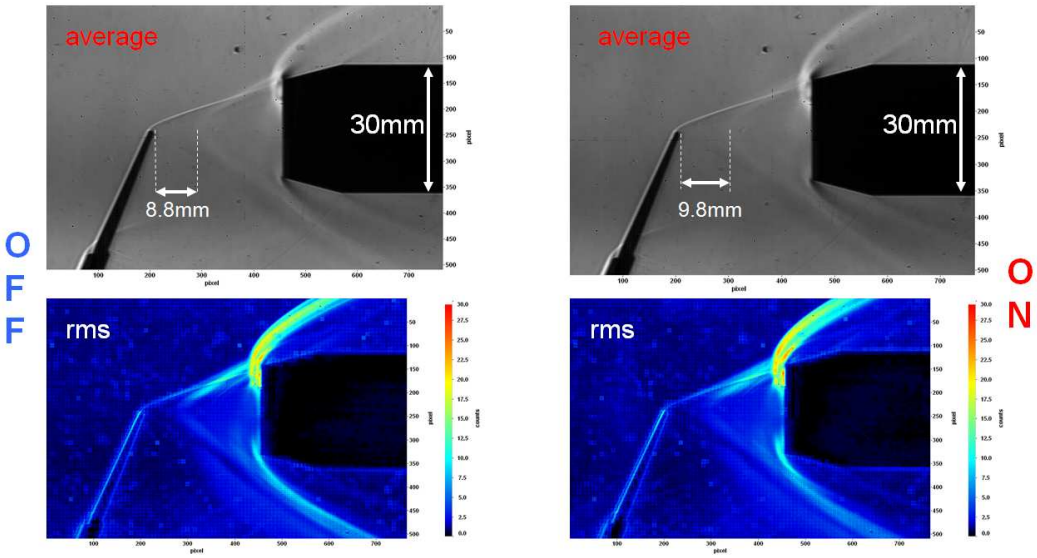

Figure 4.29: Comparison of discharge-on case with discharge-off case in terms of averaged and rms schlieren images over a truncated cone-cylinder with $d_t/d_b = 0.75$ and $l/d_t = 1.3$.

Drag force measurements

Fig. 4.30 shows measured drag force signals for the truncation cone-cylinder with $d_t/d_b = 0.75$ with varying distances between the electrodes and the truncated face. Three repeats are conducted for each case without and with discharge. The repeatability of the tests without discharge is very good and nearly as good as model only tests (see Table 4.3) especially for shorter arc to nose distances (i.e. $l/d_t = 0.9, 1.3$). Nonetheless for slightly longer distances, oscillations start to appear yet the repeatability is still very good. In addition the drag force history in all cases exhibits a steady decrease during the test runs, which is found to be around 5% throughout the run due to small downstream movement of earthed electrode. As the arc to nose distance is increased drag levels first start to decrease up to $l/d_t = 1.5$ then they start to increase. This behaviour is because of the aerodynamic shadowing of the electrodes however after some distance this phenomenon becomes less pronounced. In the work of Satheesh and Jagadeesh [82] and Schulein and Zheltovodov [83], arc to nose distance is kept very long to have a very small effect on drag and significant amount of power is added to the arc to modify the flowfield. The effect of the added energy was clearly demonstrated in the formation of the free circulation bubble before the body for the case of Schulein and Zheltovodov [83]. Nevertheless a significant amount of the input energy was dissipated in the long wake region until it reached the body and interacted with the bow shock wave. In the current work only a small amount of energy is added, therefore shorter arc to nose distances are favoured. In essence drag level reduces considerably just by the presence of the electrodes (from 14.75N up to 6.5N) due to the significant modification of the bow shock, a passive effect namely. This is consistent with the idea that the wake behind the electrode tips provides a subsonic precursory column. In case of the tests with discharge, non negligible test to test variations and increased level of fluctuations owing to the unsteady interaction of the heated channel with the compression waves are apparent. At the nearest distance, i.e $l/d_t = 0.9$ the drag levels have the highest value around 10N, however the drag reduction is very clear between the discharge off and on. As the distance increases, the drag deficiency become smaller up to $l/d_t = 1.5$ and for $l/d_t = 1.8$ the reduction is very small, which might be due to the ineffectiveness of the energy deposition as the heated zone has 5mm of relaxation distance as it is mentioned above.

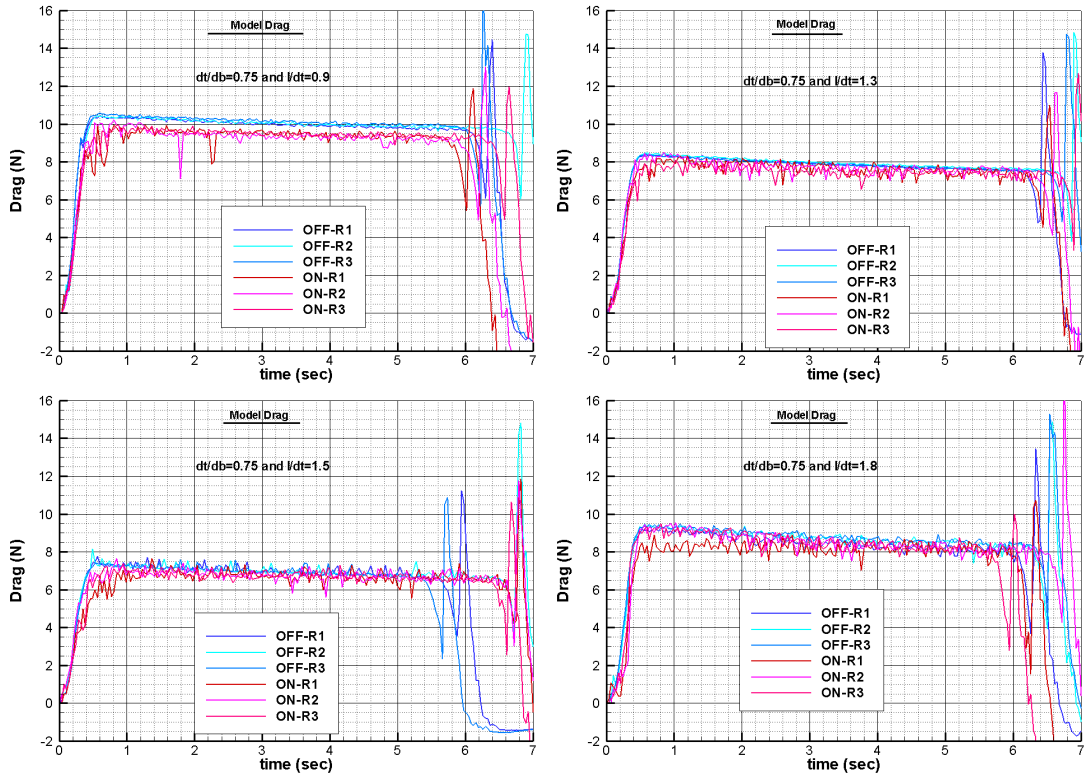

Figure 4.30: Comparison of discharge-on case with discharge-off case in terms of drag force histories over the truncation cone-cylinder with $d_t/d_b = 0.75$; top left: $l/d_t = 0.9$, top right: $l/d_t = 1.3$, bottom left: $l/d_t = 1.5$, bottom right: $l/d_t = 1.8$.

Moreover FFT of the drag signals, which are acquired at 300Hz using 3 component force balance, are taken to examine whether there are any dominant frequencies involved either due to the electrodes and arc discharge as it is shown in Fig. 4.31. Both signals are clipped at the region of useful running time and the mean values are subtracted from instantaneous values to assess the fluctuations properly. The mean and the variance of the signals are also specified. The variance (closely related to standard deviation) of the "On" signal is nearly twice of the "Off" signal and the oscillations are bigger in magnitude. However there is not a dominant frequency related to arc discharge observed. This might be due to the limited frequency response of the drag measurement (300Hz), and any dominant frequency in the kHz range folds back to lower frequencies.

Figure 4.32 shows measured drag force signals for the truncation cone-cylinder with $d_t/d_b = 0.5$ with varying distances between the electrodes and the truncated face. There are three repeats conducted for each case without and with discharge.

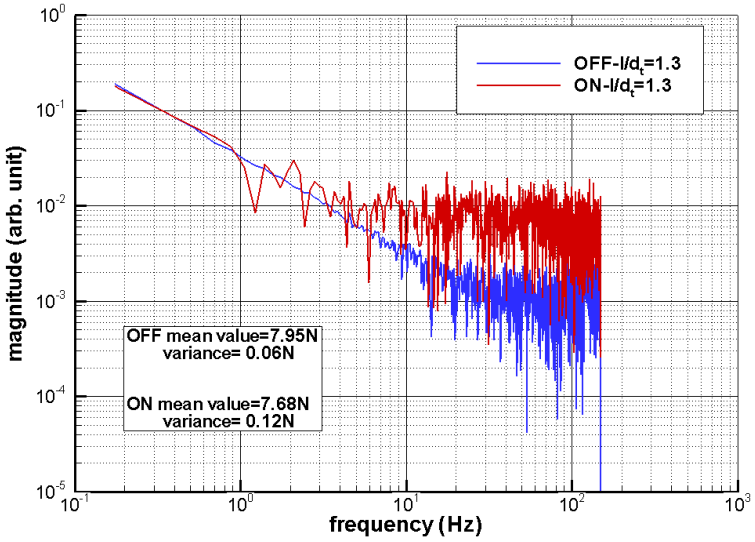

Figure 4.31: Frequency content of the drag signals of the truncated cone with $d_t/d_b = 0.75$ with/without discharge for $l/d_t = 1.3$.

Repeatability for the off cases is very good and for on cases with arc to nose distances of 1.3 and 1.5 d_t. Nonetheless run to run repeatability for the shortest distance is degraded. The effective interaction occurs only for the shortest distance case, the reason for that might be the relatively bigger spot size to frontal face area ratio as efficiency is highly dependent on this ratio.

Figure 4.33 shows measured drag force signals for the flared truncation cone-cylinder with $d_t/d_b = 0.75$ and $l/d_t = 0.9$. There are two repeats conducted for each case without and with discharge. Repeatability for the "'off"' and "'on"' cases is very good. The drag force with the presence of the electrodes increased over the "model only drag" owing to modified stronger compression shock mentioned in Section 4.1.3 and then the arc discharge again diminished the drag value. This is a clear proof that arc discharge is effective on reducing drag force.

Table 4.3 summarises the measured drag force values for all truncated models without and with discharge. The uncertainties in experimental values are calculated using an approach mentioned in Appendix B. The force balance and the data acquisition system with signal conditioning unit are the key components contributing to uncertainties. The bias contribution is 0.074N as it is prescribed by manufacturer/calibrator and for the precision contribution $1.96 \cdot \sigma$ of the drag value is calculated from repeats. The overall uncertainty adds up to values from ± 0.2 to 3.3% in drag measurements.

The real contribution of the discharge is varying from 0.0 to 0.93N, in terms

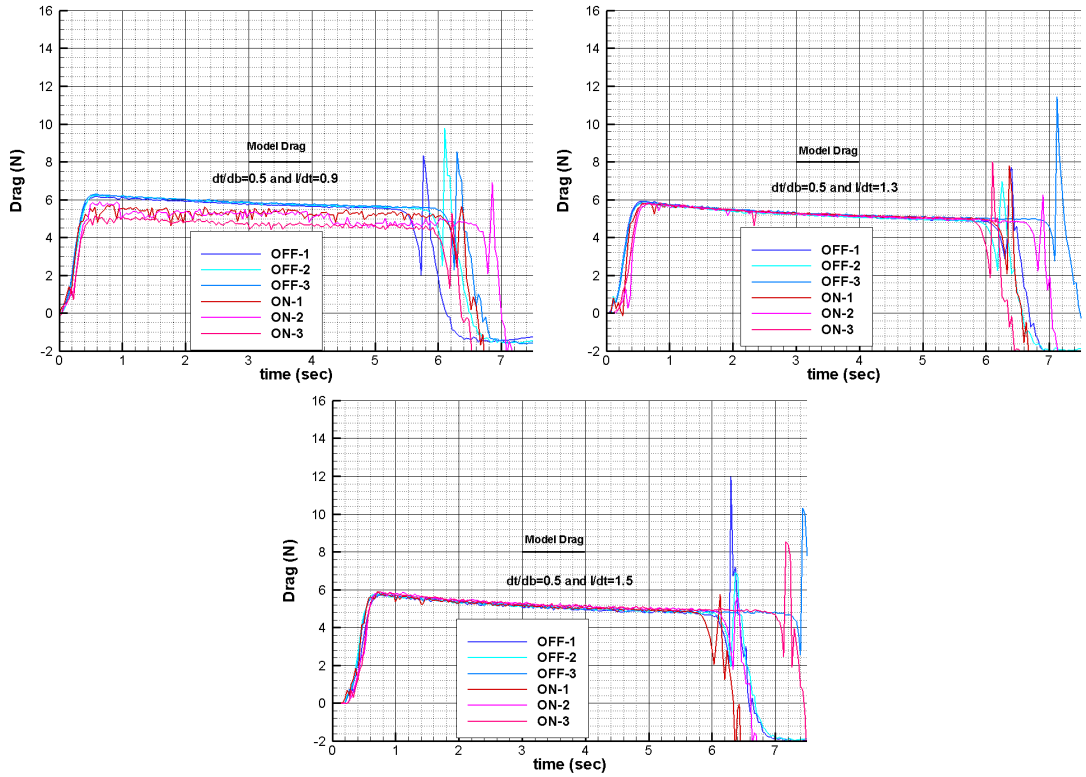

Figure 4.32: Comparison of discharge-on case with discharge-off case in terms of drag force histories over the truncation cone-cylinder with $d_t/d_b = 0.5$; top left: $l/d_t = 0.9$, top right: $l/d_t = 1.3$, bottom middle: $l/d_t = 1.5$.

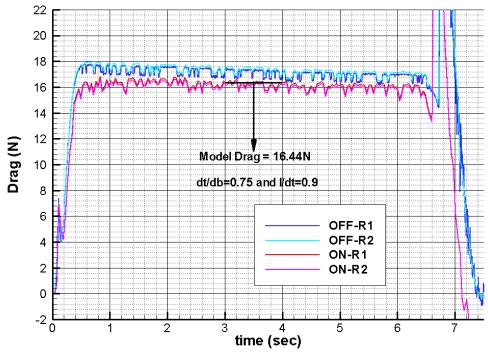

Figure 4.33: Comparison of discharge-on case with discharge-off case in terms of drag force histories over the flared truncation cone-cylinder with $d_t/d_b = 0.75$.

of efficiency (Eff) these values result from 0 up to 105 (not percent) at a speed of 790m/s. This clearly shows that the use of small amount of onboard energy to create a local focused thermal spot in front of a vehicle is an efficient way of reducing drag. Fig. 4.34 shows the effectiveness of this method for drag reduction on truncated cone-cylinder models with increasing distance between

Table 4.3: Drag force comparison of the truncated cone-cylinder models without and with discharge. All the values are in N.

Model name	$l/d_t = 0.9$	$l/d_t = 1.3$	$l/d_t = 1.5$	$l/d_t = 1.8$	
Truncated cone-cylinder ($d_t/d_b = 0.75$)	10.06±0.8%	7.91±0.7%	7.00±0.4%	8.78±0.7%	OFF
	9.42±1.1%	7.61±1.6%	6.74±0.6%	8.42±2.4%	ON
Truncated cone-cylinder ($d_t/d_b = 0.5$)	5.83±0.6%	5.24±0.5%	5.14±0.7%		OFF
	5.26±3.3%	5.23±0.8%	5.17±0.2%		ON
Truncated cone-cylinder with flare ($d_t/d_b = 0.75$)	17.11±0.8%				OFF
	16.18±2.5%				ON

the electrodes and the frontal area. Firstly for the same amount of truncation and energy input the effectiveness is slightly less for the smallest frontal area of the truncated cone-cylinder with flare compared to truncated cone-cylinder with $d_t/d_b = 0.75$. Considering the electrodes and the energy spot have a certain size adding up to 3mm, as the frontal area is increased the effectiveness increases up to 9.5% (truncated cone-cylinder with $d_t/d_b = 0.5$) and then it starts to decrease to 6.2% (truncated cone-cylinder with $d_t/d_b = 0.75$). In case of arc to nose distance, shorter distances seem to be favourable; as the distance increases the effectiveness diminishes and from thereon stays nearly constant at around 4% for $d_t/d_b = 0.75$ and vanish for $d_t/d_b = 0.5$. It might be due distance stabilisation phenomenon mentioned by Georgievskii and Levin [64], which states the effectiveness remains unchanged as the arc to nose distance is increased beyond a certain value. One important thing to note is that energy deposition at shorter distances might result higher stagnation point heating rates, which are detrimental, yet in current test campaign the amount of energy input is very small and the relaxation distance is shorter than arc to nose distance.

4.3 Energy deposition via laser focusing

In the tests with pulsed energy deposition, the truncated cone-cylinder with $d_t/d_b = 0.5$ is tested with $l/d_t = 1.3$ to evaluate the effect of laser focusing on blunt body flow field. Only a single pulse is fired at an estimated power of

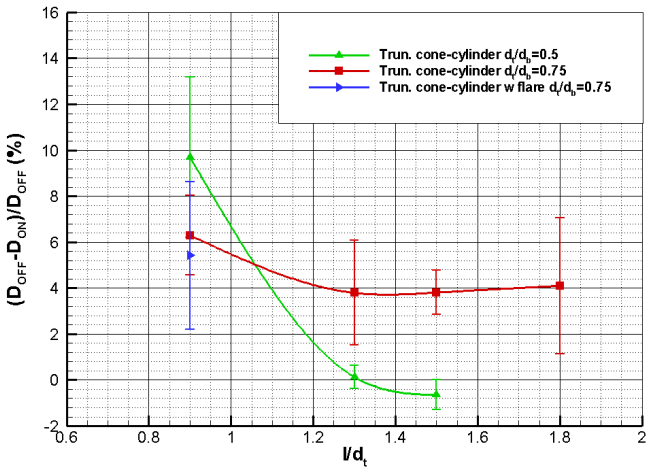

Figure 4.34: The effectiveness of arc discharge on truncated models against distance between the electrodes and the frontal area.

150mJ per pulse with the double-cavity Q-switched 532nm Nd:YAG laser. Laser beam diameter is 6mm as quoted by the manufacturer and a series of lenses is utilised to focus a very small laser spot (of size less than 1mm) in front of the model. As a crude calculation; 150mJ of energy in 4nsec pulse deposited in a spherical point of 1mm diameter result a heating power ratio of 2.36×10^6 for the flow condition specified in Section 2.3). This ratio is orders of magnitude higher than the ratio for the electric arc, therefore significant alteration in the flowfield is expected. Figure 4.35 shows schlieren visualisation of the flowfield of the truncated cone-cylinder with $d_t/d_b = 0.5$ at 36000 fps with 3.25μ sec exposure. It should be noted that the energy density for the current setup and laser system is below the air breakdown threshold at the freestream pressure, thus the laser induced breakdown/blastwave does not occur at the free stream conditions.

It can be easily deducted from the figure that significant alteration in the blunt body flowfield is achieved. The effective interaction time is 0.450msec and it is orders of magnitude longer than the pulse width of 4nsec. This phenomenon is related to the receptivity of the flow to the disturbances of energy addition. The laser focused energy spot creates a local heated area, it propagates towards the body and interacts with bow shock in front of the body. The density gradient in outward direction due to local heat addition is coupled with the pressure gradient due to the bow shock. This coupling generates baroclinic vortices as the density gradient is orthogonal to the pressure gradient, which is in horizontal direction. Thus the cross product of these two creates rotational structures as it can be seen

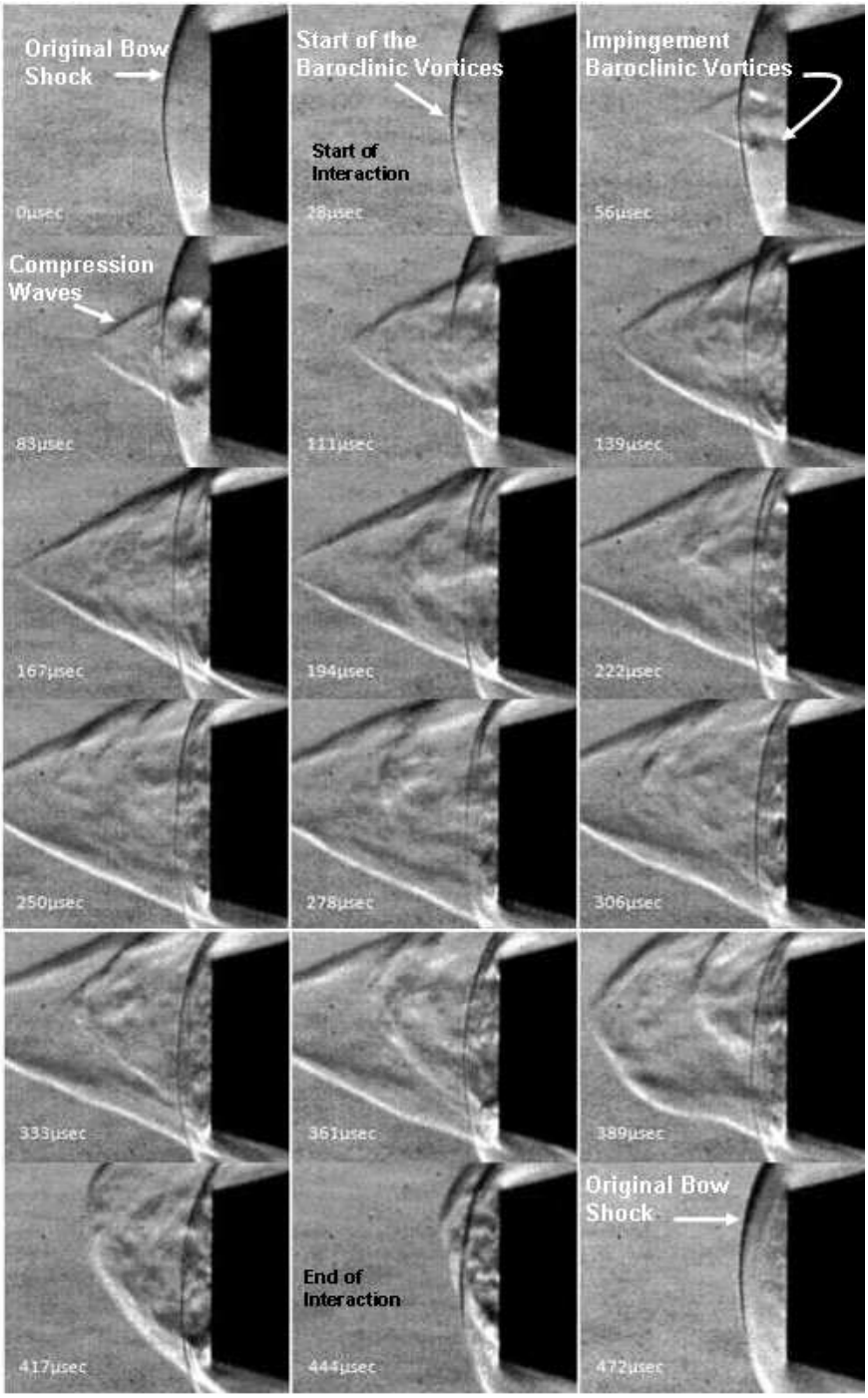

Figure 4.35: Schlieren visualisation of the effect of the focussed laser deposition on the truncation cone-cylinder with $d_t/d_b = 0.75$ and $l/d_t = 1.3$.

at the early stages of the interaction in Figure 4.35. These vortices propagate towards the body, enlarge in space. Afterwards they hit the body, get reflected from the body (Len's Effect) and significantly alter the bow shock structure in

a grand scale forming the compression waves. These compression waves extend upstream, forming a cone-like flow structure hence the aerodynamically shaping is achieved. Towards the end of the interaction these waves weaken and start to disappear. Finally the original bow shock shape is restored. Naturally drag reduction is obtained however it can not be quantified/located on drag history due to low frequency response of the body/force balance combination.

Chapter 5

Conclusion and Future Recommendations

The major outcomes of the thesis and the recommendations for the future work are described below in detail.

5.1 Transverse jets at Mach 5 cross flow

Experiments involving a sonic round jet injected into high speed cross flow at Mach 5 over a flat plate with a sharp leading edge were carried out. The effects of unit Reynolds number, type of the injectant gas and surface roughness on three dimensional jet interaction dynamics were examined with three different jet to free stream momentum flux ratio. The boundary layer developing on the flat plate was laminar and three gases were injected, air, Helium and Carbon Dioxide. Jet to free stream momentum flux ratio, J, was varied from 1.13 to 6.18, unit Reynolds number was set at 5.6, 8.1 and $13.1 \cdot 10^6 1/m$. Three different rough surfaces are used such as, P1000, P400 and P120.

As the momentum flux ratio is increased prominent curved flow structures extent in upstream and downstream directions as well as in spanwise direction, the magnitude of non-dimensional pressure values associated with the flow structures rises, especially the pressure peak at the upstream of the jet orifice. Jet penetration is found to be a non linear function of J and the separation location extends upstream 3.5-6 times the penetration height for laminar tests depending parameters affecting the interaction.

The baseline tests for air injection over a smooth plate with $13 * 10^6 1/m$

served as a means to get fundamental insight about the physical behaviour of the interaction between the transverse jets and Mach 5 cross flow, furthermore to build up confidence in experimental results to further examine the effects of different parameters that are mentioned above, on the interaction.

The downstream pressure distribution in all cases were not affected by the developing boundary layer on the flat plate. In case of upstream pressure distribution, as the unit Reynolds number is decreased the jet affected area grew, the pressure peaks were increased and possibly leading to the net force on the plate to be modified favourably. For the design of injection systems for hypersonic vehicles flying at different altitudes, this phenomenon has to be taken into account. The interaction force is bigger at high altitudes due to lower unit Reynolds number.

It is believed that the type of injectant gas is clearly a case changing parameter in terms of penetration and spreading behaviour in near and farfield. The injectant gas definitely influenced the pressure distribution and the size of upstream and downstream flow structures with lateral extent in spanwise direction. For the similar values of J three different gases, air, Helium and Carbon Dioxide exhibited very different penetration and mixing behaviour as well as very distinct pressure distribution. Carbon Dioxide jet provided smaller penetration but favourable interaction at the upstream region and Helium jet provided great penetration and favourable interaction at the downstream region compared to air jet. Jet interaction flow field can not be oversimplified and represented with only one parameter that is J; type of injectant gas definitely plays a role through γ especially on downstream region. Considering the upstream region is much more critical for the creation of aerodynamics forces and moments, Helium or an alternative lighter gas is mainly beneficial for better penetration and mixing in the farfield for scramjet applications rather than the creation of necessary side forces. On the other hand Carbon Dioxide is more useful for aerodynamic steering and also flame holding in the near field of the jet where it suspends dominantly. For the design of injection systems for hypersonic vehicles flying at different altitudes, this characteristics have to be taken into account.

The magnitudes of the upstream pressure distributions and pressure peak were incremented by the presence of roughness. Hence the effectiveness of jet interaction is increased. P1000 and P400 were found to be favourable surfaces due to their ability to augment pressure distribution without significantly modifying the state of the upstream boundary layer. However one important fact to be

aware of is that roughness also augments the heat transfer rate. For the design of injection systems for hypersonic vehicles flying through harsh environments and subjecting to ablation, collective augmentation of pressure and heat transfer distribution has to be considered.

Two dimensional CFD simulations for the case of Spaid and Zukoski [1] were carried out to validate the numerical solver and to gain confidence in numerical procedure. Computed non-dimensional wall pressure distributions showed very good agreement with experimental data. In addition transition locations were captured with acceptable accuracy. $\kappa - \omega$ SST model provided quite accurate results over a wide range of pressure ratios for such a complex flow field. Afterwards a three dimensional case is simulated and compared to the current experimental data. The agreement is found to be good in terms of flow structures and non-dimensional wall pressure distributions.

5.2 Energy deposition

Experiments addressing the effect of energy deposition via arc discharge and laser focusing on 15° half angle truncated cone-cylinder configurations and a truncated cone-cylinder-flare configuration in Mach 5 flow were carried out. The models included cone-cylinders without truncation for baseline comparison as well. The flowfields around the baseline models were characterised via Schlieren photography and CFD. The force measurements were conducted in addition and the results were compared with CFD and Newtonian theory. The experimental results are in very good agreement with CFD in terms of flowfield features and drag forces demonstrating the quality of measurements.

The arc discharge was accomplished using a setup that consisted of power supply, high voltage unit and tungsten electrodes. The aerodynamic interference of electrodes without the arc discharge was also assessed and tried to be minimised. Discharge-on cases were always compared to "discharge-off" to evaluate the net effect of energy deposition. Visual observations revealed that there was a certain size of the relaxation distance as the test gas sweeps the energy spot downstream forming a heated wake. The compression waves occurred on top of the wake of the heated channel and oscillatory in nature. The amount of energy deposited was found to be around 7W which is very small compared flow energy, nonetheless its influence on drag force was observed systematically for all the

models. Repeatable drag reduction (compared to discharge-off cases naturally) was achieved for all the cases. The effectiveness of this method was found to be increasing with increased truncation or the frontal area. In case of the distance between the energy spot and the frontal face, the efficiency was maximised when the distance is shortest and from thereon it decreased and became ineffective as it is located far from the body. However an important thing to note is that energy deposition at shorter distances might result higher stagnation point heating rates which are detrimental. As a final conclusion test campaign clearly renders that the use of small amount of onboard energy to create a local focused thermal spot in front of a vehicle is an efficient way of reducing drag.

In terms of laser focusing in front of a blunt body, the energy spot was accomplished by focusing a Q-switched 532nm Nd:YAG laser with a series of optics in front of a truncated cone-cylinder model. The amount of energy added is orders of magnitude higher than the arc discharge, therefore significant bow shock moderation was achieved. The baroclinic vortices were formed, propagated towards the body and reflected from it forming compression waves, which aerodynamically shaped the shock structure. As the interaction occurred very quickly, force balance could not sense it.

5.3 Future recommendations

Future work/recommendations include the following for transverse jet interaction phenomenon;

- To assess the complex three dimensional behaviour of jet cross flow interaction, stereoscopic PIV has to be carried out at various off-centre planes as well as parallel planes above the flat plate.
- Proper orthogonal decomposition of PIV data is necessary to decompose the convecting jet shear layer structures spatially as these structures are responsible for far-field mixing.
- The Mach 5 crossing flow has to be seeded with particles to assess the jet interaction phenomenon from the main flow point of view.
- Force measurements can provide performance details about the effectiveness of jet interaction phenomenon on the flat plate.

- CFD examination of transverse jet interaction flows especially on rough surfaces for laminar boundary layers is a challenge that has to be tried.

Future work/recommendations include the following for energy deposition phenomenon;

- Stagnation point pressure/heat transfer rate have to measured to evaluate the overall effect of arc discharge on the frontal surface.
- Laser focusing experiments at various repetition rates have to be realised as local heat addition via laser focusing is the only applicable scenario in real flight conditions.

Bibliography

[1] Spaid F. W. and Zukoski E. E.: Study of the Interaction of Gaseous Jets from Transverse Slots with Supersonic External Flows. AIAA J. Vol. 6, No. 2, 205–212, 1968

[2] Spaid F. W.: Two-Dimensional Jet Interaction Studies at Large Values of Reynolds and Mach Numbers. AIAA J. Vol. 13, No. 11, 1430–1434, 1974

[3] Schetz J. A. and Billig F. S.: Penetration of Gaseous Jets Injected into a Supersonic Stream. J. of Spacecraft and Rockets Vol. 3, No. 11, 1658–1665, 1966

[4] Parthasarathy K. and Zakkay V.: An Experimental Investigation of Turbulent Slot Injection at Mach 6. AIAA J. Vol. 8, No. 7, 1302–1307, 1969

[5] Hawk N. E. and Amick J. L.: Two-Dimensional Secondary Jet Interaction with a Supersonic Stream. AIAA J. Vol. 5, No. 4, 555–660, 1967

[6] Werle M.J., Driftmyer R.T., and Shaffer D.G.: Jet-Interaction-Induced Separation:The Two-Dimensional Problem. AIAA J. Vol. 10, No. 2, 188–193, 1971

[7] Broadwell J.E.: Analysis of Fluid Mechanics of Secondary Injection for Thrust Vector Control. AIAA J., Vol. 1, No. 10, 1067–1075, 1963

[8] Masuya G.: Secondary Gas Injection into a Supersonic Conical Nozzle. AIAA J., Vol. 15, No.3, 301–302, 1977

[9] Inouye T.: Experiments on Rocket Thrust Vector Control by Hot Gas Injection. J. of Spacecraft and Rockets, Vol. 3, No.4, 737–739, 1966

[10] Zeierman I. and Timnat Y. M.: Full Control of Solid Propellant Rockets by Secondary Injection. J. of Spacecraft and Rockets , Vol. 10, No. 3, 1973

[11] Papamoschou D. and Roshko A.: The Compressible Turbulent Shear Layer: An Experimental Study. J. Fluid Mech. 197, 453, 1988

[12] Sandham N. D. and Reynolds W. C.: Compressible Mixing Layer: Linear Theory and Direct Simulation. AIAA J. 38, 618, 1990

[13] Leep L. J., Dutton J. C. ,and Burr R. F.: Three Dimensional Simulations of Compressible Mixing Layers: Visualizations and Statistical Analysis. AIAA J. 31, 2039, 1993

[14] Samimy M. and Elliott G. S.: Effects of Compressibility on the Characteristics of Free Shear Layers. AIAA J. 28, 439, 1990

[15] Goebel S. G. and Dutton J. C.: Experimental Study of Compressible Turbulent Mixing Layers. AIAA J. 29, 538, 1991

[16] Messersmith N. L. and Dutton J. C.: Characteristic Features of Large Structures in Compressible Mixing Layers. AIAA J. 34, 1814, 1996

[17] Papamoschou D. and Bunyajitradulya A.: Evolution of Large Eddies in Compressible Shear Layers. Phys. Fluids 9 (3), 1997

[18] Ben-Yakar A.: Experimental Investigation of Mixing and Ignition of Transverse Jets in Supersonic Crossflows. Ph.D. Thesis, Department of Mechanical Engineering, Stanford University, CA, USA, 2001

[19] Gutmark E. J., Schadow K. C., and Yu K. H.: Mixing Enhancement in Supersonic Free Shear Flows. Annu. Rev. Fluid Mech. 1995.27: 375-417

[20] Gruber M. R., Nejad A. S., Chen T. H., and Dutton J. C.: Mixing and Penetration Studies of Sonic Jets in a Mach 2 Freestream. J. of Propulsion and Power, Vol. 11, No. 2, 1995, pp. 315-323

[21] Bushnell D. M.; Hypervelocity Scramjet Mixing Enhancement. J. Propulsion and Power, Vol. 11, No. 5, 1995

[22] Drummond J. P. and Makunda H. S.: A Numerical Study of Mixing Enhancement in Supersonic Reacting Flow Fields. AIAA 88-3260

[23] King P. S., Thomas R. H., Schetz J. A., and Billig F. S.: Combined Tangential-Normal Injection into a Supersonic Flow. J. of Propulsion and Power, Vol. 7, 420–460, 1991

[24] Sutton, G.W.: Rocket Propulsion Elements, 7th ed., John Wiley and Sons, 2001.

[25] Erdem E., Albayrak K., and Tinaztepe H. T.: Parametric Study of Secondary Gas Injection into a Conical Rocket Nozzle for Thrust Vectoring. AIAA Paper 2006-4942.

[26] Newton J. F. and Spaid F. M.: Interaction of Secondary Injectants and Rocket Exhausts for Thrust Vector Control, J. of the American Rocket Society, 1203–1211, 1962

[27] Balu R.: Analysis of Performance of a Hot Gas Injection Thrust Vector Control System. J. of Propulsion and Power, Vol. 4, 580–585, 1991

[28] Ko H. and Yoon W.: Performance Analysis of Secondary Gas Injection into a Conical Rocket Nozzle. J. of Propulsion and Power, vol: 18, 585–591, 2002

[29] Kumar D., Stollery J. L., and Smith A.J.: Hypersonic Jet Control Effectiveness. J. Shock Waves, Vol. 7, 1–12, 1997

[30] Kontis K. and Stollery J. L.: Control Effectiveness of a Jet-Slender Body Combination at Hypersonic Speeds. J. of Spacecraft and Rockets, Vol. 34, No. 6, 762–768, 1997

[31] Brandeis J. and Gill J.: Experimental investigation of super-and hypersonic jet interaction on missile configurations. J. of Spacecraft and Rockets, Vol. 35, No. 3, 296–302, 1998

[32] Seiler F., Gnemmi P., Ende H., Schwenzer M., and Meuer R.: Jet interaction at supersonic cross flow conditions. J. of Shock Waves, Vol. 3, No. 1, 13–23, 2003

[33] Gulhan A., Schutte G., and Stahl, B.: Experimental study on aerothermal heating caused by jet-hypersonic crossflow interaction. J. of Spacecraft and Rockets, Vol. 45, No. 5, 891–899, 2008

[34] Viti V., Neel R., and Schetz, J. A.: Detailed flow physics of the supersonic jet interaction flow field. Phys. Fluids 21, 2009

[35] Zukoski E. E. and Spaid F. W.: Secondary Injection of Gases into a Supersonic Flow. AIAA J., Vol.2, No.10, 1964

[36] Chenault C. F., Beran P. S., and Bowersox R. D. W.: Numerical Investigation of Supersonic Injection Using a Reynolds-Stress Turbulence Model. AIAA J., Vol. 37, No. 10, 1999

[37] Santiago J. G. and Dutton J. C.: Crossflow Vortices of a Jet Injected into a Supersonic Crossflow. AIAA J., Vol. 35, No. 5, 1997

[38] Haven B. A. and Kurosaka M.: Kidney and anti-kidney vortices in crossflow jets. J. Fluid Mech. 352, 1997

[39] Srinivasan R. and Bowersox R. D. W.: Characterization of Flow Structures and Turbulence in Hypersonic Jet Interaction Flowfields. AIAA 2005-0895

[40] Cassel L.A.: Applying jet interaction technology. J. of Spacecraft and Rockets, Vol. 40, No. 4, 523–537, 2003

[41] Rizzetta D. P.: Numerical Simulation of Slot Injection into a Turbulent Supersonic Stream. AIAA J., Vol. 30, No. 10, 2434–2439, 1992

[42] Dhinagaran R. and Bose T. K.: Numerical Simulation of Two-Dimensional Transverse Gas Injection into Supersonic External Flows. AIAA J., Vol. 36, No. 3, 485–487, 1998

[43] Chenault C. and Beran P. S.: κ–ϵ and Reynolds Stress Turbulence Model Comparisons for Two-Dimensional Flows. AIAA J., Vol. 36, No. 8, 1401–1412, 1998

[44] Qin N. and Redlich A.: Massively Separated Flows due to Transverse Sonic Jet in Laminar Hypersonic Stream. J. Shock Waves, Vol. 9, 87–93, 1999

[45] Won S., Jeung I., and Choi J. Y.: DES Study of Transverse Jet Injection into Supersonic Cross Flows. AIAA Paper 2006-1227

[46] Sriram A. T. and Mathew J.: Improved Prediction of Plane Transverse Jets in Supersonic Crossflows. AIAA J., Vol. 44, No. 2, 405–408, 2006

[47] Erdem E. and Kontis K.: Numerical and experimental investigation of transverse injection flows. J. Shock Waves, Vol. 20, No. 2, 103–118, 2010

[48] Everett D. E. and Morris M. J.: Wall Pressure Measurements for a Sonic Jet Injected Transversely into a Supersonic Crossflow. J. of Propulsion and Power, Vol. 14, No. 6, 861–868, 1998

[49] Sriram A. T. and Mathew J.: Numerical simulation of transverse injection of circular jets into turbulent supersonic streams. J. of Propulsion and Power, Vol. 24, No. 1, 45–54, 2008

[50] Kawai S. and Lele S. K.: Large-eddy simulation of jet mixing in supersonic crossflows. AIAA J., Vol. 48, No. 9, 2063–2083, 2010

[51] Latin R. M. and Bowersox R. D. W.: Flow Properties of a Supersonic Turbulent Boundary Layer with Wall Roughness. AIAA J. Vol. 38, No. 10, 1804–1821, 2000

[52] Disimile P. J. and Scaggs N. E.: An investigation into wedge-induced turbulent boundary layer separation on a uniformly roughened surface at Mach 6. AIAA 1989

[53] Christoph G. H. and Fiore A. W.: Experimental and Computational Study of Roughness Effects at Mach 6. AIAA 1984

[54] Babinsky H. and Edwards J.: Large-scale roughness influence on turbulent hypersonic boundary layers approaching compression corners. J. of Spacecraft and Rockets, Vol. 34, No.1, 70–75, 1997

[55] Babinsky H. and Inger G. R.: Effect of Surface Roughness on Unseparated Shock-Wave/Turbulent Boundary-Layer Interactions. AIAA J., Vol. 40, No. 8, 1567–1573, 2002

[56] Prince S. A., Vannahme M., and Stollery, J. L.: Experiments on the hypersonic turbulent shock-wave/boundary-layer interaction and the effects of surface roughness. Aero. Journal, Vol. 109, 177–186, 2005

[57] Satheesh K. and Jagadeesh G.: Effect of concentrated energy deposition on the aerodynamic drag of a blunt body in hypersonic flow. Phys. Fluids 19, 031701, 2007

[58] Riggins D., Nelson H. F., and Johnson, E.: Blunt-body wave drag reduction using focused energy deposition. AIAA J., Vol. 37, No. 4, 460–467, 1999

[59] Bogdonoff S. M. and Vas I. E.: Preliminary investigations of spiked bodies at hypersonic speeds. J. Aero, Vol. 26, No. 2, 65–74, 1959

[60] Finley, P.J.: The Flow of a Jet from a Body Opposing a Supersonic Stream. Journal of Fluid Mechanics, 26(2), 1966, 337–368

[61] Shang, J. S., Hayes, J., Wurtzler, K., Strang, W.: Jet-Spike Bifurcation in High-Speed Flows. AIAA J., Vol. 37, No. 6, 2001, 1159–1165

[62] Shang J. S.: Plasma Injection for Hypersonic Blunt Body Drag Reduction. AIAA J., Vol. 40, 1178–1186, 2002

[63] Bletzinger P., Ganguly B. N., VanWie D., and Garscadden A.: Plasmas in High Speed Aerodynamics. Journal of Physics D: Applied Physics 38 R33, 2005

[64] Georgievskii P. and Levin V.: Supersonic Flow over a Body with Heat Supply Ahead of it. Proceedings of the Steklov Inst. of Mathematics, Steklov Inst. of Mathematics, American Mathematical Society, Providence, RI, 1991, 229–234.

[65] Myrabo L. N. and Raizer Y. P.: Laser Induced Air Spikes for Advance Trans Atmospheric Vehicles. AIAA 1994-2451

[66] Levin V. A., Afonina N. A., and Gromov V. G.: Navier-Stokes Analysis Of Supersonic Flow With Local Energy Deposition. AIAA-99-4967

[67] Kolesnichenko Y., Brovkin V., Azarova O., Grudnitsky V., Lashkov V., Mashek I.: Microwave Energy Release Regimes for Drag Reduction in Supersonic Flows. AIAA 2002-0353

[68] Girgis I. G., Shneider M. N., Macheret S. O., Brown G. L., and Miles R. B.: Creation of Steering Moments in Supersonic Flow by Off-Axis Plasma Heat Addition. AIAA 2002-0129

[69] Georgievskii, P., and Levin, V.: Control of the Flow Past Bodies using Localized Energy Addition to the Supersonic Flow. Fluid Dynamics, Vol. 38, No. 5, 794–805, 2003

[70] Zheltovodov A. A., Pimonov E. A, and Knight D. D.: Energy Deposition Influence on Supersonic Flow Over Axisymmetric Bodies. AIAA 2007-1230

[71] Knight D.:Survey of Aerodynamic Drag Reduction at High Speed by Energy Deposition. J. of Propulsion and Power, Vol. 24, No. 6, 1153–1167, 2008

[72] Lashkov V. A., Mashek I. C., Anisimov Yu. I., Ivanov V. I., Kolesnichenko Y. F., Ryvkin M. I., Gorynya A. A.: Gas Dynamic Effect of Microwave Discharge on Supersonic Cone-Shaped Bodies. AIAA 2004-0671

[73] Exton R., Balla R., Shirinzadeh B., Brauckmann G., Hering G., Kelliher W., Fugitt J., Lazard C., Khodataev K.: On-Board Projection of a Microwave Plasma Upstream of a Mach 6 Bow Shock, Physics of Plasmas, Vol. 8, No. 11, 2001

[74] Tretyakov P., Garanin A., Kraynev V., Tupikin A., Yakovlev V.: Investigation of Local Laser Energy Release Influence on Supersonic Flow by Methods of Aerophysical Experiments. Proceedings of the 8th International Conference on Methods in Aerophysical Research, Inst. of Theoretical and Applied Mechanics, Russian Academy of Sciences, Siberian Division, Novosibirsk, Russia, 200–204, 1996

[75] Adelgren R. G., Yan H., Elliott G. S., Knight D., Beutner T. J., Zheltovodov A. A., Ivanov M., Khotyanovsky D.: Localized flow control by laser energy deposition applied to Edney IV shock impingement and intersecting shocks. AIAA Aerospace Sciences Meeting and Exhibit, 41st, Reno, NV, 2003

[76] Yan H., Adelgren R., Elliott G., Knight D., Beutner T., and Ivanov M.: Laser Energy Deposition Intersecting Shocks. AIAA 2002-2729

[77] Salyer T. R., Collicott S. H., and Schneider S. P.: Characterizing Laser Generated Hot Spots for Receptivity Studies, AIAA J., Vol. 44, No. 12, 2006

[78] Sakai T., Sekiya V., Mori K., and Sasoh A.: Interaction between laser-induced plasma and shock wave over a blunt body in a supersonic flow. Proc. IMechE Vol. 222 Part G: J. Aerospace Engineering, 2008

[79] Minucci M. A. S., Toro P. G. P., Oliveira A. C., Ramos A. G., Chanes J. B. Jr., Pereira A. L., Myrabo L. N., Nagamatsu H. T.: Laser-Supported Directed-Energy Air Spike in Hypersonic Flow. Journal of Spacecraft and Rockets, Vol. 42, No. 1, 2005, 51–57.

[80] Oliveira A. C., Minucci M. A. S., Toro P. G. P., Chanes J. B. Jr., Myrabo L. N., Nagamatsu H. T.: Bow Shock Wave Mitigation by Laser-Plasma

Energy Addition in Hypersonic Flow. Journal of Spacecraft and Rockets, Vol. 45, No. 5, 2008, 921–927

[81] Myrabo L. N., Raizer Y. P., Shneider M. N., and Bracken R.: Reduction of Drag and Energy Consumption during Energy Release Preceding a Blunt Body in Supersonic Flow. Heat and Mass Transfer and Gasdynamics, High Temperature, Vol.42, No.6, 2004, 901–910

[82] Satheesh K. and Jagadeesh G.: Experimental Investigations on the Effect of Energy Deposition in Hypersonic Blunt Body Flow Field. J. of Shock Waves, 18:53-70, 2008

[83] Schulein E. and Zheltovodov A.: Effects of steady flow heating by arc discharge upstream of non-slender bodies. J. Shock Waves, Vol. 20, No. 2, 1–14, 2011

[84] Settles G. S.: Schlieren and Shadowgraph Techniques. Springer-Verlag Berlin 2001.

[85] Kontis K.: Projectile Aerodynamics: Measurement and Computation. PhD Thesis, Cranfield College of Aeronautics, 1997

[86] Melling A.: Tracer particles and seeding for particle image velocimetry. Meas. Science and Technology, Vol. 8, 1997

[87] Scarano F.: Overview of PIV in Supersonic Flows. A. Schroeder, C.E. Willert (Eds.): Particle Image Velocimetry, Topics Appl. Physics 112, 445-463, 2008

[88] Samimy M. and Lele S. K.: Motion of particles with inertia in a compressible free shear layer. Phys. of Fluids, Vol.3, 1991

[89] Pope A. and Goin K. L.: High-speed wind tunnel testing. RE Krieger Pub. Co. 1965.

[90] Moffat R. J.: Describing the uncertainties in experimental results. Exp. Thermal Fluid Sci. 1(1), 3–17 (1988)

[91] Fluent v.6.3.26 Documentation (2006)

[92] Smits A. J. and Dussauge J. P.: Turbulent shear layers in supersonic flow. Springer Verlag Berlin 2006.

[93] Simeonides G. A. : Correlation of laminar-turbulent transition data over flat plates in supersonic/hypersonic flow including leading edge bluntness effects. J. of Shock Waves, Vol. 12, pp. 497-508, 2003

[94] Anderson J. D.: Hypersonic and High Temperature Gas Dynamics, McGraw Hill, 2006

[95] Needham D. A.: Laminar Separation in Hypersonic Flows. PhD Thesis, University of London, 1965

[96] Popinski Z. and Ehrlich C.F.: Development Design Methods for Predicting Hypersonic Aerodynamic Control Characteristics. AFFDL-TR-66-85, 1966

[97] Eckert E. R. G.: Engineering Relations for Friction and Heat Transfer to Surfaces in High Velocity Flow. J. Aeronautical Science, vol.22, 585–587, 1955

[98] Perurena B. J., Asma C. O., Theunissen R., and Chazot O.: Experimental investigation of liquid jet injection into Mach 6 hypersonic crossflow. Exp. in fluids, Vol. 46, No. 3, 403–417, 2009

[99] Joshi P. B. and Schetz J. A.: Effect of Injector Geometry on the Structure of a Liquid Jet Injected Normal to a Supersonic Airstream. AIAA J., Vol. 13, No. 9, 1137–1138, 1975

[100] Ames Research Staff: Report 1135: equations, tables and charts for compressible flow. Naca, 1953.

[101] Liepman H. W. and Roshko A.: Elements of Gas Dynamics. John Wiley, New York, 1957, Reprint 2001.

[102] Bertin J. J.: Hypersonic aerothermodynamics. AIAA, 1994

[103] Simeonides G. and Haase W.: Experimental and computational investigations of hypersonic flow about compression ramps. J. of Fluid Mech., Vol. 283, 17–42, 1995

[104] Yang L., Erdem E., and Kontis K.: Pressure-Sensitive Paint Application on Two-Dimensional and Axisymmetric Model in Hypersonic Flow. AIAA 2011

[105] Savino R. and Paterna D.: Blunted cone-flare in hypersonic flow. Comp. and Fluids, Vol. 34, No. 7, 859–875, 2005

[106] Erdem E., Yang L. and Kontis K.: Drag Reduction Studies by Steady Energy Deposition at Mach 5. AIAA 2011

[107] Stollery J. L. and Bates L.: Turbulent Hypersonic Viscous Interaction. J. of Fluid Mech., Vol.63, part1, pp145-156, 1974

[108] Van Driest E. R.: The turbulent boundary layer with variable Prandtl number, in 50 Jahre Grenzschichtforschung, 1955

[109] White F. M.: Viscous Fluid Flow. McGraw-Hill New York 2006.

[110] Schlichting H. and Gersten K.: Boundary Layer Theory. Springer-Verlag Berlin 2001.

Appendix A

Flat Plate Theory in Hypersonic Flow

A.1 Hypersonic viscous interactions

In the high supersonic and hypersonic flow regimes strong viscous interaction occurs if attached boundary layer becomes very large, which is associated with high Mach numbers M and relatively low Reynolds numbers Re. In fact the boundary layer thickness, δ, is proportional to $M/\sqrt{Re_x}$ at these flight regimes. At the leading edge of vehicles sudden growth of boundary layer deflects incoming flow extensively and consequently outer flow sees an effectively thicker body with growing thickness. In return outer flow has to go through a smaller streamtube area and has to change its direction; this occurs with a curved shock wave forming at the leading edge. As a consequence the outer flow at the edge of boundary layer is altered, pressure levels are increased and the changes are fed back to the boundary layer affecting its growth and properties as it is shown in Fig. A.1. This mutually interacting flow pattern is called "hypersonic viscous interaction" and it can have important effects on the surface pressure, shear stress and heat transfer distributions of hypersonic vehicles thus modifying their lift, drag and stability characteristics. If this interaction is severe then it is called strong viscous interaction especially occurring in laminar regimes and if it is not considerable, it is called weak viscous interaction [94].

The pressure distribution over a flat surface in the presence of viscous interaction can be written as a function of hypersonic similarity parameter, K, expressed in Eqn. A.1 below.

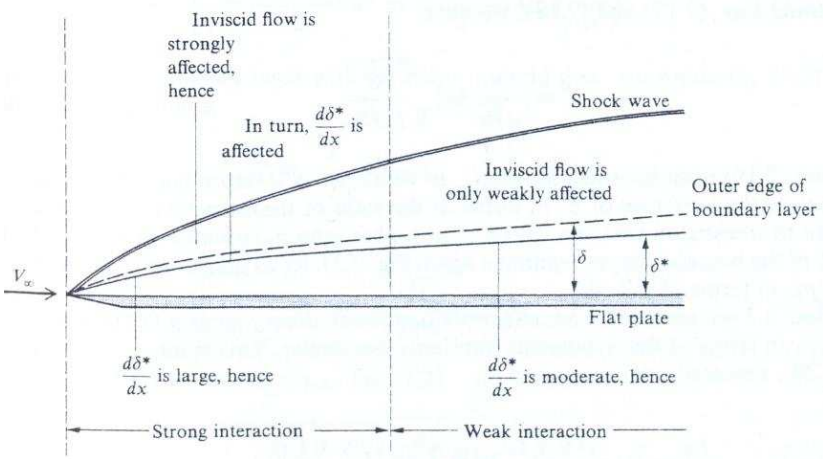

Figure A.1: Hypersonic viscous interaction phenomenon by Anderson [94].

$$\frac{p_e}{p_\infty} = 1 + \frac{\gamma(\gamma+1)}{4} + \gamma K^2 \sqrt{\left(\frac{\gamma+1}{4}\right)^2 + \frac{1}{K^2}} \tag{A.1}$$

where

$$K = M_\infty \frac{d\delta^*}{dx}$$

The pressure at the edge of the boundary is certainly greater than the free-stream pressure due to viscous interaction. Depending on the value of K the strength of the phenomenon varies and some terms drop, some prevail. The governing parameter determining how severe this interaction is, is called laminar viscous interaction parameter and given in Eqn. A.2.

$$\bar{\chi} = M_\infty^3 \sqrt{\frac{C_w}{Re_x}} \equiv K^2 \tag{A.2}$$

where C_w is Chapman Rubesin constant at the wall and expressed below in Eqn. A.3;

$$C_w = \frac{\rho_w \mu_w}{\rho_e \mu_e} \approx \left(\frac{T_w}{T_e}\right)^{-1/3} \tag{A.3}$$

If $\bar{\chi}$ is small, less than three, weak interaction occurs if it is greater than three strong interaction dominates [94]. For strong interaction;

$$\delta^* \propto x^{3/4},\ d\delta^*/dx \propto x^{-1/4} \text{ and } \frac{p_e}{p_\infty} = 1 + a_1 \bar{\chi}$$

For weak interaction;

$$\delta^* \propto x^{1/2},\ d\delta^*/dx \propto x^{-1/2} \text{ and } \frac{p_e}{p_\infty} = 1 + b_1\bar{\chi} + b_2\bar{\chi}^2$$

Strong and weak interaction formulas for an insulated plate ($T_w \approx T_{aw}$) reveal [94] ;

$$\frac{p_e}{p_\infty} = 0.759 + 0.514\bar{\chi} \tag{A.4}$$

$$\frac{p_e}{p_\infty} = 1 + 0.31\bar{\chi} + 0.05\bar{\chi}^2 \tag{A.5}$$

For a cold plate ($T_w < T_{aw}$); strong and weak interaction formulas reveal;

$$\frac{p_e}{p_\infty} = 1 + 0.15\bar{\chi} \tag{A.6}$$

$$\frac{p_e}{p_\infty} = 1 + 0.078\bar{\chi} \tag{A.7}$$

$\bar{\chi}$ actually varies along the surface due to local Re; at the leading edge it is at its highest and decreases along the plate. Therefore if incoming Re is moderately high and transition location is close to the leading edge turbulent viscous interaction can occur and this is governed by turbulent viscous interaction parameter [107] as depicted in Eqn. A.8.

$$\bar{\chi}_t = \left[\frac{M_\infty^9 C_w}{Re_x}\right]^{0.2} \tag{A.8}$$

A.2 Exact solutions from Van Driest

Flat plate skin friction and heat transfer coefficients were calculated by Van Driest in 1950s for various Mach numbers and wall temperatures. These plots are shown in Fig. A.2. For the computations he used Sutherland's law of viscosity together with a constant Prandtl number of 0.75. For a specific Mach number and wall to edge temperature ratio the specific constant value can be extracted.

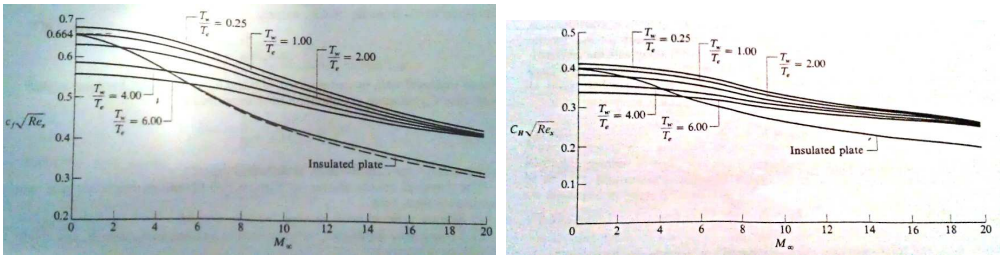

Figure A.2: Flat plate skin friction coefficients (left) and Stanton numbers (right) by van Driest [108]

A.3 Reference temperature concept and Reynolds analogy

An approximate method to estimate skin friction coefficient, c_f, and heat transfer coefficient (Stanton number), c_H, in hypersonic laminar/turbulent flat plate flow is used, called Reference Temperature method. In this method incompressible flat plate formulas are corrected using a correction evaluated at the reference temperature (a kind of average temperature) in the boundary layer. In general c_f and c_H are expressed as functions of following fluid flow variables [94];

$$c_f = \frac{F\left(M_e, Pr, \gamma, \frac{T_w}{T_e}\right)}{\sqrt{Re_x}} \tag{A.9}$$

$$c_H = \frac{G\left(M_e, Pr, \gamma, \frac{T_w}{T_e}\right)}{\sqrt{Re_x}} \tag{A.10}$$

Thus c_f and c_H can be related using the Reynolds analogy as;

$$\frac{c_H}{c_f} = H\left(M_e, Pr, \gamma, \frac{T_w}{T_e}\right) \tag{A.11}$$

where

$$Re_x = \frac{Ux}{\nu}, \quad M_e = \frac{U_e}{\sqrt{\gamma R T_e}} \quad \text{and} \quad Pr = \frac{\mu c_P}{k}$$

Finally skin friction and heat transfer coefficients take the form of;

$$c_f = \frac{0.664}{\sqrt{Re_x^*}} \tag{A.12}$$

$$c_H = \frac{0.332}{\sqrt{Re_x^*}} Pr^{*-2/3} \tag{A.13}$$

where Re^* and Pr^* are evaluated at reference temperature, T^* such as:

$$Re_x^* = \frac{U_e x}{\nu^*} \quad \text{and} \quad Pr^* = \frac{\mu^* c_p^*}{k^*}$$

There are several expressions obtained from different researchers [94, 109, 97] for reference temperature calculations. The expression from Eckert [97] is adapted for this thesis as shown below in Eqn. A.14. This equation is implicit in T^* due to T_{aw} as explained below and requires few iterations to converge.

$$\frac{T^*}{T_e} \approx 0.28 + 0.5\left(\frac{T_w}{T_e}\right) + 0.22\left(\frac{T_{aw}}{T_e}\right) \tag{A.14}$$

Viscosity and thermal conductivity can be expressed at the reference temperature using Sutherland's law below.

$$\mu^* = \frac{c_1}{1 + c_2/T^*}\sqrt{T^*} \quad and \quad k^* = \frac{d_1}{1 + d_2/T^*}\sqrt{T^*}$$

Afterwards using equation of state at free-stream, boundary layer edge and reference temperature as expressed below; and assuming pressure is constant along the boundary layer (but different than free stream value due to viscous interaction); Eqn. A.15 is obtained.

$$p_\infty = \rho_\infty R T_\infty, \quad p_e = \rho_e R T_e \quad and \quad p^* = \rho^* R T^*$$

$$\rho^* = \frac{T_\infty}{T^*}\frac{p_e}{p_\infty}\rho_\infty \tag{A.15}$$

Adiabatic wall temperature is the temperature at the wall when the flow is decelerated to zero velocity adiabatically. However due to viscous dissipation some of the energy is dissipated in the boundary layer. In fact compressible boundary layers are neither adiabatic nor isentropic, a thermal boundary layer forms even in the presence of adiabatic conditions [110]. Therefore the adiabatic wall temperature is obtained when stagnation temperature outside the boundary layer is corrected with a recovery factor, r, as shown in Eqn. A.16.

$$T_{aw} = T_e \left(1 + r\frac{\gamma - 1}{2} M_e^2\right) \tag{A.16}$$

The recovery factor is equal to $\sqrt{Pr^*}$ for laminar flows and $r = \sqrt[3]{Pr^*}$ for turbulent flows. After calculating all the required fluid properties at the reference temperature, c_f and c_H can be calculated along the flat plate and these formulas can be extension to cones simply by multiplication of $\sqrt{3}$.

In terms of boundary layer thickness, δ, an estimate from Popinski and Ehrlich [96] is used which reveals laminar boundary layer thickness for blunt and sharp leading edge flat plates as;

$$\delta = \frac{5.2}{\sqrt{\frac{p}{p_\infty}}} \sqrt{\frac{d_n x}{Re^*_{\infty d_n}}} \tag{A.17}$$

$$\delta = \frac{5.2x}{\sqrt{\frac{p}{p_\infty} Re^*_\infty}} \tag{A.18}$$

respectively, where

$$\frac{Re^*_\infty}{x} = \frac{Re_\infty}{x} \left(\frac{T_\infty}{T^*}\right)^{1.76} \tag{A.19}$$

and T^* is calculated as in Eqn. A.14 by Eckert [97]. In case of turbulent boundary layer thickness, following equation is proposed;

$$\delta = \frac{0.154x}{\left(Re_\infty (\frac{T_\infty}{T^*})^{1.67}\right)^{1/7}} \tag{A.20}$$

Appendix B

Experimental Uncertainty Calculation

The uncertainty of an experimentally measured quantity is composed of two contributions; systematic (bias) error and random error. Systematic (bias) error is repeatable and it is a measure of quality of the experimental technique, experimental setup and experimenter, etc. on the other hand random error is a measure of distribution of the many realisations nearly at the same condition and how widespread these realisations are distributed. Systematic (bias) error is related to accuracy and random error is related to precision in essence. The uncertainties in this thesis are calculated using standard techniques based on precision and bias calculations described by Moffat [90]. In general a quantity, R is dependent on many independent variables, x_i as shown below. The uncertainty in R is denoted as ΔR and it is expressed in Eqn. B.1.

$$R = R(x_1, x_2, x_3, ..., x_n)$$

$$\Delta R = \sqrt{\sum_{i=1}^{n} \left(\frac{\partial R}{\partial x_i} \Delta x_i \right)^2} \tag{B.1}$$

Using a common approximation of partial derivatives (sensitivity coefficients) to finite differences, Eqn. B.1 takes the form of Eqn. B.2. The reason for that is the complexity of deriving an analytical expression for a dependent quantity especially computing sensitivity coefficients.

$$\frac{\partial R}{\partial x_i} \approx \frac{\Delta R}{\Delta x_i} \quad then \quad \Delta R = \sqrt{\sum_{i=1}^{n} {\Delta R_i}^2} \tag{B.2}$$

The procedure to compute the uncertainty from thereon is expressed as follows:

- The mean value of the desired quantity is computed using the mean values of each input quantities up to n
- n values of the desired quantity are computed by adding successively to each variable its uncertainty
- The difference between each value and the mean value of the desired quantity is computed (ΔR_i)
- The overall uncertainty on the mean value of the desired quantity, ΔR is calculated as in Eqn. B.2

This value corresponds to the bias contribution.

In terms of precision contribution, several realisations are to be conducted. The mean and standard deviation of the desired values are obtained from the set of realisations as they are shown in Eqn. B.3. Afterwards Gaussian distribution of the desired value is assumed usually and for 95% confidence interval the standard deviation is calculated as $1.96 \cdot \sigma$.

$$\overline{R} = \sum_{i=1}^{n} R_i \quad and \quad \sigma = \sqrt{\frac{\sum_{i=1}^{n} \left(R_i - \overline{R}\right)^2}{n-1}} \tag{B.3}$$

If m number of realisations are performed then the standard deviation of the average becomes;

$$\overline{\sigma_R} = \frac{1.96 \cdot \sigma}{\sqrt{n}}$$

Finally the contributions from bias and precision are squared together as shown in Eqn. B.4 to give a final uncertainty value.

$$\delta R = \sqrt{\overline{\sigma_R}^2 + \Delta R^2} \tag{B.4}$$

Appendix C

Publication Information

C.1 Journal articles

1. Erdem E., Kontis K., "Experimental and numerical predictions for transverse injection flows", Journal of Shock Waves, 2010

2. Erdem E., Yang L., Kontis K., "Experimental and numerical investigation of sharp/truncated cone-cylinder-flare Configurations at Mach 5 flow", accepted to the International Journal of Aerospace Innovations, 2011

3. Erdem E., Kontis K., Yang L., "Steady energy deposition at Mach 5 for drag reduction", submitted to the Journal of Shock Waves, 2011

C.2 Conference articles

1. Erdem E., et al., "Effect of roughness in jets in Mach 5 cross flow", ISSW2001, 28th International Symposium on Shock Waves, Manchester, UK, 2011

2. Erdem E.,et al., "Steady energy deposition at Mach 5 for drag reduction", ISSW2001, 28th International Symposium on Shock Waves, Manchester, UK, 2011

3. Erdem E., Yang L., Kontis K., "Drag reduction studies by steady energy deposition at Mach 5", 49th AIAA Aerospace Sciences Meeting and Exhibit, Orlando, FL, 2011

4. Yang L., Erdem E., Kontis K., "Pressure-sensitive paint application on two-dimensional and axisymmetric models in hypersonic flow", Orlando, FL, 2011

5. Yang L., Erdem E., Kontis K., "Pressure-sensitive paint visualization on double ramp in hypersonic flow", ISFV14 - 14th International Symposium on Flow Visualization, Korea, 2010

6. Yang L., Erdem E., Kontis K., "Flow control using thermal bumps in hypersonic flow", 48th AIAA Aerospace Sciences Meeting and Exhibit, Orlando, FL, 2010

7. Erdem E., Yang L., Kontis K., "Study of non-plasma and plasma jets in transverse hypersonic cross flow", CEAS2009, 2nd CEAS European Air and Space Conference, Manchester, UK, October 2009

8. Erdem E., Kontis K., "Non-plasma and plasma transverse jets in hypersonic cross flow", 16th AIAA/DLR/DGLR International Space Planes and Hypersonic Systems and Technologies Conference, Bremen, Germany 2009

9. Erdem E., Yang L., Kontis K., "Drag reduction by energy deposition in hypersonic flows", 16th AIAA/DLR/DGLR International Space Planes and Hypersonic Systems and Technologies Conference, Bremen, Germany 2009

10. Erdem E., Kontis K., "Numerical predictions for transverse injection flows", ISSW2009, 27th International Symposium on Shock Waves, St.Petersburg, Russia, 2009

11. Erdem E., Kontis K., "The investigation of dependence of low frequency motion on upstream flow conditions in hypersonic flows", ICAS2008-3.7ST, 26th International Council of the Aeronautical Sciences, Anchorage, Alaska, 2008

12. Erdem E., et al., "Numerical investigation of the flow field inside a conical rocket nozzle in the presence of transverse injection", 46th AIAA Aerospace Sciences Meeting and Exhibit, Reno, NV, 2008

13. Erdem E., et al., "Parametric study of secondary gas injection into a conical rocket nozzle for thrust vectoring", 42nd AIAA/ASME/SAE/ASEE Joint

Propulsion Conference and Exhibit, Sacramento, CA, 2006 (Also presented in 1st National FLUENT Users conference in Ankara July 2006)

14. Erdem E., et al., "The experimental and numerical investigation of the flow field inside a solid propellant booster in presence of slag accumulation", AIAC2005-032, 3rd Ankara International Aerospace Conference, Ankara, August 2005